2014-09-30

Integration of Geomechanical Parameters and Numerical Simulation for an Offshore Reservoir in the Gulf of Mexico

Manzano Angeles, David

UNIVERSITY OF CALGARY

Integration of Geomechanical Parameters and Numerical Simulation for an Offshore Reservoir in the Gulf of Mexico

by

David Manzano Angeles

A THESIS

SUBMITTED TO THE FACULTY OF GRADUATE STUDIES

IN PARTIAL FULFILMENT OF THE REQUIREMENTS FOR THE

DEGREE OF MASTER OF ENGINEERING

GRADUATE PROGRAM IN CHEMICAL AND PETROLEUM ENGINEERING

CALGARY, ALBERTA

SEPTEMBER, 2014

Abstract

The primary objective of this thesis is the evaluation of geomechanical behavior of two offshore soft sandstone gas reservoirs located in the Gulf of Mexico with a view to quantifying the geomechanical risk associated with subsidence and compaction.

To meet this objective a 3D Mechanical Earth Model (3D MEM) was built that included: (1) a reservoir model capable of handling equations governing multiphase flow in porous media and heat transfer, (2) a geomechanical model that handles equations governing the relationship between principal stresses, pore pressure, temperature and porosity. Fluid flow models have been used in the petroleum industry for several decades. On the other hand geomechanical models are generally considered as newcomers.

Original contributions for the study area include:

(1) Development of correlations between static and dynamic Young's modulus and Poisson's ratio.

(2) Development of correlations that relate the internal friction angle and unconfined compressive strength to Young's modulus and porosity.

(3) Quantification of subsidence and compaction.

Basic data for development of items (1) and (2) were provided by sonic-wave velocities and mechanical laboratory experiments conducted in soft sandstone cores collected in the reservoirs under consideration.

Item (3) was developed using the 3D MEM. Distribution of rock mechanical properties in the 3D MEM was developed applying geostatistical data analysis and Sequential Gaussian Simulation (SGS) methods. The simulation process was used to produce equally probable maps of mechanical properties.

Computed results using the 3D MEM indicate that average subsidence will be -0.74 m and average compaction of the upper reservoir -1.37 m under the anticipated production schedule. This collapse could induce catastrophic damage of subsea production facilities if not taken into account. Understanding of these displacement processes as presented in this thesis should help to develop mitigation strategies in order to minimize down to a minimum any risks associated with well integrity and deep water facilities.

Acknowledgements

Completion of this thesis was possible thanks to those persons who provided support and advice throughout its development. I express my gratitude to:

My supervisor Dr. Roberto Aguilera for giving me the opportunity to be part of the GFREE research group. My thanks for his guidance, supervision, teaching and encouragement during the time we worked together. His knowledge and ability to share ideas have made the completion of this thesis possible.

My co-supervisor Dr. Gaisoni Nasreldin (Schlumberger) for his supervision, guidance, advice and recommendations during construction of the Mechanical Earth Model and simulation runs. He made possible the culmination of this thesis.

Pemex Exploration and Production (PEP) and Conacyt (Mexico) for providing the financial support that made possible my entire experience as a graduate student in the Department of Chemical and Petroleum Engineering at the University of Calgary. I thank to Dr. Jorge Alberto Arévalo Villagrán (PEP) for his support and advice.

My friend and colleague Nicolas Gomez Bustamante, MEng. (Schlumberger, Calgary) for his support and help during the donation process of Visage software to the University of Calgary.

GFREE members for their continuous support and collaboration. Particularly, thanks to Bruno A. Lopez Jimenez for his support and advice.

My wife and children for their love, understanding and support during my career development and for helping me to overcome all difficulties during this time.

Dedication

I dedicate this thesis to my family, especially wife Candy Ochoa, to my daughter Isabella Manzano and my son David Manzano Ochoa. I also dedicate this thesis to my country Mexico.

"We all have dreams. But in order to make dreams come into reality, it takes an awful lot of determination, dedication, self-discipline, and effort."

Jesse Owens

Table of Contents

List of Tables

List of Figures and Illustrations

List of Symbols, Abbreviations and Nomenclature

Acronyms	**Definition**
1D	One-dimensional
2D	Two-dimensional
3D	Three-dimensional
BHP	Bottom hole pressure
CCE	Constant composition expansion experiment
CBM	Coal bed methane formations
DST	Drill stem test
EOS	Cubic equations of state
FGPR	Field gas production rate
FGPT	Field gas production total
FPR	Field reservoir pressure
GFREE	Integrated geoscience (G), formation evaluation (F), reservoir drilling, completion and stimulation (R), reservoir engineering (E), economics and externalities (EE)
LVDTs	Linear variable differential transformer
LOT	Leak off test
MDT	Modular Dynamic Tester
MEM	Mechanical earth model
MI-1	Lower reservoir
MI-2	Upper reservoir
NTG	Net to gross ratio
OGIP	Original gas in place
PVT	Pressure-volume-temperature
SGS	Sequential Gaussian Simulation
SSTVD	Subsea true vertical depth
TOTSTRXX	Total stress in x direction
TOTSTRYY	Total stress in y direction
TOTSTRZZ	Total stress in z direction
UCS	Unconfined compressive strength
V	Velocity
XPT	Express pressure temperature

Nomenclature	**Definition**
A	Area
$B(\alpha 1, \beta 1)$	Beta function
C_f	Fluid compressibility
D	Reservoir depth
E	Young's Modulus
E_{dy}	Dynamic Young's modulus
E_{st}	Static Young's modulus

$\vec{F}$	Restoring force
g	Gravitational acceleration constant
G	Shear modulus
h	Reservoir thickness
H	Physical constant in Biot's theory
J(Sw)	Leverett J function
k	Proportionality constant
K	Permeability
K_b	Bulk modulus
K_{dy}	Dynamic bulk modulus
K_{st}	Static bulk modulus
K_{fr}	Bulk modulus of the skeleton
Kr_{nw}	Non-wetting relative Permeability
$Kr_{nw}*$	Normalized non-wetting phase relative permeability
K_{rw}	Water relative permeability
$K_{rw}*$	Normalized water relative permeability
K_s	Bulk modulus of the solid grain
L	Length
M_L	Molecular fraction
n	Number of samples
NF	Normal Faulting
P	Compressional
Pc	Confining pressure
P_{cap}	Capillary pressure
P_p	Pore pressure
r	Radius
ra	Rank
R	Physical constants in Biot's theory
R^2	Coefficients of determination
RF	Reverse faulting
s	Normal score
S	Shear
S_{Hmax}	Maximum horizontal stress
S_{hmin}	Minimum horizontal stress
S_o	Shear strength of the rock
S_{rnw}	Residual non-wetting phase saturation
SS	Strike- Slip Faulting
S_v	Vertical stress
Sw*	Effective saturation
Swi	Irreducible water saturation
U	Reservoir subsidence
ν_{dy}	Dynamic Poisson's ratio
ν_{st}	Static Poisson's ratio
ν	Poisson's ratio
var	Variance in beta function

v_c	Poisson's ratio for cap rock
V_{clay}	Clay volume
V_p	Compressional wave velocity
V_s	Shear wave velocity
W_{bo}	Angle of breakout width.
$\vec{x}$	Displacement distance
$\bar{x}$	Mean
Z	Depth of interest
Zi	Mole fraction
Z_w	Water depth

Greek Symbols	**Definition**
α	Biot's coefficient
$\alpha 1$	Beta function coefficient
β	Grain compressibility
$\beta 1$	Beta function coefficient
γ	Shear strain
γ_L	Gas relative density
δK	Changes in permeability
δL	Change in length
δQ	Change in wave velocity
δr	Change in radius
δS_w	Increment of water per unit volume of rock
δz	Change of stress in z direction
ΔC	Reservoir compaction
ΔP	Change in pressure
Δtc	Compressional slowness
Δts	Shear slowness
ε_x	Axial strain
ε_y	Transversal strain
ε_{vol}	Volumetric strain.
ϵ	Volume increase of soil per unit volume
η	Quartile point
θ	Failure plane angle
θ_b	Breakout angle
λ	Pore size distribution.
μ	Internal friction coefficient
ξ	$1/\phi$
ρ_b	Bulk density
ρ_w	water density
$\bar{\rho}$	Mean overburden density
σ_f	Stress acting on the fluid,
σ	Total stress
σ_{eff}	Effective stress
σ_h	Stress acting on the fluid

σ_t	Interfacial tension.
σ_x	Axial stress
σ_z	Stress in z direction
τ	Shear stress
τ_{max}	Critical shear stress
ϕ	Porosity
ϕe	Effective porosity
φ	Internal friction angle

Note: This thesis uses mixed units normally employed in the oil and gas industry. The unit kg is referred as kilogram force. SI units are included in brackets.

Pressure and stress

1 MPa = 10.197 kg/cm^2 = 145.037 psi = 10 bar

Chapter One: Introduction

1.1 Justification

Reservoir engineers historically have paid little attention to mechanical properties of the rock despite the fact that many physical phenomena occurring in the reservoir's porous media including for example sand production, subsidence, compaction drive, water flooding, wellbore stability, and fracturing can be explained and modeled more easily by considering the effect of the principal in-situ stresses acting on the mechanical properties of the rock.

In general, better understanding of stresses acting on a reservoir and their effect on mechanical properties of the rock will improve reservoir characterization and will provide more accuracy on production forecasts, changes in porosity and permeability, and predictions of compaction and subsidence.

Analysis of principal stresses acting on the rock and their effect on mechanical properties require coupling of reservoir flow and rock mechanics models. The integration process is commonly called Coupled Geomechanical Modeling and can be developed using different methods which are discussed in more detail later in this thesis.

1.2 Objective

The main objective of this work is to quantitatively evaluate rock compaction and subsidence in GML Field offshore Mexico, the possibility of sand production, and the reduction of permeability and porosity during the production stage of the field.

To achieve the objective, three important tasks must be completed,

1) Determine the initial elastic moduli of the rock within the reservoir in the overburden, underburden and sideburden based on experimental data coming

from triaxial tests, wireline logs and correlations to correct the dynamic moduli to static moduli.

2) Build a coupled reservoir and geomechanical three-dimensional model to simulate the current stress-strain acting on the porous medium of the reservoir.

3) Compare gas production, pore pressure, pore volume, sand production and subsidence results with and without the coupled geomechanics modeling. Based on results, prepare recommendations for proper modeling of the field.

1.3 Area of study

The GML Field is located in the slope and base of the basin floor in the Gulf of Mexico 131 km northwest of Coatzacoalcos, Veracruz, Mexico. The water leg in this area is around 1200 m. The GML Field presents two stacked sandstone reservoirs in the lower Miocene formation isolated by a cap of shale. Each reservoir is composed by thin layers of soft sandstone intercalated with thin layers of shale. **Figure 1-1** shows the location of GML Field.

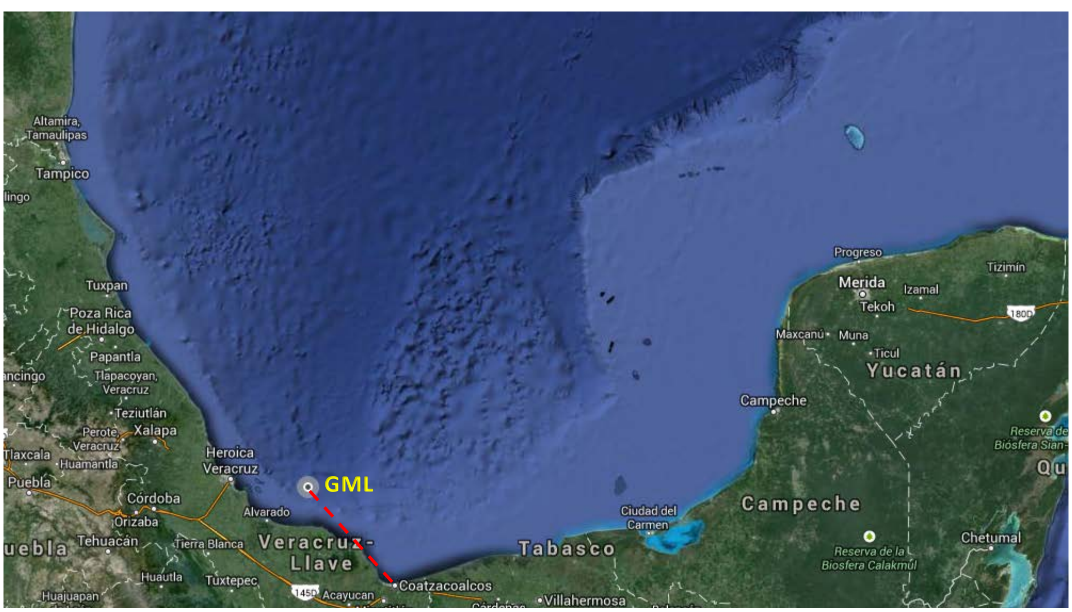

Figure 1-1 Location of GML field.

1.3.1 Geologic interpretation and reservoir description

The structural model of GML field was defined using seismic interpretation (fast track post-stack in time) calibrated with data of wells GML-1, GML-2 and GML-3. It is conceptualized as an elongated anticline with average dimensions of 10.5 km long, 2.1 km wide and 40 m thick, and major axis orientation in azimuth N 13° W. This structure is limited in the north by a sealing normal fault and all around by the layer's dip. It contains 13 principal normal faults with azimuth N30°E and 80° dip distributed along the structure. The faults are the result of overburden load as shown in **Figure 1-2**. The figure does not show all the faults due to their very low displacement and the scale used in the figure.

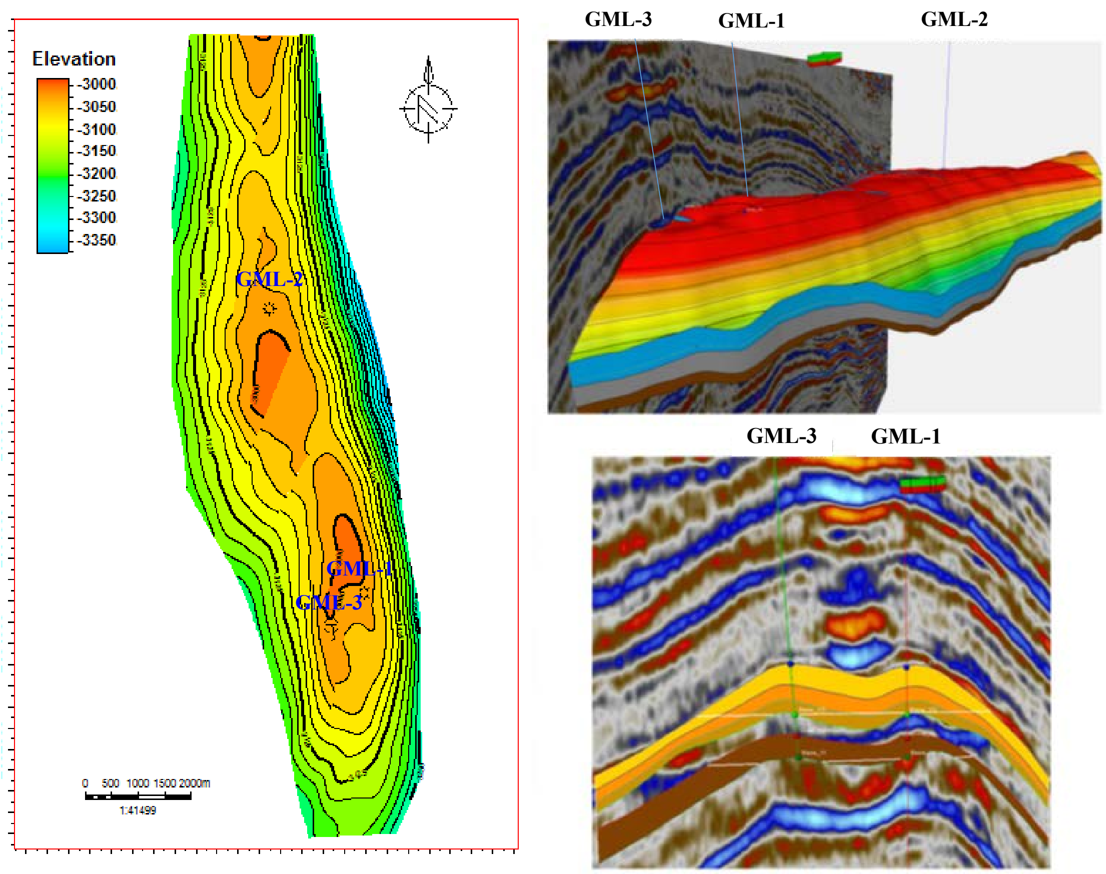

Figure 1-2 Structural model of GML field defined with the use of seismic data.

The Lower Miocene sedimentary model was conceptualized using different sources of information such as core analysis, drill cuttings, wireline logs, seismic stratigraphy and paleontological analysis. The data analysis indicated that these reservoirs present facies of levee channel within turbidite deposits corresponding to bathyal depositional environment. The sedimentary structures are notable because of the presence of flame structures and convolute bedding of fine sands in between soft-sediment deformed structures, parallel lamination and cross-planar stratification as presented in **Figure 1-3**. The low amplitude seismic attribute allowed identifying a channel with orientation NE-SW associated with a levee channel, which is the source of the sand deposits identified during drilling of wells in both reservoirs.

The stratigraphic model was conceptualized dividing the reservoirs in two areal zones; the south-centre and north zones. The former utilized information gathered during drilling and completion operations of GML-1 and GML-3, which helped to identify the presence of intercalated laminar layers of sandstones and shales in both reservoirs. On the other hand, the north zone used information gathered during drilling and completion operations of appraisal well GML-2, which allowed distinguishing massive sandstone in the upper reservoir and laminar layers of sandstone intercalated with layers of shale in the lower reservoir.

The seal rock in both reservoirs is comprised basically of shale with an average thickness is 30 m. The isotopic analysis of gas samples from both reservoirs indicated that the source rock is most likely the Upper Jurassic in the area.

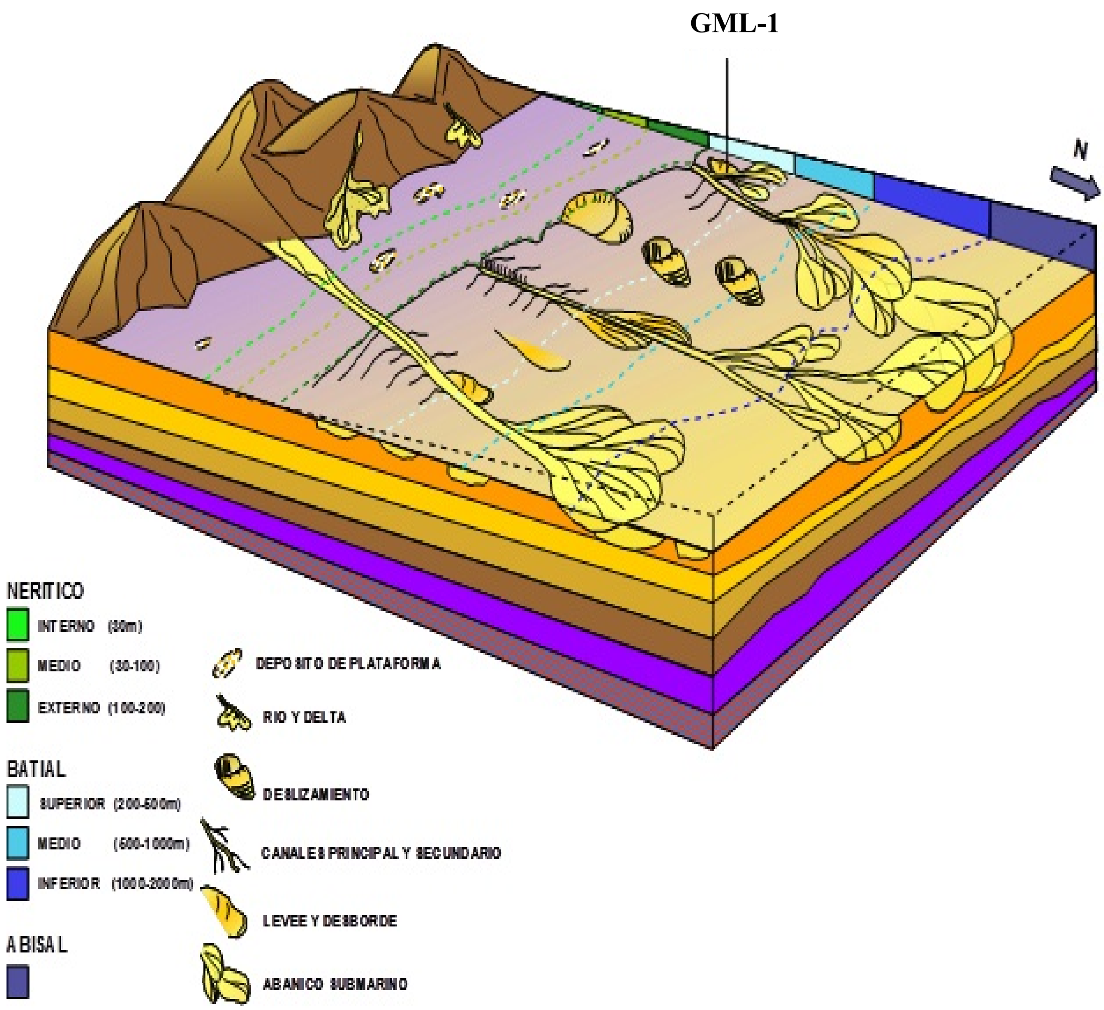

Figure 1-3 Conceptual Lower Miocene sedimentary model.

1.3.2 Petrophysical model

In general, the lithology of the rock in both reservoirs is constituted by siliciclastic sediments consisting of quartz, potassium feldspars, sodium rich plagioclase and igneous clasts cemented with calcite and clay. Both reservoirs present vertical heterogeneity mainly due to strong variation in sandstone's texture, which is related to grain size, clay content, degree of consolidation and classification. This stratification results in changes in the porous system and storage quality in the rock. Core samples and wireline logs analyses indicated that both reservoirs in the south-center area have laminated characteristics. In the north area the lower reservoir presents the same characteristic as the ones in the south-center area, but the upper reservoir has a massive structure. **Figure 1-4** shows each of the wells considered for analysis and their corresponding rock characteristics. **Table 1-1** presents the main petrophysical characteristics by reservoir and areal zone.

Table 1-1 Lower Miocene petrophysical properties of GML reservoirs.

Rock Property	Upper Reservoir		Lower Reservoir	
	Center	North	Center	North
Porosity	20 %	19.5%	19.6 %	18 %
Permeability	35 mD	37.5 mD	25.5 mD	33 mD
Clay volume	13%	14 %	16 %	17 %
Water saturation	38%	31 %	46 %	43 %
Net thickness	42 m	60 m	14 m	11 m

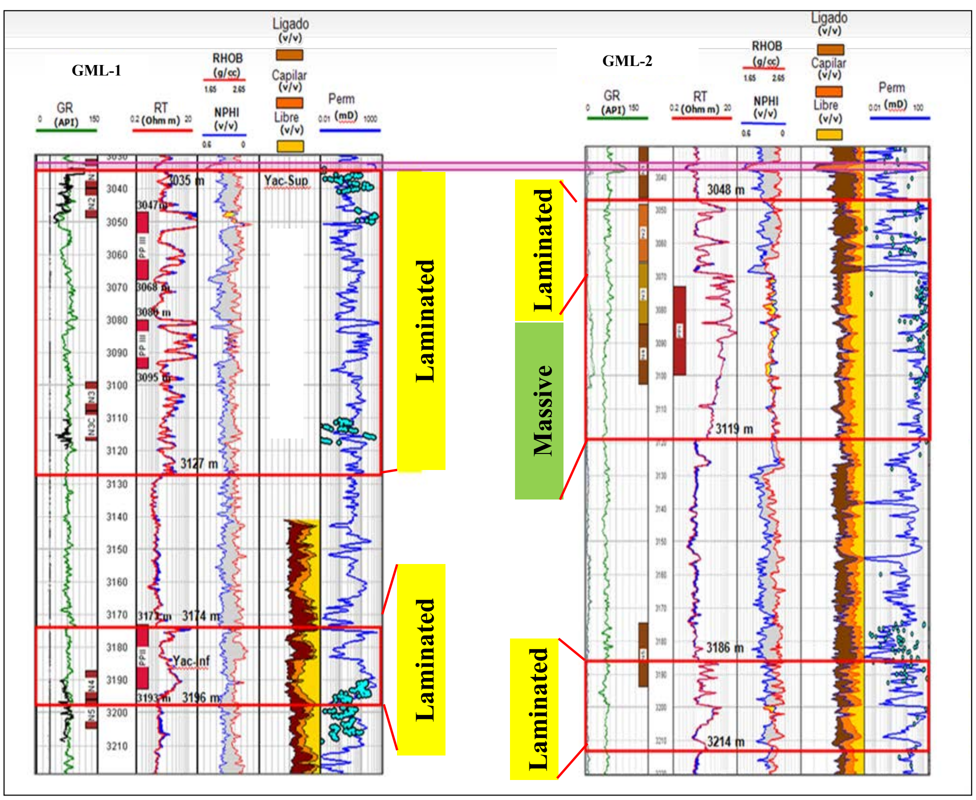

Figure 1-4 Reservoir's rock characteristics. The south-center area is characterized considering GML-1 information whereas the north area is characterized with data from GML-2. The reservoirs of interest are shown by the red boxes

1.3.3 Gas in place and reserves

Based on the number of wells completed in this field the original gas in-place (OGIP) and 2P reserves (proven reserves + probable reserves) have been estimated three times during the development life of the reservoirs. The first estimate was performed after completion of well GML-1 in March 2007. The original gas in-place was estimated at 1,733 MMMscf and the 2P reserves at 934 MMMscf. The second estimation was performed in July 2010, after completion of well GML-2 (2008), which was the first appraisal well located in the north of the field. The OGIP was revised to 1,128 MMMscf and 2P reserves were 866 MMMscf. The last reclassification was done in 2013 after completion of well GML-3, which is the second appraisal located in the south of the field. The third estimate led to an OGIP equal to 1,298 MMMscf while 2P were 922 MMMscf. According to the last reclassification, the whole reserves in the field have been categorized as 2P.

1.4 History

Well GML-1 was drilled to a depth of 3818 m between July 2006 and March 2007. The seabed was located at a depth of 870 m. The found stratigraphic column comprises recent Pleistocene and lower Miocene. The completion stage included the perforation of four zones. The lower zone was dry, two intervals in the middle zone produced natural gas and the upper zone produced 100% water. The upper part in the middle zone is named the upper reservoir and was completed in interval 3035 - 3127 m. Similarly, the lower part in the middle zone matches with the lower reservoir and was completed in interval of 3174 to 3212 m. Each interval was evaluated with the use of PVT bottom-hole samples, surface chromatography and flow testing. The PVT and chromatography analyses indicated the presence of dry gas with 96% mole fraction of methane. Flow testing conducted through a 5/8” choke size resulted in gas rates equal to 24 MMscfd and 36 MMscfd for the lower and upper reservoirs, respectively.

Well GML-2 was perforated in July 2010 at interval 3075-3100 m. Information was gathered by different means such as downhole fluid analysis using the modular formation dynamic tester (MDT), PVT bottom-hole samples, surface chromatography, well testing and wall cores during the completion process. A total of 58 pressure and temperature data points were measured using mini DST, XPT and DST to determine pressure and temperature gradients. Pressure gradients in the gas zone and water zone were 0.0232 $kg/cm^2/m$ (2.35 KPa/m) and 0.134 $kg/cm^2/m$ (13.1 KPa/m), respectively. This information was used to establish both top and base of each interval as follows,

1) Upper reservoir from 3048 to 3119 m.
2) Lower reservoir from 3186 to 3214 m.

Bottom-hole fluid samples and dynamic well testers allowed identifying the gas-water contact for both reservoirs. The lower reservoir (MI-1) gas-water contact was located at a depth of 3189 m SSTVD while gas-water contact in the upper reservoir (MI-2) was located at a depth equal to 3098 m SSTVD. **Figure 1-5** shows pressure gradients and gas-water contacts for both reservoirs.

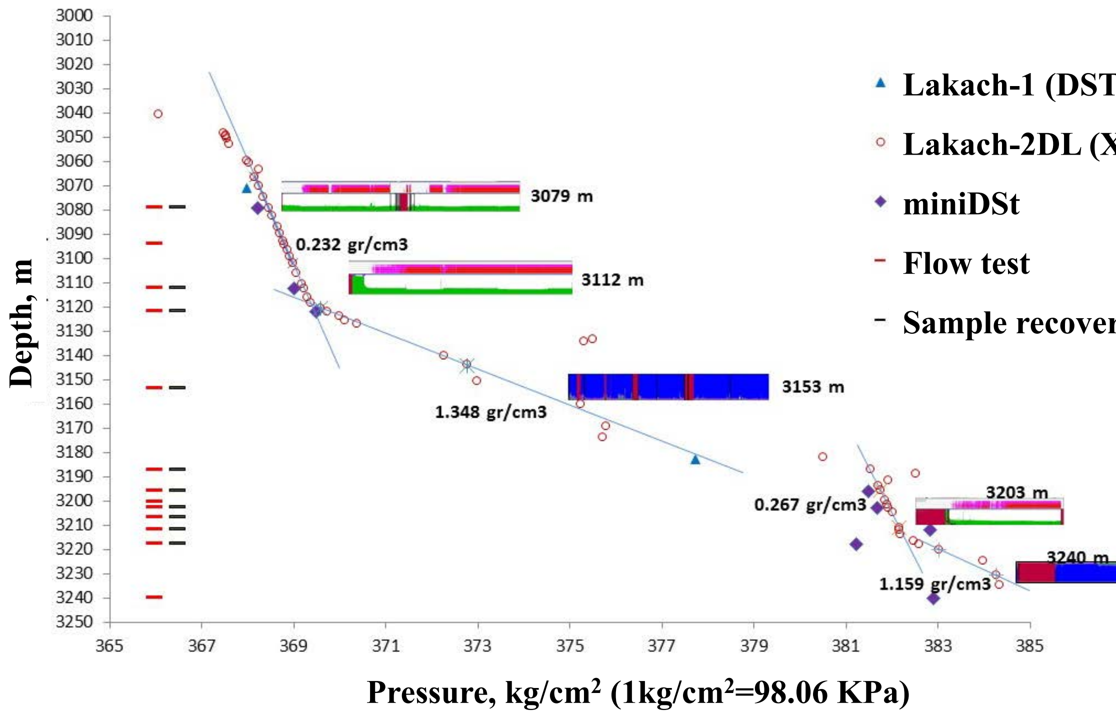

Figure 1-5 Pressure gradients and gas-water contacts corresponding to lower reservoir (MI-1) and upper reservoir (MI-2).

Chromatographic analysis was performed on both bottom-hole and recombined samples collected in the surface. Both analyses indicated that the fluid is dry gas. The composition of the fluid is shown in **Table 1-2** and indicates 0.0% mole of H_2S and 0.03-0.10% mole of carbon dioxide.

However, the fluid can also be classified as a poor gas condensate. In fact, the dew point pressure is 383 kg/cm^2 (37.55 MPa), relative gas density is equal to 0.59 and gas-oil ratio is equal to 3.9 bbl/MMscf at standard conditions. The dew pressure is larger than the initial reservoir pressure, which is an indication of a gas condensate reservoir. However, strong condensation is not expected in the reservoir since the liquid content is low.

Table 1-2 Sample composition of the reservoir fluid.

Component	Bottom-hole sample composition GML-2	GML-1
N_2	1.03	0.84
CO_2	0.03	0.10
C1	95.07	94.81
C2	1.97	1.90
C3	0.72	0.74
C4	0.38	0.20
C5	0.16	0.18
C6	0.17	0.06
C7	0.14	0.07
C8	0.34	1.11
Total	100.00	100.00

Three well-testing analyses were carried out for these reservoirs. Two of them were performed in well GML-1 and the other one in well GML-2.

The first test, conducted in December 2006, covered interval 3173-3193 m. The second test was performed in January 2007 and covered interval 3047-3095 m. The last test was performed in July 2010 at interval 3075-3100 m. The three tests consisted of drawdowns through chokes of 3/8, 5/8 and ½-inches along with build-ups, which lasted around 100 h. The model used to match the real pressure data indicated a radial homogeneous reservoir with partial penetration and boundary effects possibly representative of a facies change. **Figure 1-6** shows the build-up test for GML-2. **Table 1-3** presents the most important results obtained from the analysis.

Table 1-3 Well testing Analysis results

	GML-1	GML-1	GML-2
Interval	3173-3193 m TVD	3047-3095 m TVD	3075-3100 m TVD
Model	Radial Homogeneous with boundary	Radial Homogeneous	Radial Homogeneous
Initial pressure @ datum	37.04 MPa	36.08 MPa	36.11 MPa
Gas rate	24.8 MMSCF @ 5/8”	29.5 MMSCF @ 5/8”	28.68 MMSCF @ 11/16”
ϕ_e	19%	23%	21%
Total skin	-3	15.7	50.5
Net depth	15 m	36 m	51 m
Permeability	3.5 mD	24.7 mD	31.6 mD
Research radius		379 m	676 m
ΔP	8.5 MPa	2.8 MPa	5.3 MPa

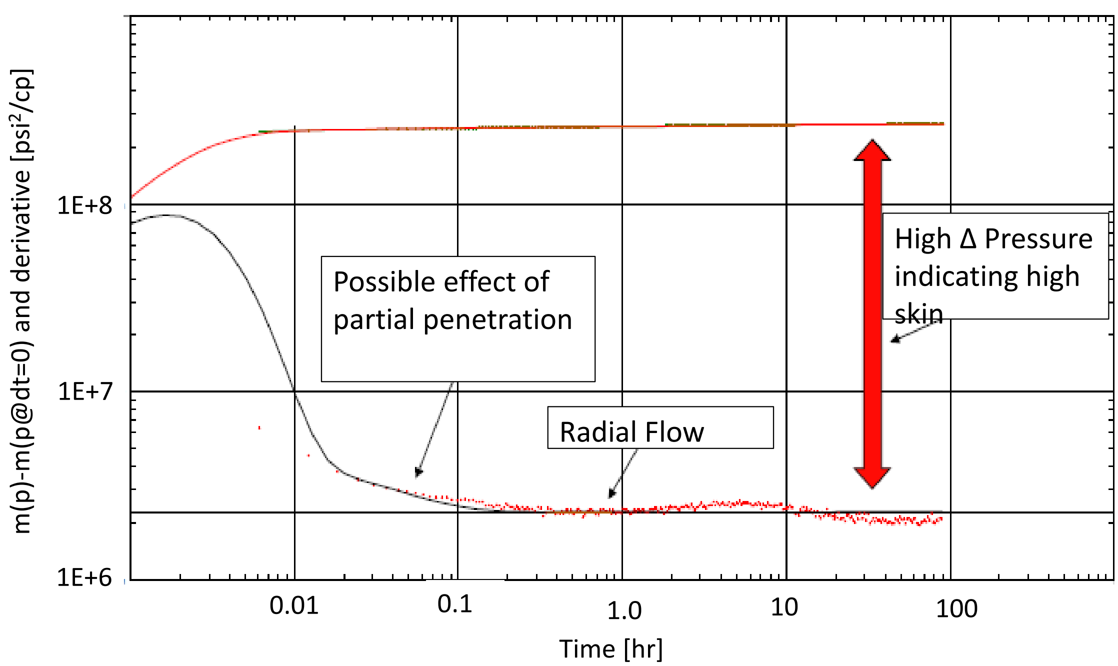

Figure 1-6 Build-up test analysis of well GML-2.

1.5 Summary

GML Field includes two stacked reservoirs of Lower Miocene age. Both of them are composed by sand layers intercalated with shale layers. The reservoir's structure is an elongated anticline with an average thickness of 30 m and an area of 20 km^2. Their average porosity is 19.3%, average initial water saturation is 39.5% and average permeability is 32.7 mD. The total volume of original gas-in-place is 1,298 MMMscf and the 2P reserves are in the order of 922 MMMscf. Three wells have been drilled in this field; an exploration well and two appraisal wells. Well testing data and basic geophysical well logs such as density, shear and compressional sonic waves velocities are available for both reservoirs. These logs are critical for estimation of geomechanical properties as explained later in this work.

1.6 Thesis Chapters

This thesis has been structured in seven chapters as follows:

Chapter 1 discusses the main objectives of this work and presents a general description of the reservoir. The description includes location, geologic summary petrophysical characteristics, original gas in-situ, reserves and production history.

Chapter 2 presents a literature review of the most important concepts and theories related to linear elasticity, poroelastic theory, effective stress, static and dynamic elastic modulus, failure theory, geomechanical modelling and coupling methods.

Chapter 3 describes the methodology followed to develop new empirical correlations that allow estimates of Young's modulus, Poisson's Ratio, uncompressive rock strength and friction angle of rocks in the study area based on laboratory tests.

Chapter 4 shows the applied methodology for numerical reservoir simulation using stochastic geostatistical models for estimating average rock characteristics, facies, petrophysical properties and fluid properties.

Chapter 5 describes the process to create the earth mechanical model (MEM); grid building and validation test, scale-up properties using well logs and empirical correlations, and stochastic geostatistical simulation to estimate reservoir properties. Also included is a discussion on elastic MEM stress-state representativeness and one-way coupling simulation to verify the current stress-strain state in the reservoir model.

Chapter 6 discusses the principal results of two-way stress-flow coupled modeling, highlighting the importance of permeability and porosity reduction due to stress changes. Production forecasts by the reservoir model and the full field geomechanical model are compared. Subsidence results and their implications during the field's production life are discussed in this chapter.

Chapter 7 states the main conclusions derived from this work and presents recommendations for future studies.

Chapter Two: Literature Review

As previously mentioned, the main objective of this thesis is to analyze the behaviour of an offshore gas reservoir using a reservoir numerical simulation model coupled with geomechanics. This is done to improve the accuracy on the forecast estimation of reservoir production, pore pressure, in-situ stresses and mechanical properties.

This chapter presents a literature review on topics related to this thesis such as linear elasticity theory, poroelastic theory, empirical relations used for determining mechanical properties of rocks as well as available techniques for coupling fluid flow and geomechanics models.

2.1 Linear Elasticity

The fundamentals of rock mechanics reside on the theory of linear elasticity also known as Hooke's law, which states that the deformation experienced by an elastic material is linearly proportional to the stress applied. Thus, the force to restore the material to equilibrium is proportional to the displacement of the material from its original position expressed as **Eq. 2-1** (Davis, 2002).

$$\vec{F} = -\mathrm{k}\vec{x} \qquad \textbf{Eq. 2-1}$$

Where $\vec{F}$ is the restoring force, k is the proportionality constant and $\vec{x}$ is the displacement distance. The minus sign indicates that the force acts in the opposite direction of the displacement.

The linear elasticity and isotropic model (Hooke's law) is the most simple and also the most practical way to model and estimate mechanical properties of a material. However, its application is only valuable as a first estimation due to its simplicity.

If a force $\vec{F}$ is applied at the end of a long thin bar with cross section area A, the length L will change by δL as shown in **Figure 2-1**.

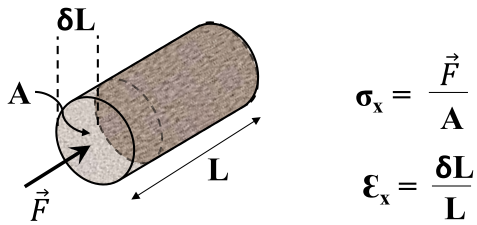

Figure 2-1 Stress and strain ratio.

The proportionally constant defined by the ratio of the axial stress $\sigma_x = \vec{F}/A$ to the axial strain $\varepsilon_x = \delta L/L$ is known as Young's Modulus (E) as defined in **Eq. 2-2**. Young's Modulus represents the stiffness of the material, i.e., the resistance of the material to be compacted under uniaxial stress (Fjaer, 2008). In addition, Zoback (2006) pointed out that this measurement of stiffness must be developed under unconfined conditions for linear elasticity purposes.

$$E = \frac{\sigma_x}{\varepsilon_x} \qquad \textbf{Eq. 2-2}$$

When an axial stress is applied on a rod as illustrated above, the body suffers either compression or extension (ε_x) depending on the direction of the stress (this work assumes that compression is caused by positive stress) and either expansion or contraction (ε_y) perpendicular to the axial stress. As shown in **Figure 2-2**, compression occurs in the direction of the stress whereas expansion is arising perpendicular to the axial stress. The ratio of lateral to longitudinal strain is known as Poisson's ratio (ν) as expressed in **Eq. 2-3**.

$$\nu = \frac{\varepsilon_y}{\varepsilon_x} \qquad \textbf{Eq. 2-3}$$

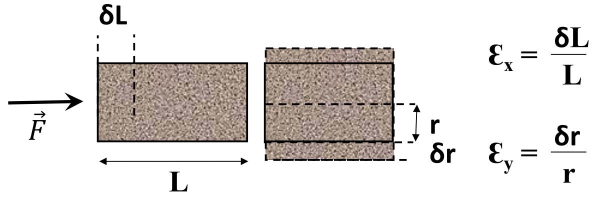

Figure 2-2 Longitudinal and transversal strain.

The stress and strain parameters previously mentioned for the case of a 1D model are known as normal stress and normal strain, respectively. However, when the 1D model is extended to 2D or 3D, shear stress and shear strain have to be considered for angular distortion.

Biot (1941) considered a small 3D (Cartesian coordinates) element of porous rock saturated with water as homogeneous and infinitesimal scale compared with the real scale of the phenomena and developed the expressions to relate strain to stress presented in **Eq. 2-4** to **Eq. 2-9**.

$$\varepsilon_x = \frac{\sigma_x}{E} - \frac{v}{E}\left(\sigma_y + \sigma_z\right) + \frac{\sigma_h}{3H} \qquad \textbf{Eq. 2-4}$$

$$\varepsilon_y = \frac{\sigma_y}{E} - \frac{v}{E}\left(\sigma_x + \sigma_z\right) + \frac{\sigma_h}{3H} \qquad \textbf{Eq. 2-5}$$

$$\varepsilon_z = \frac{\sigma_z}{E} - \frac{v}{E}\left(\sigma_y + \sigma_x\right) + \frac{\sigma_h}{3H} \qquad \textbf{Eq. 2-6}$$

$$\gamma_x = \frac{\tau_x}{G} \qquad \textbf{Eq. 2-7}$$

$$\gamma_y = \frac{\tau_y}{G} \qquad \textbf{Eq. 2-8}$$

$$\gamma_z = \frac{\tau_z}{G} \qquad \textbf{Eq. 2-9}$$

Where γ is the shear strain in a perpendicular direction to the normal strain, τ is the shear stress in the perpendicular direction to the normal stress, σ_h is the stress acting in the fluid, H is a physical constant that takes into account the effect of water pressure and G is the shear modulus, which represents the resistance of the rock to be deformed by a shear stress. The relationship between shear modulus and Young's modulus and Poisson's ratio is given by **Eq. 2-10**:

$$G = \frac{E}{2(1+v)} \qquad \textbf{Eq. 2-10}$$

The bulk modulus (K_b) is another important elastic property of the rock to be considered for geomechanical analysis. The bulk modulus represents the resistance of the rock to be compressed by hydrostatic stresses acting in all directions. It is denoted by the following **Eq. 2-11** (Fjaer, 2008),

$$K_b = \frac{\sigma_h}{\varepsilon_{vol}} \qquad \textbf{Eq. 2-11}$$

Where σ_h is the hydrostatic stress and ε_{vol} the volumetric strain.

Due to the linear relationship between the different modulus, it is possible calculate any elastic property of the rock as function of two other parameters. Several authors have proposed different relationships to calculate the elastic parameters E, v, G and K_b. Davis and Selvadurai (2005) proposed 30 different relationships, Fjaer (2008) established 21 relationships, Zoback (2002) presented more than 30 relationships and Jaeger et al. (2007) proposed 9 different equations to calculate elastic properties and a complete set of equations to calculate stress and strain for specific cases of cylindrical and polar coordinate systems either in two or three dimensions. However, special care is needed when applying these relations on rocks that do not exhibit linear stress-strain relationship.

2.2 Poroelastic Theory

As mentioned above the theory of linear elasticity presents limitations because it treats the rock as homogeneous, solid, isotropic and with a linear stress-strain relationship. Due to these limitations the linear elastic theory is not applicable to materials conformed by an elastic skeleton containing interconnected pores saturated with compressible fluid that exhibits an elastic behaviour depending on both solid stress and fluid pressure. In their study Detournay and Chen (1993) stated that the presence of a mobile fluid phase in the porous system alters the mechanical behaviour of the rock, so that any compression of the rock increases the pore pressure, which in turn induces dilation of the rock.

Terzaghi’s 1923 study (cited in Zoback, 2002) took into account the effect of fluid in the pore system over the deformation of soils. Considering a constant pressure load acting over a column of porous rock saturated with water and disallowing for lateral expansion, Terzaghi demonstrated that the behaviour of a porous rock is mainly governed by the pressure difference between the confining pressure and the pore pressure. However, Terzagui’s work has some limitations: the work was conducted on 1D models and on rocks with incompressible skeleton.

Biot’s theory (1941) was developed on a 3D model considering the following characteristics,

1. Porous system is filled with free fluid that supports part of the total stresses acting on the rock,
2. A coherent solid skeleton supports the remaining part of the total stress, so single stress is constituted by two specific elements: the hydrostatic pressure and the mean skeleton’s stress.

Some important assumptions are isotropic material, reversible stress-strain relationship, linear stress-strain behaviour, incompressible fluid, and fluid flow governed by Darcy’s Law. Detournay and Chen (1993) highlighted an additional limitation on time scale since the pressure in a single pore must be equilibrated with the pressure of the surrounding pores (deformationdiffusion process), which does not represent the basis of Biot's theory. However, the complete justification of Biot's Theory resides on the quasi-static process.

Eq. 2-12 to **Eq. 2-21** are approximations for estimating properties of the rock saturated with fluid, under strain equilibrium, isotropic soil and small strain conditions,

$$\sigma_x = 2\mathrm{G}\left(\varepsilon_x + \frac{v\epsilon}{1-v}\right) - \alpha\sigma_h \qquad \textbf{Eq. 2-12}$$

$$\sigma_y = 2\mathrm{G}\left(\varepsilon_y + \frac{v\epsilon}{1-v}\right) - \alpha\sigma_h \qquad \textbf{Eq. 2-13}$$

$$\sigma_z = 2\mathrm{G}\left(\varepsilon_z + \frac{v\epsilon}{1-v}\right) - \alpha\sigma_h \qquad \textbf{Eq. 2-14}$$

$$\tau_x = \mathrm{G}\gamma_x \qquad \textbf{Eq. 2-15}$$

$$\tau_y = \mathrm{G}\gamma_y \qquad \textbf{Eq. 2-16}$$

$$\tau_z = \mathrm{G}\gamma_z \qquad \textbf{Eq. 2-17}$$

$$\delta S_w = \alpha\epsilon + \frac{\sigma_h}{q} \qquad \textbf{Eq. 2-18}$$

$$\alpha = \frac{2(1+v)}{3(1-2v)}\frac{G}{H} \qquad \textbf{Eq. 2-19}$$

$$q = \mathrm{R} - \frac{H}{\alpha} \qquad \textbf{Eq. 2-20}$$

$$\epsilon = \frac{3(1-2v)}{E}\sigma_1 + \frac{\sigma_h}{H} \qquad \textbf{Eq. 2-21}$$

Where σ_x represents the stress acting on the skeleton, σ_h is the stress acting on the fluid, ϵ is the volume increase of soil per unit volume, α is the Biot's coefficient, δS_w is the increment of water per unit volume of rock and H and R are physical constants.

According to Biot and Willis (1957), the Biot's coefficient mentioned above can be determined using laboratory sample tests such as the jacketed and drained test. Both tests require samples saturated with fluid and allow measuring the bulk modulus of the skeleton (K_{fr}) since pore pressure is held constant while an external hydrostatic pressure is applied in such a way that the stress is supported by the solid frame. On the other hand, the unjacketed test allows for equilibrium between pore pressure and hydrostatic pressure. As a result, the stress is uniform and $\varepsilon_{vol\ tot} = \varepsilon_{vol\ pore} = \varepsilon_{vol\ solid}$ and the bulk modulus of the solid grain (K_s) can be estimated using **Eq. 2-22**. Furthermore, the aforementioned laboratory tests are used to determine porosity (ϕ), shear modules (G) and fluid compressibility (C_f). Also the five variables defined by Biot's theory are calculated from data obtained from these laboratory measurements. The mathematical expression to calculate the α coefficient as a function of the effective stress (σ_{eff}), total external stress (σ) and pore pressure (Pp) is given as follows,

$$\epsilon_{vol} = \frac{P_p}{K_s} \quad \textbf{Eq. 2-22}$$

$$\alpha = 1 - \frac{K_{fr}}{K_s} \quad \textbf{Eq. 2-23}$$

$$\sigma_{eff} = \sigma - \alpha P_p \quad \textbf{Eq. 2-24}$$

2.2.1 Effective stress

Different authors have analyzed the effective stress (σ_{eff}). For instance, Terzaghi (1949) established that σ_{eff} acting over a boundary of an element is equal to the difference between the vertical stress (σ_z) and the pore pressure (P_p) and is expressed in **Eq. 2-25**. Nevertheless, this expression is only valid for 1D cases. Biot (1941) developed the equation as represented in **Eq. 2-24**., which calculates σ_{eff} as a function of σ, P_p and Biot's coefficient (α)

$$\sigma_{eff} = \sigma_z - P_p \quad \textbf{Eq. 2-25}$$

The expression shown in **Eq. 2-24** indicates that the total external stress acting over a boundary of an element is composed by σ_{eff} and αP_p, where the fluid in the porous medium supports a fraction of the pore pressure (αP_p) and the skeleton carries the effective stress.

Meanwhile, inner stresses in the skeleton absorb the residual pore pressure (1-α) P_p (Fjaer, 2008).

2.2.2 Biot's coefficient (α)

Biot's coefficient has two physical explanations: the first one states that Biot's coefficient is the result of an elastic potential energy present in the rock; the second one indicates that it represents the fraction of pore pressure (P_p) that produces a strain equal to the total stress (σ). In any case, **Eq. 2-23** indicates that α should take values between zero and one because the bulk modulus of solid grains is always greater than the bulk modulus of the skeleton (Biot and Willis, 1957).

Based on measurements of acoustic velocities and elastic properties on sandstone samples Ojala and Fjaer (2007) developed an expression to calculate α as given by **Eq. 2-26**. In their measurements, Ojala and Fjaer (2007) considered stress and strain in both radial and vertical directions, as well as P and S wave velocities in the aforementioned directions (δQ). Their results indicated that α varies from 0.60 to 0.83 when elastic methods are used, 0.10 to 0.88 for radial P-waves, 0.57 to 0.86 for axial P-waves, and 0.75 to 1.12 for S-waves.

$$\alpha = 1 - \frac{\left(\frac{\delta Q}{\delta P_p}\right)_{\sigma_{eff}}}{\left(\frac{\delta Q}{\delta \sigma_{eff}}\right)_{P_p}} \qquad \textbf{Eq. 2-26}$$

Seismic velocity response of underground rocks is a function of overburden and pore pressure, which have an effect on the burial stress and consequently on the response of acoustic seismic velocities of the rock. Thus, a relationship between seismic velocity and effective stress must be defined. **Eq. 2-27** allows estimation of α as a function of compressional wave velocity (V_p), shear wave velocity (V_s), bulk modulus of the solids (Ks), bulk density (ρ_b) and effective stress determined from seismic velocity and the difference between confining pressure and pore pressure (ΔP). This equation has been applied to the Carnarvon basin formation to determine Biot's coefficient using P and S -wave velocity from cores. The value was found to be approximately 0.9 (Siggins et al., 2004)

$$\alpha = 1 - \rho_b \frac{\left[3\left(V_p(\Delta P)\right)^2 - 4\left(V_s(\Delta P)\right)^2\right]_{Pp}}{3K_s} \qquad \textbf{Eq. 2-27}$$

Alam and Fabricius (2012) stated that a more precise value of Biot's coefficient can be obtained measuring the bulk compressibility of samples under uniaxial strain conditions (more representative in hydrocarbon reservoirs) and not only the bulk compressibility measured under hydrostatic stress conditions as traditionally done. As a result, they developed a new expression to calculate Biot's coefficient in each main stress direction. The bulk strain is composed of both radial and axial strain, where the radial strain is the result of tension stress while the axial strain originates from compression.

When reservoir fluids are extracted, pore pressure decreases and net stress increases leading to deformation of the grain structure, which in turn reduces porosity. This modification develops variations in Biot's coefficient in different directions. Using seismic waves' velocity Alam and Fabricius (2012) determined the effective stress and the change in volume due to compression of a pack. Then, by application of **Eq. 2-28**, they found Biot's coefficient to range between 0.6 and 1 for Austin chalk (Texas) and North Sea chalk reservoirs.

$$\alpha = 1 - \frac{\left(\frac{\partial \varepsilon_x}{\partial p_p}\right)_{\sigma_{eff}}}{\left(\frac{\partial \varepsilon_y}{\partial \sigma_{eff}}\right)_{p_p}} \qquad \textbf{Eq. 2-28}$$

Vincke et al. (1998) investigated Biot coefficient for shale rocks in an elastic domain. In their work, they managed Biot coefficient either as a tensor (αij) for the case of anisotropic rocks or as a scalar for isotropic rocks. They also presented a mathematical expression to calculate Biot's coefficient for anisotropic rocks under overburden stress. They assumed that the behaviour of the stress-strain in the parallel plane to the stratification dip is the same in both directions of the orthogonal axes lying on this plane. They developed laboratory experiments on vertical and horizontal plugs and applied vertical stress to quantify the plug's vertical strain. Then, under constant overburden pressure, they increased the pore pressure and measured the vertical strain. Finally, their results indicated that Biot's coefficient is a function of the different stresses acting on the sample. Their Biot's coefficients results ranged from 0.6 to 0.8 with vertical stresses of 14MPa and 35 MPa respectively.

Qiao et al. (2011) estimated Biot's coefficient for the Nikanassin tight gas formation based on permeability measurements of samples collected in outcrops of the tight gas Nikanassin formation in the Western Canada Sedimentary Basin. The composition of the samples included quartz, shale and feldspar with grain size varying from fine to coarse.

The samples were tested and absolute permeability values were determined under various conditions. Qiao et al. (2011) applied modified methods from the relationship proposed by Ojala and Fjaer (2007) in order to determine Biot's coefficient as a function of permeability. The modified expression utilized by Qiao (2011) is as follows,

$$\alpha = -\left(\frac{\delta K_{Pc}}{\delta K_{Pp}}\right) \qquad \textbf{Eq. 2-29}$$

Where δK_{Pc} represents the changes in permeability when the confining pressure is held constant and the pore pressure is increased, and δK_{Pp} considers the changes in permeability when the pore pressure is held constant and the confining pressure is increased. Qiao et al. (2011) applied **Eq. 2-29** to estimate Biot's coefficient for the Nikanassin Formation. They found that average values are 0.701 in vertical direction and 0.174 in horizontal direction.

According to Zoback (2006), the equation for estimating effective stress presented by Biot (1941) (**Eq. 2-24**) does not work well for permeability. Thus Zoback indicates that the equation should consider a modification on the parameter α in order to be applicable. This modification leads to α values greater than 1.0 for sandstones with high content of clay mineral. This α alteration is due to the dependency of permeability on clay content, which implies that α is less sensible to the confining pressure than to the pore pressure. However Kwon et al. (2002) indicate that this alteration is not applicable for shale with high content of clay.

In practice, Biot's coefficient is a function of many factors such as grain mineralogy, pore geometry, fluid saturation, confining pressure, clay content, fluid compressibility and anisotropy of the rock. Thus, the relationship to estimate Biot's coefficient should be based on all the available information.

2.3 Rock Mechanics

2.3.1 Relation between acoustic waves and dynamic moduli

Seismic acoustic waves are disturbances generated at a specific point on the earth that transfer energy to the subsurface and travel long distances. The velocity of propagation of the waves is related to the properties of the rock in two ways; directly based on density of the rock and its stiffness, and indirectly based on other parameters such as porosity, lithology, pore pressure, and elastic moduli. Therefore, acoustic waves provide specific information about the medium of propagation.

There are two types of waves involved in water saturated rocks. The first ones are compression waves, which are also termed as primary waves (P-waves) in which the particles move in parallel direction to the propagation. The second ones are shear waves (S-waves) in which the particles move in perpendicular direction to the waves' propagation. In addition, P-waves are the only types of waves that can travel in liquids and always arrive first at the receivers. According to Fjaer et al. (2008), the elastic behaviour of a porous rock is substantially affected by the saturation fluid. An unconsolidated sandstone will present lower P-wave velocity when it is saturated with gas than when it is saturated with water. It is because the added resistance against compression provided by the fluid in the porous medium. In consolidated sandstones the influence of the pore fluid is quite less. On the other hand, it is considered that S-waves are not affected by pore saturating fluids.

The equations presented in **Table 2-1** are used to calculate the dynamic elastic moduli when density, sonic compressional slowness and sonic shear slowness are known.

Table 2-1 Elastic moduli (Rider and Kennedy, 2011, pp. 179).

Symbol	Elastic Moduli	Equation
E	Young's modulus, psi	$2G(1+v)$
v	Poisson's ratio	$\dfrac{0.5(\Delta t_s/\Delta t_c)^2-1}{(\Delta t_s/\Delta t_c)^2-1}$
G	Shear modulus, psi	$\dfrac{1.34x10^{10}\rho_b}{\Delta t_s^2}$
K_b	Bulk modulus, psi	$1.34x10^{10}\rho_b\left(\dfrac{1}{\Delta t_c^2}-\dfrac{4}{3\Delta t_s^2}\right)$
C	Bulk compressibility, psi^{-1}	${K_b}^{-1}$

Where:

Δt_c = Compressional slowness, µs/ft.

Δt_s = Shear slowness, µs/ft.

ρ_b = Bulk density, g/cm^3.

Artificial acoustic seismic waves are generated underground to gather information about the elastic properties and the structural configuration of the rock. These seismic waves can be created in two different locations: at the surface of the earth, and downhole at the well. Acoustic waves at borehole are short-length and high-frequency; for example, any underground wave-length of 0.5 m and wave frequency of 10 kHz produce a wave velocity of 5000 m/s. In contrast, subsurface seismic waves are large-length and low-frequency (Close et al., 2009).

Several authors have proposed alternate methods for estimating dynamic elastic moduli of the rock using sub seismic acoustic information. For instance, Gassmann (cited in White, 1991) derived some analytical expressions to calculate elastic parameters of a saturated porous medium by using seismic waves and sample measurements of both fluid and skeleton. However, he neglected the effect of motion solid-fluid on the seismic wave spread. In 2007, Mullen et al. suggested a methodology to calculate P-waves and S-waves velocities using petrophysical parameters from wireline logs when sonic parameters of wireline logs are not available. In 2010, Banik et al. developed a method for estimating the dynamic moduli using elastic impedance from subsurface seismic data for unconventional basins. Zhang et al. (2010) developed a methodology similar to Mullen et al. (2007), but they added 3-D seismic data to populate a geomechanical model. Trudeng et al. (2014) used a 3-D seismic inversion model to populate the mechanical properties of the rock in a 3-D geomechanical model incorporating the uncertainties of a sub seismic model.

In 1934, Conrad Schlumberger proposed a technique to measure sonic wave velocity at boreholes. In this technique, the sonic log tool measures the capacity of a rock to propagate acoustic waves. It does so by actually measuring the time that a pulse of sound takes to travel a specific distance. It is the inverse of formation slowness (1/Δt). Since then, sonic wireline logs have become one of the most important tools for measuring sonic wave velocity (cited in Rider and Kennedy, 2011). Nowadays, sonic tools can measure compressional and shear slowness along with Stoneley waves. The use of sonic logs and the application of equations in **Table 2-1** allow geoscientists to easily estimate the elastic moduli of the rock.

2.3.2 Static and dynamic moduli

Although sonic waves offer an alternate way to estimate mechanical properties of the rock, the fact is that generally there is a significant difference between mechanical properties assessed using the expressions presented in **Table 1.1** and mechanical properties determined by stress and strain measurements from uniaxial or triaxial tests and the application of equations **Eq. 2-2** or **Eq. 2-30**. The elastic properties obtained from sonic wave velocity and rock density are known as *dynamic moduli* while those estimated from stress and strain relationships are called *static moduli*.

The reasons for differences between static and dynamic moduli have been studied by several authors. For example, Fjaer (1999), based on triaxial test measurements of stress-strain, P-waves and S-waves, stated that as a result of changes in stress and strain, the continuous process of failure is one of the most important reasons for the difference between static and dynamic bulk modulus in weak sandstones. Montmayeur and Graves (1985) studied the variation of fluid saturation during testing conditions and found that this is a factor that contributes for the difference between static and dynamic moduli, especially because static moduli are best defined with differential variations in pressure, meanwhile, dynamic moduli depend on the pressure applied at the wave's direction of propagation. Based on experimental triaxial test and sonic wave velocity, Yale and Jamieson (1994) indicated that the difference between static and dynamic moduli lies on mineralogy and porosity of the rock.

As discussed above, elastic moduli play an important role in the mechanical behaviour of the rock, and these can be static or dynamic depending on the method used for estimating them. However, static methods are expensive and take up many hours of work in the laboratory. In contrast, dynamic methods are cheap and easily applied. Despite this, the elastic moduli estimated through triaxial tests are considered more representative of underground conditions.

Young's modulus is not only considered one of the most important elastic moduli but also the elastic modulus that presents the largest difference between static and dynamic conditions. There are many empirical relations available to convert dynamic moduli into static moduli. For example Eissa and Kazi (1988), based on stress and strain measurements of 342 laboratory tests with extreme variability on rock types, developed two statistical relations for estimating Young's modulus. The first is a linear relation with a correlation coefficient (r^2) equal to 0.84, and the second is a logarithmic correlation with a correlation coefficient equal to 0.96. Wang (2000) presented a linear correlation applicable to soft and hard rocks. Canady (2011) presented a non-linear correlation to correct Young's modulus in formations that vary from soft to hard rocks. Young's modulus expression is a modification of Wang's correlation where coefficients a, b and c are 1, -2 and 4.5, respectively. Morales and Marcinew (1993) presented a correlation to correct Young's modulus taking into account the degree of consolidation, porosity and mineralogy. **Table 2-2** summarizes the most common relationships mentioned above.

Table 2-2 Corrections to convert dynamic into static moduli.

Rock Type	Empirical Correlation	Author
Wide Range	$E_{st} = 0.74E_{dy} - 0.82$	Eissa and Kazi
Wide Range	$Log_{10}E_{st} = 0.77Log_{10}(\rho * E_{dy}) + 0.02$	Eissa and Kazi
Soft Rock	$E_{st} = 0.41E_{dy} - 1.06$	Wang
Wide Range	$E_{st} = \frac{Ln(E_{dy} + a) * (E_{dy} + b)}{c}$	Canady
Wide Range	$Log_{10}E_{st} = A1Log_{10}(E_{dy}) + Ao$	Morales
Berea Sandstone	$K_{st} = 0.9K_{dy}$	Cheng
Wide Range	$K_{dy} = \frac{K_{st}}{1 + 3PK_{st}}$	Fjaer

Values of Est= static and Edy= dynamic are expressed in GPa and the density in g/cm^3

Another important mechanical property of the rock that has to be corrected from dynamic conditions to static conditions is Poisson's ratio, which is an indicator of the degree of rock's consolidation and relates the principle strains of the rock. The theoretical value for a porous rock saturated with uncompressible fluid is expected to be 0.5. However, according to Spencer et al.

(1994) extensive experimental results have indicated that Poisson's ratios for clean dry sandstone are in the range of 0.15 to 0.20 when using ultrasonic techniques. Karig (1996) developed static tests on sediments from the Nankai Channel that resulted in values ranging from 0.20 to 0.25 (cited by Chang and Zoback, 1998).

Chang et al. (1999) indicated that experiments made on the Lentic sand, Wilmington sand, and Ottawa sand/Montmorillonite samples present viscoelastic behaviour (materials that present both viscous and elastic properties when undergoing deformation), which cannot be linked with pore fluid expulsion or dewatering. Therefore, there is a clear difference observed between static and dynamic moduli for poorly consolidated sand, which can be attributed to a viscoelastic mechanism.

2.4 Rock Strength

2.4.1 Failure criterion

Failure is the resulting displacement of two sides of a failure plane relative to each other due to shear stresses large enough to exceed the frictional force that presses the sides together (**Figure 2-3**). Then, the critical shear stress (τ_{max}) is a function of normal stresses (σ) acting in the failure plane. This statement is known as the Mohr's hypothesis (Fjaer et al. 2008).

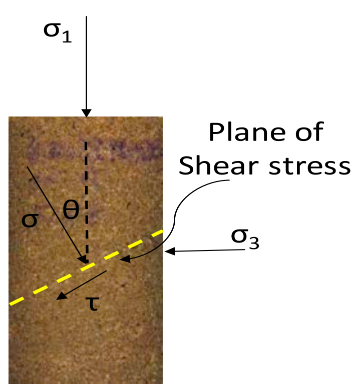

Figure 2-3 Failure plane resulting from shear and normal stresses.

There are three principal stresses acting on an underground unit element of rock, σ_1, σ_2 and σ_3, and the way to connect them is through the Mohr's circle. Shear failure depends on the maximum and minimum principal stresses. The normal and shear stresses act on a plane whose normal makes an angle of θ degrees to the maximum principal stress, σ_1 (**Figure 2-3**).

The Tresca criterion states that rock will yield when the shear stress exceeds the critical shear stress and the rock will not return to its initial state after removing the stresses. This behavior is governed by the following expression,

$$\tau_{max} = 0.5 * (\sigma_1 - \sigma_3) = S_o \qquad \textbf{Eq. 2-30}$$

Where S_o is the shear strength of the rock also known as cohesion. In **Figure 2-4,** the Tresca criterion would be represented as a straight horizontal line.

2.4.2 Coulomb criterion

Coulomb (1785) based on his study of friction force along a sliding plane between two no welded bodies, and in analogy with the shear stress that cause failure in the rock along a failure plane, stated that the friction force acting against displacement is equal to the normal force acting along this plane multiplied by a factor equivalent to tan φ (cited in Jaeger et al., 2007). Also, shear stress is affected by an additional resistance produced by an internal force of the rock known as cohesive force (S_o). Thus, Coulomb criterion is expressed as follows,

$$\tau = S_o + \sigma \tan \varphi \qquad \textbf{Eq. 2-31}$$

Where φ is the internal friction angle and is defined as the angle between the failure plane and horizontal plane.

According to Jaeger et al. (2007), Coulomb's theory has two limitations. First, experimental data indicate that σ_1 at failure increases at nonlinear rate with σ_3. On the contrary, Coulomb's theory suggests that σ_1 at failure will be linear with σ_3. Second, Coulomb's criterion can be applicable only when $\sigma_3=\sigma_2$.

The Mohr theory indicates that it is possible to define a semicircle for any state of stress that results tangent to the straight line that represents the plane where shear and normal stresses satisfies Coulomb's criterion. Therefore, Mohr (1914) suggested a more general expression to represent the failure envelope (cited in Jaeger et al., 2007).

The failure envelope can be experimentally established by plotting a series of Mohr's circles for the stresses when the rock fails. The performance of three or more triaxial tests at different confining pressure allows to build Mohr's envelope (strength envelope), which is represented by a straight-line that refers to the limit of strength. As shown in **Figure 2-4**, the circle defined by σ_1 and σ_3 and the envelope has the form $\tau= f(\sigma)$.

Mohr's strength theory involves two key assumptions:

1) The maximum horizontal stress does not have effect on the strength
2) There is no cohesion, which means that just the pressure has bearing on the shearing strength.

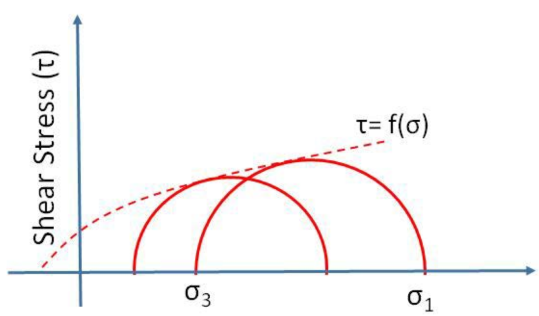

Figure 2-4 Failure stress.

The Mohr-Coulomb criterion is the most used criterion to estimate the strength of the rock and it is supported by the assumption that strength is a linear function of normal stress as presented in **Eq. 2-32**,

$$\tau = S_o + \sigma \tan\varphi = S_o + \mu \qquad \textbf{Eq. 2-32}$$

Where the coefficient of internal friction (μ) is expressed by μ=tan φ and the inherent shear strength of the rock (S_o) is measured when the internal friction angle is zero.

The Mohr's circles shown in **Figure 2-5** touch the failure envelop at a specific point of normal stress and shear stress given by the following expressions, respectively,

$$\sigma = \frac{(\sigma_1 - \sigma_3)}{2} + \frac{(\sigma_1 - \sigma_3)}{2}\cos 2\theta \qquad \textbf{Eq. 2-33}$$

$$\tau = \frac{(\sigma_1 - \sigma_3)}{2}\sin 2\theta \qquad \textbf{Eq. 2-34}$$

Where:

σ = Normal stress acting on the plane of failure.

τ = Shear stress acting on the plane of failure.

2θ = Inclined plane angle.

Once σ and τ are known, it is possible to find the plane of failure where shear stress is equal to shear strength. Mohr's circle of stress in **Figure 2-5** helps to determine if a failure will occur or not on a rock along a plane inside the rock and what will be the angle of failure. 2θ is the angle between the straight line given by the points where the failure envelope touches the Mohr's circle and the centre of Mohr' circle as shown in **Figure 2-5**. θ provides the direction of the failure plane and is related to the internal friction angle as follows,

$$\theta = \frac{\pi}{4} + \frac{\varphi}{2}$$ **Eq. 2-35**

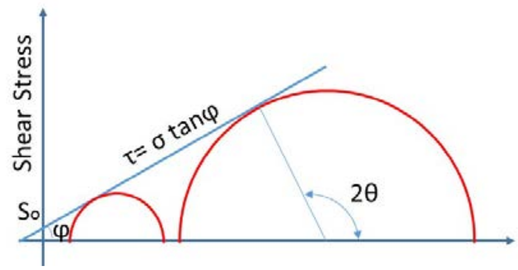

Figure 2-5 Mohr's envelope.

The rock's strength estimation is fundamental to evaluate common reservoir problems in the petroleum industry such as compaction, subsidence and sand production.

The rock's strength is defined as the value of axial compression stress at which the rock cannot support more stress and as a consequence fails. One of the most important parameters used to measures the rock strength is the unconfined compressive strength (UCS), which can be determined in two different ways: directly from both triaxial compression test or uniaxial compressive test and application of **Eq. 2-36**, or indirectly from wireline logs and correlations.

The expression for unconfined compressive strength (UCS) is,

$$UCS = 2S_o \tan\theta$$ **Eq. 2-36**

A uniaxial compressive test is that where the sample is compressed axially without any radial confining pressure and the UCS value is measured at the point when the rock fails. It should be noticed that UCS measurements are highly sensitive to cracks and heterogeneities. Therefore, high experimental uncertainty should be expected (Fjaer et al., 2008; Wood and Shaw, 2012).

In a triaxial compression test the sample is initially compressed axially until the stress reaches the confining pressure. Then, the confining pressure is held constant and the axial pressure is increased until the rock fails. It is important to mention that triaxial tests can be developed under drained and undrained conditions and these allow to measure UCS, Young's modulus, Poisson's ratio, shear modulus and bulk modulus of the framework (Fjaer et al., 2008).

The unconfined compressive strength (UCS) can be determined from triaxial tests on cylindrical rock samples. However, UCS data are scarce in many reservoirs and much more under overburden and underburden formations. Thus, empirical relations to estimate the UCS and internal friction angle (φ) from geophysical well logs have been published by several authors as alternate solutions. For example, Chang et al. (2005) compiled and summarized some of the most important empirical relations for calculating UCS and internal friction angle for sandstones and shales based on internal properties of the rock such as Young's modulus, porosity, density and acoustic velocity.

2.4.3 Relations between rock strength and physical properties

The rock strength depends on internal and external factors of the rock. Several authors have indicated that the most important internal factors governing the UCS for clastic rocks are composition, clay content, porosity, texture, degree of cementation, discontinuities, water content, frictional sliding between grains and macroscopic tensile cracks. Meanwhile, the external factors are confining pressure and temperature (Plumb, 1994; Li et al., 2012; Tziallas et al., 2013; Brace et al., 1966). Furthermore, in brittle rocks cracks occur abruptly due to the lack of strength to support compression. On the other hand, in a ductile material the failure process is gradual (Zoback, 2006).

An easy and practical way for estimating UCS is the application of empirical relations as a function of the aforementioned parameters. Plumb (1994), based on 784 unconfined compressive tests on sedimentary rocks, observed that UCS increases as porosity decreases and porosity decreases as V_{clay} content decreases. Then, he developed a correlation to estimate UCS as a function of porosity. Vernik et al. (1993) developed similar correlations to Plumb's equation but they included an additional parameter ξ to consider pore structure. Parameter ξ is the reciprocal value of porosity when UCS =0. Wood and Shaw (2012) presented a methodology to correlate UCS to dry density for sandstones based on experimental data of 134 sandstone tests and 129 siltstone tests. Tziallas et al., (2013) developed a study on heterogeneous rocks with hard and weak alternate layers and found that Young's modulus and siltstone content correlate well with UCS. They also indicated that sandstones present a USC range between 85 and 103 MPa, whereas siltstone range is between 34.6 and 53.7 MPa. They suggested that the decrease in strength of a composite specimen is directly related to the percentage of siltstone. Finally, Chang et al. (2005) proposed a correlation for weak sandstones using wireline sonic logs.

2.5 Coupling Reservoir-Geomechanical Models

In the petroleum industry, reservoir simulation models have been used during many years to simulate a wide variety of reservoir's phenomena. However there are some issues of practical importance, for instance, compaction, subsidence and sand production that cannot be adequately predicted by only the use of traditional simulation models. The common characteristic of these issues is the strong relationship between the porous medium, saturation fluids and stress-strain behaviour of the rock. Therefore, a better way to simulate these problems is required and it is achieved through the coupling of reservoir models to mechanical models.

An important question that reservoir engineers have to answer before initialization of the coupling of reservoir and geomechanical models is "*Is it necessary to consider the effect of mechanical properties of the rock to reproduce or model these phenomena?*" According to Settari et al. (2000) the answer to this question could be obtained from field and laboratory data. Settari (2008) stated the following problems where geomechanical models are useful to model reservoir's behaviour,

- Soft sands where the strength of the rock is low and the main mechanism of production is depression. Some indications of these types of formations are low recovery, high production of sand, and permeability and porosity stress-dependent (well testing diagnostic).
- Reservoirs presenting compaction and subsidence.
- Reservoirs where porosity and permeability vary with stresses.
- Low gas permeability reservoirs with stress sensitive observation.
- Hydraulic fracturing of conventional and unconventional reservoirs.
- Water injection at pressures equal to or greater than fracture pressure.
- Double porosity reservoirs with low fracture permeability.
- Oil sands with high sand production.
- Chalk reservoirs.
- Completion of wells in coalbed methane formations (CBM).

Additionally, Shchipanov et al. (2010) stated that some important parameters that can help determining the stress dependency of a reservoir are production history, sample test analyzes, well testing analyses and low accuracy in history matching and production forecasting processes of reservoir simulation when using only reservoir simulation models.

The concept of coupling numerical modeling (reservoir and geomechanical models) is complex and involves three different areas: 1) reservoir simulation to predict fluid flow and heat transfer in porous media, 2) geomechanical simulation to calculate the stress and strain behaviour of the rock, and 3) failure mechanics, which handles fault geometry and propagation (Settari and Maurits, 1998).

From the construction's model point of view, there are three types of coupled problems: 1) regional models, 2) full field reservoir models, and 3) single well models. This work focuses on full field reservoir simulation. These models aim at the investigation of the following objectives: determine the oil recovery factor by compaction mechanism, quantify the amount of subsidence and the size of the area under the effect of subsidence, determine shear stress distribution to minimize infill drilling, verify fault stability, design hydraulic fracturing jobs considering changes in stresses, and test the effect of shallow aquifers in final recovery factor.

Settari and Walters (1988), Settari and Sen (2008) and Rodriguez (2011) stated that the coupling modeling should consider the following stages:

- Definition of boundary conditions and solution domain,
    - Reservoir: Constant pressure or closed boundary
    - Geomechanics: Do not allow vertical movement at the top of the model, at the bottom of the model, and at the sides in the normal direction
- Gridding characteristics: Geomechanical grids must consider a side-burden at least 3 to 5 times the size of the reservoir model, in offshore reservoirs overburden from the sea floor (but taking into account the effect of sea water), in

onshore reservoirs overburden from the ground surface, and underburden as large as possible. The stress model requires to be populated with geomechanical properties of the rock. Both geomechanical and reservoir grids should be independent but compatible.

- Model initialization.
- Selection of coupling method.

According to Tran et al. (2002), there are four methods available in the literature to couple reservoir flow model to rock stress-strain models. These methods are briefly described as follows:

1) Explicit coupled (one way coupling method): The governing equations of both models are solved at each time-step considering the last existing calculations of the coupling term. One-way indicates that any alteration in pore pressure will cause alterations in the stress-strain behaviour. However, no alteration will occur in pore pressure when alteration on stress-strain occurs. The main disadvantage of this method is thus that it does not consider porosity and effective permeability alterations as the stresses in the rock change.

   Theoretically this method is appropriate when the reservoir compaction is small. There is not significant error since rock compressibility is governed primarily by gas compressibility. Consequently, the mass balance is ruled by gas pressure instead of stresses in the rock. However, this method is not applicable in stress-sensitive gas reservoirs because dynamic permeability affects fluid flow in porous medium (Gonzalez, 2012).

2) Iteratively Coupled: This two-way coupling scheme satisfies both flow and stress-strain governing equations of the models. Coupling terms (porosity and permeability) are iterated during each time step. In this method the data are explicitly passed forth and back while waiting for achieving convergence tolerance. For example, if volume coupling is the target, the information passing from the reservoir simulator to the geomechanical module is pressure and temperature, which are considered as external loads for displacement calculations. Whereas the information from the geomechanical module to reservoir simulator is a porosity function, which is computed after stresses and strains are calculated. The number of iterations is a function of the tolerance criterion on pressure or stress changes between the last two iterations. An iterative method is recommended for cases where the compressibility of the rock could produce a strong deformation on the rock (Tran et al., 2002).
3) Fully coupled: This method implies simultaneous solution of a system of equations with displacement, temperature and pressure as unknowns. This model is recommended for modeling complex problems such as plasticity.
4) Decoupled: Commercial reservoir simulators have options to solve fluid flow problems by themselves since they evaluate stress changes through pore volume changes and vertical displacements. Porosity and permeability are updated in the simulator by means of introduction of tables of these variables as a function of pressure. This method runs fast, easy to use and could be utilized as a first approximation for preliminary understanding of the reservoir physics.

Consideration of the stress-strain effects in a reservoir simulator is a very difficult and time consuming task due to the following three key reasons: 1) the lack of reliable input data for the geomechanical modeling, which can lead to misleading results, 2) the huge number of grid cells required to model the reservoir volume and its surroundings, and 3) the required coupling method to model the mechanical behavior of the reservoir and surroundings. Hence, it is highly recommended to analyze the existing direct and indirect input data for determining if the reservoir stress-strain dependency is significant (Gonzalez, 2012).

2.6 Reservoir Compaction and Subsidence

Compaction is an irreversible mechanism that produces the rock's shrink by means of increasing the effective stress when there is a reduction in reservoir pore pressure. As a result, the stresses exceed the compressive strength of the rock and consequently porosity and permeability are permanently reduced. The important consequence above the reservoir is the seabed or ground surface deformation also known as subsidence.

Morita (1989) indicated that in-situ stresses change as pore pressure changes; then, the rock deforms axially with horizontal strain. He presented a methodology that allows estimating the degree of compaction and subsidence in reservoirs with a simple geometry by assuming that in-situ stresses are composed of induced and original in-situ stresses. The methodology provides a good approximation but it is limited to reservoirs with low Young's modulus.

Settari in 2002 indicated that compaction is subjected to the initial stress state on the rock and the stress path developed during reduction of pressure once the reservoir goes on production. When the mechanism of compaction is only a function of the mean effective stress, the decrease in porosity follows a smooth trend during the depletion process. However, if the compaction process involves shear failure as in the case of chalk reservoirs or when temperature increases, then porosity is a function of a combination of stresses and more complex stress-strain models should be used to simulate the volumetric strain response. In **Figure 2-6a** the elastic behavior of the rock can be approached based on the rock compressibility. Plastic deformation starts once the compressive strength exceeds point A. Following plastic deformation to point B any unload at this point will follow a hysteresis path and the slope will be less than for the initial elastic loading. In **Figure 2-6b** the same process is presented using a cap model. Note that the pore collapse mechanism occurs when the stress path reaches the cap envelope.

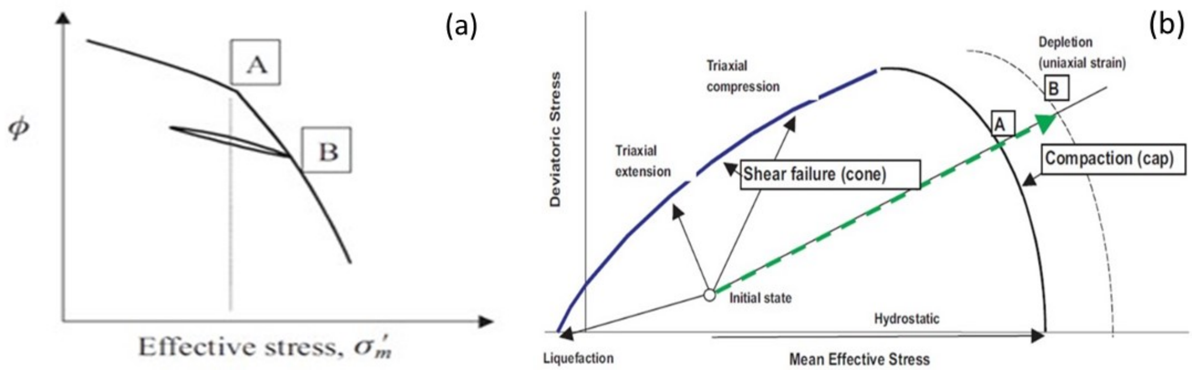

Figure 2-6 (a) Rock compaction versus effective stress, (b) Rock compaction in Mohr-Coulomb diagram. (Source: Settari, 2002)

Chapter Three: Mechanical Properties and In-Situ Stresses

This chapter describes the methodology followed to estimate the in situ stresses and pore pressure at reservoir conditions and to evaluate the situ rock mechanical properties using sources of information such as core samples, wireline logs, and well tests. New empirical correlations are developed in this thesis to convert dynamic moduli to static moduli for the case of Young's modulus, Poisson's Ratio, unconfined compressive strength and friction angle of rocks in the area of study.

3.1 Static and Dynamic Moduli

As previously mentioned in Chapter Two, there are two key sources of information for determining rock mechanical properties: 1) direct measurements from triaxial tests in the laboratory that provide properties known as "static moduli", and 2) calculations using wireline logs such as bulk density, compressional acoustic velocity and shear acoustic velocity that provide properties known as "dynamic moduli". The static elastic moduli are different from the dynamic elastic moduli since they are determined under different conditions; however, they can be related. The first step to relate these two sources of information is to correct the static moduli on the basis of effective in-situ stress and then correlate it to the dynamic moduli. In order to correct the results of triaxial test at reservoir conditions, the confining stresses must be determined at reservoir conditions.

3.2 Experimental Data

Triaxial tests on samples from wells GML-2 (located in the field of interest), GMK-1 and GMK-2 (located in a neighbouring field) were performed using a triaxial cell equipped with gauges that control the radial confining pressure, screw-ball press for high precision on axial load, strain-gauges in the load cell, linear variable differential transformer (LVDTs) to measure radial deformation, ultrasonic sources to generate P and S waves, and detectors to measure the porosity, grain density and waves velocities in different directions. **Figure 3-1** presents an illustration of a triaxial cell (not to scale) similar to that used for GML elastic moduli determination.

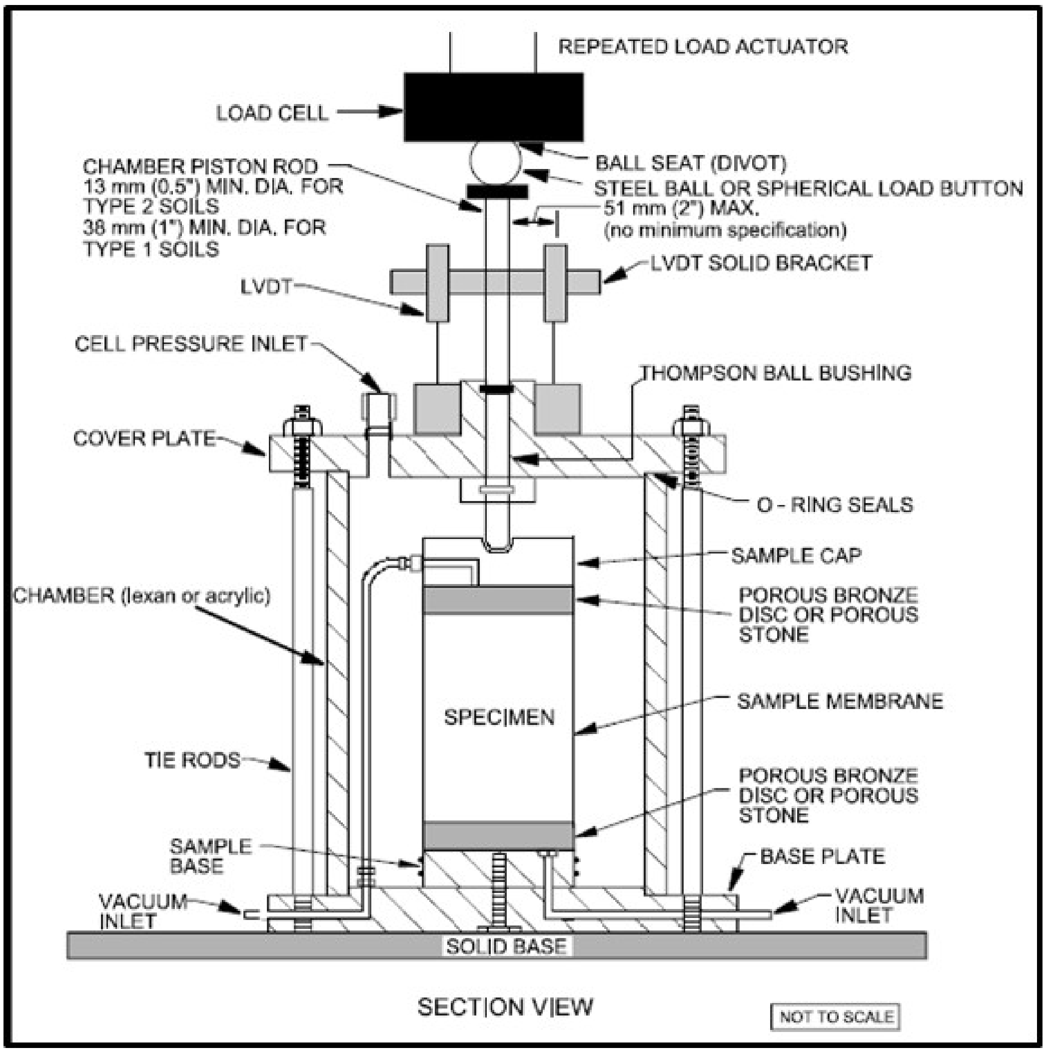

Figure 3-1 Triaxial cell (Source: FHWA, 2007)

The testing procedure considered four stages:

1) Collection of 3 or 4 plugs at every depth of interest to guarantee the Mohr-Coulomb envelope's reliability.

2) Preparation of cylindrical plugs (1 inch in diameter and 2 inches in length) and placing of them in the triaxial cell.
3) Scanning of samples with a CT-scan to guarantee their homogeneity and integrity.
4) Testing of samples under different confining pressures. At this point the samples are hydrostatically pressurized until reaching the confining pressure. Measure acoustic velocities (acoustic tests were only carried out for wells GMK-1 and GMK-2).
5) Holding the confining pressure constant increase the axial load until the rock fails.

Mechanical and acoustic information were gathered from these tests. Some of the mechanical information includes confining pressure, axial stress, axial strain and lateral strain. The acoustic measurements include P and S wave velocities.

The case of a poroelastic rock with a nonlinear stress-strain relationship is shown in **Figure 3-2a.** For this case, the static bulk modulus can be estimated from the hydrostatic phase since the stresses are equal in all directions and the relation between stress and strain is linear. The Young's modulus can be determined using the tangent method, where the slope of a straight-line tangent to the stress-strain curve in the triaxial phase is equal to Young's modulus. Poisson's ratio is equal to the ratio between the radial stress-strain slope and the axial stress-strain in the triaxial phase. Shear modulus can be calculated from any of the other two moduli determined previously and the use of one of the expressions listed in **Table 2-1**.

Figure 3-2a shows the relationship between strain and axial stress for three triaxial tests under different confining pressures 200, 400 and 800 psi (1.37 MPa, 27.5 MPa 55.15 MPa) and for well GML-2. However none of them represent the reservoir conditions as will be shown later in this Chapter. The stress-strain relationship for each test exhibits linear behavior previous to rock failure, which indicates that the rock is acting as an elastic material. It can also be observed that as long as the confining pressure decreases, the rock behaves as a poroelastic material and as a consequence the failure stress also decreases.

Figure 3-2b shows Mohr's circles for three different confining pressures and the Mohr-Coulomb failure line. The failure line allows estimating the inherent shear strength (cohesion) and the internal friction angle.

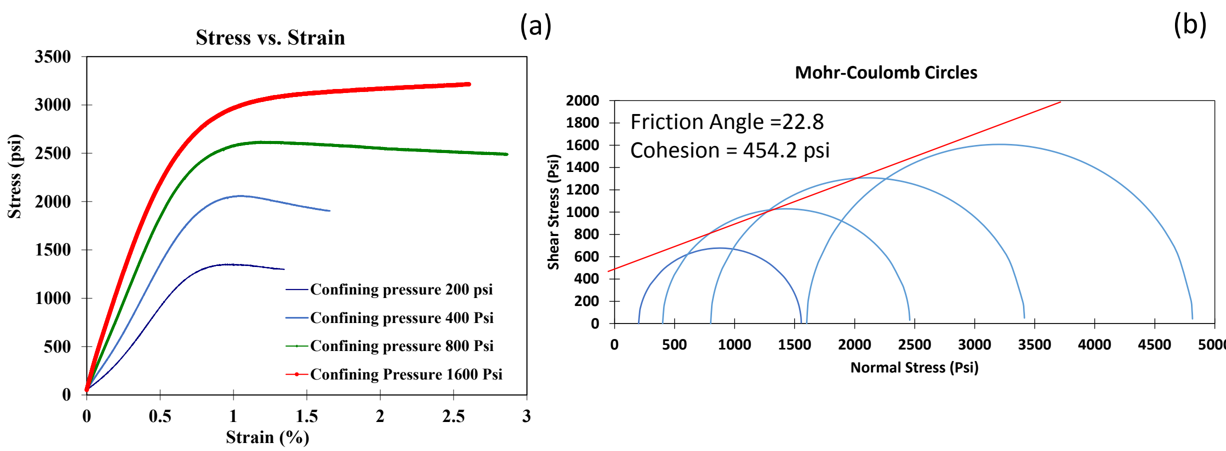

Figure 3-2 Triaxial test results. (a) Stress versus strain and (b) Mohr-Coulomb circle with failure line.

Similar plots were built for each one of the 30 sets of triaxial tests. **Table 3-1**, **Table 3-2** and **Table 3-3** show the calculated values of bulk modulus, shear modulus, Poisson's ratio and Young's modulus for both static and dynamic conditions. These tables also present information for the triaxial tests including well name, sampling's depth, facies, porosity and confining pressure. Sonic velocity test data from laboratory is also included for wells in GMK field.

Table 3-1 GML experimental data.

Well	Plug	Rock Type	Depth m	Confining Pressure Psi	Axial Strengh Psi	Poroelastic moduli Young 10^6 Psi	Shear 10^6 Psi	Bulk 10^6 Psi	Poisson Ratio
GML-2	N2MC14A	Shale	3057.43	200	2270	223.0	88.3	153.2	0.262
GML-2	N2MC14C	Shale	3057.43	400	2882	249.5	102.8	145.1	0.213
GML-2	N2MC14B	Shale	3057.43	800	4144	558.0	235.3	295.9	0.186
GML-2	N3MC1G	Sand	3072.98	200	1373	1790.0	695.0	1406.0	0.288
GML-2	N3MC1H	Sand	3072.98	400	2038	2320.0	916.5	1650.0	0.266
GML-2	N3MC1I	Sand	3072.98	800	2600	2930.0	1170.0	1970.0	0.252
GML-2	N3MC5E	Sand	3078.54	200	1355	185.0	74.4	120.1	0.243
GML-2	N3MC5F	Sand	3078.54	400	2059	262.7	109.4	146.2	0.200
GML-2	N3MC5L	Sand	3078.41	800	2615	371.2	156.3	197.9	0.187
GML-2	N3MC5N	Sand	3078.41	1600	3215	453.3	191.9	236.6	0.181
GML-2	N3MC5C	Sand	3078.54	200	1393	160.0	61.9	128.3	0.292
GML-2	N3MC5D	Sand	3078.54	400	1779	244.8	101.6	137.9	0.204
GML-2	N3MC5O	Sand	3078.41	1600	3250	411.9	178.6	198.0	0.153
GML-2	N4MC1A	Sand	3083.60	200	5275	1100	465.3	576.5	0.182
GML-2	N4MC1C	Sand	3083.65	400	8630	1450	614.9	752.9	0.179
GML-2	N4MC1D	Sand	3083.65	800	12048	1900	814.1	951.0	0.167
GML-2	N4R5H2	Sand	3086.52	200	1522	183.0	72.0	129.0	0.263
GML-2	N4R5H3	Sand	3086.56	400	1741	188.0	76.0	116.0	0.230
GML-2	N4R5H4	Sand	3086.61	800	2433	308.0	129.0	166.0	0.191
GML-2	N4R5H5	Sand	3086.65	1600	3809	312.0	136.0	149.0	0.151
GML-2	N4MC3A	Sand	3087.83	200	1702	253.0	98.8	191.7	0.280
GML-2	N4MC3B	Sand	3087.83	400	2319	315.0	123.7	231.3	0.273
GML-2	N4MC3C	Sand	3087.83	800	2951	456.0	184.5	287.9	0.236
GML-2	N5MC1H	Shale	3175.17	200	1978	204.0	82.6	128.3	0.235
GML-2	N5MC1I	Shale	3175.17	400	2358	215.0	87.4	132.8	0.230
GML-2	N5MC1K	Shale	3175.17	800	3201	314.0	137.8	145.0	0.139

Table 3-2 GMK-1 experimental data.

STATIC PROPERTIES											DYNAMIC PROPERTIES						
							Poroelastic moduli				Wave Velocity			Poroelastic moduli			
Well	Plug	Facie	Porosity	Depth m	Confining Pressure Psi	Axial Strengh Psi	Young 10^6 Psi	Shear 10^6 Psi	Bulk 10^6 Psi	Poisson Ratio	Compres. ft/sec	Shear ft/sec	Relación Vp/Vs	Young 10^6 Psi	Shear 10^6 Psi	Bulk 10^6 Psi	Poisson Ratio
GMK-1	N1DC8V12	Shale	0.211	2856.7	100	684	0.055	0.021	0.049	0.313	3019	1807	1.67	0.237	0.097	0.142	0.220
GMK-1	N1DC8V2	Shale	0.190	2856.6	500	872	0.068	0.028	0.040	0.218	3027	1828	1.78	0.243	0.095	0.175	0.283
GMK-1	N1DC8V4	Shale	0.240	2856.6	900	927	0.044	0.018	0.024	0.203	3056	1845	1.66	0.248	0.102	0.144	0.212
GMK-1	N1DC8V1	Shale	0.180	2856.6	1300	1119	0.036	0.016	0.018	0.158	3100	1905	1.63	0.259	0.108	0.142	0.196
GMK-1	N2DC18H1	Shale	0.011	2885.15	100	464	0.036	0.013	0.038	0.346	2452	1468	1.67	0.144	0.059	0.086	0.220
GMK-1	N2DC18H3	Shale	0.010	2885.18	500	661	0.020	0.007	0.019	0.331	2906	1674	1.74	0.199	0.080	0.134	0.251
GMK-1	N2DC18H2	Shale	0.009	2885.15	900	904	0.018	0.007	0.012	0.255	2927	1750	1.67	0.210	0.086	0.126	0.222
GMK-1	N2DC18H4	Shale	0.006	2885.21	1300	1029	0.018	0.007	0.011	0.230	2933	1753	1.67	0.217	0.089	0.130	0.222
GMK-1	N4CV85C	Toba	0.255	3951.62	100	6037	0.886	0.409	0.354	0.083	9944	5425	1.83	1.997	0.775	1.571	0.288
GMK-1	N4CV85A	Toba	0.246	3951.62	600	6534	0.941	0.437	0.370	0.076	9735	5344	1.82	1.987	0.774	1.535	0.284
GMK-1	N4CV85B	Toba	0.254	3951.62	1100	6672	0.953	0.434	0.396	0.099	9835	5418	1.82	1.996	0.778	1.527	0.282
GMK-1	N4CV85D	Toba	0.254	3951.62	1600	6663	1.004	0.470	0.386	0.067	9947	5462	1.82	2.027	0.789	1.565	0.284
GMK-1	N4V4B	Sand	0.102	3916.44	100	8385	1.328	0.529	0.905	0.255	14043	7771	1.81	5.044	1.972	3.808	0.279
GMK-1	N4V4A	Sand	0.100	3916.44	600	10479	1.739	0.710	1.051	0.224	14383	8173	1.76	5.529	2.192	3.865	0.262
GMK-1	N4V4C	Sand	0.102	3916.44	1100	12596	1.909	0.804	1.016	0.187	14664	8495	1.73	5.927	2.376	3.911	0.247
GMK-1	N4V4D	Sand	0.102	3916.44	1600	14643	2.333	0.987	1.223	0.182	14644	8768	1.67	6.171	2.528	3.679	0.220
GMK-1	N4V34B	Sand	0.192	3920.37	100	1423	0.210	0.075	0.379	0.408	8965	4323	2.07	1.525	0.565	1.678	0.349
GMK-1	N4V34C	Sand	0.188	3920.37	600	3039	0.334	0.134	0.216	0.243	9726	4778	2.04	1.892	0.705	1.982	0.341
GMK-1	N4V34D	Sand	0.191	3920.37	1100	3462	0.355	0.142	0.239	0.252	9850	4845	2.03	1.947	0.726	2.033	0.340
GMK-1	N4V34E	Sand	0.193	3920.37	1600	4093	0.441	0.178	0.280	0.237	10047	5166	1.94	2.182	0.826	2.024	0.320
GMK-1	N4CV12A	Sand	0.152	3936.2	100	2268	0.340	0.127	0.350	0.338	8959	3951	2.27	1.358	0.492	1.876	0.379
GMK-1	N4CV12B	Sand	0.150	3936.2	600	3370	0.498	0.199	0.329	0.248	9828	5102	1.93	2.182	0.829	1.971	0.316
GMK-1	N4CV12C	Sand	0.150	3936.2	1100	4090	0.810	0.324	0.540	0.250	9992	5359	1.86	2.379	0.916	1.964	0.298
GMK-1	N4CV12F	Sand	0.153	3936.2	1600	4447	0.622	0.252	0.388	0.233	10017	5402	1.85	2.420	0.934	1.967	0.295
GMK-1	N4CV30A	Sand	0.204	3939.58	100	2466	0.329	0.124	0.312	0.324	8481	4842	1.75	1.809	0.719	1.247	0.258
GMK-1	N4CV30C	Sand	0.203	3939.58	600	3562	0.455	0.177	0.358	0.288	9065	5320	1.70	2.160	0.873	1.371	0.237
GMK-1	N4CV30D	Sand	0.203	3939.58	1100	4126	0.541	0.221	0.324	0.222	9481	5637	1.68	2.415	0.984	1.472	0.227
GMK-1	N4CV30E	Sand	0.205	3939.58	1600	4836	0.674	0.278	0.393	0.214	9723	5817	1.67	2.560	1.048	1.531	0.221
GMK-1	N5V22A	Sand	0.233	4011.8	100	1239	0.123	0.049	0.081	0.248	8842	4764	1.86	1.805	0.697	1.471	0.295
GMK-1	N5V22B	Sand	0.229	4011.8	600	2577	0.294	0.121	0.174	0.218	9382	5017	1.87	2.038	0.784	1.696	0.300
GMK-1	N5V22C	Sand	0.233	4011.8	1100	3138	0.329	0.136	0.188	0.208	9747	5364	1.82	2.285	0.891	1.753	0.283
GMK-1	N5V22D	Sand	0.231	4011.8	1600	3839	0.353	0.149	0.186	0.183	9946	5558	1.79	2.466	0.969	1.810	0.273
GMK-1	N5V53A	Sand	0.173	4019.2	100	1645	0.166	0.065	0.127	0.282	9970	4684	2.13	1.910	0.703	2.248	0.358
GMK-1	N5V53C	Sand	0.169	4019.2	600	3271	0.372	0.150	0.240	0.241	10579	4846	2.18	2.082	0.761	2.613	0.367
GMK-1	N5V53E	Sand	0.171	4019.2	1100	4211	0.431	0.178	0.247	0.209	10863	5345	2.03	2.508	0.935	2.616	0.340
GMK-1	N5V53F	Sand	0.172	4019.2	1600	5037	0.531	0.222	0.292	0.197	10938	6266	1.75	3.233	1.287	2.206	0.256
GMK-1	N5V59A	Sand	0.241	4019.89	100	1033	0.094	0.039	0.056	0.220	8680	3817	2.27	1.177	0.426	1.637	0.380
GMK-1	N5V59B	Sand	0.240	4019.89	600	2576	0.185	0.077	0.102	0.198	9930	4767	2.08	1.911	0.707	2.127	0.350
GMK-1	N5V59C	Sand	0.239	4019.89	1100	3610	0.235	0.100	0.122	0.179	10218	5038	2.03	2.128	0.794	2.209	0.339
GMK-1	N5V59D	Sand	0.240	4019.89	1600	4681	0.271	0.115	0.139	0.175	10310	5656	1.82	2.586	1.006	2.002	0.285
GMK-1	N5V78A	Sand	0.253	4022.18	100	1390	0.159	0.063	0.112	0.263	8514	4210	2.02	1.438	0.537	1.481	0.338
GMK-1	N5V78B	Sand	0.249	4022.18	600	2574	0.273	0.110	0.173	0.237	9036	4712	1.92	1.792	0.682	1.599	0.313
GMK-1	N5V78C	Sand	0.248	4022.18	1100	3444	0.341	0.141	0.196	0.210	9224	4835	1.91	1.892	0.722	1.665	0.311
GMK-1	N5V78D	Sand	0.251	4022.18	1600	3877	0.433	0.181	0.236	0.194	9369	4946	1.89	1.971	0.754	1.701	0.307

Table 3-3 GMK-2 experimental data.

STATIC PROPERTIES											DYNAMIC PROPERTIES						
Well	Plug	Rock Type	Porosity	Depth	Confining Pressure	Axial Strengh	Poroelastic moduli			Poisson Ratio	Wave Velocity		Relación Vp/Vs	Poroelastic moduli			Poisson Ratio
							Young	Shear	Bulk		Compres.	Shear		Young	Shear	Bulk	
				m	Psi	Psi	10^6 Psi	10^6 Psi	10^6 Psi		ft/sec	ft/sec		10^6 Psi	10^6 Psi	10^6 Psi	
GMK-2	N1R3V3A	Sand	0.168	4261.93	150	1697	0.158	0.064	0.098	0.231							
GMK-2	N1R3V3D	Sand	0.171	4261.93	700	3244	0.258	0.104	0.163	0.236							
GMK-2	N1R3V3C	Sand	0.169	4261.93	1250	4272	0.622	0.255	0.373	0.222							
GMK-2	N1R3V3B	Sand	0.165	4261.93	1800	4733	0.442	0.191	0.213	0.154							
GMK-2	N1R2V1B	Sand	0.209	4253.18	150	1159	0.154	0.067	0.075	0.156							
GMK-2	N1R2V1C	Sand	0.208	4253.18	700	2773	0.181	0.08	0.081	0.127							
GMK-2	N1R2V1A	Sand	0.211	4253.18	1250	3985	0.196	0.09	0.08	0.092							
GMK-2	N1R2V1D	Sand	0.2	4253.18	1800	5443	0.270	0.124	0.109	0.087							
GMK-2	N2R1V5A	Sand	0.261	4304.03	150.00	1731	0.213	0.084	0.153	0.268	9056	3818	2.37	1.856	1.204	0.432	0.392
GMK-2	N2R1V5B	Sand	0.281	4304.03	700	2994	0.338	0.142	0.184	0.193	9741	4326	2.25	2.079	1.536	0.558	0.377
GMK-2	N2R1V5C	Sand	0.257	4304.03	1250	3712	0.444	0.192	0.214	0.155	9712	4294	2.26	2.073	1.512	0.548	0.378
GMK-2	N2R1V5D	Sand	0.262	4304.03	1800	4225	0.468	0.204	0.222	0.148	9853	4430	2.22	2.112	1.598	0.582	0.374
GMK-2	N2R1V14D	Sand	0.182	4310.82	150	1456	0.09	0.04	0.041	0.133	9436	4124	2.29	2.131	1.509	0.546	0.382
GMK-2	N2R1V11A	Sand	0.204	4310.7	700	3049	0.263	0.118	0.115	0.117	10867	5143	2.11	2.729	2.363	0.871	0.356
GMK-2	N2R1V14C	Sand	0.181	4310.82	1250	4615	0.236	0.108	0.097	0.096	10090	5052	2.00	2.277	2.285	0.857	0.333
GMK-2	N2R1V11B	Sand	0.209	4310.7	1800	5095	0.406	0.183	0.175	0.112	10341	5355	1.93	2.286	2.513	0.954	0.317
GMK-2	N2R1V20D	Sand	0.24	4314.3	150	1469	0.097	0.044	0.041	0.104	9838	5024	1.96	2.000	2.119	0.801	0.324
GMK-2	N2R1V20B	Sand	0.24	4314.3	700	2986	0.212	0.097	0.087	0.097	10391	5387	1.93	2.141	2.361	0.897	0.316
GMK-2	N2R1V20A	Sand	0.241	4314.3	1250	4092	0.276	0.126	0.114	0.097	10867	6059	1.79	2.131	2.884	1.132	0.274
GMK-2	N2R1V32A	Sand	0.259	4318.18	150	1566	0.148	0.065	0.078	0.185	8881	4065	2.18	1.774	1.411	0.516	0.367
GMK-2	N2R1V32C	Sand	0.26	4318.18	700	2892	0.277	0.121	0.129	0.142	9720	4906	1.98	1.888	1.936	0.728	0.329
GMK-2	N2R1V32D	Sand	0.259	4318.18	1250	3751	0.341	0.153	0.148	0.115	10196	5119	1.99	2.093	2.116	0.795	0.331
GMK-2	N2R1V32E	Sand	0.262	4318.18	1800	4595	0.384	0.172	0.168	0.118	10412	5391	1.93	2.125	2.336	0.887	0.317
GMK-2	N3R1V2B	Sand	0.173	4381.55	100	2027	0.208	0.083	0.143	0.257	8639	4677	1.85	1.449	1.801	0.697	0.293
GMK-2	N3R1V2A	Sand	0.171	4381.55	800	4776	0.47	0.193	0.279	0.219	9951	5372	1.85	1.942	2.396	0.926	0.294
GMK-2	N3R1V5A	Sand	0.171	4381.65	1500	6223	0.581	0.238	0.346	0.22	10488	5747	1.83	2.116	2.723	1.060	0.285
GMK-2	N3R1V5B	Sand	0.175	4381.65	2200	7518	0.69	0.297	0.339	0.161	10753	5904	1.82	2.187	2.832	1.103	0.284
GMK-2	N3R1V14A	Sand	0.148	4393.62	100	3750	0.458	0.185	0.29	0.237	9093	4616	1.97	1.808	1.887	0.712	0.326
GMK-2	N3R1V14B	Sand	0.149	4393.62	800	5660	0.735	0.308	0.4	0.194	10285	5617	1.83	2.126	2.710	1.052	0.287
GMK-2	N3R1V14C	Sand	0.152	4393.62	1500	7516	0.921	0.385	0.502	0.194	10884	6141	1.77	2.275	3.192	1.263	0.265
GMK-2	N3R1V14D	Sand	0.148	4393.62	2200	9090	1.06	0.446	0.567	0.188	11330	6274	1.81	2.536	3.362	1.314	0.279

3.3 Mean Effective Stress

In order to establish a relationship between static and dynamic moduli, the first step is to define the mean effective stresses in the reservoir. According to Zoback (2006), three principal stresses have to be known to completely represent the state of stress of a reservoir: the principal vertical stress perpendicular to the earth surface represented by the overburden weight (S_v), and two main stresses in the horizontal direction expressed as maximum horizontal stress (S_{Hmax}) and minimum horizontal stress (S_{hmin}). The principal stresses magnitude indicates the faulting regimes. In normal faulting S_v is the maximum stress, in a strike-slip regime S_v is the intermediate stress and in reverse faulting S_v is the minimum stress. For the offshore field under study, these parameters are calculated for the GML-2 area since this is the only well that has triaxial tests in the field.

3.3.1 Pore pressure

Pore pressure was measured using a formation dynamic tester tool and performing pressure transient analysis for well GML-2. The interpretation indicated a pore pressure equal to 365.6 kg/cm^2 at depth of 3078 m (upper reservoir datum).

3.3.2 Vertical stress

Vertical stress is a function of depth and rock density. For the case of onshore reservoirs it is calculated by integration of rock density from the surface to the upper reservoir datum. In the case of offshore reservoirs the rock density must be corrected for seabed depth. The following expression is used for calculating S_v values,

$$S_v = \rho_w g Z_w + \bar{\rho} g (Z - Z_w) \qquad \textbf{Eq. 3-1}$$

Where ρ_w is water density, g is the gravitational acceleration, Z is the depth of interest, Z_w is the water depth, and $\bar{\rho}$ is the mean overburden density.

At shallow depths where density log data were not available, a pseudo density log was generated as an exponential function of depth in such a way that it follows the density log trend at other depths as shown in **Figure 3-3**. For this case the vertical stress is calculated with the use of **Eq. 3-1** to be 545.14 kg/cm^2 at 3078 m as shown in the calculation below.

$$S_v = \frac{1020kg}{m^3} * \frac{9.81m}{s^2} * 1200m + \frac{2250kg}{m^3} * \frac{9.81m}{s^2} * (3078m - 1200m)$$

S_v = 53.45 MPa=545.14 kg/cm^2

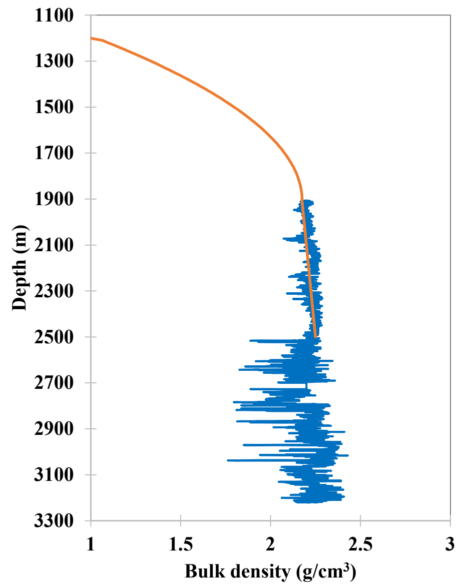

Figure 3-3 GML-2 bulk density log.

3.3.3 Minimum horizontal stress

The most reliable and accepted method for estimating the minimum horizontal stress (S_{hmin}) from field data is based on fracturing the rock and recording the closure pressure (leak off test, LOT). This method requires a radius of penetration into the formation 2 to 3 times larger than the wellbore radius in order to capture only the internal stress. The LOT is usually carried out during the drilling stage, after the casing is in place by drilling some additional meters into the formation. This test helps to determine the fluid density required for the next drilling stage and is the more common method used for determining the minimum horizontal stress (Fjaer et al., 2008).

It is important to highlight that hydraulic fracturing can only be used to determine the magnitude of S_{hmin} in normal faulting or strike-slip environments. GML reservoirs satisfy this condition as will be demonstrated later in this chapter.

The minimum horizontal stress of the lower Miocene reservoirs in GML-2 area are determined from the analysis of 2 leak off tests. The first test was performed at a depth of 2273 m in the lower Pliocene formation and the closure pressure was estimated in 304.5 kg/cm^2 (29.86 MPa). The second test was an extended leak off test and it was performed at a depth of 2742 m. The closure pressure was calculated as 386.3 kg/cm^2 (37.88 MPa).These two minimum horizontal stress values were used to estimate a gradient of 0.17 $kg/cm^2/m$ (16.6 KPa/m) as shown in **Figure 3-4**. This gradient was used to calculate the minimum horizontal stress at 3078 m resulting in S_{hmin} equal to 461.6 kg/cm^2 (45.26 MPa).

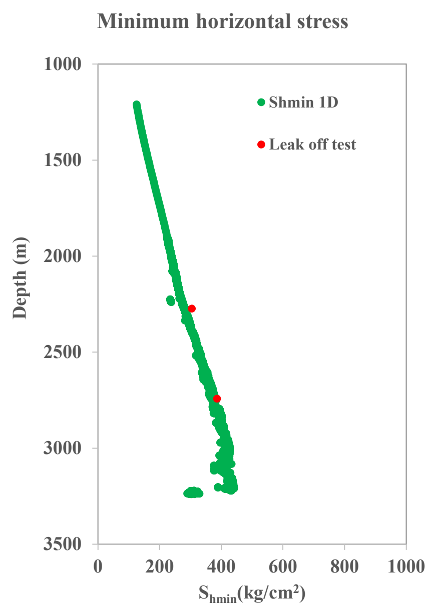

Figure 3-4 Minimum horizontal stress profile (green line) and leak off test data (red dots).

3.3.4 Maximum horizontal stress

The stress polygon presented in **Figure 3-5** helps to estimate a possible range of maximum (S_{Hmax}) and minimum (S_{hmin}) horizontal stress values corresponding to a pore pressure profile (Zoback, 2006). Some important considerations to take into account while building this polygon are presented next. If $S_{Hmax} \geq S_{hmin}$ any possible stress is above the 45° straight line.

Vertical and horizontal lines intersect at a common point where $S_v = S_{Hmax} = S_{hmin}$. Stress boundaries are associated with reverse faulting (RF), normal faulting (NF) and strike-slip (SS). The lowest minimum horizontal stress value in **Figure 3-5** is represented by the vertical line located to the left of the 45° straight line. This vertical line also limits the normal faulting as predicted by **Eq. 3-2**. On the other hand, the highest maximum horizontal stress value is represented by the horizontal line located at the top of **Figure 3-5**. This horizontal line also limits the reverse faulting predicted by **Eq. 3-3**. The diagonal line limiting the strike-slip zone corresponds to a value of S_{Hmax} at which strike-slip faulting occurs for a given value of S_{hmin} and the red dashed lines represent the maximum horizontal stress as function of breakout angle (Zoback, 2002).

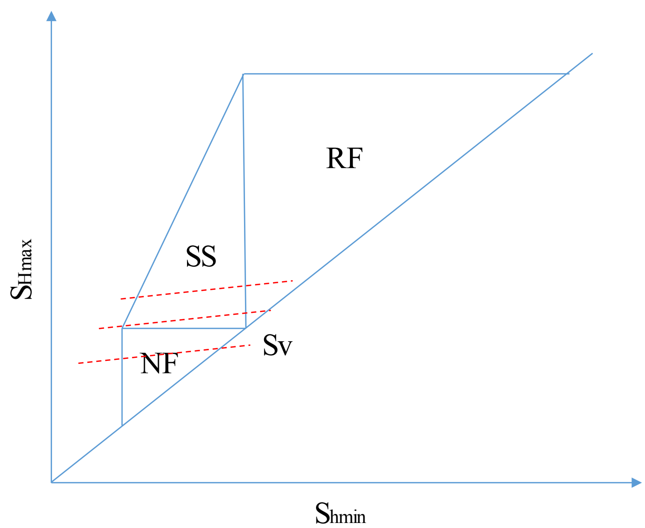

Figure 3-5 Stress polygon.

$$NF: \frac{\sigma_1}{\sigma_3} = \frac{S_v - P_p}{S_{hmin} - P_p} \leq \left[(\mu^2 + 1)^{\frac{1}{2}} + \mu\right]^2 \qquad \textbf{Eq. 3-2}$$

$$RF: \frac{\sigma_1}{\sigma_3} = \frac{S_{Hmax} - P_p}{S_v - P_p} \leq \left[(\mu^2 + 1)^{\frac{1}{2}} + \mu\right]^2 \qquad \textbf{Eq. 3-3}$$

$$SS: \frac{\sigma_1}{\sigma_3} = \frac{S_{Hmax} - P_p}{S_{hmin} - P_p} \leq \left[(\mu^2 + 1)^{\frac{1}{2}} + \mu\right]^2 \qquad \textbf{Eq. 3-4}$$

In addition, Barton et al. (1988) suggested a procedure for calculating S_{Hmax}, which requires the rock strength and wellbore breakout width angle (Wbo) as input data. **Eq. 3-5** shows the expression to estimate S_{Hmax} determined by Barton et al. (1988),

$$S_{Hmax} = \frac{\left(UCS + 2P_p + \left(\Delta P_p\right)\right) - S_{hmin}(1 + 2cos2\theta_b)}{1 - 2cos2\theta_b} \qquad \textbf{Eq. 3-5}$$

Where:

$2\theta_b = \pi - W_{bo}$

UCS = Unconfined Compression Strength

P_p = Pore pressure

ΔP = Difference between mud pressure and pore pressure

W_{bo} = Angle of breakout width.

θ_b = Angle of breakout initiation in reference with S_{Hmax}

The application of **Eq. 3-5** to estimate S_{Hmax} for a given Wbo and UCS results in a line that represents the maximum horizontal stress required to cause a breakout under the specific conditions of rock strength and Wbo of interest.

Applying the previous methodology to GML-2 data, a stress polygon is created as follows,

1) $S_v = S_{Hmax} = S_{hmin}$ = 545.14 kg/cm^2 @ 3078 m on the 45° straight line.
2) Calculation of minimum horizontal stress assuming normal faulting: The triaxial test indicated that UCS = 1400 psi = 98.4 kg/cm^2 and frictional angle (φ)=30.5°

for sand. UCS = 1600 psi = 112.5 kg/cm^2 and frictional angle (φ)=30.4° for shale. μ= tan (φ). Using **Eq. 3-2**, S_{hmin} is calculated as follows,

$$\frac{545 - 365.6}{S_{hmin} - 365.6} = \left[(0.577^2 + 1)^{\frac{1}{2}} + 0.577\right]^2$$

S_{hmin}=425.4 kg/cm^2 (41.7 MPa)

3) Calculation of maximum horizontal stress (S_{Hmax}) assuming reverse faulting and using **Eq. 3-3:**

$$\frac{S_{Hmax} - 365.6}{545 - 365.6} = \left[(0.577^2 + 1)^{\frac{1}{2}} + 0.577\right]^2$$

S_{Hmax}= 903.8 kg/cm^2 (88.6 MPa).

4) Lines representing the S_{Hmax} required creating a breakout in the rock for different unconfined compressive strength values can be generated using equation **Eq. 3-5**.

The plot shown in **Figure 3-6** represents the stress polygon built with the stresses previously calculated and the red diagonal line corresponds to the values of S_{Hmax} required to induce breakouts with constant W_{bo} of 30° in the rock for specific rock strength and different minimum horizontal stresses.

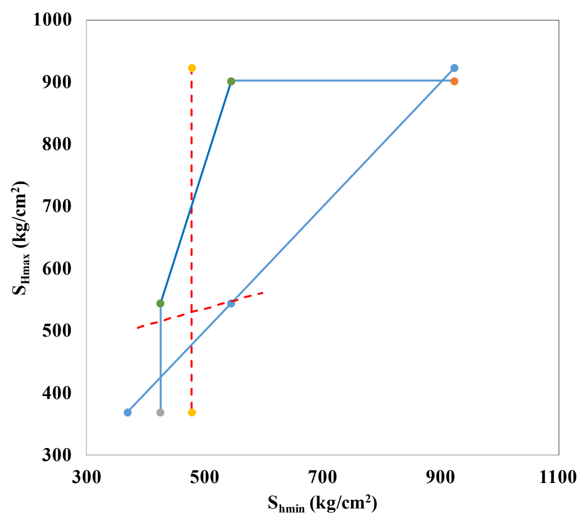

Figure 3-6 GML-2 stress polygon.

Based on **Figure 3-6**, the stress regime for GML field is located in the transition between normal and strike-slip faulting and the maximum horizontal stress with constant Wbo of 30° and unconfined compressional strength of 105.5 kg/cm^2 (10.34 MPa) is equal to 532.5 kg/cm^2 (52.2MPa). The results indicate that the degree of anisotropy is not very significant as the maximum horizontal stress is 532.5 kg/cm^2 (52.2MPa) and the minimum is 461.6 kg/cm^2 (45.26 MPa); a ratio of only 1.15.

3.3.5 Mean effective stress

Reservoirs under normal faulting regime are characterized by a maximum principal vertical stress (S_v), the intermediate stress is the maximum horizontal stress (S_{Hmax}) and the least stress is the minimum horizontal stress (S_{hmin}). So for this case $S_v > S_{Hmax} > S_{hmin}$.

The poroelastic moduli obtained from laboratory tests are determined with the use of stress-strain relationships, which exhibit non-linear behavior when the porous rock is saturated. Under this condition, the poroelastic moduli are calculated using a Biot's coefficient (α) lower than 1. However, if triaxial tests are performed letting the outlet opened to the atmosphere, then, pore pressure is equal to zero, and Biot's coefficient is considered equal to 1. Consequently the poroelastic moduli only depends on Terzaghi effective stress equation expressed as the difference between the confining pressure (Pc) and pore pressure (Pp) (Detournay & Cheng, 1993; Fjaer et al., 2008). Therefore, assuming α=1, the mean effective stress is expressed as shown in **Eq. 3-6**,

$$\sigma_{eff} = \frac{S_{hmin} + S_{Hmax} + S_v}{3} - P_p \qquad \textbf{Eq. 3-6}$$

Upon substitution of the previously calculated vertical stress, minimum horizontal stress and maximum horizontal stress, GML mean effective stress at reservoir conditions is,

$$\sigma_{eff} = \frac{461.6 + 532.5 + 545}{3} - 365.6 = 147.4\frac{\text{kg}}{cm^2} = 14.45\text{MPa} = 2097 \text{ psi}$$

3.4 Static Moduli

The maximum confining pressure applied to GML-2 samples during the triaxial tests was 1600 psi. However, the mean effective in-situ stress calculated above is 2097 psi. However, the comparison between dynamic elastic moduli calculated from acoustic wave velocity data and the static elastic moduli estimated from triaxial tests is only valid under the same confining pressure conditions. For this reason, the experimental static elastic moduli are extrapolated to a confining pressure equal to the reservoir's mean effective stress.

Young's modulus is extrapolated using a logarithmic function as follows,

$$E = a * Ln(P_c) - b \qquad \textbf{Eq. 3-7}$$

Where coefficients a and b are functions of the input data that correspond to each set of triaxial tests. The coefficients of determination (R^2) of each equation applied to each well analyzed in this study vary from 0.84 to 1. **Figure 3-7a** presents the extrapolated Young's modulus corresponding to 2100 psi associated with well GML-2.

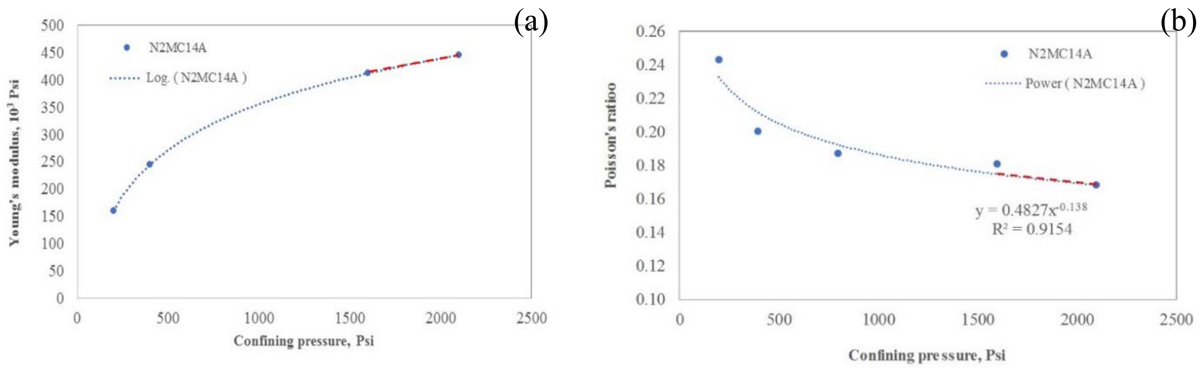

Figure 3-7 Elastic moduli. (a)Young's modulus extrapolation and (b) Poisson's ratio extrapolation.

Poisson's ratio extrapolation is done by means of a power function with the general expression indicated in **Eq. 3-8**.

$$v = a * {P_c}^b \qquad \textbf{Eq. 3-8}$$

The coefficients of determination (R^2) associated with these correlations ranged from 0.87 to 0.99. **Figure 3-7b** shows the extrapolation of Poison's ratio to 2100 psi for well GML-2.

Young's moduli and Poisson's ratios obtained from the above analyses are shown in **Table 3-4**.

Table 3-4 Static Young's moduli (E) and Poisson's ratios (v) estimated at confining pressure equal to 2100 Psi.

Well Name	Rock Type	E (psi)	v	Well Name	Rock Type	E (psi)	v
GMK-1	Shale	21310.5	0.138	GMK-2	Sand	481587.8	0.136
GMK-1	Shale	15052.2	0.174	GMK-2	Sand	416566.4	0.098
GMK-1	Toba	994833.5	0.064	GMK-2	Sand	311834.7	0.091
GMK-1	Sand	2409548.4	0.177	GMK-2	Sand	390711.2	0.108
GMK-1	Sand	432726.9	0.204	GMK-2	Sand	646349.4	0.175
GMK-1	Sand	741658.8	0.216	GMK-2	Sand	990978.5	0.186
GMK-1	Sand	644250.9	0.212	GML-2	Sand	490890.0	0.168

GMK-1	Sand	384769.1	0.187	GML-2	Sand	444975.3	0.137
GMK-1	Sand	557527.2	0.196	GML-2	Sand	395017.5	0.144
GMK-1	Sand	293478.0	0.174	GML-2	Sand	584124.5	0.214
GMK-1	Sand	353285.4	0.193	GML-2	Shale	241320.6	0.105
				GML-2	Shale	312962.2	0.144

3.5 Dynamic Moduli

Wireline logs were run during the drilling stage of three wells in the field under consideration. Bulk density, sonic compressional slowness and sonic shear slowness data as a function of depth are available. Dynamic moduli are calculated from wireline log data applying equations presented in **Table 2-1**. In well GML-2, wireline logs were run from 1900 to 3200 m. **Figure 3-8a** shows both dynamic Young modulus and shear modulus profiles, whereas **Figure 3-8b** presents bulk modulus and Poisson's ratio profiles corresponding to well GML-2.

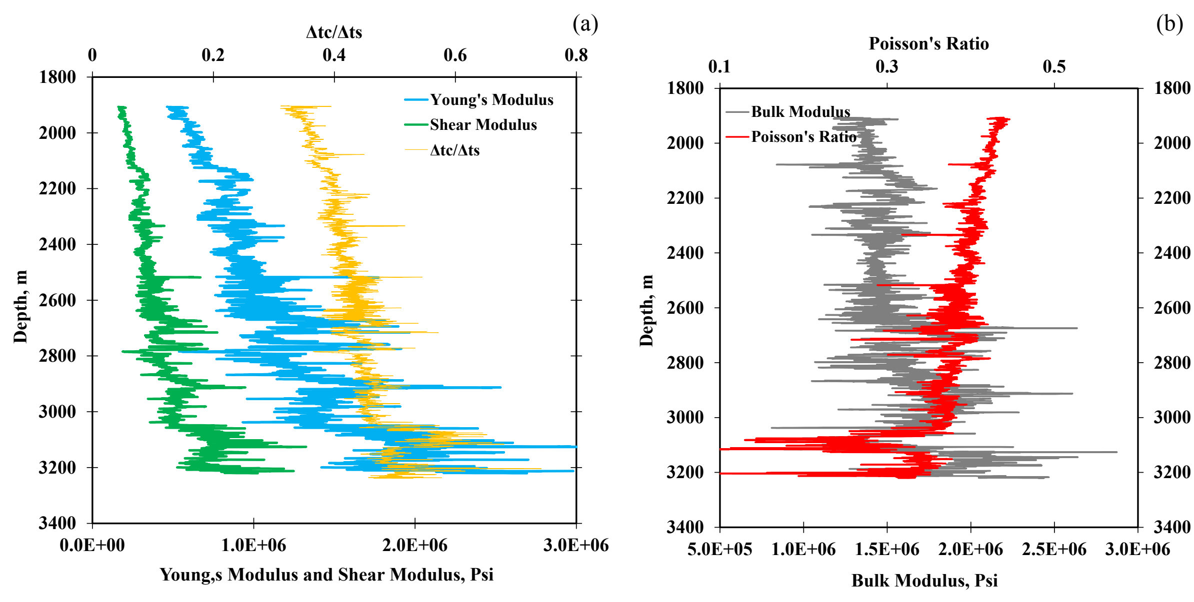

Figure 3-8 Dynamic moduli. (a) Young's modulus, shear modulus and compressional over shear slowness from wireline logs, (b) Bulk modulus and Poisson's ratio profiles from wireline logs.

The above profiles correspond to dynamic properties since their estimation is developed from well logs under undrained conditions, i.e., high frequency (10 kHz) and slight strain. These conditions lead to higher stiffness of the rocks than the values measured in the laboratory under static loading (Qiu, 2005).

The best way to correct dynamic elastic moduli is developing both triaxial tests and sonic wave velocity measurements on rock samples and generating relationships to correct the continuous dynamic elastic moduli.

In order to correct the dynamic elastic moduli of GML-2, some triaxial tests were performed and validated with tests run in two neighboring wells (GMK-1 and GMK-2). Although, GMK's tests were developed at different confining pressure, these were corrected using GML's confining pressure.

Figure 3-9a and **Figure 3-9b** present a comparison between static and dynamic Young's modulus and Poisson's ratios, respectively.

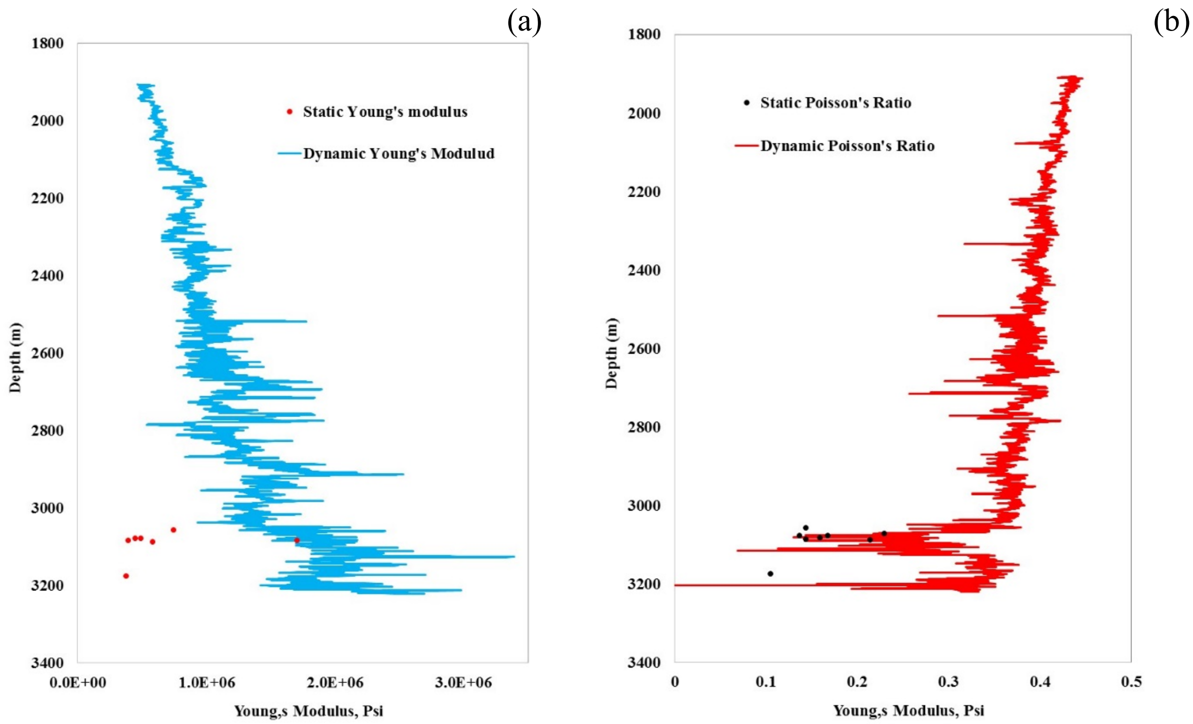

Figure 3-9 Static and dynamic moduli. (a) Red points represent static Young's moduli and the blue continuous line corresponds to the dynamic Young's moduli, (b) Black points represent static Poisson's ratio values and the red continuous line corresponds to dynamic Poisson's ratios.

3.6 Dynamic to Static Young's Modulus Correlation

There are several empirical relations to convert dynamic moduli into static moduli. However, the majority of them only apply to hard rocks, which require smaller Young's modulus corrections as compared to the ones for soft rocks. The empirical equations presented in **Table 2-2** are relationships between static and dynamic elastic Young's modulus applicable to particular sets of conditions and types of rocks. These equations can be used to predict static moduli when laboratory tests are not available.

Static moduli data from triaxial tests and dynamic moduli data from acoustic sonic wave velocity measurements on rock samples for sandstones and shales are available for GML and GMK fields.

The following procedure is established to develop an empirical relationship to accurately estimate static Young's modulus from dynamic data,

1) Transform static elastic Young's moduli of GML and GMK fields to the field mean effective in-situ stress.
2) Build a cross-plot of dynamic versus static Young's moduli.
3) Apply available empirical relationships to predict static data from dynamic data.
4) Compare predicted values against measured data.

Figure 3-10a shows the variety of available correlations to predict static Young's moduli. The graph shows that the best match to experimental data is obtained with Wang's linear correlation, which was developed for soft rocks, while the other correlations were developed for hard sandstones. This is consistent with the fact that the reservoirs in GML and GMK fields are composed of soft sandstones. The coefficient of determination obtained using Wang's equation is 0.62. Although not perfect, the fit provided by Wang's equation is superior to the match obtained from other relationships.

However, since the coefficient of determination obtained from the match of predicted and real data is only 0.62, this thesis develops a new non-linear function to improve the prediction accuracy of static Young's modulus by minimizing the square of the residuals. This new relationship is developed from 22 triaxial tests conducted in GML and GMK fields and it can be applied to either sands or shales.

A linear regression of E_{dy} vs. E_{st} with an R^2 equal to 0.78 is proposed. It is pointed out, however, that this model tends to underestimate values as compared with experimental data for dynamic Young's modulus above 40 GPa. This linear function is mathematically expressed by the following equation,

$$E_{st} = 0.395 * E_{dy} - 1.993 \quad \textbf{Eq. 3-9}$$

Finally, a non-linear relation between $\log_{10} E_{dy}$ and $\log_{10} E_{st}$ with a R^2 equal to 0.89 is established. This results in a better approach for estimating static Young's Modulus values. The non-linear regression is mathematically expressed as follows,

$$\log_{10} E_{st} = 1.494 * \log_{10} E_{dy} - 1.2355 \quad \textbf{Eq. 3-10}$$

Where E_{st} and E_{dy} are expressed in GPa.

Figure 3-10b presents both linear and non-linear regression models introduced in this work. It can be clearly observed that the static Young's modulus is calculated with a higher degree of accuracy. **Figure 3-11** presents dynamic Young's Moduli and converted static Young's Moduli as compared to the real experimental data. The yellow continuous line represents the calculated static Young's Modulus from **Eq. 3-10**. The outliers in **Figure 3-11** are due to failures during the triaxial tests.

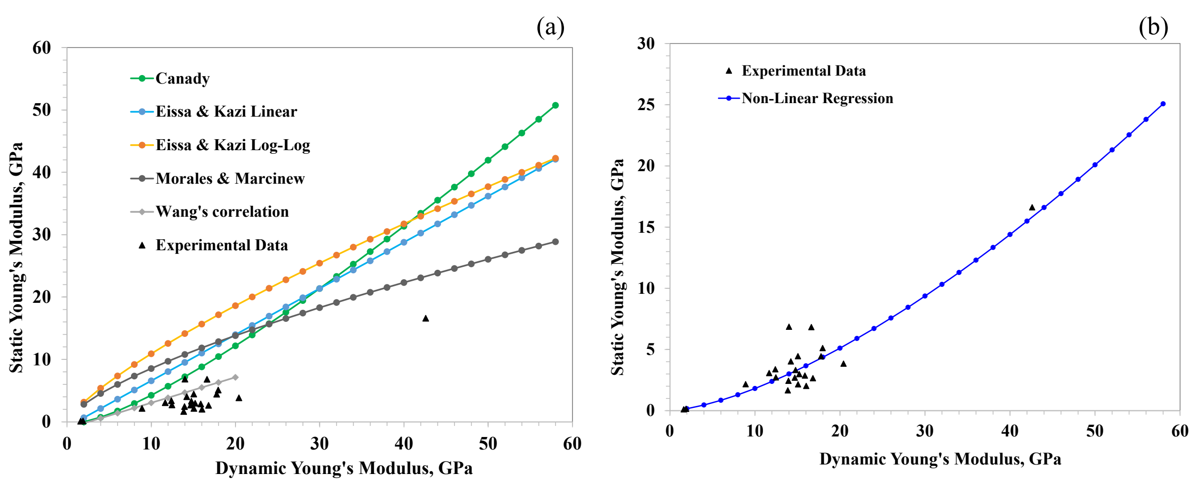

Figure 3-10 Young's modulus correlations. a) Available relationships vs. experimental data, b) Relationships developed in this work vs. experimental data.

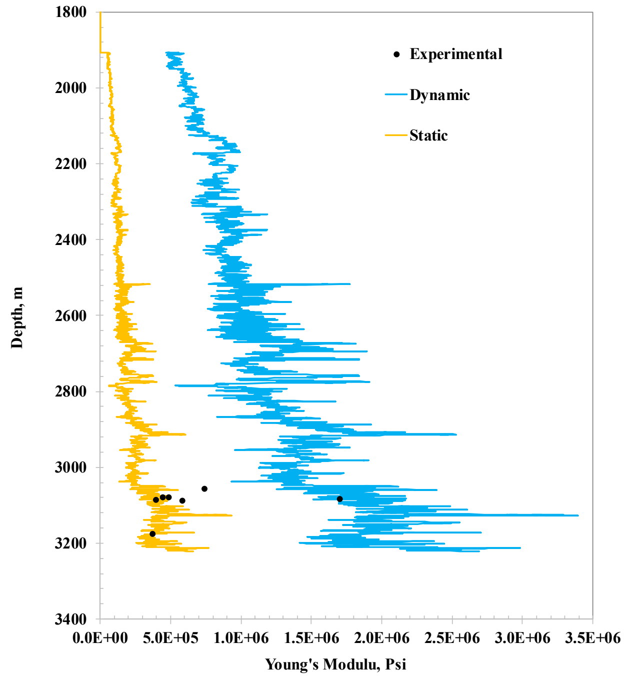

Figure 3-11 Dynamic Young's moduli in the blue continuous line and converted static Young's modulus in the yellow continuous line as compared to real experimental data.

3.7 Dynamic and Static Poisson's Ratio Correlation

Poisson's ratio (ν) is analyzed at mean effective in-situ stress conditions based on experimental data from GML and GMK fields for both shales and sandstones. **Figure 3-12a** shows a cross-plot of dynamic Poisson's ratio (ν_{dy}) versus static Poisson's ratio (ν_{st}). Two different trends are observed for the sandstone reservoir, one for the GML-2 and GMK-1 data and other for GMK-2. A straight line drawn through the data points show a low coefficient of determination (R^2 =0.019). A line is not shown for shales as there are only two points in each field and there is no correlation between them.

Since the priority of this section is to correlate ν_{dy} and ν_{st} for the sandstone reservoir in GML field, two actions were performed in order to order to improve the quality of the correlation between these two variables: a) the shale data and GMK-2 sandstone data were removed, and b) it was assumed that the maximum value for the dynamic Poisson's ratio is 0.5 whereas the maximum value for static Poisson ratio is 0.3. The application of the aforementioned assumptions leads to the results shown in **Figure 3-12b**, where the correlation between ν_{dy} and ν_{st} is a R^2=0.7078. This correlation is expressed by **Eq. 3-11**.

$$v_{st} = 0.476 * v_{dy} + .0565 \qquad \textbf{Eq. 3-11}$$

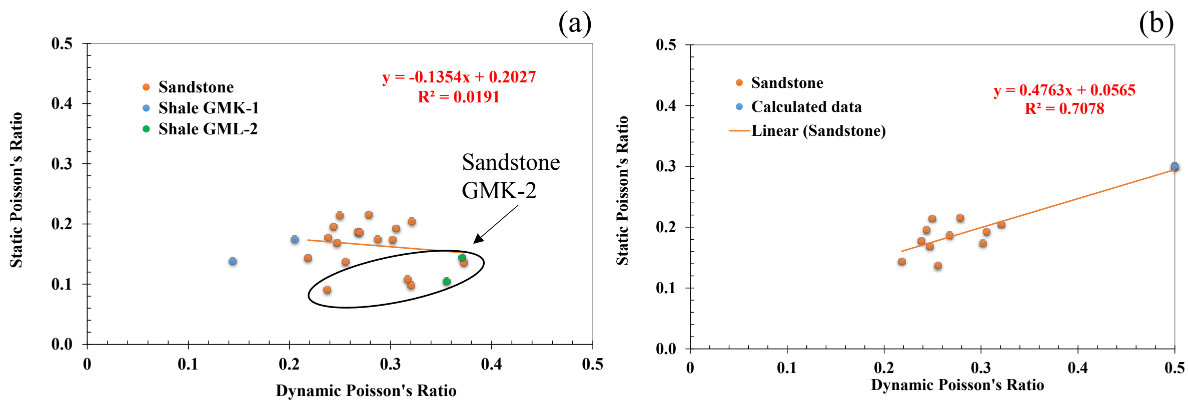

Figure 3-12 Poisson's ratio in sandstones. (a) Poor linear fit as a results of experimental data for sandstone of well GMK-2. (b) The linear fit improves when experimental data for sandstone GMK-2 are removed from the analysis.

Applying Eq. 3-11**,** dynamic Poisson's ratio is converted to static Poisson's ratio as shown in **Eq. 3-11**.

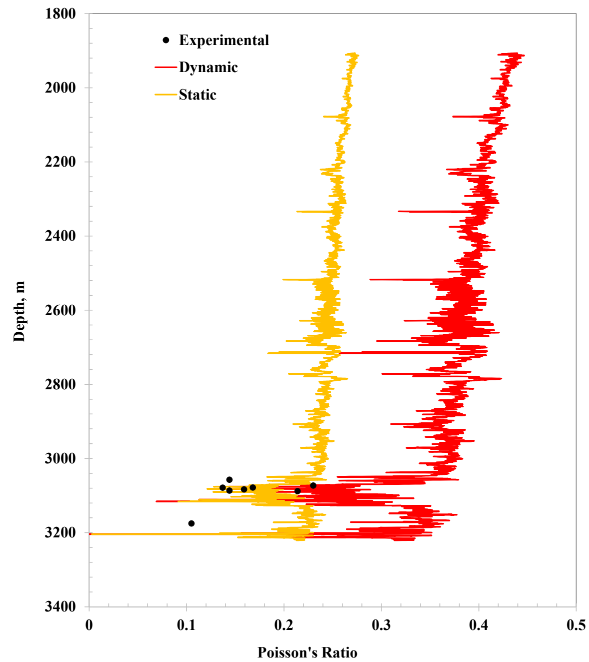

Figure 3-13 Conversion of dynamic Poisson's ratios (red line) to static Poisson's ratios (yellow line) and its comparison to experimental data.

Once Young's modulus and Poisson's ratio are corrected, shear modulus and bulk modulus are calculated using **Eq. 3-12** and **Eq. 3-13**, respectively. The same methodology is

$$G = \frac{E}{2 + 2v} \quad \textbf{Eq. 3-12}$$

$$K = G\frac{2(1 + v)}{3(1 - 2v)} \quad \textbf{Eq. 3-13}$$

applied to the wells located close to GML field.

3.8 UCS and Internal Friction Angle Estimation

The internal friction angle (φ) and unconfined compressive strength (UCS) are two other important geomechanical parameters that have to be considered during the analysis of geomechanical problems. These parameters are traditionally determined from triaxial tests on cylindrical samples of rock. The fact, however, is that these data are not always available for the reservoir zone and much less for the overburden and underburden rocks. For this reason, several authors have published empirical correlations for estimating φ and UCS from some other variables such as porosity, grain volume, acoustic velocity, gamma ray and, Young's modulus.

The φ and UCS data for the upper reservoir in GML are estimated from the interpretation of triaxial tests. However, there is lack of data for the overburden and underburden. Because of this the empirical correlations developed are used to predict φ and UCS both inside and outside the reservoir.

In this work, a relationship as a function of Young's modulus is established based on experimental data from19 UCS measurements conducted on sandstone samples collected in lower Miocene formation (3 from GML field and 16 from GMK field), and 4 UCS measurements carried out on shale samples (2 from GML and 2 from GMK).

Figure 3-14 shows a cross-plot of Young's modulus vs. UCS. Scattering of the data is observed in this figure, However, a positive correlation can be clearly established since the larger the value of Young's modulus, the larger the UCS. There are no outliers affecting this correlation, which is applicable to either sandstones or shales because it indistinctly describes both types of rock. A coefficient of determination (R^2) larger than 0.95 is obtained in this case. **Figure 3-14** also presents the empirical correlation developed by Bradford (1998) for comparison with the empirical relation for GML and GMK developed in this thesis. The graph shows that Bradford's correlation overestimates the UCS in comparison with GML data. Therefore, **Eq. 3-14** is used to predict UCS values in the reservoir under consideration since the equation is valid for soft sandstones with relatively low UCS, which is the case of the reservoir considered in this study.

$$UCS = 3.1081 * E + 1.44$$ **Eq. 3-14**

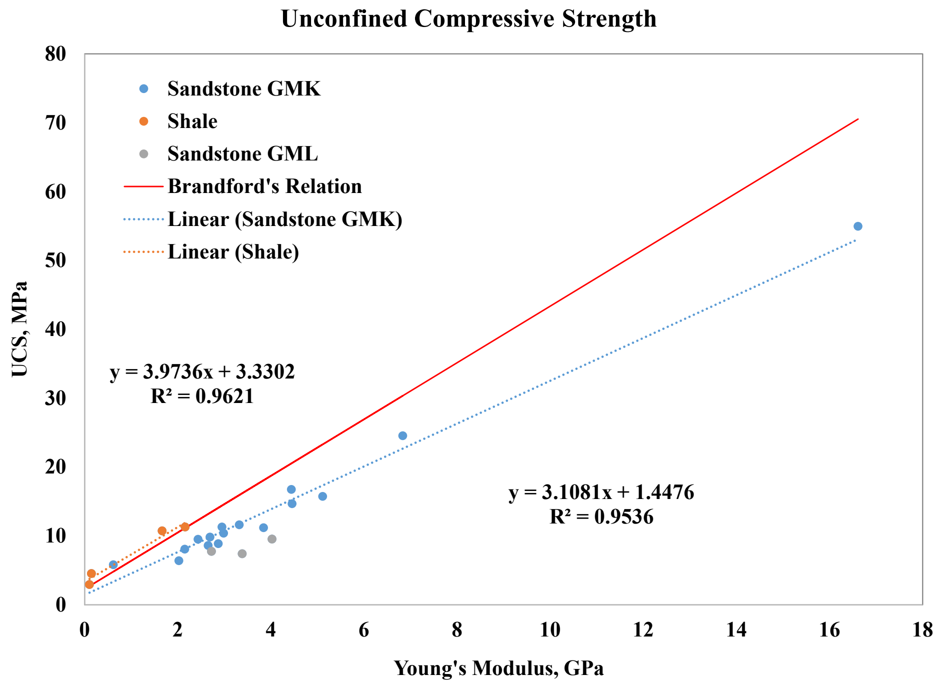

Figure 3-14 Young's modulus versus UCS.

The internal friction angle (φ) of a rock is barely unique since the strength of the rock is a function of confining pressure, and also because the failure envelope in the Mohr-Coulomb diagram is not always a straight line. For this reason, the internal friction angle is obtained from the best straight line to Mohr circles. Due to the simplicity of the aforementioned method for estimating φ, some authors have tried to correlate φ to porosity, acoustic velocity and gamma ray logs.

Perkins and Weingarten (1988) observed that there is a strong correlation between porosity and internal fiction angle. Instead of calculating internal friction angle from Mohr-Coulomb envelope as the common practice dictates, they calculated it from the angles of failure planes of samples with a wide range of porosity. Perkins and Weingarten based their correlation on their own experimental data and data available in the literature. Their correlation for estimating the internal friction angle (φ) as a function of porosity (ϕ) is expressed by **Eq. 3-15**.

$$\varphi = 57.75 - 1.05\emptyset \qquad \textbf{Eq. 3-15}$$

In order to verify the validity of Perkins and Weingarten equation for GML field, a crossplot of ϕ versus φ was built based on the information of 14 pairs of ϕ and φ data measured on sandstones samples collected in the lower Miocene formation in GMK Field. Unfortunately, porosity values were not reported for the triaxial tests conducted on samples of GML field so this procedure could not be applied to this field.

Figure 3-15 shows a cross-plot of ϕ vs. φ for GMK field. The blue points represent measured data and the orange straight-line represents Perkins and Weingarten empirical correlation. Perkins and Weingarten correlation does not properly reproduce the real data and it overestimates the values of φ. Therefore, an alternative is to draw a best fit straight line through the GMK data. A negative correlation can be clearly established since at larger values of porosity, lower values of φ are obtained. There are not outliers affecting the correlation. Thus the empirical relation proposed in this work for estimating φ from porosity for soft sandstones is expressed in **Eq. 3-16**.

$$\varphi = 44.86 - 67.42\emptyset \qquad \textbf{Eq. 3-16}$$

The coefficient of determination associated with the empirical correlation introduced in this work is low (R^2=0.48), which indicates that results should be considered carefully and interpreted as directionally correct approximations. However, this correlation represents better the experimental data as compared with Perkins and Weingarten relation.

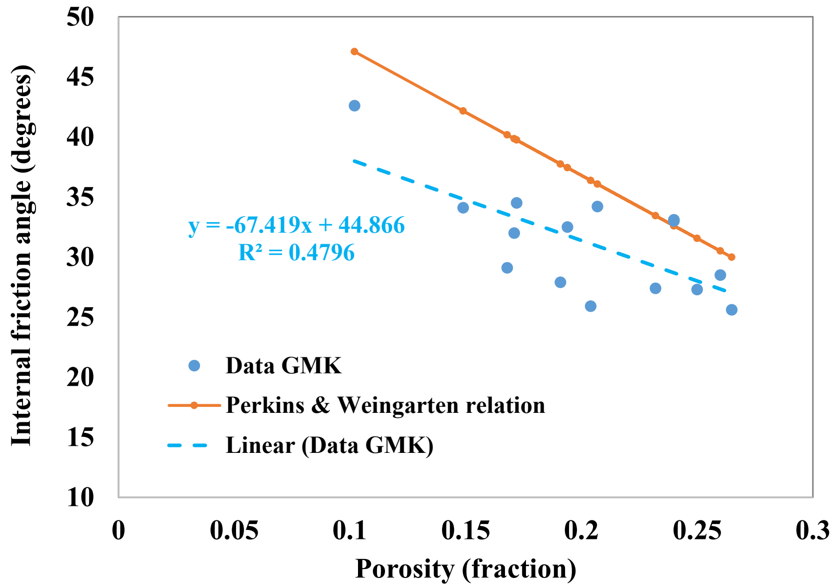

Figure 3-15 Porosity versus internal friction angle.

Since, there is not static information in the overburden, sideburden and underburden for GML field for estimating the geomechanical properties in the Mechanical Earth Model (MEM), **Eq. 3-10, Eq. 3-11, Eq. 3-12, Eq. 3-13, Eq. 3-14, Eq. 3-16** are for estimating the static mechanical properties of the rock in the MEM from dynamic data.

Chapter Four: Numerical Reservoir Simulation Model

Geomechanics and fluid flow coupling for field performance evaluation requires two basic models: 1) a reservoir model that is described in this chapter for the field under study and 2) a geomechanical model that is covered in Chapter Five. The reservoir model corresponds to a single porosity laminated sandstone with intercalations of shale. The fluid is natural gas which is mainly composed to methane. As a result a multiphase black oil model (gas, oil and water) is selected for the study.

4.1 Structural Grid

Construction of the reservoir numerical simulation model was developed using Petrel and Eclipse software. The effort started with interpretation of seismic surfaces using amplitude attributes and continued with the match of these surfaces to well tops identified during drilling of wells GML-1, GML-2 and GML-3. The structural grid was built considering seismic surfaces as a guide, faults' azimuths and dips as trends and flat spots observed in the reflectivity seismic attribute Mu Rho ($\mu\rho$) as the limit around the reservoir. **Figure 4-1a** shows the match between seismic surfaces and well tops.

The grid's specifications are as follows:

- Grid orientation: 67 degrees.
- Faults and boundary edge as type zigzag.
- Block size in both i and j directions 50 m.
- Block size in k direction 1 m.

Figure 4-1b presents the grid skeleton with the three principal planes utilized to build the 3D grid as a way to honour the faults found in the reservoir.

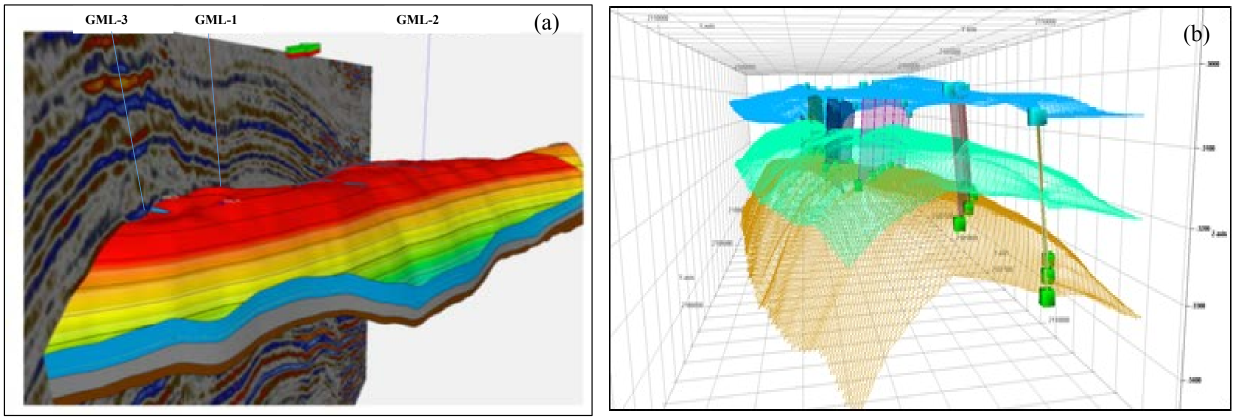

Figure 4-1 Reservoir model. (a) Seismic surface and well tops. (b) 3D view of reservoir grid skeleton.

The structural grid was divided into three zones in the vertical direction; the upper reservoir, the lower reservoir, and the intermediate shale layer, which represents the seal between the two reservoirs. Each zone was subdivided into layers; 40 layers in the upper reservoir, 20 in the lower reservoir, and 1 layer for the seal zone. The number of layers in each zone was determined based on vertical thicknesses observed in the lithofacies log indicating that the reservoirs had laminar characteristic. The reservoir grid has 171 blocks in I direction, 291 blocks in J direction and 61 layers; therefore the total number of blocks is 3,035,421.

Three geometric attributes were considered for assessing the quality of the grid: cell volume attribute, cell inside-out attribute and cell angle attribute. The first attribute is used to identify blocks with negative volume whereas the second one indicates when a cell is good if its value is equal to zero. The third attribute measures the internal angle of a corner referred to the IJ plane and represents the deviation from 90 degrees. A cell with an angle equal to 0 degrees is a regular block. Both cell angle and cell inside-out attributes determine the degree of deformation of the blocks.

The histogram corresponding to the cell volume attribute is shown in **Figure 4-2a,** which indicates that there are not negative values in the structural grid. The minimum value of this histogram is 1000 m^3 whereas the maximum is 9750 m^3. **Figure 4-2b** shows a histogram corresponding to the cell angle attribute. It is noticed that more than 96% of the cells have values smaller than 12 degrees. The maximum cell angles for this grid are approximately equal to 45 degrees and are located in the region associated with faults and at the boundary edge. The cell inside-out attribute resulted in values equal to zero for all cells.

Based on the above results, it is possible to state that the geometry of the structural grid is acceptable as it did not present either negative volumes or severe deformation of the blocks.

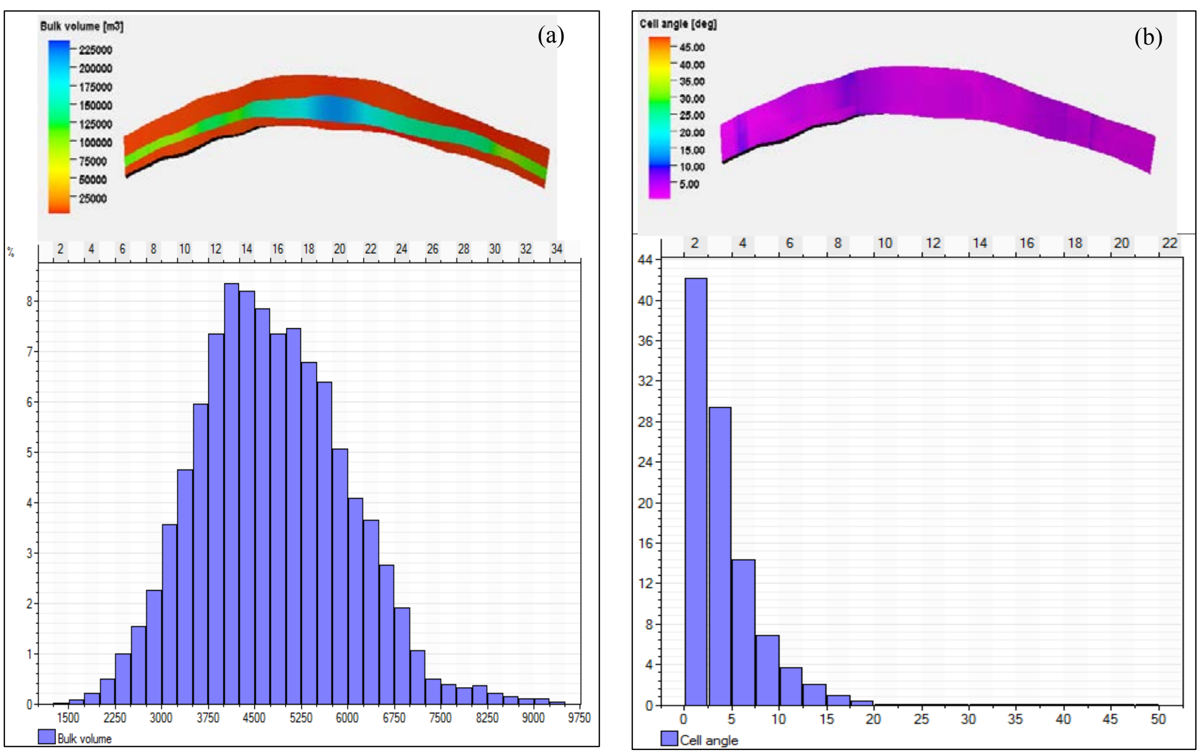

Figure 4-2 Grid quality control. (a) Cell volume attribute and resulting histogram. (b) Cell angle attribute and resulting histogram indicating good geometry in the majority of the cells.

4.2 Facies Modeling

Ideally the modelling of facies in numerical reservoir simulation should include information from a large number of wells with enough core analyses and wireline logs for proper determination of facies in the vertical direction and for performing 3D geostatistical estimations by the use of kriging or co-kriging methods. However, due to the lack of information in the study field (only three wells) a facies modelling process combined with a stochastic method was applied to conceptualize the 3D facies model.

The process of sedimentary facies modeling and lithofacies modeling considers two steps; 1) development of the vertical interpretation and, 2) areal estimation. During the first step, sedimentary facies logs and lithofacies logs are created using information from cores and geophysical logs. As a result of the implementation of this first step, three types of sedimentary facies are defined: channel levee, channel margin, and channel fill, while five lithofacies are defined as fine sandstone, coarse sandstone, shale, silt and toba.

The second step (areal estimation) considers seismic interpretation using spectral decomposition techniques for creating maps with high resolution for the channels in the reservoirs as shown in **Figure 4-3a**. Then, a correlation and match of facies is performed with the seismic attribute $\mu\rho$ and porosity logs for properly defining pore fluid zones and for delineating the channel's polygons. The channels bodies and levees zones are defined with seismic attributes and trends for each level and sublevel of the reservoirs as shown in **Figure 4-3b**.

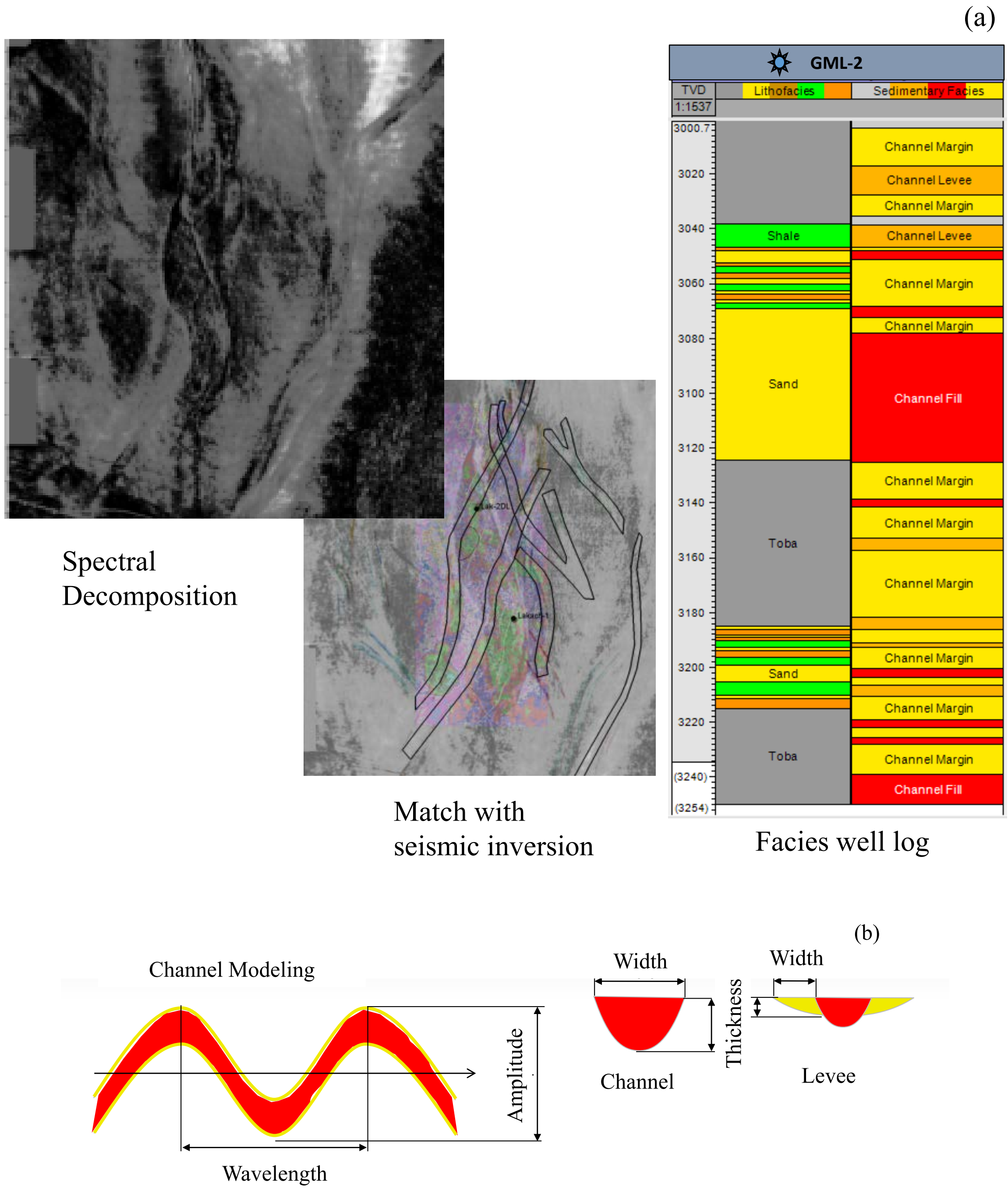

Figure 4-3 Facies modeling process.

The 3D sedimentary facies models are developed for each zone using well logs, channel polygons, and probability distributions for estimating orientation, amplitude, wavelength, width and thickness for both levees and channels. The upper reservoir is characterized by 5 different facies bodies and the lower reservoir by 8 different facies. Each body has a specific percentage of sedimentary facies. **Figure 4-4** shows a 3D sedimentary facies distribution plot resulting from the stochastic process and sedimentary facies modeling.

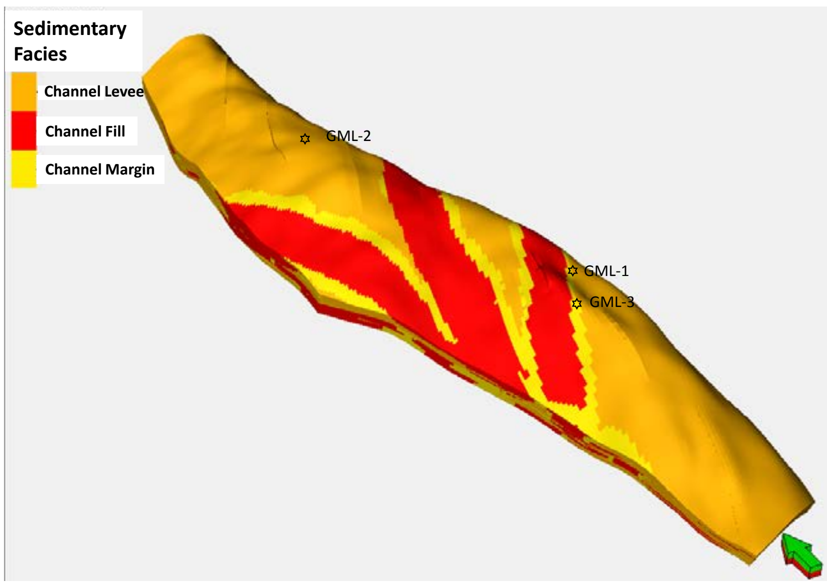

Figure 4-4 3D Sedimentary facies model.

The lithofacies model is simultaneously characterized by zonal and sedimentary facies. Each lithofacie in the 3D model is estimated using the sequential indicator simulation method. According to the zone and sedimentary facies, a variogram and percentage of the lithofacie is assigned to rule the distribution and the anisotropy in both vertical and horizontal directions. The initial percentage of each lithofacie is taken from the scaled up cells. **Figure 4-5** shows a 3D sedimentary facies distribution resulting from the stochastic process and sedimentary facies modeling.

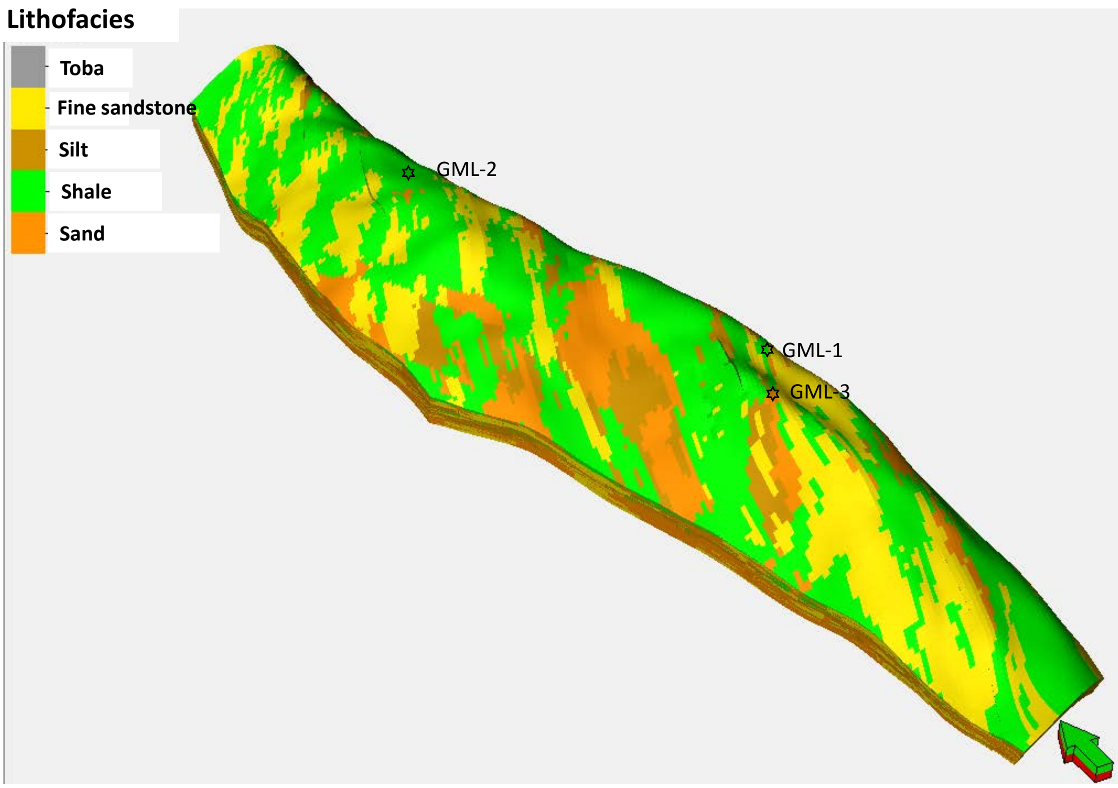

Figure 4-5 3D lithofacies model.

4.3 Petrophysical Modeling

The procedure for estimating grid petrophysical properties is summarized in the following steps:

1) Well logs scale-up process. During this process petrophysical properties are scaled up from well logs to cells crossed by the well's trajectory and a value is assigned to each block. Properties such as porosity, water saturation, shale volume, permeability and lithofacies are considered primary variables when applying stochastic methods for estimating properties for the whole grid. **Figure 4-6** presents effective porosity versus depth for two wells in the field of study. The graph shows the geophysical well log to the left and the scaled up grid cells crossed by the well trajectory to the right. An arithmetic average method is used for scaling up porosity. The log is made up of

points, which implies that the sample data within each block are used for the averaging. All neighbouring cells around the main cell to be scaled are averaged.

The same process is followed for other petrophysical properties. The settings used during the scale-up process are presented in **Table 4-1**.

Table 4-1 Well logs scale-up process and corresponding settings.

Property	**Average Method**	**Treat log**	**Method**
Porosity	Arithmetic	As points	Neighbour cell
Sedimentary facies	Most of	As lines	Neighbour cell
Lithofacies	Most of	As lines	Neighbour cell
Vclay	Arithmetic	As points	Neighbour cell
Permeability	Geometric	As points	Neighbour cell
Water saturation	Arithmetic	As points	Neighbour cell

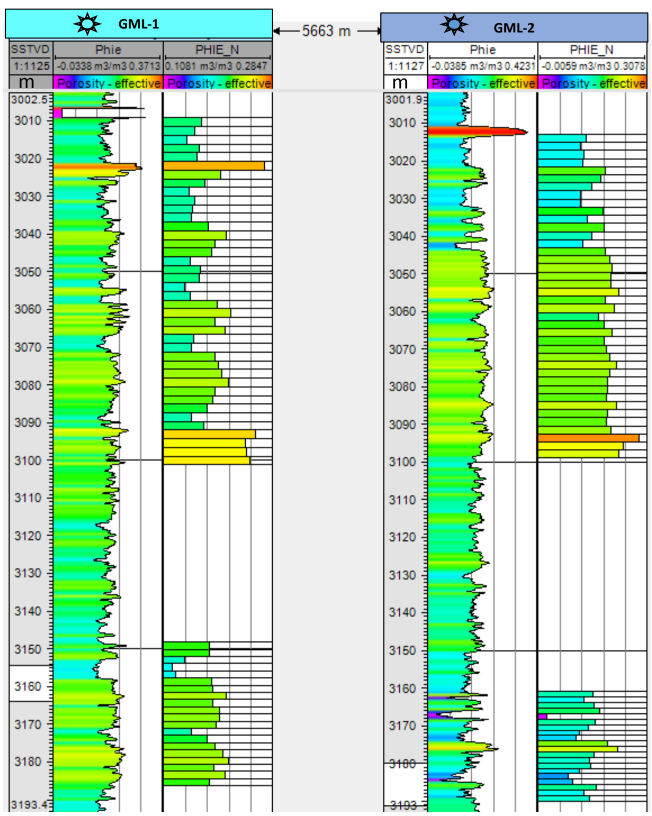

Figure 4-6 Scaled-up effective porosity (phie).

2) Areal estimation. Data analysis by zone and lithofacies is performed for each petrophysical property (for example porosity, water saturation, shale volume, permeability, NTG). Variograms are created for determining anisotropy in vertical and horizontal directions. Porosity estimation uses the seismic porosity attribute as a secondary variable to perform co-kriging. Other properties are calculated in the same fashion, with the only difference that the secondary variable for the rest of the properties is the porosity estimated previously. **Figure 4-7** shows two histograms that compare porosity and permeability distributions from three different sources utilized for the scaling-up process and the construction of the stochastic 3D model. Although there are small differences the comparisons are reasonable indicating a good representation of the petrophysical properties.

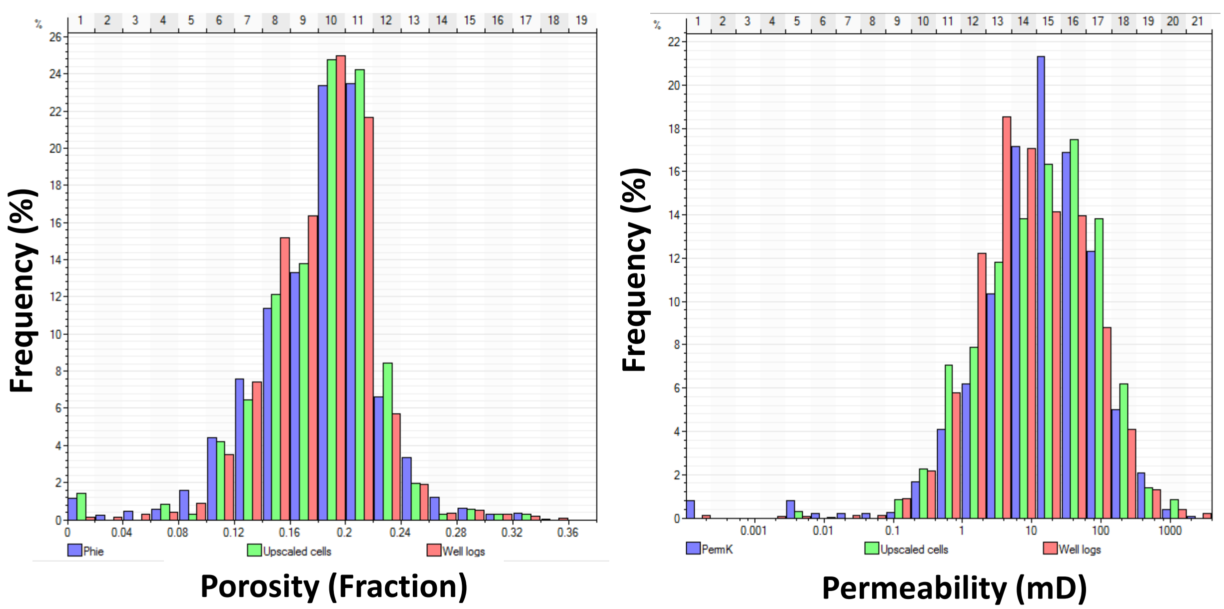

Figure 4-7 Porosity and permeability histograms.

4.4 Rock Type Definition

Aguilera (2003) indicated that reservoir porosity type can be classified as a function of pore size and pore geometry. The pore size can be characterized by means of the pore throat radius using different methods: Aguilera r_p35, Winland r_{35}, and Pittman r_{apex}, where the subscripts 35 and apex indicate 35% mercury saturation during capillary pressure estimation. For $r_{35} \geq 10$ microns the pore sizes are classified as megapores, for $2 \leq r_{35} < 10$ microns as macropores, for $0.5 \leq r_{35} < 2$ microns as mesopores and for $r_{35} < 0.5$ microns as micropores.

Pittman (1992), based on 202 uncorrected air permeability and porosity analyses on sandstone core samples developed **Eq. 4-1** for determining the pore aperture size distribution corresponding to 40% mercury saturation.

$$\log r_{40} = 0.360 + 0.582 \log K - 0.680 \log \emptyset \qquad \textbf{Eq. 4-1}$$

where K is uncorrected air permeability in mD, ϕ is porosity in percentage and r_{40} is the pore throat aperture in microns at 40% mercury saturation during a capillary pressure test.

Based on matrix porosity and matrix permeability data from core samples, a semi-log crossplot of porosity versus permeability is created as shown in **Figure 4-8**. The dashed lines in this figure represent Pittman r_{40} pore throat apertures.

According to the pore throat aperture, the analysis indicates that five rock types (TR) are present in each reservoir.

- Rock type 1, TR1 ≥ 10μ
- Rock type 2, 2μ ≤ RT 2 < 10μ
- Rock type 3, 0.5μ ≤ RT 3 < 2μ
- Rock type 4, 0.1μ ≤ RT 4 < 0.5μ
- Rock type 5, TR 5 < 0.1μ

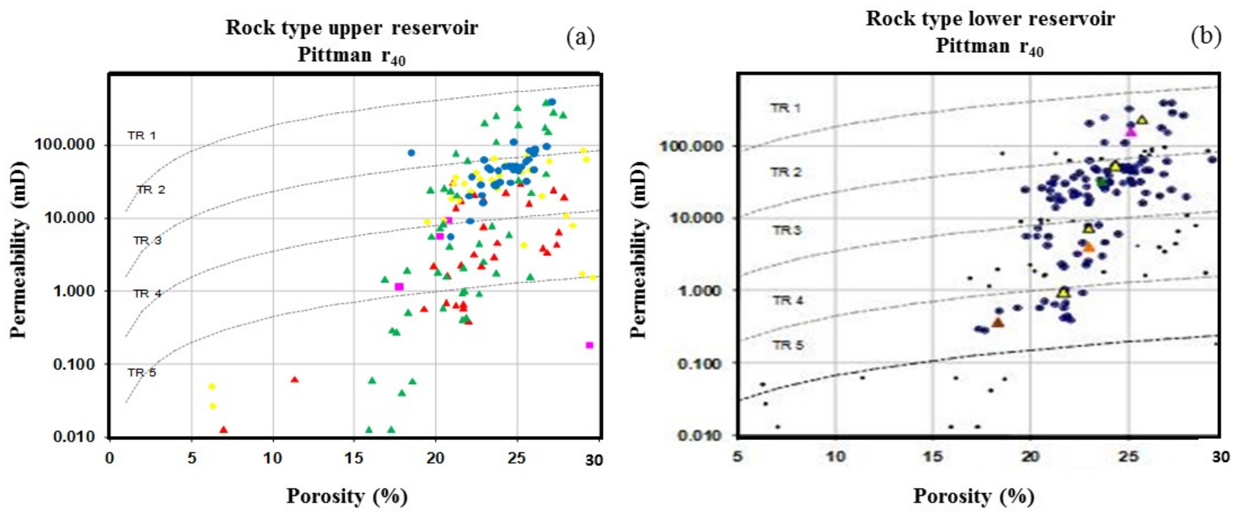

Figure 4-8 Rock type definition using Pittman r_{40}. (a) Upper reservoir. (b) Lower reservoir.

4.5 Reservoir Limits

The vertical and horizontal limits of the reservoir are defined as follows: the top limit is the top surface of each reservoir, which corresponds to the base of the seal rock. For the upper reservoir the top is found at a depth of 3048 m whereas for the lower reservoir it is at 3186 m. The horizontal limits around the reservoir are defined by the intersection between the top surface dip and the gas-water contact. At the northern part of the reservoir, the horizontal limit is defined by a sealed fault. The gas-water contact was estimated using pressure gradient data acquired during drilling of well GML-2 and corroborated with well GML-3. The gas-water contact for the upper reservoir is at a depth of 3119 m and for lower reservoir at 3214 m.

Based on the pore volume located below the gas-water contact, the aquifer volume is estimated to be 1.2 times larger than the pore volume of the upper reservoir and 2 times larger than the pore volume of the lower reservoir. The aquifer pressure support effect on the reservoir was insufficient during the drawdown tests. The numerical aquifer included in the reservoir model to add energy for matching the drawdown test is shown in **Figure 4-9**.

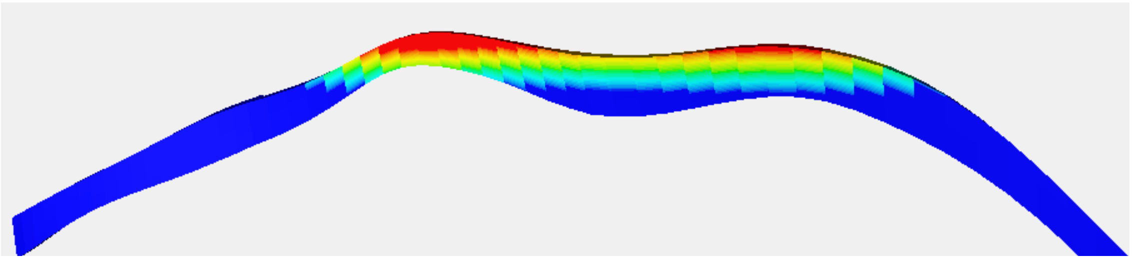

Figure 4-9 Aquifers associated with the upper and lower reservoirs.

4.6 Saturation Functions

Capillary pressure (P_{cap}) and relative permeability curves are defined for each rock type in order to establish fluid distribution, initial water saturation and fluid flow in the porous media. A total of 10 of capillary pressure sets and relative permeability curves are defined for the reservoir.

4.6.1 Capillary pressure

Experimental capillary pressure data for each rock type were obtained from core samples. However the responses for each type of rock are not unique since they are a function of porosity, pore radius and interfacial tension. Moreover, data coming from core samples represent a very small fraction of the reservoir. Hence, it is necessary to use functions for scaling-up the data from a core scale to a reservoir scale. The Leverett J-function is a dimensionless saturation function that attempts to extrapolate capillary pressure data from a specific rock sample to rocks in the reservoir presenting different porosity, permeability and wetting properties (Kantzas at al., 2012).

The Leverett J-function defined in **Eq. 4-2** integrates different capillary pressures into a common curve. Thus, it is possible to scale-up the capillary pressure for different porosity and permeability values. Leverett J-function is mathematically expressed as follows,

$$J(S_w) = c\frac{P_{cap}}{\sigma_t}\sqrt{\frac{K}{\emptyset}} \qquad \textbf{Eq. 4-2}$$

where c is a constant, K is permeability, ϕ is porosity, P_{cap} is capillary pressure and σ_t is interfacial tension.

Figure 4-10a presents an example of a J-function versus water saturation curve and its corresponding capillary pressure curve scaled-up for rock type 1 using a porosity of 0.24 and a permeability of 100 mD. These values of porosity and permeability are average values for a specific rock type.

4.6.2 Relative permeability

Empirical correlations are often required for estimating relative permeability values, especially in reservoirs where information is scarce due to technical and/or economical limitations. One of the most important methods for estimating relative permeability data is the Corey relationship (Brooks and Corey, 1964) presented in **Eq. 4-3, Eq. 4-4** and **Eq. 4-5**. Two important parameters have to be considered for relative permeability estimation: the end-points and the curvature.

$$Sw^* = \frac{S_w - S_{wi}}{1 - S_{wi}} \qquad \textbf{Eq. 4-3}$$

$$Kr_w = (Sw^*)^{\psi} \qquad \textbf{Eq. 4-4}$$

$$Kr_{nw} = (1 - Sw^*)^2(1 - Sw^{*\omega}) \quad \textbf{Eq. 4-5}$$

$$Kr_{nw}^* = \frac{Kr_g}{\left(Kr_g\right)_{S_{wi}}} \quad \textbf{Eq. 4-6}$$

$$Kr_w^* = \frac{Kr_w}{(Kr_w)_{Sr_{nw}}} \quad \textbf{Eq. 4-7}$$

Where:

$\psi = (2+3\lambda)/\lambda$

$\omega = (2+\lambda)/\lambda$

λ = Pore size distribution.

Sw^* = Effective saturation.

Swi = Irreducible water saturation.

K_{rw} = Water relative permeability.

K_{rnw} = Non-wetting relative permeability.

S_{rnw} = Residual non-wetting phase saturation.

K_{rnw}^* = Normalized non-wetting phase relative permeability.

K_{rw}^* = Normalized water relative permeability.

The relative permeability analysis for the reservoirs under study starts with normalization of the curves available for each rock type by applying **Eq. 4-3, Eq. 4-6** and **Eq. 4-7**. Next the average relative permeability curves are reproduced with Corey expressions using exponents as tuning parameters to match the curvature. Finally, the normalized curves are converted to relative permeability curves using average end-points (S_{wi} and S_{rnw}) for each rock type. During each realization of the stochastic process to estimate porosity and absolute permeability, the end-points change. **Figure 4-10b** is an example of relative permeability curves for rock type 1 using in the model. Relative permeability curves for other rock types are estimated following the same methodology described above.

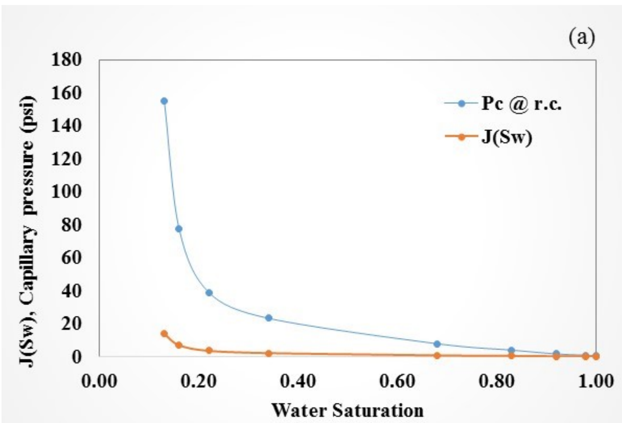

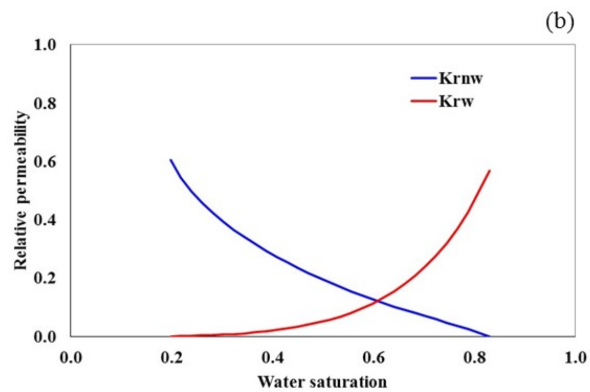

Figure 4-10 Saturation functions. (a) Leverett J-function and capillary pressure for rock type 1. (b) Relative permeability for wetting and non-wetting phases for rock type 1.

4.7 Fluid Characterization

The characterization of reservoir fluids by means of PVT analysis and cubic equations of state (EOS) allows estimating fluid properties and phase behaviour as a function of pressure, volume and temperature. Phase behaviour is required for numerical reservoir simulation and design of production facilities.

Bottom-hole samples and surface samples were recovered during completion of wells GML-1 and GML-2. Both samples were analyzed using a chromatographic analyzer, which indicated that the fluids in both reservoirs correspond to dry gas. As mentioned in Chapter One, the reservoir fluid presents 0.0% mole H_2S, 0.09-0.13% mole carbon dioxide. Dew point pressure is equal to 383 kg/cm^2, relative gas density is 0.59 and gas oil ratio is 3.9 bbl/MMscf at standard conditions. The fluid was analyzed using the Peng-Robinson EOS, Whitson lumping method and Lee mixing rules. The total number of components after the lumping process was 25 and their mole fractions are shown in **Table 4-2**.

Table 4-2 Reservoir fluid composition.

Name	Zi	Name	Zi
N2	1.02	*nC7*	*0.087*
CO2	0.026	*Metil-Ciclo-Hexano*	*0.042*
C1	95.063	Tolueno	0.028
C2	1.965	nC8	0.091
C3	0.714	Etil-Benceno	0.004
iC4	0.167	p-Xylene	0.007
nC4	0.203	o-Xylene	0.004
iC5	0.082	C9+	0.116
nC5	0.075	C12+	0.071
C6	0.093	C15+	0.037
Metil-Ciclo-Pentano	0.03	C18+	0.024
Benceno	0.023	C23+	0.016
Ciclo-Hexano	0.012		

The saturation pressure of the new mixture is matched to the experimental data using critical properties of the pseudo components. **Figure 4-11** shows the phase behaviour diagram before and after the match. Dew point pressure is 383 kg/cm^2 and initial pressure is 368 kg/cm^2.

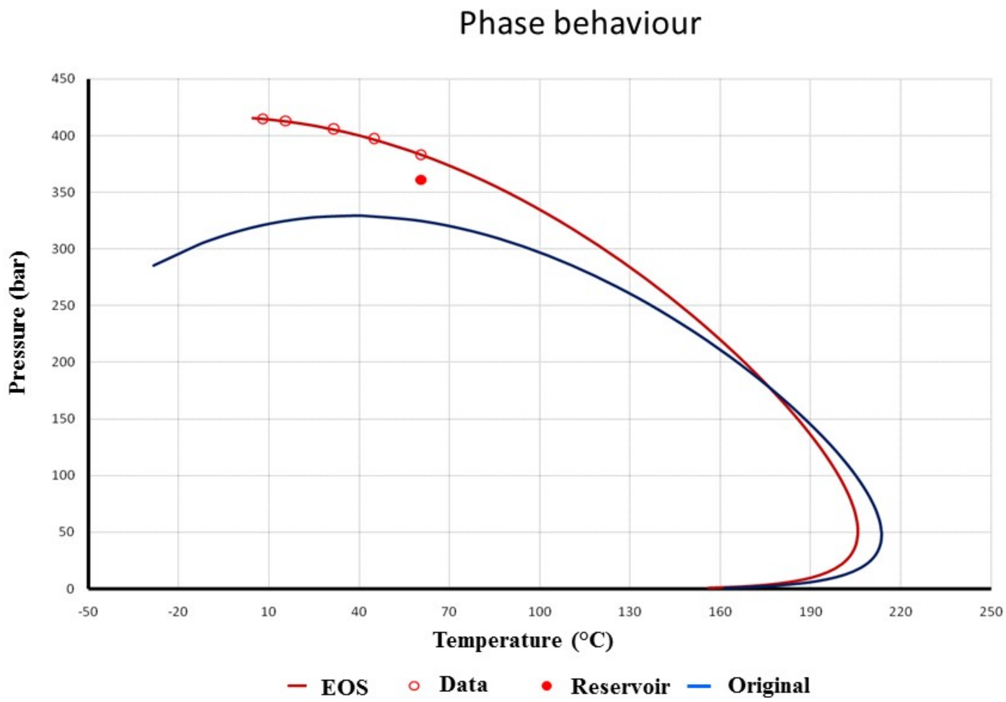

Figure 4-11 Phase behaviour diagram before and after the match.

Results of the simulation of the constant composition expansion experiment (CCE) are shown in **Figure 4-12**, which presents a reasonable match between the experimental data and the simulated data. Thus, the Peng-Robinson EOS is used in the numerical reservoir simulation model to properly represent fluid behaviour.

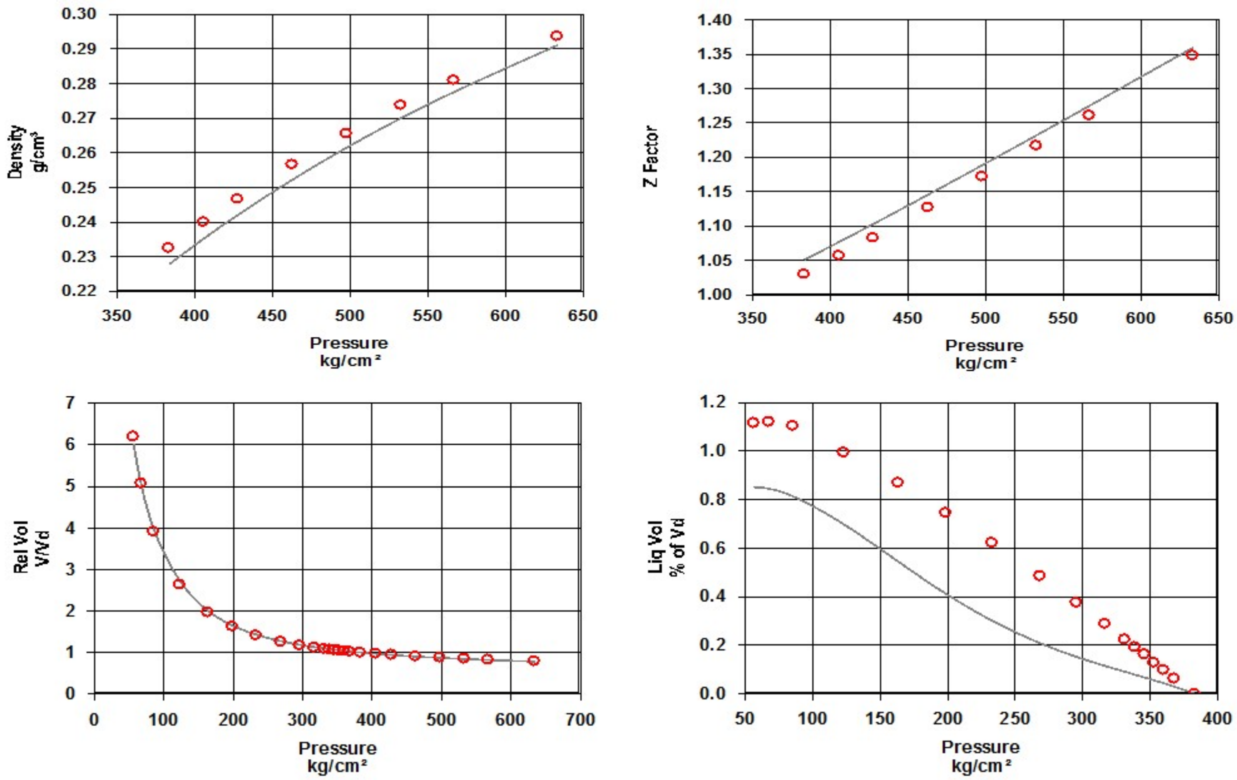

Figure 4-12 Constant composition expansion experiment at 60.5 °C. Red dots represent experimental data. The lines represent the simulated data.

In summary, GML fluid presents a high concentration of methane (95% mole) and a low gas-oil solubility ratio (191,836 ft^3/bbl), which is an indicator of a gas and condensate reservoir but with very low content of condensate. The condensate density is 35 °API, which is low as compared with the density of a typical gas condensate reservoir (60 °API). Also **Figure 4-11** shows that reservoir pressure and temperature are within the phase envelope, which indicates that condensation is present in the reservoir. However, reservoir pressure and temperature conditions are above the critical point of the mixture (high concentration of methane). Therefore, the reservoir can be classified as atypical gas reservoir with very low content of condensate.

4.8 Vertical Flow Performance

Gas production at surface conditions is governed by the pressure drop along the production tubing during the lifting of fluids from the bottom of the hole to the surface. Thus, vertical flow performance tables were used for estimating the relationship between pressure and fluid flow rate as the reservoir goes on production. Taking into account the possibility of vertical and directional well's trajectories during the development of the field, tables were designed considering vertical and directional trajectories, 5- inche choke, and tubing head pressure ranging from 36 bar to 297 bar. Therefore, the simulated well gas production rate varies up to 3 million m^3/day as illustrated in **Figure 4-13.**

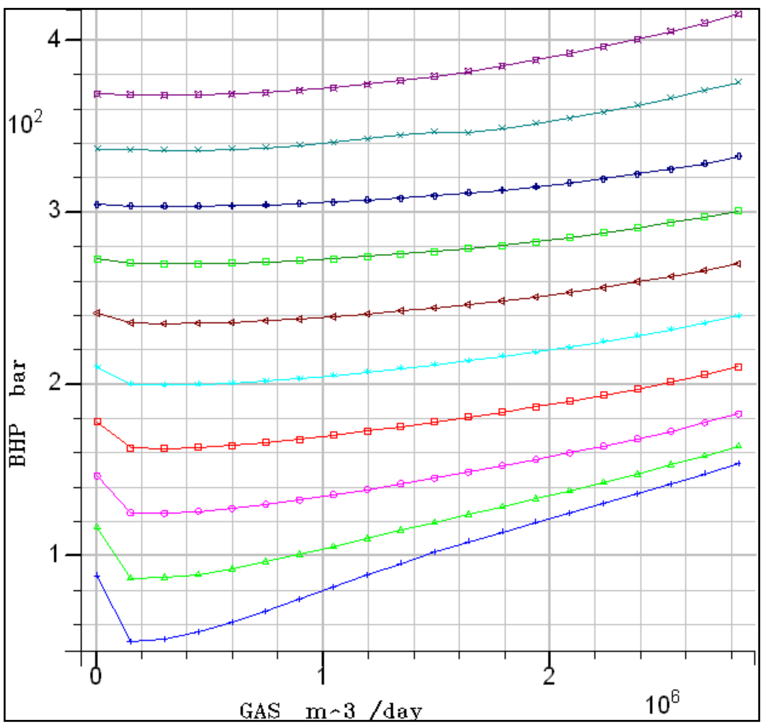

Figure 4-13 Vertical flow performance table (well gas production rate versus bottom hole pressure) used in well gas production simulation.

4.9 Development Strategy

The production strategy implanted in the reservoir was defined using the following assumptions:

- 7 comingled producer wells (the appraisal wells are considered as development wells).
- The well trajectory crosses both reservoirs.
- Wells are located along the top of the reservoir.
- Minimum drainage radius is 650 m.
- Maximum field gas production rate is 400 MMscfd.
- Minimum economical production rate is 50 MMscfd.
- Tubing head pressure is 80 bar along the production life of the reservoir.

Based on the assumptions mentioned above, 7 wells are defined throughout the reservoirs as shown in **Figure 4-14.** Three wells will be active during the first 6 months of production with a total rate equal to 200 MMscfd. The remaining wells will enter production after 6 months to reach a maximum field gas production rate equal to 400 MMscfd. Both bottom-hole pressure and tubing head pressure will govern the extension of the production plateau of the field.

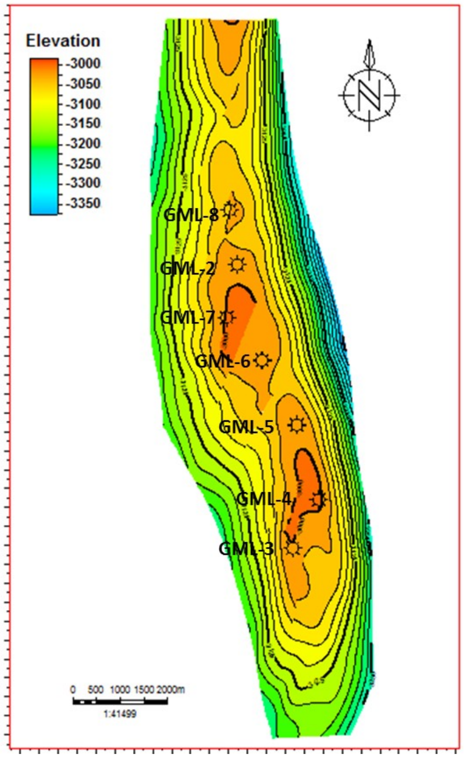

Figure 4-14 Location of the wells throughout the reservoir under study.

4.10 Reservoir Numerical Simulation Results

The Sequential Gaussian Simulation (SGS) or any other stochastic methods such as Monte Carlo method and Gaussian random function are conditional simulation processes used to generate equally probable maps of properties that are within the uncertainty estimates made by the kriging or cokriging processes (Hirsche, 1996). Consequently, SGS is used for handling spatial uncertainty. These simulations are conducted using specialized software, which gives the option to constrain the simulations by a histogram distribution of values; however, due to the limited sample size in the study field this option is not used. Thus, cokriging model is chosen to perform the stochastic simulation.

300 realizations are created using the reservoir numerical simulation model to determine a reservoir model with 50% probability of concurrency of original gas in-place. The original gas

in-place volume distribution presents a standard deviation equal to 93 Bscf and the mean is 1,180 Bscf. The original gas in-place percentiles are shown in **Figure 4-15a**: P(10) is 998 Bscf, P(50) 1,150 Bscf and P(90) 1311 Bscf.

Considering the realization corresponding to P(50) original gas in-place, the numerical reservoir simulation model is run under the constrains indicated in the development strategy section. The estimated field gas production rate (FGPR) is characterized by three stages as illustrated in **Figure 4-15b**. The first stage corresponds to the four wells producing a total of 200 MMscfd during the first 6 months of production life of the field. The second stage of production is characterized by the 7 wells producing a total rate equal to 400 MMscfd during 38 months. Finally, the third stage of production represents the decline of the production during 40 months until the minimum economical production (50 MMscfd) is reached. The cumulative gas production at the end of the production life of the field (FGPT) is 733 Bscf.

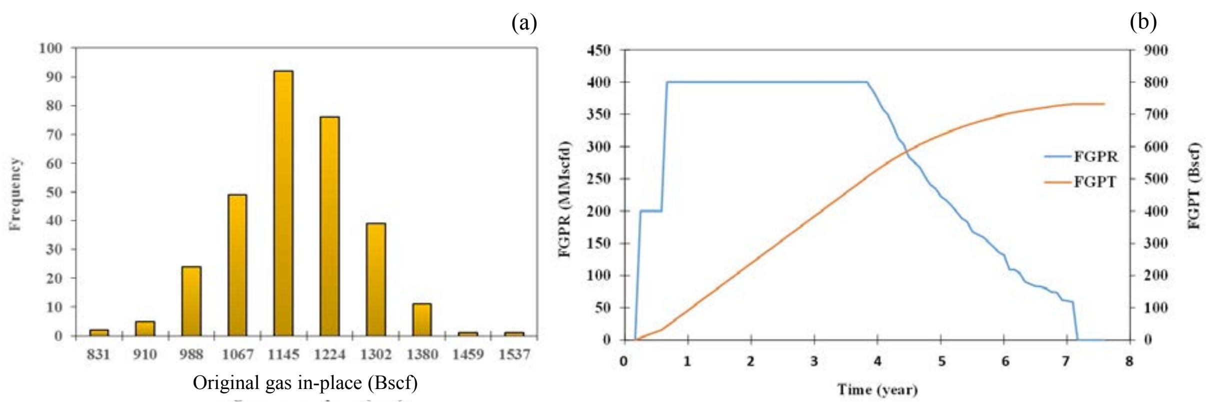

Figure 4-15 Reservoir simulation model results. (a) Original gas in-place histogram built from 300 realizations. (b) Field daily gas production rate and its corresponding cumulative gas production.

Chapter Five: Mechanical Earth Model

The Mechanical Earth Model (MEM) is a small scale numerical representation of mechanical properties and state of stress for a particular volume of rock in a field or basin. The MEM captures geological, geophysical and mechanical properties of the rock along with the relationship between mechanical properties and stresses (Serra et al., 2012). The MEM is constructed in this thesis using petrel, eclipse and visage software, data from wells in the field under study and neighboring wells, which help to estimate the mechanical properties of the rock outside the reservoir through stochastic methods. Data includes information such as sonic, density and gamma ray logs, and elastic moduli from core analyses. The following sections of this chapter describe the process to construct and validate the MEM for the offshore field considered in this study.

5.1 Grid

The construction of the 3D mechanical earth mode (3D-MEM) has as its starting point embedding the reservoir grid by the inclusion of sideburden, underburden and overburden. The motivation of this embedding process is to eliminate boundary effects from the computed results at the reservoir level.

The MEM grid for the offshore field considered in this study has been built by embedding the reservoir grid in three zones: sideburden, overburden including the water depth and underburden, each one with specific characteristics described in the following sections.

5.1.1 The Sideburden

The cells in this zone were generated by extending the embedding reservoir grid in I and J directions. The grid was prolonged by 36.0 km and 40.0 km at each side respectively and subdivided into 10 geometrically spaced cells with a factor equal to 1.3. There are two reasons for these specific distances in I and J directions. First, it is recommended for the model to have a square areal shape (Schlumberger Information Solutions, 2011); second, the MEM grid has to be aerially larger (it is recommended between 3 and 5 times) than the unembedded grid. Additionally, a stiff plate was considered and 50 m cells were added around the sideburden to guarantee uniform applications of loads to the embedded grid. The final areal extension is 84 km by 84 km. The rotation angle is 67 degrees. **Figure 5-1** shows the cell distribution in the sideburden zone.

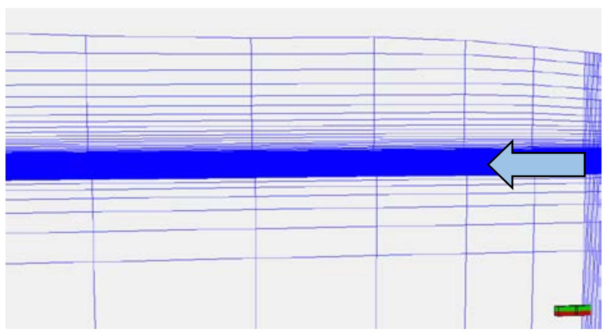

Figure 5-1 Sideburden cells distribution considering geometrical spacing.

5.1.2 The Overburden

The study field is located offshore in the Gulf of Mexico in water depths ranging from 980 m in the southern part of the field to 1,200 m in the northern part. In order to honour these water depth variations in the MEM, a seabed surface was created using seismic information and well tops from 8 wells drilled in the study area. The surface is presented in **Figure 5-2a**. In similar manner, a subsurface for the Upper Pliocene formation was generated as shown in **Figure 5-2b**.

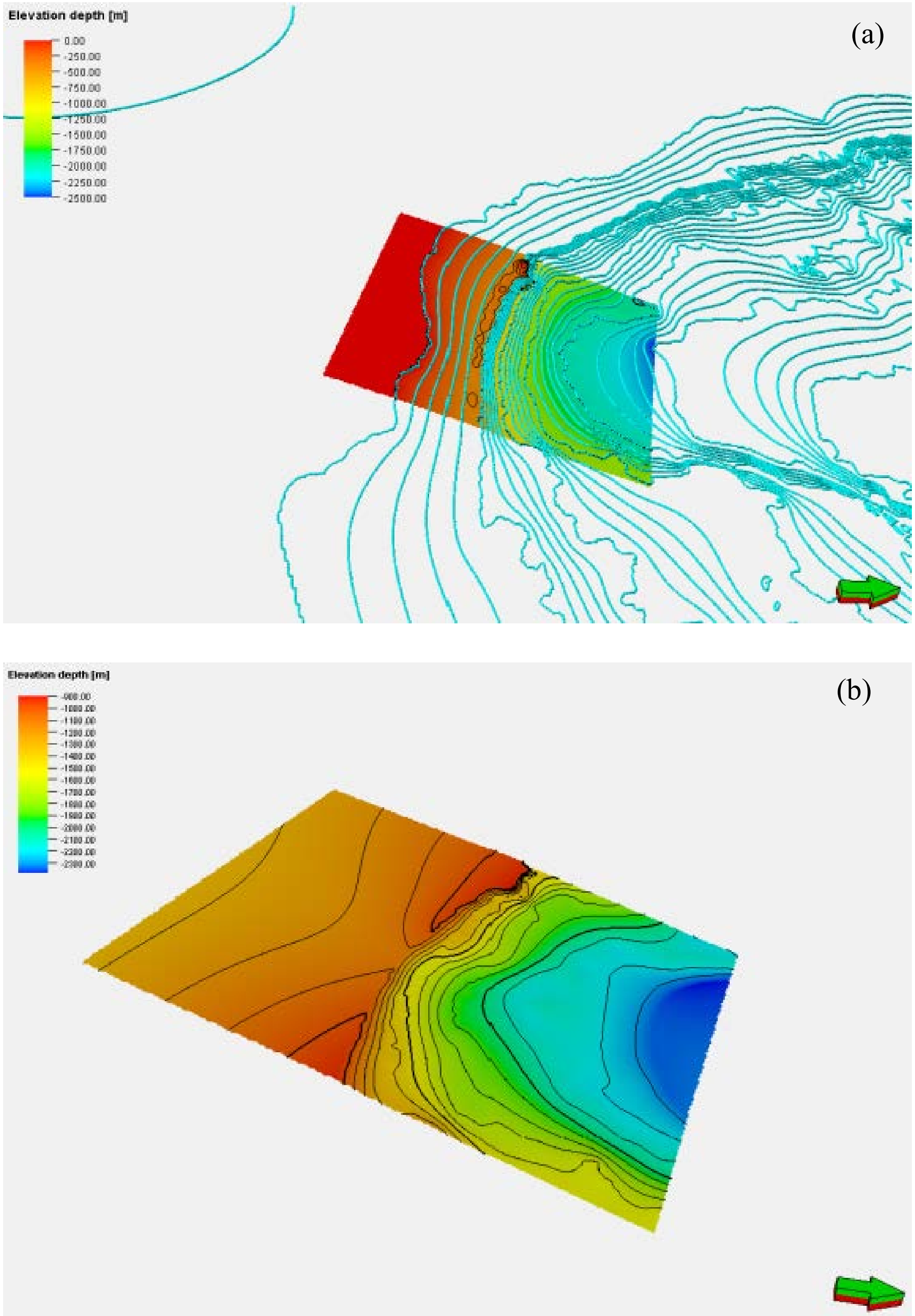

Figure 5-2 Surface maps. (a) Seabed surface configuration and (b) Upper Pliocene surface.

The overburden cells were built using the previously mentioned surfaces and the top surface of the upper reservoirs. The distance between the seabed surface and the upper Pliocene surface was divided in 2 proportional layers with equal sizes and the distance between the upper Pliocene surface and the top surface of upper reservoir was split in 20 layers following a geometric progression. In order to make the layer with a similar size to the corresponding layer in the reservoir, a geometric progression factor of 1.2 was defined. **Figure 5-3** shows the layers distribution in the overburden.

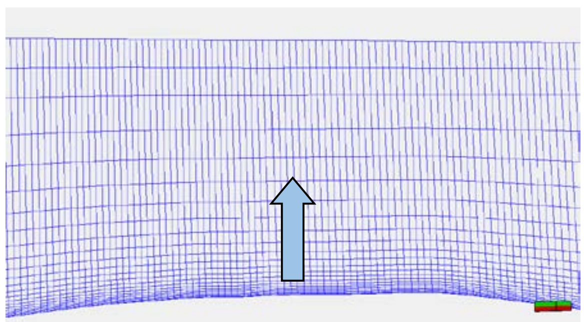

Figure 5-3 Overburden cells distribution.

5.1.3 The Underburden

The underburden was divided into three zones for layering purposes. The first zone was divided in 7 layers using the geometric progression method and a factor equal to 1.5. These 7 layers go from the base of the lower reservoir to a depth of 5500 m. There is well log data for some wells that go down to this depth. The second zone was defined from 5,500 m to 17,000 m and was split into 5 layers using a geometric progression method and a factor equal to 1.5. The third zone was defined from 17,000 m to 29,000 m. with 4 layers of equal sizes. The reason for this final depth is because the aspect ratio in the model is recommended to be greater than 3:1 and the thickness of each layer should be approximately the depth of the reservoir's base including the water depth (Schlumberger Information Solutions, 2011). For example, 6 km of horizontal extension requires at least 2 km of depth and a reservoir's base at 3,000 m implies 4 layers with thickness of 3,000 m. **Figure 5-4** presents the underburden distribution.

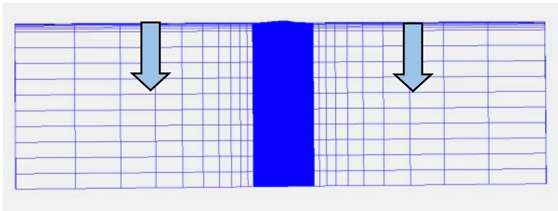

Figure 5-4 Underburden cells distribution.

5.1.4 MEM grid

The final MEM grid is a cube with dimensions of 84 km x 84 km x 29 km. The total number of cells is 6,239,376 cells, with 303 cells in I direction, 208 cell in J direction and 99 layers. **Figure 5-5** is shown the final MEM grid with all the specifications previously mentioned.

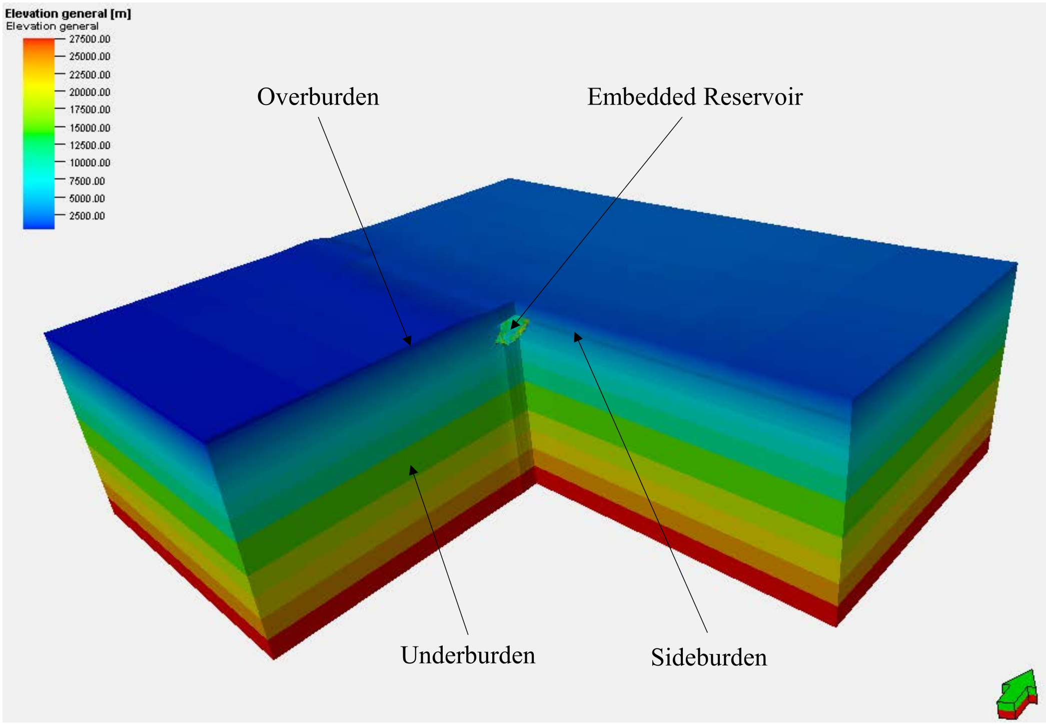

Figure 5-5 MEM 3D grid. Reservoir, underburden, overburden and sideburden.

5.2 Grid Quality Control

This is an important phase during grid construction and helps to guarantee that the grid is usable for the MEM. The quality control helps to meet the following simple conditions.

Cell volume: The block volume must be bigger than zero and negative values will produce errors. The most common cause of negative volume is associated with faults that cross each other. The lowest cell volume in this study is 1,363 m3. Therefore, the grid covers the requirement of no negative volumes.

Gaps: The grid must not include gaps. Although the reservoir grid contains a shale layer between the two reservoirs that is a seal for the lower reservoir, the later was considered to be active and part of the MEM to avoid gaps in the grid.

Cell inside-out: This property measures the quality of a grid block. When the cell inside-out value of a grid block is equal to zero, the block has good geometry; otherwise the cell has a certain degree of distortion and poor geometry. All MEM grid cells developed in this study have values of cell inside-out equal to zero.

Pinch-outs: They occur when two corners have the same coordinate. The 3D-MEM has no pinch-out problems.

Cell angle: This property represents a deviation from the 90 degrees angle reference. In this thesis, the IJ plane was used to extract the internal angle of deviation for every cell and the results indicate that there are some cells with angles differences between 30 and 48 degrees (maximum). Since the number of cells with high angle is small (798 cells), just 0.02% of total cells, it is considered that these cells do not generate a convergence problem during the simulation.

5.3 Single Material Test

The first step for evaluating the suitability of the grid geometry for a gravity/pressure stress state analysis is the creation of a single material MEM with average properties to analyse the total stresses at zero time step and elastic conditions. The data presented in **Table 5-1** were the input to the single material MEM. This considers sandstone with isotropic and intact rock material.

Table 5-1 MEM single material properties.

Property	Value
Young's Modulus =	10 GPa
Poisson's Ratio =	0.3
Bulk density =	2.3 g/cm^3
Biot Elastic constant =	1
Termal Expansion Coeff =	1.3E-05 1/°K
Porosity =	0.3

The initial conditions for application of the gravity/pressure method were defined as follows:

- Minimum horizontal gradient= 0.20 bar/m = 20 KPa/m
- S_{hmin} offset= 0
- S_{Hmax}/S_{hmin} = 1.2
- Sea fluid pressure gradient= 0.101 bar/m = 10.1 KPa/m
- Pressure of undefined cells= 0 bar/m = 0 KPa/m
- Offset= 0
- Minimum horizontal stress Azimuth = 0 degree

5.3.1 Single material test results

The cube shape and single material characteristics allow boundary stresses to be applied uniformly to the model where the faulting regime is assumed normal. The vertical gradient input, based on bulk density, was 0.225 bar/m (22.5 KPa/m), whereas in the model it is 0.229 bar/m (22.9 KPa/m). Likewise, the minimum horizontal stress gradient input was 0.20 bar/m (20 KPa/m), while in the model the minimum horizontal stress, acting in the "y" direction and its gradient is 0.192 bar/m (19.2 KPa/m). The maximum horizontal stress gradient in the model is acting in "x" direction and is equal to 0.24 bar/m (24 KPa/m). Thus, the resulting ratio S_{Hmax}/S_{hmin} in the model is 1.25, which is slightly larger than the input ratio (1.20).

Figure 5-6 shows a cross plot of stresses extracted at GML-2 location vs. depth, where TOTSTRXX is the total stress in the x direction, TOTSTRYY is the total stress in y direction and TOTSTRZZ is the total stress in z direction. All of them exhibit a linear gradient. Hence, it can be concluded that the MEM grid is working well and applies correctly the boundary stresses to the model.

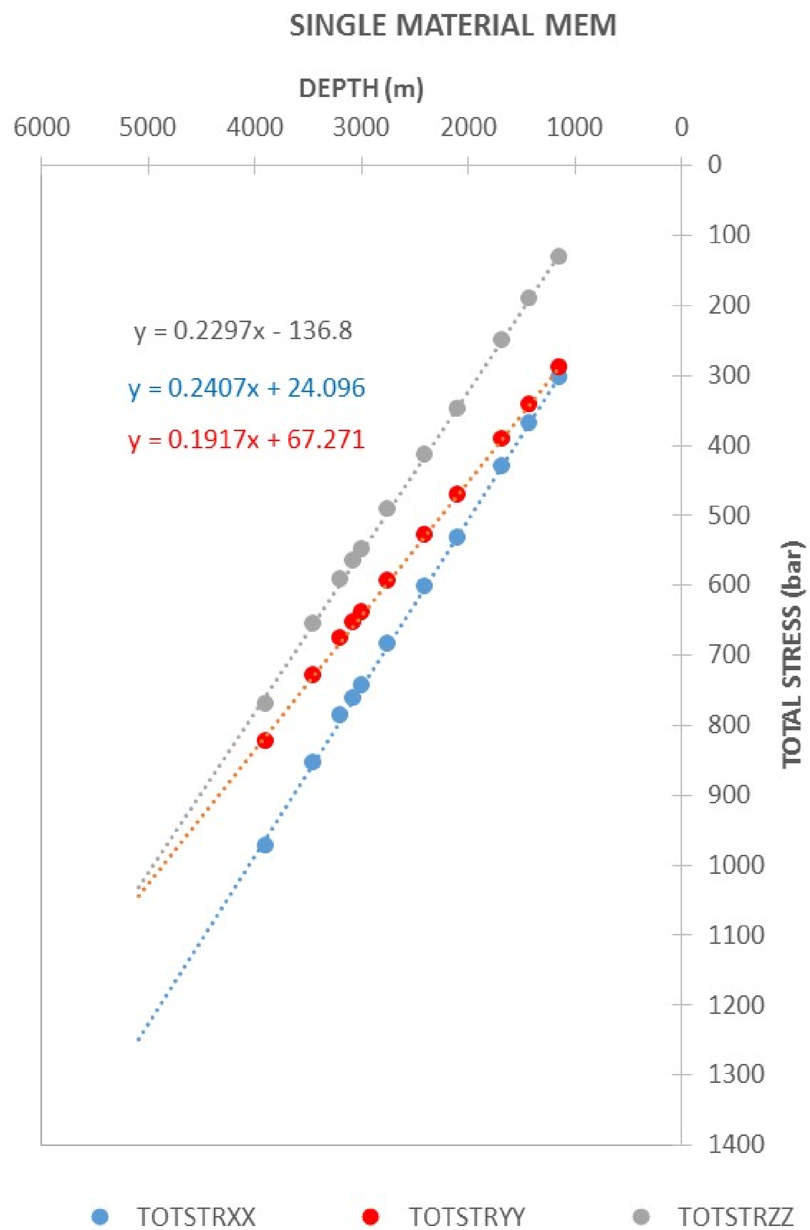

Figure 5-6 Single material test using the MEM 3D grid.

5.4 Mechanical Properties Extrapolation

There are different ways of assigning mechanical properties to the MEM grid. For example the properties can be transferred from one grid to another grid, or calculated from well logs and extrapolated to the entire grid using kriging interpolation method, or co-kriging in combination with stochastic methods. Other way to do it is using the graded method which is explained next.

For the offshore reservoir under consideration the MEM grid geomechanical properties of the overburden and sideburden were estimated with the use of the following two steps:

1) Scale-up from well log to well grid cells.
2) Populate the whole MEM grid using stochastic methods.

The first step is related to the vertical property estimation in the grid cells that pass-through the well trajectory. It was developed using the settings indicated in **Table 5-2**.

Table 5-2 Settings for scale-up of properties from well logs

Scale-up property	Average Method	Treat log	Method
Porosity	Arithmetic	As point	Neighbor cell
Young's Modulus	Mid-point	As point	Neighbor cell
Poisson's ratio	Maximum	As point	Neighbor cell
UCS	RSM	As point	Through cell
Bulk density	Median	As point	Neighbor cell
Friction	RMS	As point	Neighbor cell

The average method selected to scale-up the well logs was based on the match between the log property and the final average property in the grid cells. **Figure 5-7a** to **Figure 5-7d** show histograms for some of the properties listed in the previous table. The graphs show good matches indicating that the data are represented properly in the MEM.

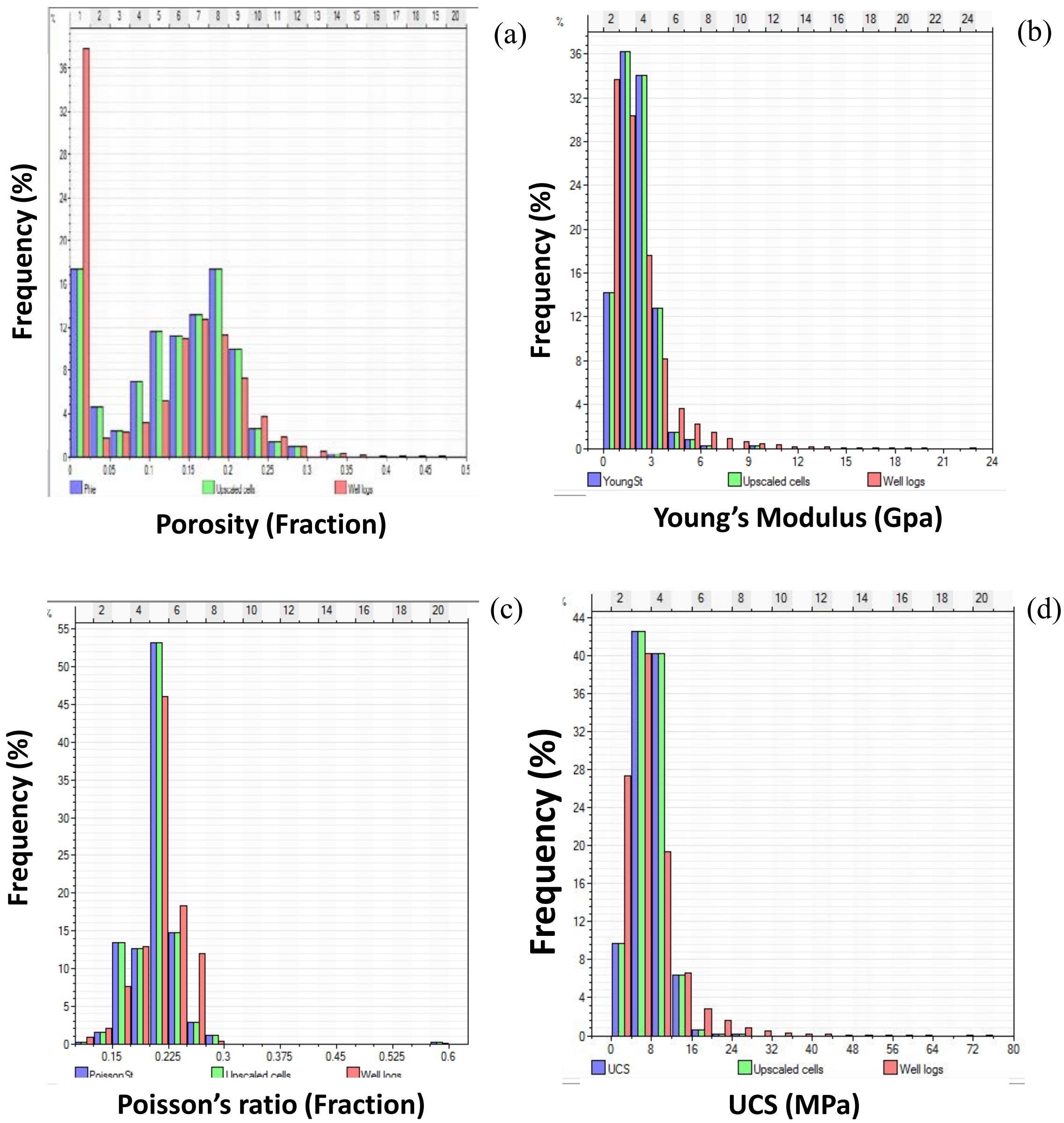

Figure 5-7 Scale-up properties from well logs, well log in solid pink color, scale-up cells in solid green color. (a) Porosity, (b) Young's modulus, (c) Poisson's ratio and (d) UCS.

The second step considers the areal and vertical estimation. According to Isaak and Srivastava (1989), the estimation of a variable when there is no sample requires a model of how the variable behaves in that specific area. Without a model it is impossible to estimate a value in a location that was not sampled. Base on the quality of input data, petrophysical modeling process allows estimating values of a property in a location that has not been sampled, using either deterministic or probabilistic methods.

The deterministic methods will always predict the same result with the same input data. The most common deterministic method is Kriging. In contrast, the probabilistic or stochastic methods predict different results with the same input data.

The stochastic (probabilistic) simulation is the action of producing different models with the same probability of occurrence in a random field. There are several methods for creating stochastic models. However, the most common is Sequential Gaussian simulation, which must satisfy three requirements: data values at specific location, histogram with normal distribution and random function model (variogram).

The field MEM property modeling was performed by vertical zones (7 vertical zones). However not all the zones were modeled. These vertical zones were defined as follow:

- Zone 1, from seabed to upper Pliocene top
- Zone 2, from upper Pliocene to upper reservoir top
- Zone 3, from upper reservoir top to Upper reservoir base
- Zone 4, from upper reservoir base to lower reservoir top
- Zone 5, from lower reservoir top to lower reservoir base
- Zone 6, from lower reservoir base to -5,500 m.
- Zone 7, from 5,500 m. to a depth -29,000 m.

The last zone was not modeled using deterministic nor stochastic methods because there are not well logs to scale-up. Instead, this zone was populated using the graded method explained next.

Due to lack of areal sample data (only 6 points), it was not possible to apply any deterministic method such as kriging, and instead the Sequential Gaussian simulation method was applied for estimating values of geomechanical properties in the MEM.

In general the properties do not present normal distributions. Therefore, transformation of input distribution into normal distribution for each vertical zone was carried out with 2 different methods: the Normal score and the Beta transformation functions. Then the data are back-transformed,

The normal score transformation converts the input data into a standard normal distribution with the use of Blom's equation (**Eq. 5-1**) ("Normal Score", n.d.). Thus, each cell value in the property domain has a value in the normal score domain through the same cumulative probability in both domains. This type of transformation is not recommended when there are few input data points available because the resulting histogram will be poor of resolution.

$$s = \eta\left(\frac{ra - \frac{3}{8}}{n - \frac{1}{4}}\right) \quad \textbf{Eq. 5-1}$$

Where, s is the normal score for an observation, ra is the rank for that observation, n is the sample size and η is the point quartile from the standard normal distribution (cdf).

The Beta distribution transformation assumes that the input distribution can be matched with a beta distribution function and then transformed it into a standard normal distribution. The probability density function is expressed by equation **Eq. 5-2**.

$$f(x;\alpha 1,\beta 1) = \frac{x^{\alpha-1}(1-x)^{\beta-1}}{B(\alpha 1,\beta 1)} \quad \textbf{Eq. 5-2}$$

where B(α1, β1) is the Beta function that is normalized to ensure the total probability is equal to 1. α1 and β1 are defined as function of variance (var) and mean ($\bar{x}$) are defined as shown in equations **Eq. 5-3** and **Eq. 5-5** and η is a positive integer (Soong, 2004).

$$\alpha 1 = \bar{x}\left(\frac{\bar{x}(1-\bar{x})}{var} - 1\right) \quad \textbf{Eq. 5-3}$$

$$\beta 1 = (1-\bar{x})\left(\frac{\bar{x}(1-\bar{x})}{var} - 1\right) \quad \textbf{Eq. 5-4}$$

$$B(\alpha 1, \beta 1) = \frac{\Gamma(\alpha 1)\Gamma(\beta 1)}{\Gamma(\alpha 1, \beta 1)};\ \Gamma(\eta 1) = (\eta 1 - 1)! \quad \textbf{Eq. 5-5}$$

If an input histogram exhibits a Beta distribution function, the algorithm transforms it closely to a Gaussian distribution. Thus, the more similar the data distribution to the Beta function the better the output accuracy in the model. The data analysis for the distribution properties in the overburden is shown in **Appendix A**.

The stiff plate is modeled elastically and it is recommended to have a Young's modulus that could be twice the mean value or 50% of the pick; further it is recommended to have Poisson's ratio corresponding to a low value of the data (Schlumberger Information Solution, 2011). For bulk density and the UCS it is recommended to use the highest value of the data. The values so defined for the stiff plate are shown in **Table 5-3**. The material type selected is intact rock material with isotropic elastic model and Mohr-Coulomb yield criteria.

Table 5-3 Stiff plate properties.

Property	Value	Property	Value
Young's Modulus =	4.12 GPa	UCS =	2.48 MPa
Poisson's Ratio =	0.12	Friction Angle=	46 deg
Bulk density =	2.55 g/cm3	Dilation Angle =	23 deg
Biot Elastic constant =	1	Tensile Stress =	2.5 MPa
Termal Expansion Coeff =	1.3E-05 1/K	Hardening/Softening Coeff =	0
Porosity =	0.01		

As mentioned above the underburden was layered in three vertical zones; however, the estimation of properties was divided into two zones: the first from the base of the embedded reservoir to -5500 m and the second from -5500 to -2900m. Characterization of the first zone is good because there are some well-logs. Properties were estimated using the methods described previously. However the second zone does not have logs and as a result the grid was populated using the graded method. The graded method is recommended when log data are not available.

The method considers a linear gradient between the values at the underburden top and the underburden base. The value for the underburden top can be equal to the average value of the layer just above of it or the average value observed in the reservoir. The value for the underburden base is equal to the value used for the stiff plate. **Table 5-4** presents the linear equations used for calculating properties in the underburden using the graded method. The underburden is modeled elastically.

Table 5-4 Underburden properties using graded method.

Property	Linear Equation
Young's Modulus	= (9.447E-05 * Depth) + 1.380
Poisson's ratio	= (-5.489E-06 * Depth) + 0.2792
Bulk Density	= (1.234E-05 * Depth) + 2.192
Porosity	= (-4.98E-06 * Depth) + 0.1544
UCS	= (4.596E-03 * Depth) + 114.7
Friction angle	= (4.255E-04 * Depth) + 32.66
Tensile	= UCS * 0.1
Dilation angle	= Friction Angle * 0.5

5.5 Pre-Production Stress State

5.5.1 Minimum horizontal stress

As mentioned in Chapter 3, the most reliable and accepted method for estimating the minimum horizontal stress is fracturing the formation and logging the closure pressure. This closure pressure is assumed to be equal to the minimum of the three principal stresses affecting the rock. In this model this minimum stress is considered horizontal (Barree, 2009).

Eight leak-off tests were performed in the study field; four in well GML-1, two in GML-2 and 2 more in GML-3. Each leak-off test was analyzed using a methodology presented by Lopez et al. (2014), based on a derivative plot of $\sqrt{t}$ vs. $\sqrt{t}*\Delta P/(\Delta\sqrt{t})$. Application of the methodology is illustrated in **Figure 5-8** with data of a leak-off test carried out in well GML-3 at a depth of 2996 m. The obtained closure pressure at surface conditions is equal to 1435 psi (9.89 MPa or 98.9 bars).

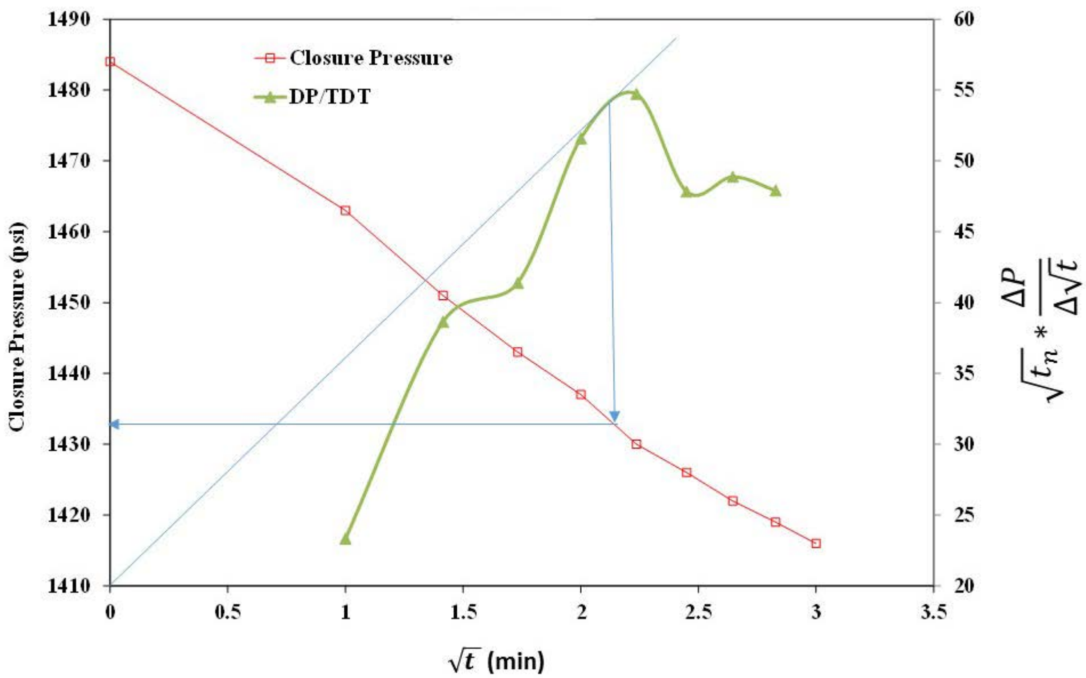

Figure 5-8 Leak off test developed in well GML-3 at depth of 2996 m.

Table 5-5 summarizes the main results of the leak off test interpretation. **Figure 5-9** presents the minimum horizontal stress gradient at reservoirs depth. The gradient varies from 0.17 to 0.20 bar/m (17-20 KPa). Minimum horizontal stress is expected to be between 439 and 506 bars at datum depth of the upper reservoir. The minimum and maximum horizontal stresses for well GML-2 at reference depth were calculated in Chapter 3 and are equal to 452.7 bar (45.2 MPa) and 522.3 bar (52.23 MPa) respectively. Therefore, the ration S_{Hmax}/S_{hmin} is equal to 1.15.

Table 5-5 Minimum horizontal stress from leak Off Test

Well	Depth (m)	S_{hmin} (bar)
GML-1	1440	171
GML-1	1937	268
GML-1	2665	397
GML-1	3500	601
GML-2	2273	299
GML-2	2742	379
GML-3	1996	288
GML-3	2996	475

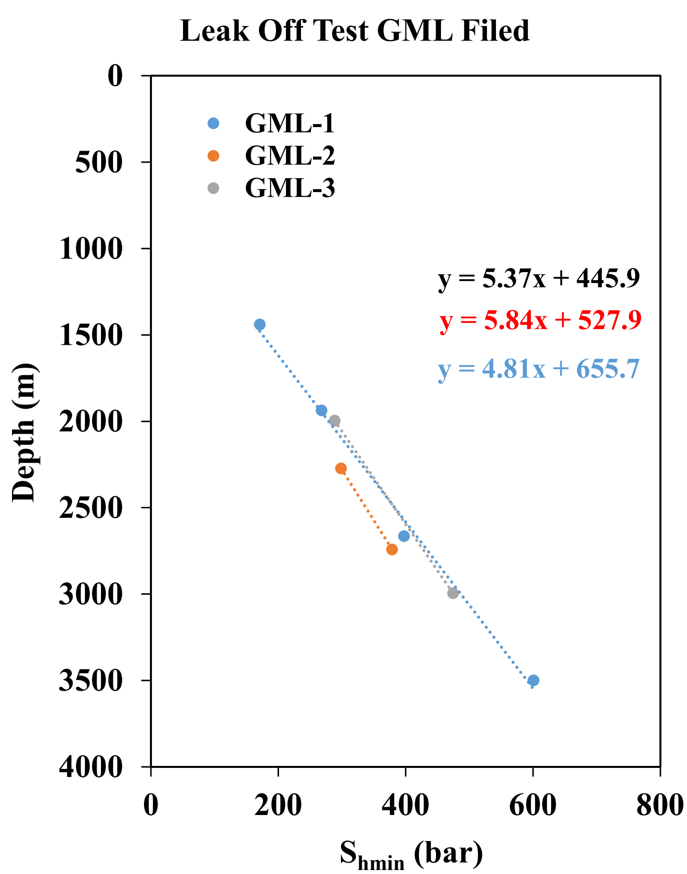

Figure 5-9 Leak off tests carried out in offshore field under study. There are three different gradients for the minimum horizontal stress: 0.17, 0.18 and 0.19 bar/m

5.5.2 Stresses orientation

Well breakouts are zones that present compressive failure or wellbore enlargements. The minimum horizontal stress azimuth is located in the zone of the wellbore wall where the stress state is more compressive. Thus, the minimum horizontal stress azimuth is in the orientation of the breakout (Zoback, 2006).

An easy way to identify wellbore breakouts orientation and opening angle is using the 4-arm caliper log. This tool helps to identify breakouts by measuring the displacement of four arms held at 90°, generally configured in such a way that opposite arms move the same amount and assuming that the tool is always centered (Rider and Kennedy, 2011). To calculate breakouts orientation the bit size should be known. Two independent caliper logs are measured by two pairs of arms, resulting in two orthogonal borehole sizes. This permits calculating breakouts from the displacements and azimuth ratio to north from one of the arms acting as an azimuth tool.

The caliper log for well GML-1 indicates the presence of breakout zones at about 1975 m with an azimuth of approximately 120°. This was the only zone that presented clear displacement (**Figure 5-10a**). Faults are also indicators of the principal stresses orientation at the moment in which the faults were generated. **Figure 5-10b** shows normal faults in the field with orientation N30°E as a consequence of convergence of stresses to the East.

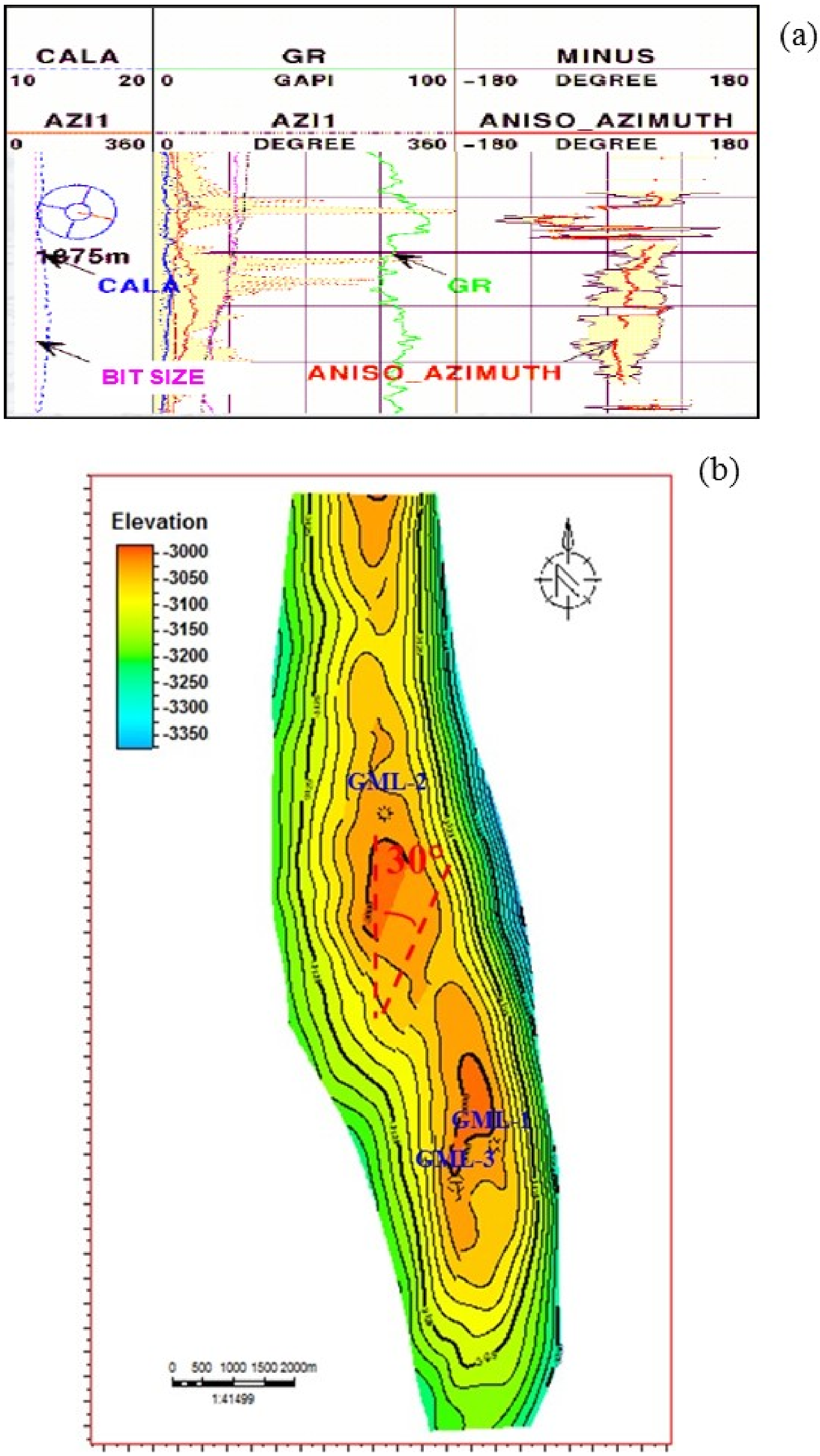

Figure 5-10 Minimum horizontal stress orientation from caliper log and maximum horizontal stress orientation from faults.

Initial conditions for the pre-production stress state analysis are as follows:

- Minimum horizontal gradient= 0.15 bar/m = 15 KPa
- S_{hmin} Offset= 0
- S_{Hmax}/S_{hmin} = 1.1
- Minimum horizontal Stress azimuth = 120 degree
- Sea fluid pressure gradient= 0.101 bar/m = 10.1 KPa
- Pressure of undefined cells= 0.15 bar/m = 15 KPa
- Offset= 0

The model configuration was controlled using the following rules:

- Pinchout tolerance method= Factor
- Pinchout tolerance= 1.0 E-006
- Iterative solver tolerance= 1.0 E-007
- Number of increments= 4

The minimum horizontal gradient and the ratio S_{Hmax}/s_{hmin} are the result of field stress calibrations.

5.5.3 Discontinuity modelling

The reservoir model has 8 faults. However, only the three most important faults were considered in the geomechanics simulation for simplicity. One is the fault located in the north of the field; this is a sealing fault and boundary for both reservoirs. The two other important faults are in the center of the field, they do not present significant displacement and are considered opened to flow. However, there is a possibility that these faults could be a barrier to fluid flow between the side bocks. If this is the case it could have a negative impact in the cumulative gas production. It is recommended to include all the faults in future simulation work.

In a MEM model the perfect fault to be modeled would be the fault whose extension can be determined from seismic interpretations. This is not the case for this offshore field as faults were only mapped between the top and base of the reservoirs. For this study they were extended from the lower Miocene surface to a depth of -4500 m in the underburden using the same azimuth and dip shown in **Figure 5-11**. The fault properties were defined using the material library included in Visage software. Where the normal and shear stiffness are 40000 and 15000 bar/m respectively; the cohesion and tensile strength are 0.01 bars; friction and dilation angles are 20 degrees and 10 degrees, respectively.

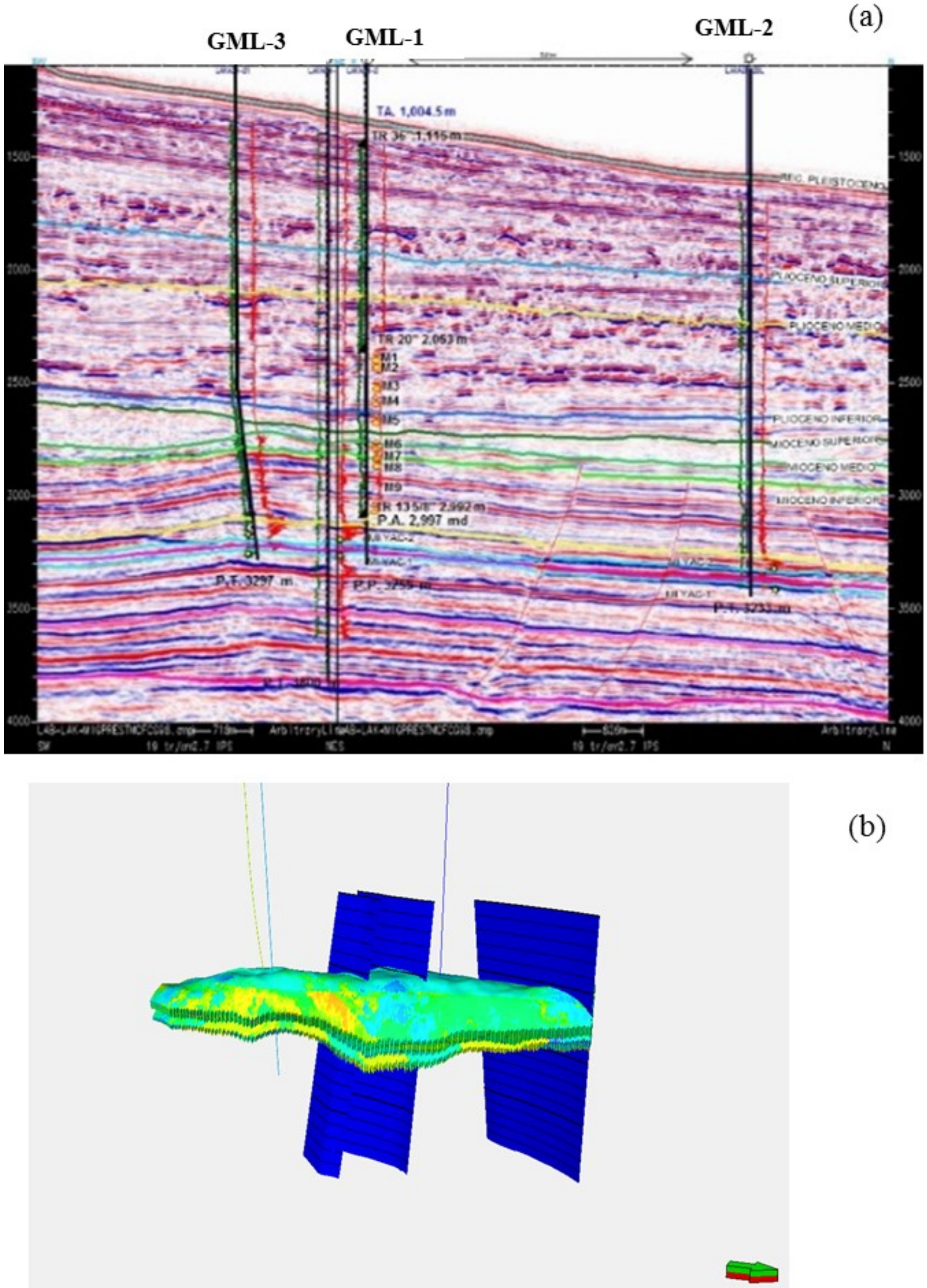

Figure 5-11 Fault extension from lower Miocene to -4500 m. (a) seismic image indicating the fault's extension in the reservoir, (b) fault's extension in the geomechanics model.

5.5.4 Pre-production stress state results (elastic run)

In similar way as described in the single material test results (section 5.3.1), a single material model was built for gradients stress comparisons. The pre-production stresses state analysis indicates that the input vertical gradient based on bulk density log is 0.225 bar/m (22.5 KPa/m), whereas in the model the average value is 0.216 bar/m (21.6 KPa/m). Likewise, the input of minimum horizontal stress gradient is 0.15 bar/m (15 KPa/m), while the model it yields an average of 0.156 bar/m (15.6 KPa/m). As opposed to the model discussed in section 5.3.1, the minimum horizontal stress in this model is acting in the "x" direction with an azimuth of 120 degrees. The maximum horizontal stress gradient is 0.189 bar/m (18.9 KPa/m) and the ratio S_{hmax}/S_{hmin} is 1.21 slightly larger than the input ratio of 1.1. The resulting vertical gradient, total minimum horizontal stress gradient and total maximum horizontal stress gradient in the MEM are presented in **Figure 5-12**.

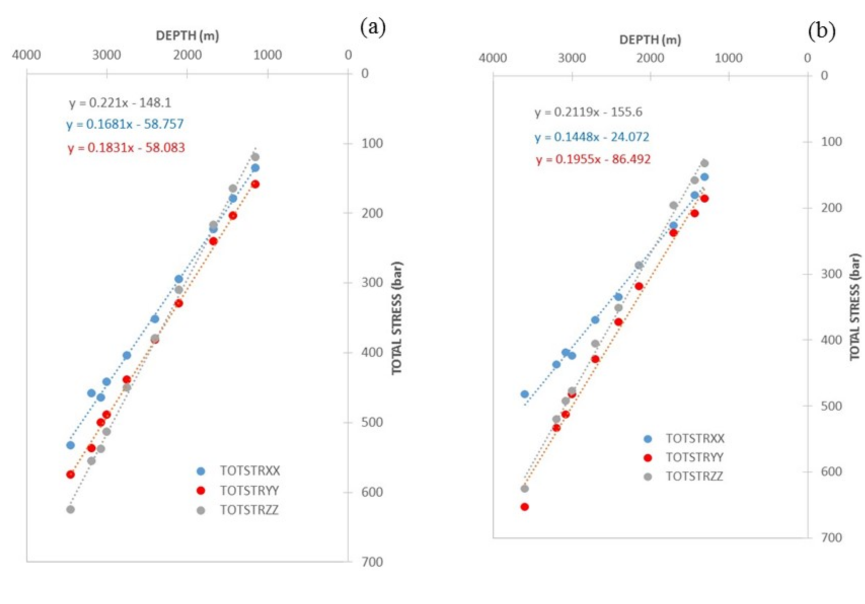

Figure 5-12 Vertical gradient (grey marks), minimum horizontal stress gradient (blue marks) and maximum horizontal stress gradient (orange marks), (a) GML-1, (b) GML-2.

In order to compare the 1D MEM and the 3D MEM stresses, graphs of stress versus depth at well location for GML-1 and GML-2 were created. **Figure 5-13** presents the vertical stress and minimum horizontal stress versus depth. In the 3D MEM the vertical stress corresponds to the total stress in the z direction while the minimum horizontal stress matches with the stress in the x direction.

Not always are the principal stresses aligned with either the vertical axis or the well. Frequently they are altered as a result of stress rotation particularly around discontinuities. The principal 1D stresses can be compared with minimum and maximum horizontal stresses in the 3D regime because of their representativeness (Schlumberger Information Solutions, 2011). The total stress in z direction and the vertical 1D stress are nearly aligned and can be compared. In the same way, the minimum and maximum horizontal 1D can be compared with the total stresses in x and y directions because they are approximately aligned. The grid orientation is the same as the maximum stress azimuth.

Examining the graphs in **Figure 5-13**, the conclusion is reached that the gradients defined in the 3D model are similar and consistent with the vertical, minimum and maximum horizontal stress especially at reservoir depth.

The study field has not gone on production yet. However as the 3D MEM has been properly calibrated it is considered to be suitable for forecasting purposes and for performing post production analysis.

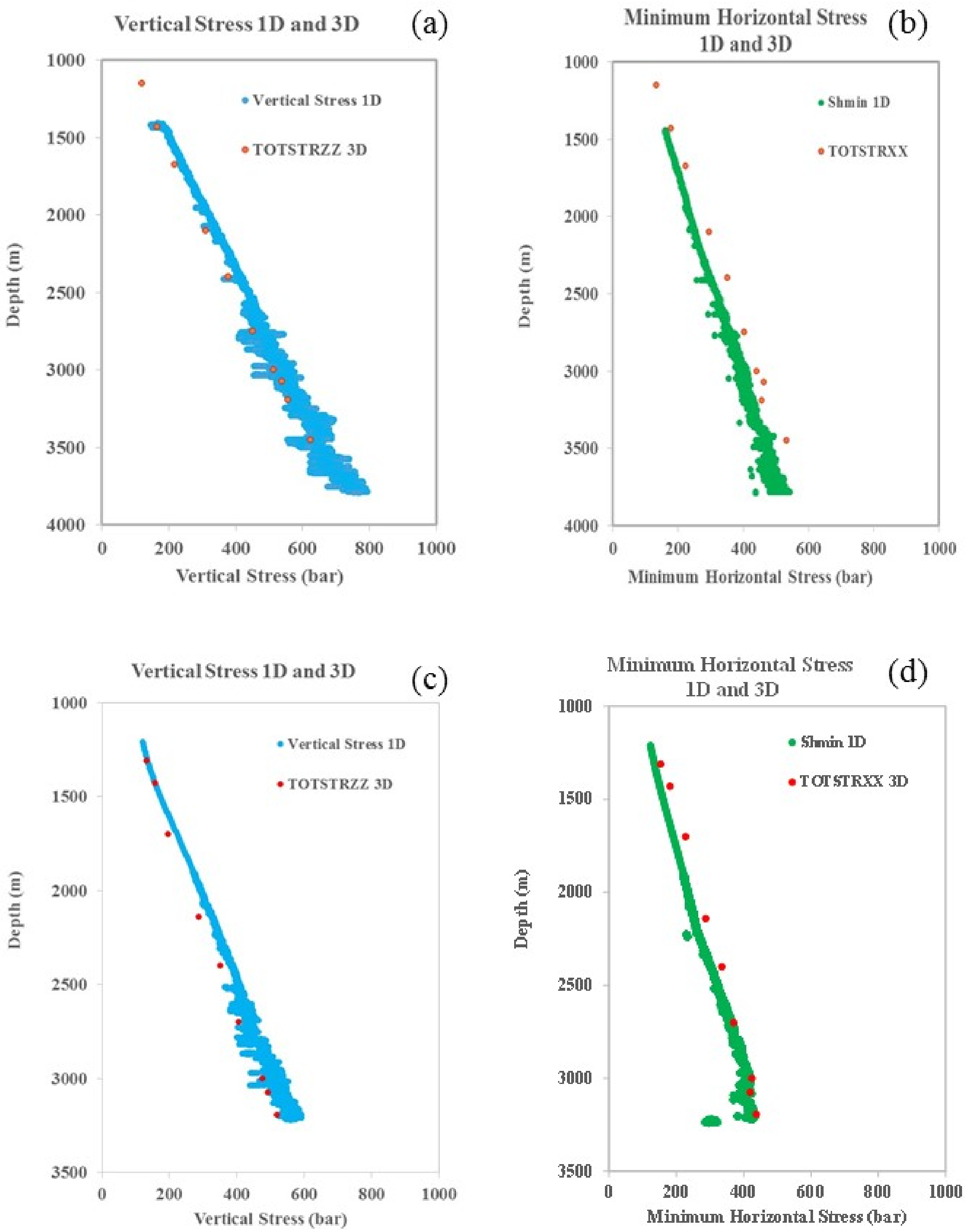

Figure 5-13 1D and 3D comparison for vertical and minimum horizontal stress. (a) and (b) GML-1, (c) and (d) GML-2

Chapter Six: Mechanical Earth Model Results

6.1 Stresses State Analysis

Stresses state is governed by pore pressure and three principal stresses mutually perpendicular. The principal total horizontal stresses are not equal because the tectonic stresses components act in different magnitude and direction. Thus, when analysing underground stresses both principal directions and magnitudes are the main concern.

The use of a 3D mechanical earth model (MEM) to simulate the underground stress state in a reservoir is more realistic than the use of 1D model. The 3D MEM takes into account the spatial variation in the mechanical properties of the rock, the complexity in reservoir geometry and the presence of discontinuities. Therefore, the one-way coupled modeling process permits updating the stress state as function of pore pressure and fluid flow in the reservoirs. In addition, any change in these variables can potentially affect the reservoir behaviour. The stress state in a 3D MEM is considered valid from the point of view that the initial stresses have been calibrated.

6.1.1 In-situ stresses orientation

For the field of interest, the stresses orientation in the 3D MEM coincide with the orientation of 30 degree for the maximum horizontal stress and 120 degrees for the minimum horizontal stress as indicated during its construction and measured by the wells. The arrows with green head and red stem in **Figure 6-1** show the calculated initial maximum horizontal stress orientation. The minimum horizontal stress is perpendicular to the arrows.

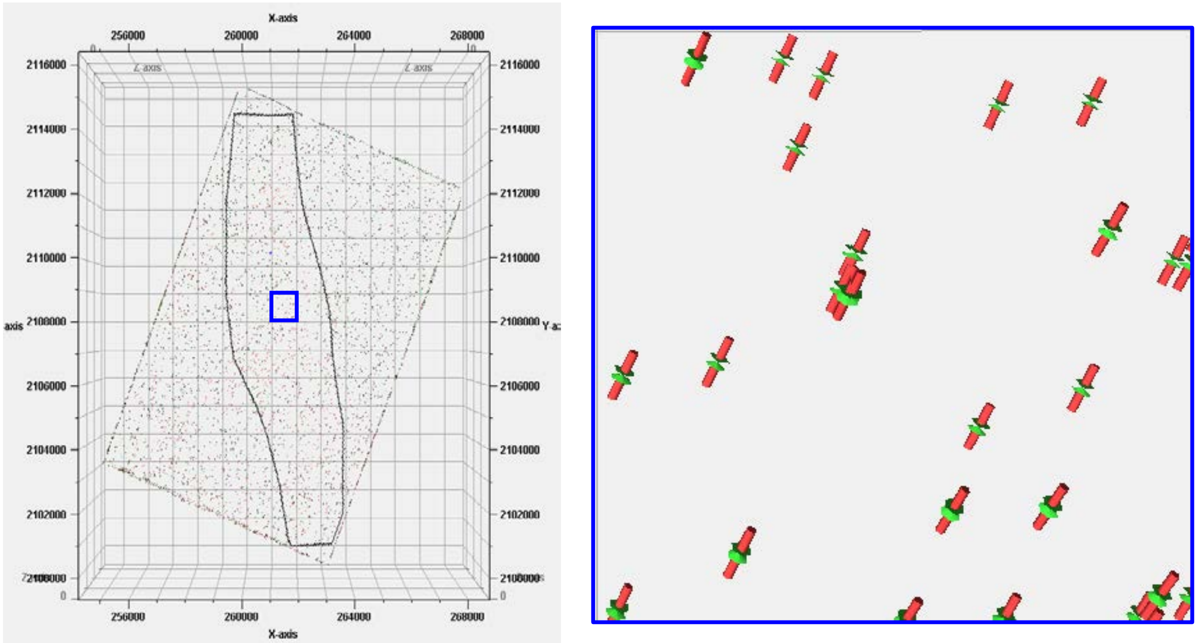

Figure 6-1 XY plane showing the initial maximum horizontal stress orientation in the reservoir and close-up in blue square.

6.1.2 In-situ stress condition

The in-situ stresses determined using hydraulic fracturing and estimated through the stress polygon indicated that the reservoir is already fractured as the stress regime for both reservoirs is located in the transition between normal faulting and strike-slip faulting. Moreover, the Mohr circles calculated in the 3D MEM at reservoir depth also indicate that under present in-situ stress condition the reservoir rock has failed. This is shown in **Figure 6-2** where the solid blue line semicircle representing the initial condition of principal stresses in the reservoir has crossed the red line representing the failure envelop of the rock.

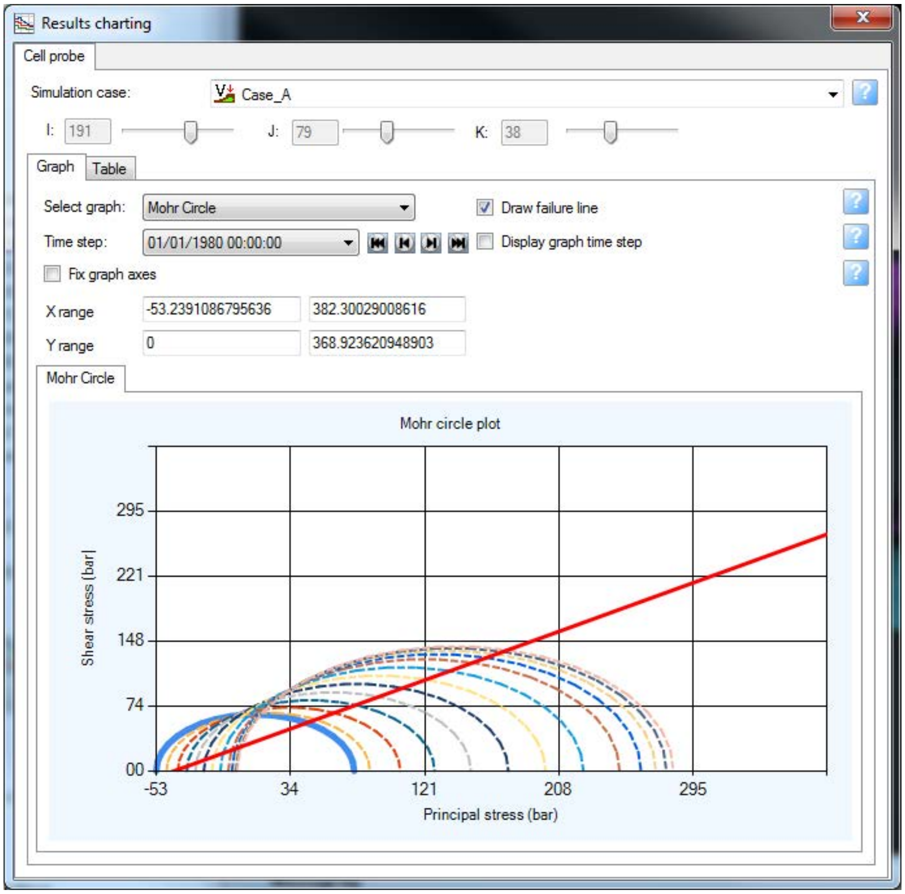

Figure 6-2 Mohr circles calculated in the 3D MEM and failure envelop at reservoir depth.

The relevance of this information resides in the fact that the current conceptualization of the porous media for these reservoirs considers only single porosity. However the above analysis suggests that the porous media could be naturally fractured.

The preliminary evidence indicating the presence of natural fractures in these reservoirs is found in the rock thin section slides but should be corroborated with other sources of information such as image logs and more detailed core and petrographic work. **Figure 6-3** and **Figure 6-4** are two examples that illustrate the type of fractures that could be interpreted in these reservoirs. **Figure 6-3** is a photomicrograph of a sandstone in well GML-3 at depth of 3091.3 m.

The petrographic study shows primary intergranular porosity with grain sizes of approximately 0.2 mm and secondary porosity developed by partial dissolution and microfractures in grains partially cemented. **Figure 6-4** is a photomicrograph from the petrographic study showing a sandstone in GML-2 at a depth of 3068.7 m. It shows fine grains with average size of 0.07 mm that originate primary intergranular porosity and secondary porosity developed by partial dissolution and fractures opened and filled with organic matter.

In both examples there is a slight perception of deformation bands because of the presence of cataclasis, dissolution and cementation as deformation mechanism. Deformation bands are also known in the literature as gouge-filled fractures and/or granulation seams. They occur mainly in sandstone reservoirs.

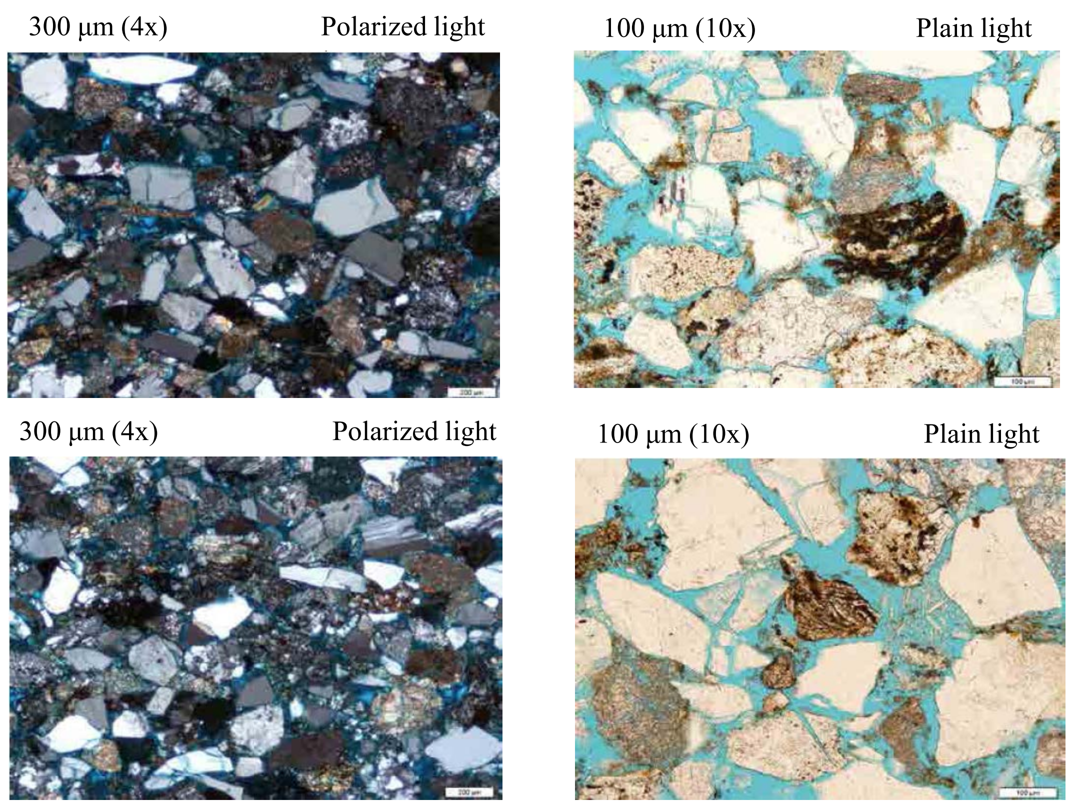

Figure 6-3 Photomicrographs of thin sections, 4x and 10x, 100 µm and 300 µm, plane light and polarized light for GML-3 at depth of 3091.3 m.

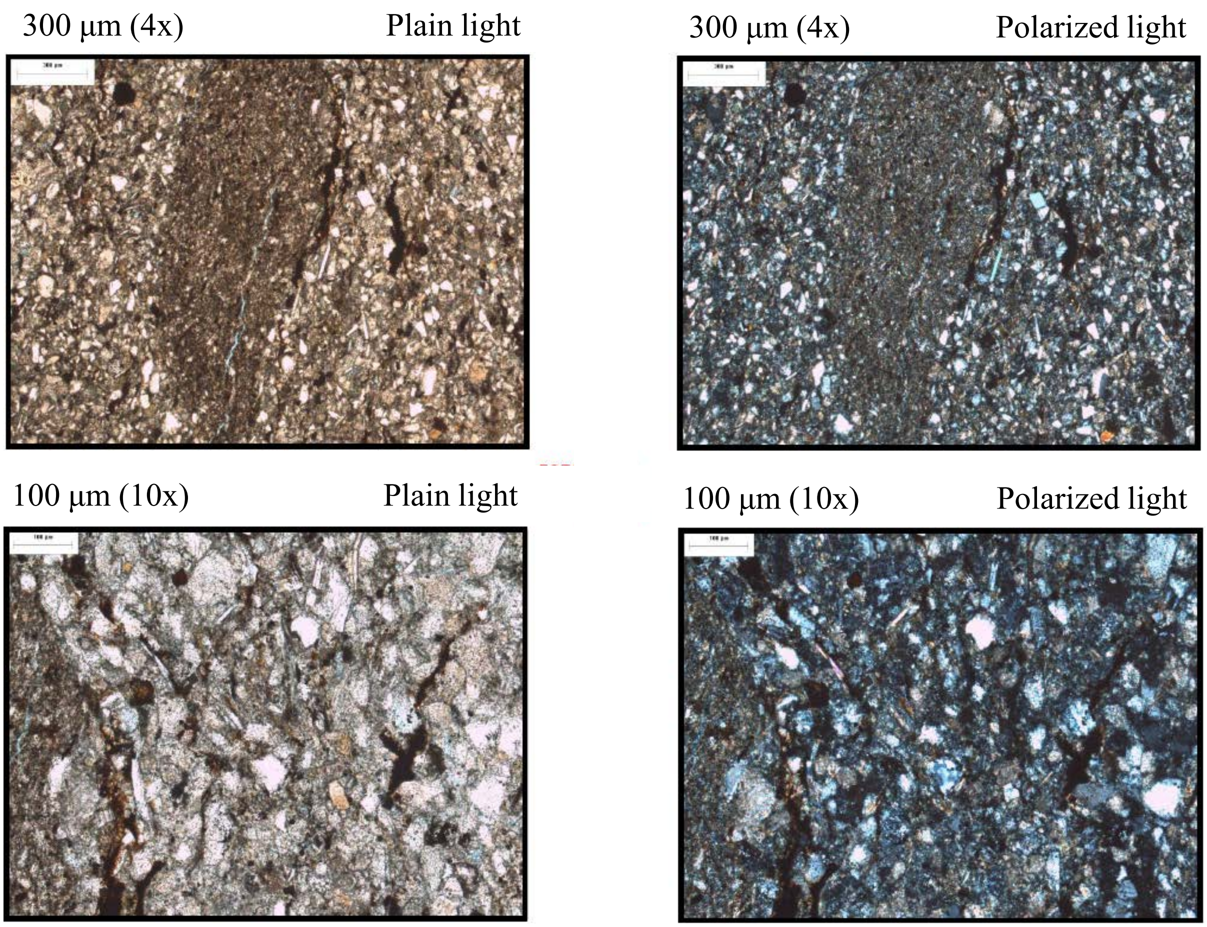

Figure 6-4 Photomicrographs of thin sections, 4x and 10x, 100 µm and 300 µm, plane light and polarized light for GML-2 at depth of 3068.7 m.

According to Fossen et al. (2007), deformation bands are limited to porous granular media with relatively high values of porosity and encompass significant quantity of grain translation and rotation, along with grain crushing (they are not slip surfaces). Deformation bands occur hierarchically as individual bands and zones with band thicknesses of millimetres or centimeters that show smaller offsets than classical slip surfaces. Deformation bands can be classified, as shear bands, compaction bands and dilation bands (shear bands are the most widely described in the literature) as shown in **Figure 6-5** . They are characterized by four principal deformation mechanisms: "(1) granular flow (grain boundary sliding and grain rotation); (2) cataclasis (grain fracturing and grinding or abrasion); (3) phyllo-silicate smearing; (4) dissolution and cementation." (p. 757).

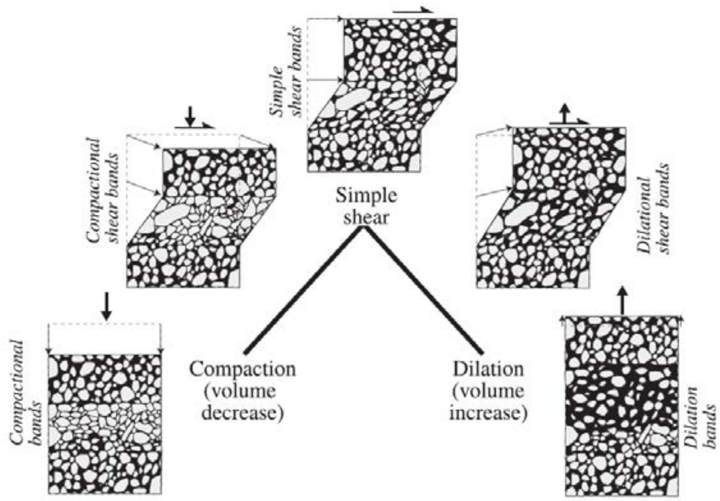

Figure 6-5 Kinematic classification of deformation bands. (Source: Fossen et al., 2007).

Generally, deformation bands cause a decrease in porosity and permeability, which create anisotropy and affect fluid flow. Consequently they have direct implications on management of hydrocarbon reservoirs. Additional work is recommended previous to reaching a definitive conclusion with respect to the presence of deformation bands.

6.2 Sequential Gaussian Simulation

Sequential Gaussian Simulation (SGS) was used to produce maps of mechanical properties in the model with equal probability of occurrence; 10 realizations were created and all of them honored the input data. For example, Young's modulus average standard deviation for the upper reservoir is 0.864 GPa and the mean is 2.131 GPa. For the lower reservoir they are 0.735 GPa and 2.547 GPa, respectively. Similarly, Poisson's ratio average standard deviation for the upper reservoir is 0.043 and the mean is 0.232. For the lower reservoir they are 0.064 and

0.222, respectively. **Figure 6-6** shows two examples of SGS realizations for Young's modulus and Poisson's ratio.

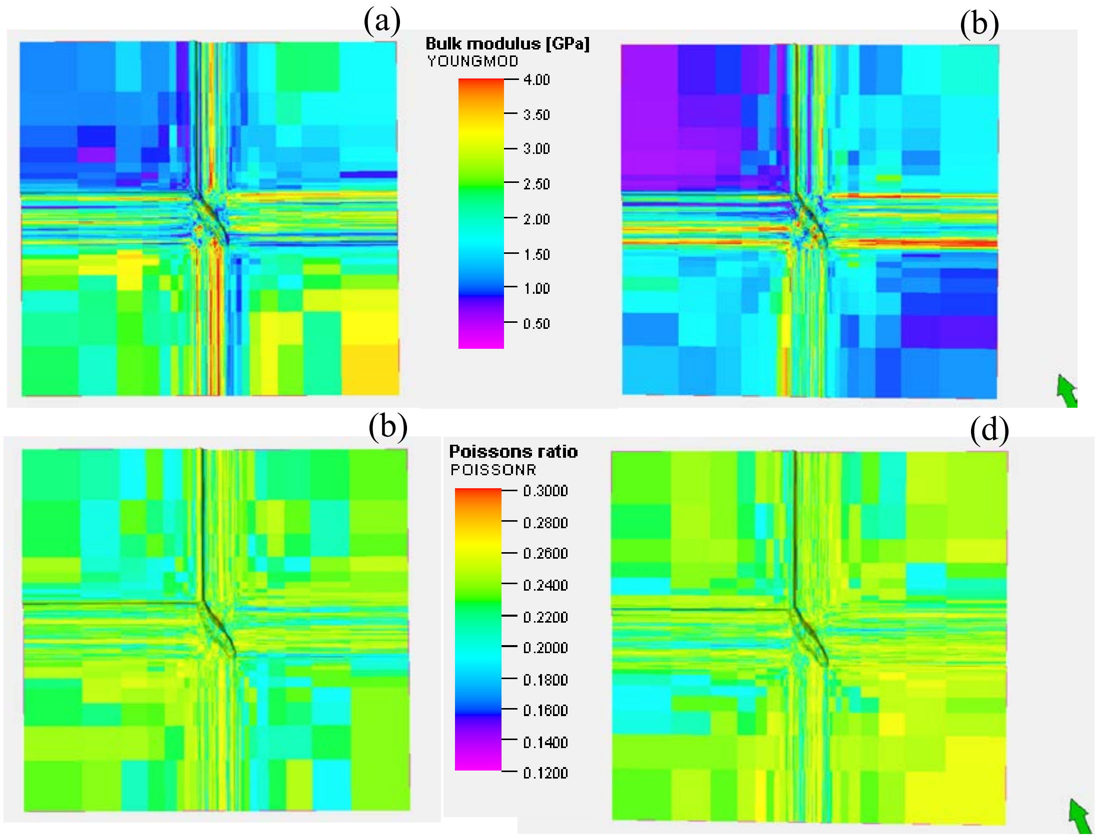

Figure 6-6 Two sequential Gaussian simulations realizations. (a) and (b) Young's modulus. (c) and (d) Poisson's ratio.

Preproduction initialization of these 10 models permits calculation of the initial stress state according to the mechanical properties and initial pore pressure in the reservoirs. The 3D stress state is used to verify the match between the predicted stresses and the input data. **Figure 6-7** shows the distribution of principal total stresses and pore pressures at initial conditions. The statistics for these distributions are summarized in **Table 6-1**. The mean values as determined in Chapter two were S_{hmin}=452.7 bar (45.7 MPa), S_{Hmax}=522.2 bar (52.2 MPa), S_v=534.6 bar (53.6 MPa) and Pp=358.5 bar (35.8 MPa). The difference between these values and the mean values calculated in the model is low in spite that these properties are determined applying stochastic methods.

Table 6-1 Statistics for distribution of minimum horizontal stress, maximum horizontal stress, vertical stress and pore pressure.

Statistic	S_{hmin} (bar)		S_{Hmax}		Sv		Pp	
Variable	Upper	Lower	Upper	Lower	Upper	Lower	Upper	Lower
Min (bar)	228.5	219.0	132.3	163.8	235.9	265.8	97.1	98.0
Max (bar)	534.3	549.9	651.8	636.3	858.5	899.5	524.6	540.5
Mean (bar)	419.0	445.6	444.6	503.8	540.6	585.5	402.8	407.3
St dev (bar)	46.3	45.46	107.8	84.78	46.7	51.5	147.4	110.7

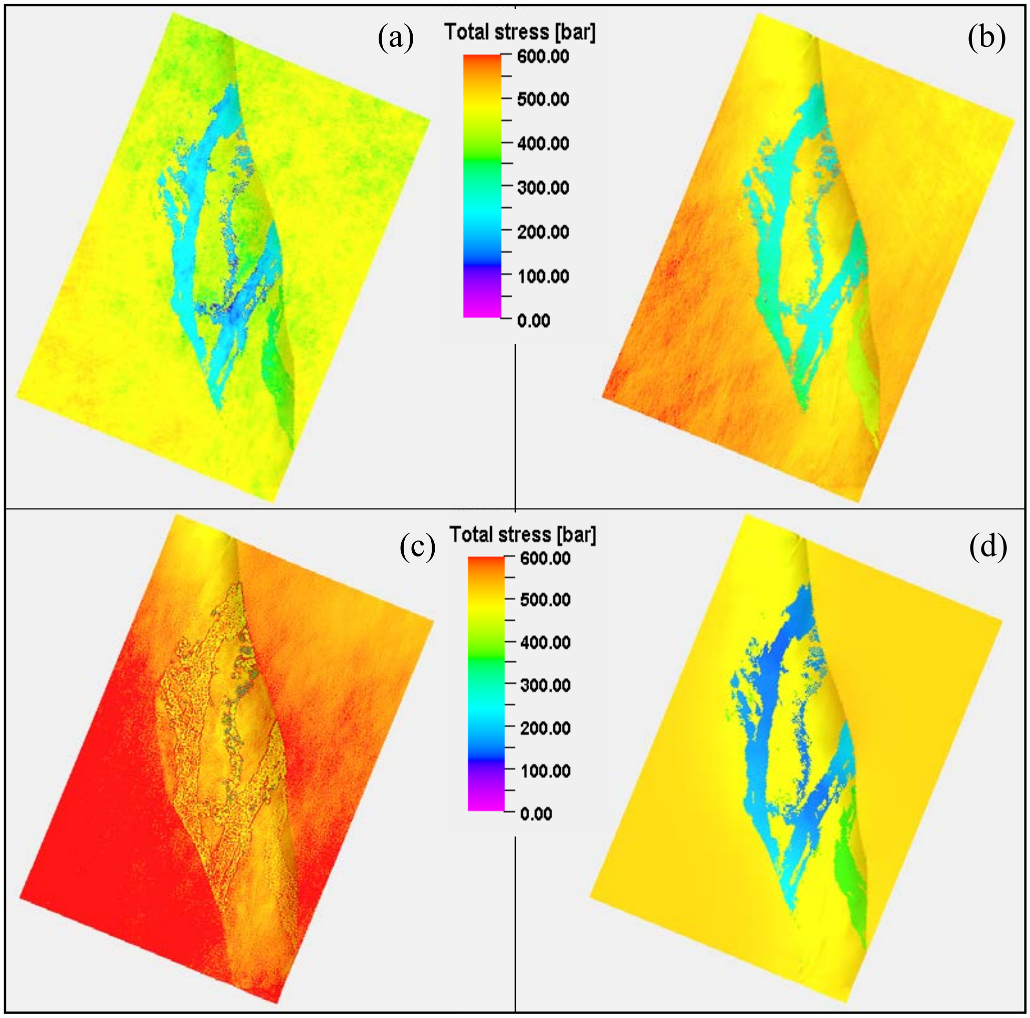

Figure 6-7 Principal stresses distribution at upper reservoir datum depth. (a) Minimum horizontal stress. (b) Maximum horizontal stress. (c) Vertical stress. (d) Pore pressure.

6.3 Subsidence and Reservoir Compaction

Coupling of the models is time-consuming because the stress solution takes more time than the flow solution when using the same grid and because the grid that considers solid problems is at least 3 times larger the fluid flow grid. This is the reason why the coupled models are prime candidates for high performance parallel computing.

As discussed previously in this thesis there are different ways to couple a reservoir model with a mechanical earth model. However, previous to coupling the models it is necessary to select the time steps at which the stress analysis will be performed in order to reduce the running time. The most convenient way to select the time steps is using the average of field pressure reservoir (FPR) forecast that results from the reservoir simulation model. This is used to identify times when there is significant change in the pressure slope. In **Figure 6-8** the field gas production rate (FGPR) and FPR are plotted against time. The FPR profile does not present strong variations. Therefore, just four stress steps were selected in order to optimize the running time. The vertical doted red lines in the graph indicate the time step at which the stresses should be calculated during the coupled analysis.

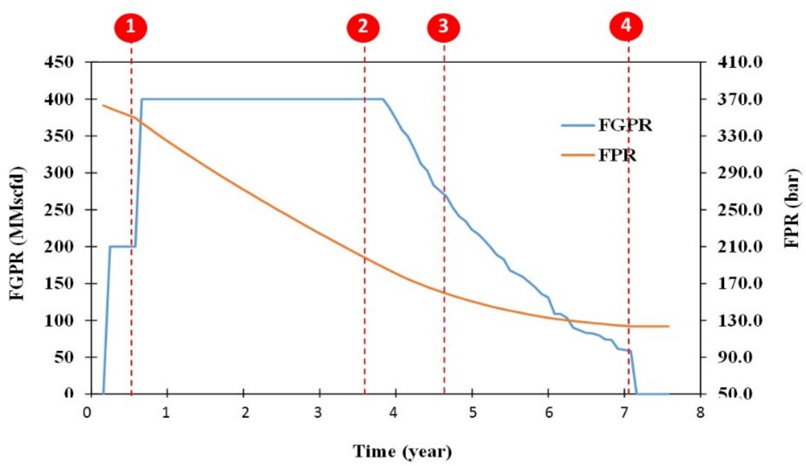

Figure 6-8. Time step selection to perform coupling modeling.

Although the one-way coupled method is simple and has limitations compared to other coupling methods, it is computationally efficient and accurate when reservoir compaction is small. This method is valuable and can be applied in gas reservoir with low error in predicting stress, strain and displacement (probably insignificant) since the rock compressibility is considerably much lower than the gas compressibility (Gonzalez, 2012).

The one-way coupled method is the simplest one and considers the average pressure at each time step for computing stress, strain and displacement. In this type of coupling method the fluid flow equations are solved in the reservoir model and the results (pressure, temperature and saturation) are passed on to the geomechanical simulator. However, no results are transferred from the geomechanical simulator to the reservoir simulator.

In order to determine subsidence and reservoir compaction, the 10 models mentioned previously were run using the one-way coupled method. Both, subsidence and upper reservoir compaction were measured at final conditions (last day after 7 years of production). Statistical results are summarized in **Table 6-2**.

Table 6-2 Univariate Statistics for subsidence and compaction

Statistic Variable	Subsidence	Compaction
Mean, (m)	-0.7413	-1.3691
Median (m)	-0.7337	-1.3413
Standard Deviation (m)	0.0730	0.2250
Variance (m^2)	0.0053	0.0506
Skewness	-1.207	0.258
Minimum (m)	-0.9084	-1.7084
Maximum (m)	-0.6396	-0.9774
Count	10	10

The univariate statistics mean for subsidence is equal to -0.7413 m and the median is -0.7337 m. These two values are similar and could indicate a small dispersion on the data. The standard deviation of 0.073 m indicates the dispersion of data. The coefficient of skewness is negative and relatively large (-1.2), which means a large tail of lower values to the left of the mean. This is observed in the histogram in **Figure 6-9a**.

The univariate statistics for upper reservoir compaction seems to present a left-skewed bimodal distribution as shown on **Figure 6-9b**. The mean is 1.37 m and the median is 1.34 m, the standard deviation is 0.22 m which represents a large dispersion.

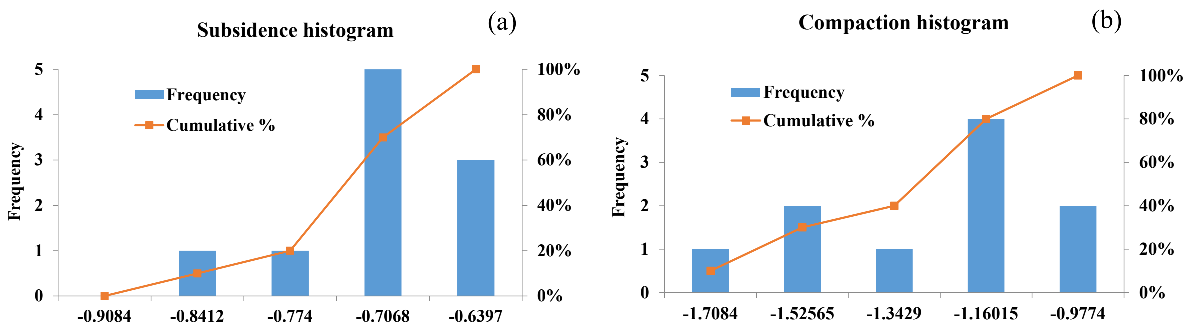

Figure 6-9 Univariate histogram using 10 realizations. (a) Subsidence. (b) Upper reservoir compaction.

As a result of pore pressure changes in the GML reservoirs, rock collapse in the central part of the reservoirs and significant vertical displacements are observed. The strongest depletion occurs during the first four years when pore pressure drops 180 bars. During this period subsidence occurs at ratio of approximately -0.003 m/bar. After the 4th year of production, the subsidence ratio change to -0.0035 m/bar. **Figure 6-10a** presents the vertical displacement distribution in the seabed at final conditions (when the reservoir reaches the economic limit). The dark blue color in the northern part of the field highlights the zone with the largest subsidence. **Figure 6-10b** shows a cross section in the j direction (AA') that displays vertical displacement and overburden at final conditions. The major reservoir compaction develops in the upper reservoir and is propagated to the neighboring layers in the overburden. It is attenuated by the overburden layer near the surface.

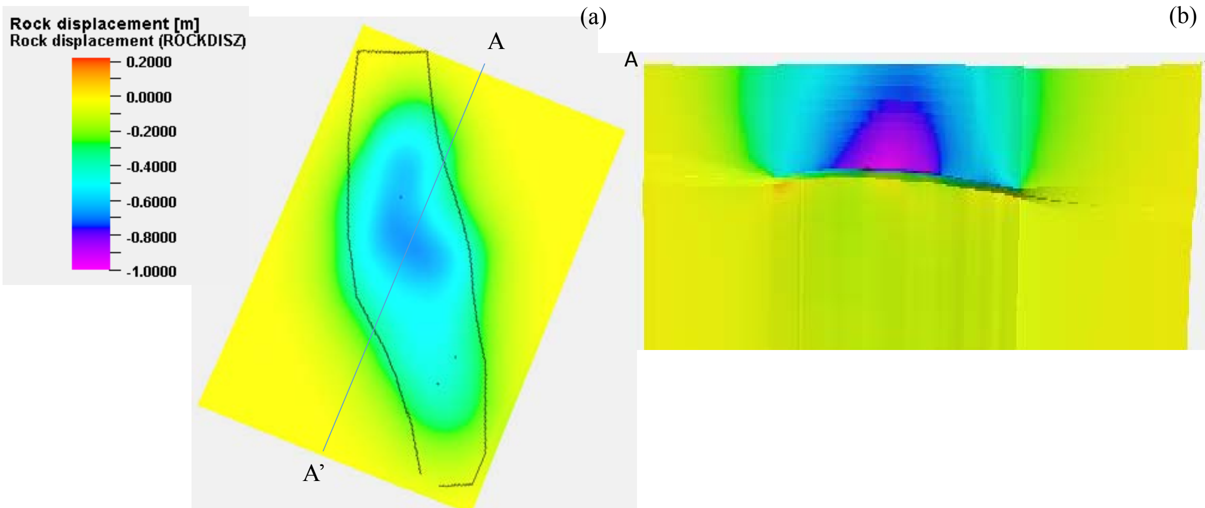

Figure 6-10 3D MEM rock displacement. (a) Seabed subsidence. (b) Reservoir and overburden compaction.

The upper reservoir compaction (80% of the cumulative gas production comes from this reservoir) is characterized by two linear relationships between the vertical displacement and the pore pressure during the production period. In chronological order, the first linear relationship occurs at a ratio of -0.0054 m/bar during the first four years of production when the pore pressure drops 180 bars. The second linear relationship occurs at a ratio of -0.0061 m/bar during the last 5 years of production when the pore pressure drops 83 bars. **Figure 6-11** shows a crossplot of vertical displacement against reservoir pressure. From the graph two correlations were developed for estimating the upper reservoir compaction (ΔC) and subsidence (U) as function of reservoir pressure.

$$U = 0.0031P_p - 1.1125 \qquad \textbf{Eq. 6-1}$$

$$\Delta C = 0.0055P_p - 2.0344 \qquad \textbf{Eq. 6-2}$$

Where Pp is pore pressure in bars, U is subsidence expressed in meters and ΔC is reservoir compaction also expressed in meters.

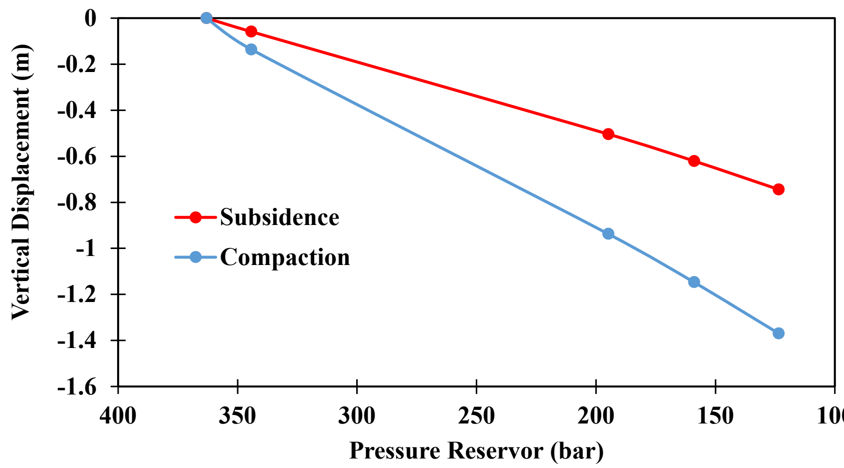

Figure 6-11 Verical displacement vs. reservoir pressure. Subsidence measured at seabed is shown in red. Compaction measured at the upper reservoir depth is shown in blue.

The analytical method proposed by Morita (1989) was applied to the field under study with a view to provide a comparison with the numerical geomechanical model. Morita's analytical model allows quick estimation of reservoir compaction and subsidence for reservoirs with simple geometries. The method is valuable when information is scarce as there is still a need to make decisions on downhole and surface facility designs. Compaction in the middle of the reservoir is estimated using **Eq. 6-3** and subsidence above the reservoir center is calculated with **Eq. 6-4**.

$$\Delta C = C_1 \frac{1 + v_r}{1 + v_r} k \beta h \Delta P_p \qquad \textbf{Eq. 6-3}$$

$$U = C_3[2(1 - v_c)]\left(1 - \frac{\frac{D}{r}}{\sqrt{1 + \left(\frac{D}{r}\right)}}\right)\Delta c \qquad \textbf{Eq. 6-4}$$

Where:

C_1, C_3: Coefficient function

V_r: Poisson's ratio for reservoir

V_c: Poisson's ratio for cap rock

k: Bulk modulus

β: 1-b_m/Ks

Ks: Rock bulk

β: Grain compressibility

h: Reservoir thickness

Pp: Pore pressure

D: Reservoir depth

r: Reservoir radius

Subsidence and upper reservoir compaction were calculated using data presented in Table 6-3. Coefficients C_1 and C_3 were estimated by interpolation from graphs presented by Morita (1989). These coefficients are functions of Log (G_r/G_c) where Gc is shear modulus for the cap rock and Gr is shear modulus for the reservoir.

Table 6-3 Data required for estimating subsidence and upper reservoir compaction

Parameter	Value	Units
ΔPp	3769.095	psi
Er	3.80E+05	psi
Vr	0.2	
Ec	2.20E+05	psi
Vc	0.3	
D	10453	ft
h	232.9396325	ft
r	11365.16278	ft
ϕ	0.2	fraction

Assuming that grain compressibility approaches to zero Eq. 6-3 yields:

$$\frac{b_m}{b} \sim 0$$

$$\beta = 1 - \frac{b_m}{b} = 1$$

$$\log \frac{G_r}{G_c} = \log \frac{E_r/\left(2(1+v_r)\right)}{E_c/\left(2(1+v_c)\right)} = 0.27$$

$$\Delta C = 0.95 \frac{1+0.17}{1-0.17} * 1.17E - 06 * 1 * 232 * 3769 * 0.3048 = 0.386\, m$$

And applying Eq. 6-4,

$$U = 0.8[2(1-0.3)]\left(1 - \frac{0.9197}{\sqrt{1+(0.9197)}}\right) 0.386 * .3048 = 0.218\, m$$

Average subsidence from the geomechanical model is -0.74 m and compares with 0.22 m from Morita’s analytical method. Average upper reservoir compaction from the geomechanical model is -1.37 m and compares with 0.39 m calculated from Morita’s method. The most reliable results are predicted using the 3D MEM because it considers rock heterogeneity and variations in the elastic moduli and stresses. Although there are differences Morita's method can be used as a first approximation if data for the MEM model are not available. The recommendation, however, is to always collect the necessary data for building reliable MEM models. In the field under study both the 3D MEM and Morita's analytical method indicate that compaction and subsidence will occur.

The production strategy for this field considers commingled exploitation of both reservoirs using 7 subsea wells in water depths ranging from 990 to 1200 m. The plan is to install deep water subsea tieback production facilities integrated by 2 flow lines from the field to the onshore terminal, two manifolds, and 7 subsea vertical trees. **Figure 6-12** shows a schematic illustrating the main parts of the subsea facilities. Due to the considerable vertical displacement observed in the 3D MEM, damage in the subsea facilities could be catastrophic if these phenomena are not taken into account.

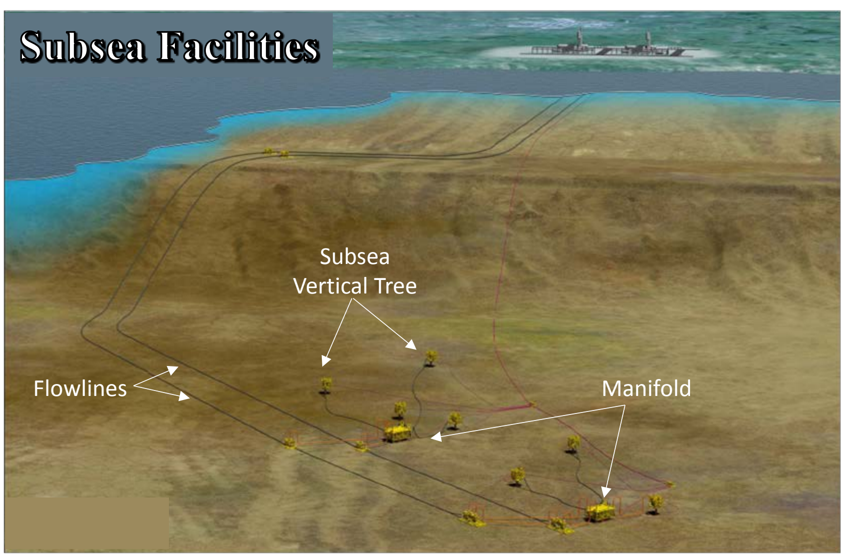

Figure 6-12 Schematic ilustrating the main parts of a deepwater subsea tieback production facilities.

It is concluded that understanding and quantification of these displacement processes can help to develop mitigation strategies to minimize and/or eliminate subsea risks. For example, Schwall and Denney (1994) presented the case of casing deformation in the Ekofisk field (Norway) as a result of subsidence and reservoir compaction. The consequences were axial tubing shifts with severity ranging from slight bends to plastic tubing shear and tubing collapse. The identification of the deformation mechanisms helped to develop techniques for minimizing casing loading. Another case was presented by Christensen et al. (1992) who evaluated the impact of horizontal movements related to subsidence of seabed on flowlines of the Ekofisk field. They emphasized that these movements produced alterations in the riser conditions that violated safety regulations; this led to the necessary equipment replacements.

As indicated above, operating companies should take into consideration the estimates of subsidence and reservoir compaction for designing facilities and for developing mitigation strategies that minimize or eliminate risks.

Chapter Seven: Conclusions and Recommendations

7.1 Conclusions

The integration of geomechanical parameters and relationships between deformation and stress in a 3D Mechanical Earth Model (MEM) for an offshore gas field with two stacked separate reservoirs in the Gulf of Mexico has been studied as function of changes in pore pressure and stresses. Based on this analysis, the following conclusions have been reached:

1. New correlations have been developed to correct dynamic moduli to static conditions in the offshore GML and GMK fields. Static and dynamic mechanical properties determined on core samples were used for this purpose. These correlations were used to assist in construction of a 3D MEM.
2. Average subsidence from the 3D MEM was determined to be -0.74 m. Average compaction of the upper reservoir was determined to be -1.37 m.
3. Damage of subsea facilities could be catastrophic if subsidence and compaction computed with the 3D MEM are not taken into account. Understanding of the displacement processes as presented in this thesis can help to develop mitigation strategies to minimize or eliminate risks that would damage subsurface installations.
4. The initial in-situ stress state analysis indicates that both the upper and lower reservoirs are fractured. Their stress regime is located in the transition between normal faulting and strike-slip faulting with a maximum horizontal stress orientation of 30 degrees.
5. Thin sections show that secondary porosity is due to partial dissolution and micro fractures in grains partially cemented.
6. Spatial distribution of properties in the embedded reservoir; sideburden, overburden and underburden were estimated using petrophysical parameters from the field under study

and neighboring fields. Geostatistical data analysis along with stochastic simulation methods helped to generate reservoir models that honored all well data and assisted in the uncertainty evaluation of the constructed maps.

7.2 Recommendations

1. Seismic data provides a dense sampling of the reservoir and together with petrophysical properties and geostatistical techniques reduce the uncertainty in the distribution of rock properties. Although the spatial distribution of properties in the reservoir models was performed using seismic data, this was not the case for the MEM. Thus it recommended collecting and interpreting seismic data for the whole MEM area.
2. As layers in the reservoir simulator are thin it is recommended to create a model that coarsens up the sideburden and underburden gradually away from the reservoir.
3. Results presented in this work were developed using the one-way coupling method. However, implementation of the two-way coupling method is recommended to handle possible changes in porosity and permeability once the reservoir goes on production. This approach will also provide a more rigorous production forecast.
4. Evaluate plastic deformation in order to stablish a relationship between deformation and stresses and to analyze cap integrity.
5. Update the 3D MEM with data of new wells drilled during development of the field. Uncertainty with respect to the future of the field will decrease as more wells are integrated in the 3D MEM.

6. The mechanical property modeling has been carried out using available information but the data bank is not considered to be complete enough for a more rigorous study. Once new wells are drilled and more information is collected the model should be updated.

References

Aguilera, R. (2003, February). Geologic and engineering aspects of naturally fractured reservoirs. *CSEG Recorder*. Calgary, Canada. Retrieved from http://209.91.124.56/publications/recorder/2003/02feb/feb03-fractured-reservoirs.pdf

Alam, M. M. & Fabricius, I. L. (2012, January). Effective stress coefficient for uniaxial strain condition. *American Rock Mechanics Association*. Retrieved from https://www-onepetro-org.ezproxy.lib.ucalgary.ca/download/conference-paper/ARMA-2012-302?id=conference-paper%2FARMA-2012-302

Barree, R. D., Gilbert, J. V., & Conway, M. (2009, January). Stress and rock property profiling for unconventional reservoir stimulation. *Society of Petroleum Engineers*. doi:10.2118/118703-MS

Banik, N., Koesoemadinata, A., & El-Kaseeh, K. G. (2010). Young's modulus from point-receiver surface seismic data. *SEG Technical Program Expanded*. 5(3), 2794–2798. doi:10.1190/1.3513424

Barton, C. A., Zoback M. D., & Burns, K. L. (1988, May). In-situ stress orientation and magnitude at the Fenton geothermal site, New Mexico, determined from wellbore breakouts. *Geophysical Research Letters*. 15(5), 467-470. doi: 10.1029/GL015i005p00467

Biot, M. A. (1941, February). General theory of three-dimensional consolidation. *Journal of Applied Physics*, 12(2), 155-164. Retrieved from http://www.pmi.ou.edu/Biot2005/papers/FILES/040.PDF

Biot, M. A., & Willis, D. G. (1957, December). The elastic coefficients of the theory of consolidation. *Journal of Applied Mechanics*. 594-301. Retrieved from http://www.pmi.ou.edu/Biot2005/papers/FILES/068.PDF

Brace, W. F., & Byerlee, J. D. (1966). *Recent experimental studies of brittle fracture of rocks*. Dept. of Geology and Geophysics, Cambridge. Mass.

Brooks, R. H., & Corey A. T. (1964). Hydraulic properties of porous media. *Hydrology Papers*. Colorado State University. Retrieved from http://digitool.library.colostate.edu///exlibris/dtl/d3_1/apache_media/L2V4bGlicmlzL2R0bC9kM18xL2FwYWNoZV9tZWRpYS8xNTIyNTc=.pdf

Canady, W. J. (2011, January). A Method for full-range Young's modulus correction. *Society of Petroleum Engineers*. doi:10.2118/143604-MS

Chang, Ch., Zoback, M.D. and Khaksar, A. (2005). Empirical relations between rock strength and physical properties in sedimentary rocks. *Journal of Petroleum Science and Engineering*, 51(3-4), 223-237. doi: 10.1016/j.petrol.2006.01.003

Chang, Ch., Zoback, M.D. (1998, January). Viscous Rheology and State of Stress in Unconsolidated Sands. Society of Petroleum Engineers. doi:10.2118/47401-MS

Cheng, C. H., & Johnston, D. H. (1981, January). Dynamic and static moduli. *Geophysical Research Letters*, 8(1), 39–42. doi: 10.1029/GL008i001p00039

Close, D., Cho, D., Horn, F., & Edmundson, H. (2009). The sound of sonic: A historical perspective and introduction to acoustic logging. *CSEG Recorder*, pp 34-43. Retrieved from http://209.91.124.56/publications/recorder/2009/05may/May2009-Sound-of-Sonic.pdf

Davis, R. O., & Selvadurai, A. P. S. (2005). *Plasticity and Geomechanics*. United Kingdom: Cambridge University Press. Retrieved from https://app.knovel.com/web/toc.v/cid:kpPG000011

Detournay, E. & Cheng, A. H. D. (1993). Fundamentals of poroelasticity. *Comprehensive rock engineering,* 2, 138-139. Ed. J. A. Hudson, (Pergamon Press). doi: 10.1016/0148-9062(94)90606-8

Eissa, E. A., & Kazi, A. (1988, December). Relation between static and dynamic Young's moduli of rocks. *International Journal of Rock Mechanics and Mining Sciences & Geomechanics Abstracts*, 25(6), 479–482. doi:10.1016/0148-9062(88)90987-4

FHWA. (2007). Long term pavement performance project laboratory materials testing and handling guide. Retrieved from http://www.fhwa.dot.gov/publications/research/infrastructure/pavements/ltpp/07052/pro46/004.cfm.

Fjaer, E. (1999, January). Static and dynamic moduli of week sandstones. American *Rock Mechanics Association*. Retrieved from https://www-onepetro-org.ezproxy.lib.ucalgary.ca/conference-paper/ARMA-99-0675

Fjaer, E., Holt, R. M., Horsrud, P., Raaen, A. M., & Risnes, R. (2008). *Petroleum related rock mechanics* (2nd Ed.). Amsterdam: Elsevier. Retrieved from http://app.knovel.com/hotlink/toc/id:kpPRRME001/petroleum-related-rock/petroleum-related-rock

Fossen, H., Schultz, R. A., Shipton, Z. K., & Mair, K. (2007). Deformation bands in sandstone: a review. *Journal of the Geological Society*, *164*, 755-769. doi: 10.1144/0016-76492006-036

Jaeger, J. C., Cook, N. G. W., & Zimmerman, R. W. (2007). *Fundamentals of Rock Mechanics* (4th ed.). Malden, MA: Blackwell Publishing.

Hirsche, K. & Hirsche, J. (2001). The use and abuse of Geostatistics. *Western Geophysical*. Calgary, Canada. Retrieved from http://Library.seg.org.

Isaak, E. H., & Srivastava R. M. (1989). *An introduction to applied geostatistics*. New York, USA: Oxford University Press.

Gonzalez, L. (2012). Numerical 3D modeling of multistage hydraulic fractures and two-way coupling geomechanics-fluid flow simulation of a horizontal well in the Nikanassin tight gas formation. MSc Thesis, Chemical and Petroleum Engineering Department, *University of Calgary*, Canada.

Kantzas, A., Bryan, J., & Taheri, S. (2012). *Fundamental of fluid flow in porous media*. University of Calgary, Canada.

Kwon, O., Kronenberg, A. K., Gangi. A., & Johnson, B. (2001, September). Permeability of Wilcox shale and its effective pressure law. *Journal of Geophysics Research.* 106(B9), 19339-19353. doi: 10.1029/2001JB000273

Li, D., Wong, L. N. Y., Liu, G., & Zhang, X. (2012). Influence of water content and anisotropy on the strength and deformability of low porosity meta-sedimentary rocks under triaxial compression. *Engineering Geology*, 126, 46–66. doi: 10.1016/j.enggeo.2011.12.009.

Lopez, B., Yu, G., Aguilera, R., & Settari, A. (2014, February). Calibration of well logs with mini-frac data for estimating the minimum horizontal stress in the tight gas Monteith Formation on the western Canada sedimentary basin: A case of Study. *Society of Petroleum Engineers.* doi:10.2118/168594-MS

Montmayeur, H. & Graves, R. M. (1985, January). Prediction of static elastic/mechanical properties of consolidated and unconsolidated sands from acoustic measurements: Basic measurements. *Society of Petroleum Engineers*. doi:10.2118/14159-MS

Morales, R. H., & Marcinew, R. P. (1993, October). Fracturing of high-permeability formations: Mechanical properties correlations. *Society of Petroleum Engineers*. doi:10.2118/26561-MS

Morita, N., Whitfill, D. L., Nygaard, O., & Bale, A. (1989, January). A Quick Method to Determine Subsidence, Reservoir Compaction and In-Situ Stress Induced by Reservoir Depletion. *Journal of Petroleum Technology*. doi:10.2118/17150-PA

Mullen, M., Roundtree, R., & Barree, B. (2007, January). A composite determination of mechanical rock properties for stimulation design (What to do when you don't have a sonic log). *Society of Petroleum Engineers*. doi:10.2118/108139-MS

Normal Score. (n.d.). Retrieved from https://www.statsdirect.com/help/data_preparation/normal_scores.htm

Ojala, I. O., & Fjær, E. (2007, January). The effective stress coefficient in porous sandstone. American Rock Mechanics Association. Retrieved from https://www-onepetro-org.ezproxy.lib.ucalgary.ca/download/conference-paper/ARMA-07-101?id=conference-paper%2FARMA-07-101

Perkins T. K., & Weingarten J. S. (1988, January). Stability and Failure of Spherical Cavities in Unconsolidated Sand and Weakly Consolidated Rock. *Society of Petroleum Engineers*. doi: 10.2118/18244-MS

Pittman, E. D. (1992). Relationship of porosity and permeability to various parameters derived from mercury injection-capillary pressure curves for sandstone. *The American Association of Petroleum Geologists*. 76(2) 191-198. Retrieved from http://archives.datapages.com.ezproxy.lib.ucalgary.ca/data/bulletns/1992-93/images/pg/00760002/0000/01910.pdf

Plumb, R. A. (1994). Influence of composition and texture on the failure properties of clastic rocks. *Proceedings of Rock Mechanics in Society of Petroleum Engineers*. doi: 10.2118/28022-MS.

Qiao, L. P., Wong, R. C. K., Aguilera, R., & Kantzas, A. (2009, January). Determination of Biot's effective-stress coefficient for permeability of Nikanassin sandstone, *Petroleum Society of Canada.* doi: 10.2118/2009-105

Qiu, K., Marsden, J. R., Solovyov, Y., Safdar, M., Chardac, O., & Agoco, M. S. (2005). Downscaling geomechanics data for thin-beds using petrophysical techniques. *Society of Petroleum Engineers*. doi: 10.2118/93605-MS

Rider, M. & Kennedy, M. (2011). *The geological interpretation of well logs* (3rd Ed.). Scotland: Rider-French Consulting Ltd.

Rodriguez, H. I. (2011, January). Numerical Reservoir Simulation Coupled with Geomechanics State of the Art and Application in Reservoir Characterization, *Society of Petroleum Engineers.* doi: 10.2118/152364-STU

Schlumberger Information Solutions. (2011*). Advanced reservoir geomechanics with visage: workflow/solutions training.*

Serra, A. L., Braz, J. A., Bechara, M. G., Palma, N. V., & Passos, C. R. (2012, January). Reservoir geomechanics study for deepwater field identifies ways to maximize reservoir performance while reducing geomechanics risks. *Society of Petroleum Engineers*. doi: 10.2118/160329-MS

Settari, A., Walters, D., & Behie, G. (2000). Use of Coupled Reservoir and Geomechanical Modelling for Integrated Reservoir Analysis and Management. *Proceedings of Canadian International Petroleum Conference.* doi: 10.2118/2000-078.

Settari, A., & Maurits, F. M. (1998, September). A Coupled Reservoir and Geomechanical Simulation System. *Society of Petroleum Engineers.* doi: 10.2118/50939-PA

Settari, A. T., & Walters, D. W. (1999). Reservoir Geomechanics: New approach to reservoir engineering analysis and a powerful tool for reservoir management Field Examples, 206–208. *Petroleum Society of Canada*. Retrieved from http://dx.doi.org.ezproxy.lib.ucalgary.ca/10.2118/99-116

Settari, A. T., & Sen, V. (2008, January). Geomechanics in Integrated Reservoir Modeling. Offshore Technology Conference, doi: 10.4043/19530-MS

Shchipanov, A. A., Kolboth, L., & Surguchev, L. M. (2010, January). A new approach to deformable fractured reservoir characterization: Case study of the Ekofish field. *Society of Petroleum Engineers.* doi: 10.2118/130425-MS

Schwall, G. H., & Denney C. A. (1994, January). Subsidence induced casing deformation mechanisms in the Ekofisk field. *Society of Petroleum Engineers.* doi: 10.2118/28091-MS

Siggins, A. F., Dewhurst, D. N., Dodds, K., (2004, January). Effective stress and the Biot-Willis coefficient for reservoir sandstones. *Society of Exploration Geophysicists*. Retrieved from https://www-onepetro-org.ezproxy.lib.ucalgary.ca/conference-paper/SEG-2004-1770

Soong, T. T. (2004). *Fundamentals of probability and statistics for engineers*. New York, Buffalo: John Wiley & Sons.

Spencer, J., Jr., Cates, M., and Thompson, D. (1994). Frame moduli of unconsolidated sands and sandstones. *Geophysics*, 59(9), 1352–1361. doi: 10.1190/1.1443694.

Terzaghi, K., & Beck R. B. (1949). *Soil mechanics in engineering practice*. John Wiley and Sons. New York.

Tran, D., Settari, A., & Nghiem, L. (2002, January). New iterative coupling between a reservoir simulator and a geomechanics module. *Society of Petroleum Engineers.* doi: 10.2118/78192-MS

Trudeng, T., Garcia-Teijeiro, X., Rodriguez-Herrera, A., & Khazanehdari, J. (2014, January). Using stochastic seismic inversion as input for 3D geomechanical models. *International Petroleum Technology Conference*. doi: 10.2523/17547-MS.

Tziallas, G. P., Saroglou, H., & Tsiambaos, G. (2013). Determination of mechanical properties of flysch using laboratory methods. *Engineering Geology*, 166, 81–89. doi: 10.1016/j.enggeo.2013.09.002.

Veeken, C. A. M., Walters, J. W., Kenter, C. J., & Davies, D. R. (1989, January). Use of plasticity models for predicting borehole stability. *International Society for Rock Mechanics*. Retrieved from https://www-onepetro-org.ezproxy.lib.ucalgary.ca/download/conference-paper/ISRM-IS-1989-106?id=conference-paper%2FISRM-IS-1989-106.

Vernik, L., Bruno, M., & Bovberg, C. (1993). Empirical relations between compressive strength and porosity of siliciclastic rocks. *International Journal of Rock Mechanics and Mining Sciences & Geomechanics Abstracts*, 30(7), 677–680. doi: 10.1016/0148-9062(93)90004-W.

Vincke, O., Longuemare, P., Bouteca, M., & Deflandre, J. P. (1998). Investigation of the poromechanical behaviour of shales in the elastic domain. Proceedings of SPE/ISRM Rock Mechanics in Petroleum Engineering. doi: 10.2118/47589-MS.

Wang, Z. N. (2000). *Seismic and acoustic velocities in reservoir rocks: Recent developments*. vol. 3: Tulsa: Society of Exploration Geophysicists.

White, J. E. (1991). Underground sound: Appled seismic waves: Amstedam: Elseiver.

Wood, D., & Shaw, N. (2012, May). The correlation of unconfined compressive strength with dry density and grainsize for different aged sedimentary rock. *International Society for Rock Mechanics*. Retrieved from https://www-onepetro-org.ezproxy.lib.ucalgary.ca/conference-paper/ISRM-EUROCK-2012-111

Wu, R. S. (1994). Wide-angle elastic waves one-way propagation in heterogeneous media an elastic wave complex-screen method. *Journal of Geophysical Research*, 99(B1), 751-766. Retrieved from http://webapps2.ucalgary.ca/~lcrtest/search/index.php?q=Wide-angle+elastic+waves+one-way+propagation

Yale, D. P., & Jamieson, W. H. (1994). Static and dynamic mechanical properties of carbonates. *American Rock Mechanics Association*. Retrieved from https://www-onepetro-org.ezproxy.lib.ucalgary.ca/conference-paper/ARMA-1994-0463

Zhang, Y. G., Wang, X. J., Zhang, Z. X., Fan, K. M., & Yu, Y. M. (2010, January). Predicting inter-well rock mechanics parameters using geophysical logs and 3-D seismic data. American Rock Mechanics Association. Retrieved from https://www-onepetro-org.ezproxy.lib.ucalgary.ca/conference-paper/ARMA-07-016

Zoback, M. D. (2006). *Reservoir Geomechanics*: Earth stress and rock mechanics applied to exploration, production and wellbore stability. Standford: Cambridge University Press.

Appendix A: Geostatistical Data Analysis

A.1 Data Analysis Models

Geostatistical characterization techniques help to relate petrophysical properties measured at the wells and describe their spatial continuity. These techniques provide estimations of properties where sample data are not available and help predicting uncertainties associated with those estimations.

Isaaks and Srivastava (1989) indicated that geostatistical data analysis is based on the fact that a semivariogram can describe the spatial structure of a variable. A semivariogram is defined as half the average square distance between a pair of data values separated by a distance h. This is expressed by **Eq. A-1** .

$$\gamma(h) = \frac{1}{2N(h)} \sum_{i=1}^{N(h)} [z(x_i - h) - z(xi)]^2 \qquad \textbf{Eq. A-1}$$

Where N(h) represents the number of pairs separated by a distance h, also called lag.

Isaaks and Srivastava (1989) also presented some useful concepts related to semivariograms that can be describes as follows:

Nugget: It is used to introduce a discontinuity at the origin of a semivariogram model. Explanations for this discontinuity comprise sampling short scale variability and error.

Sill: Maximum semivariance value observed in the spatial structure for a variable.

Range: The distance at which the data are no longer correlated.

The necessity of a semivariogram model resides in the fact that a semivariogram value for a specific distance or orientation cannot be available in the sample semivariogram values.

There are two types of variograms, those that never reach a sill and those that do. The models that reach a sill are basically spherical, exponential and/or Gaussian models. Occasionally it is necessary to combine these models to have a representation for the experimental semivariogram sample.

The **spherical model** is very common and is expressed by **Eq. A-2**:

$$\gamma(h) = 1.5\frac{h}{a} - 0.5\left(\frac{h}{a}\right)^3 \qquad \textbf{Eq. A-2}$$

The **exponential model** is another common method. It is represented by **Eq. A-3**:

$$\gamma(h) = 1 - \exp\left(-\frac{3h}{a}\right) \qquad \textbf{Eq. A-3}$$

The **Gaussian model** is used particularly to handle continuous phenomena. Its standardized expression is given by **Eq. A-4**:

$$\gamma(h) = 1 - \exp\left(-\frac{3h^2}{a^2}\right) \qquad \textbf{Eq. A-4}$$

Where a is the range

A.2 Distribution of Properties

The estimation of petrophysical properties in a 3D MEM model is developed by applying the following three steps: (1) Scale-up the well logs in the cell crossed by the well trajectory. (2) Determine semivariogram models in the vertical direction and in the major and minor directions. (3) Estimate petrophysical properties in the models using the semivariograms and the stochastic Sequential Gaussian Simulation. This process was applied for estimating properties in the sideburden and overburden. The following figures summarize the results by property and zone.

A.2.1 Young's modulus

Zone 2 (Upper Pliocene)

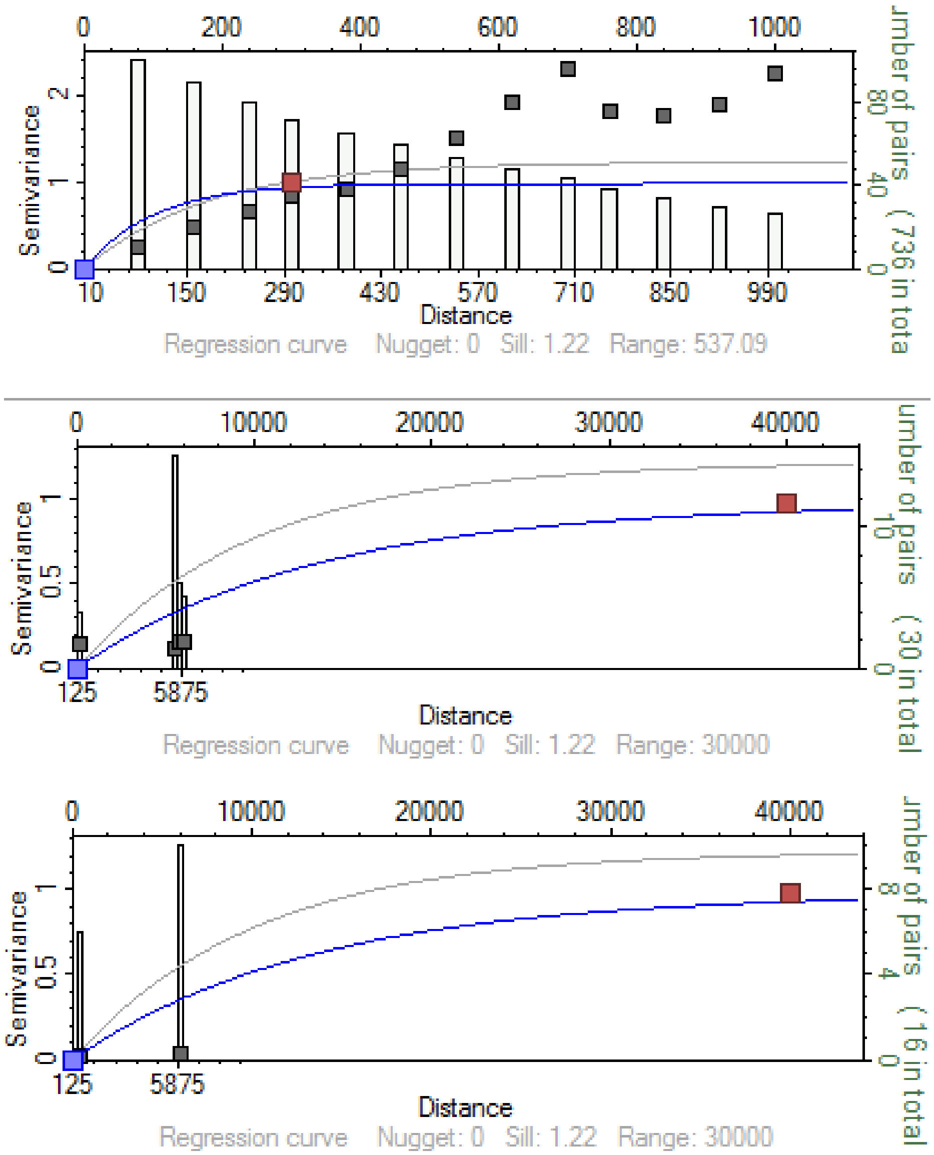

Figure A-1 Black squares represent the experimental data, the black line the regression variogram and the blue line the variogram model. (Upper variogram in vertical direction, middle variogram in major direction and lower variogram in minor direction).

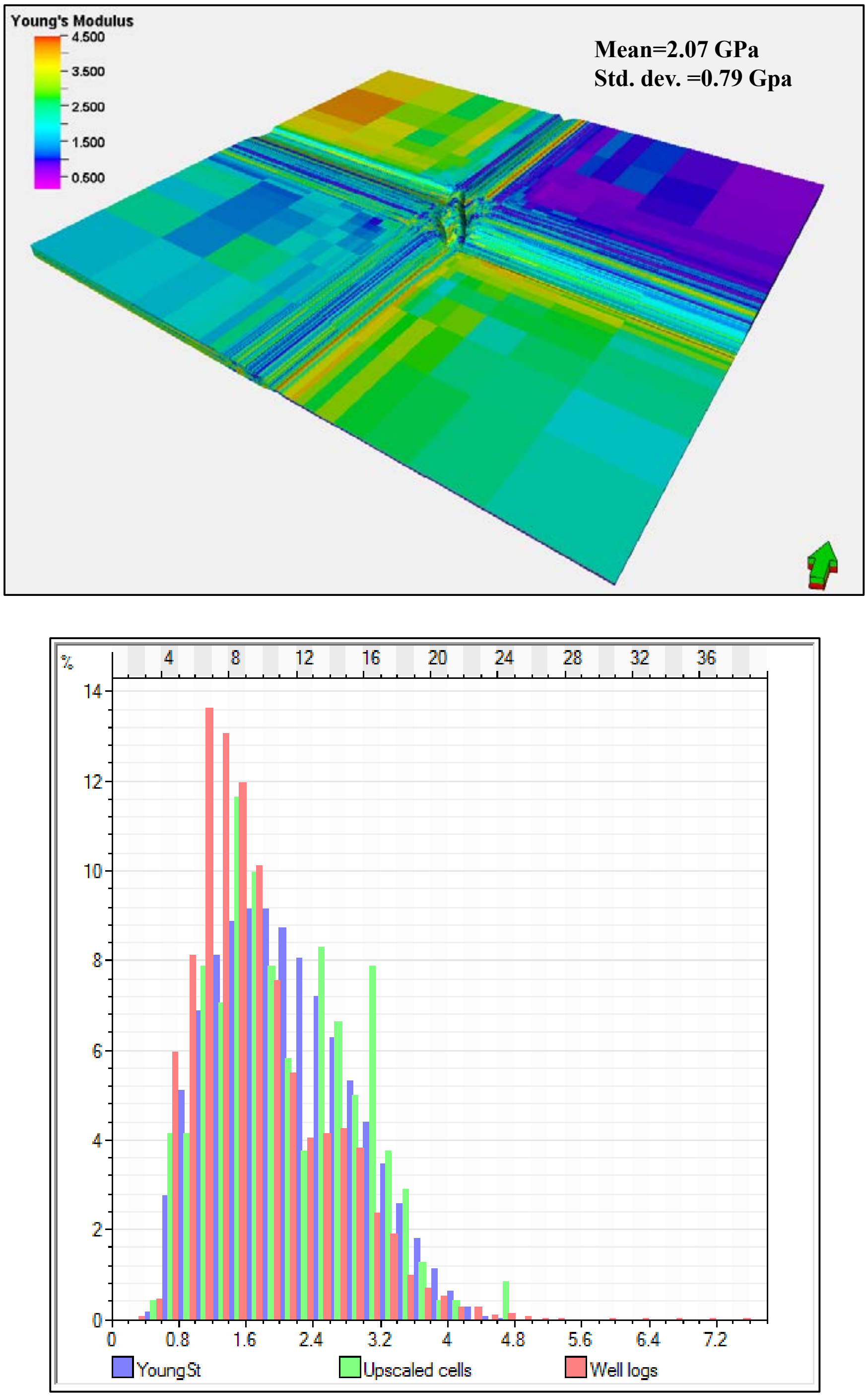

Figure A-2 3D MEM property distribution. (Top graph) Property distribution in the model. (Bottom) Histogram showing a comparison between results from well logs used for upscaling, the upscaled well log in the cell crossed by the well and the cells in the model.

Zone 3 (MI-2)

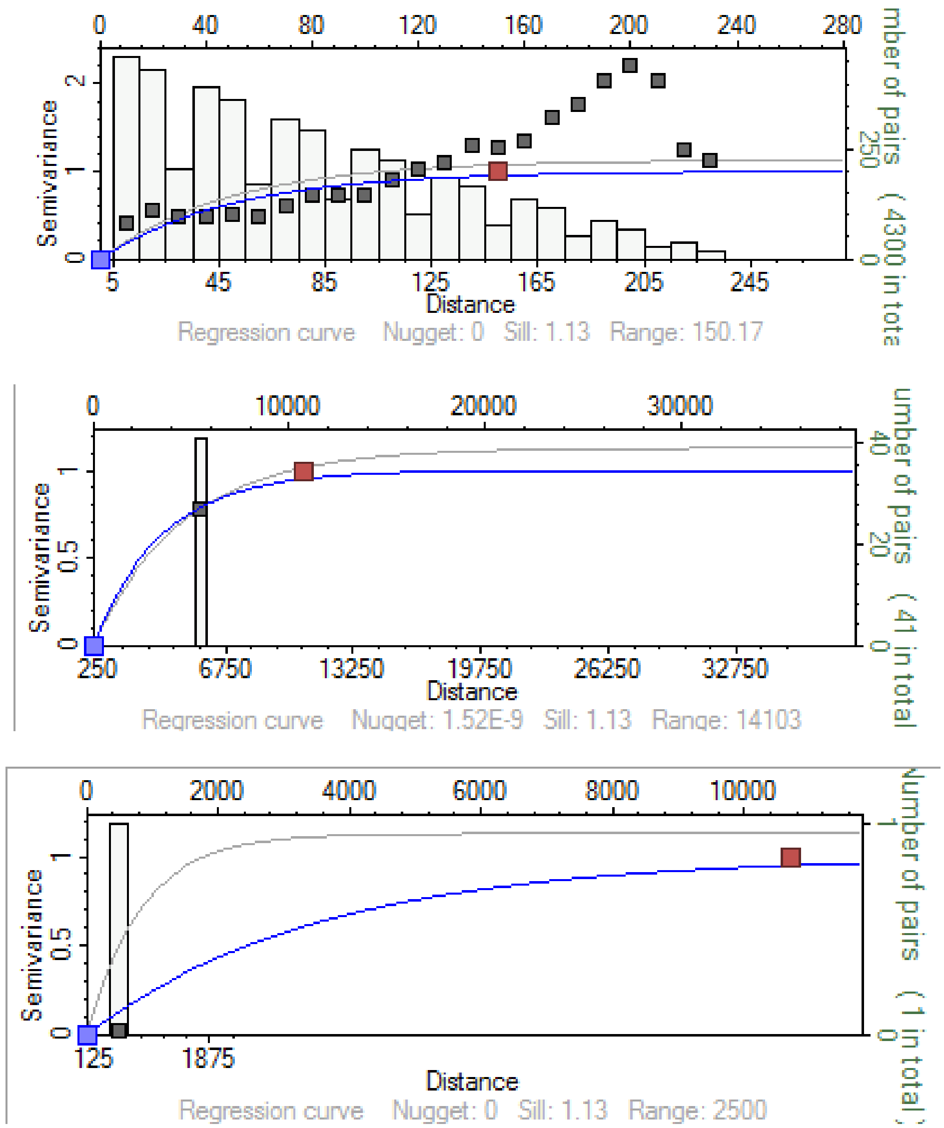

Figure A-3 Black squares represent experimental data, the black line is the regression variogram and the blue line the variogram model. (Upper variogram in vertical direction middle variogram in major direction and lower variogram in minor direction).

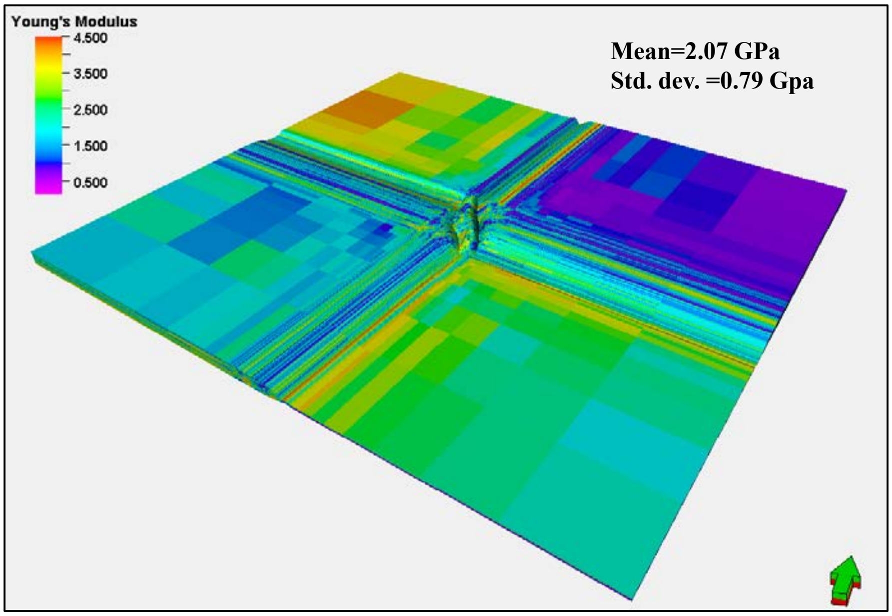

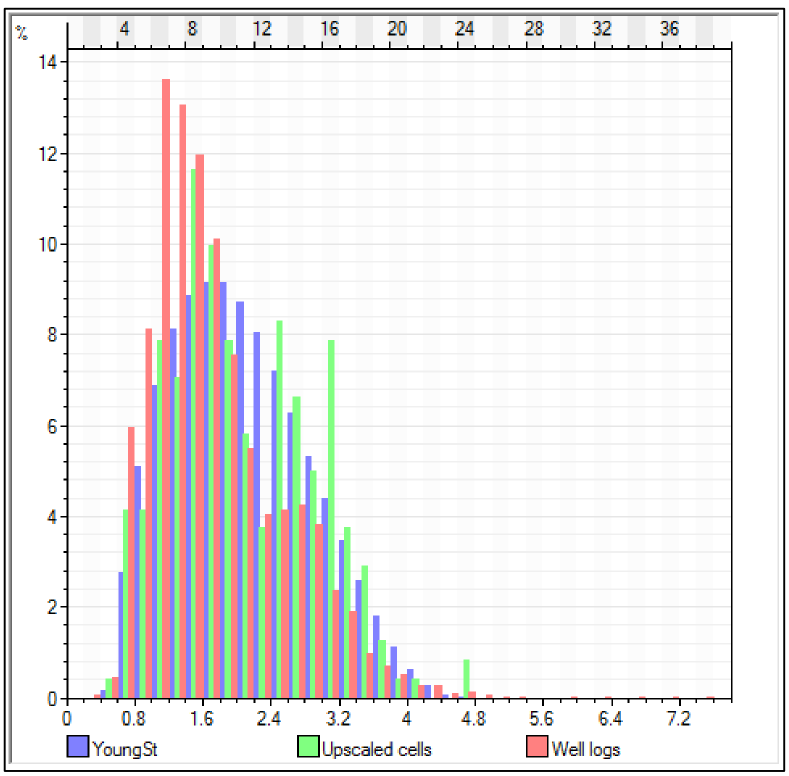

Figure A-4 3D MEM property distribution. (Top graph) Property distribution in the model. (Bottom) Histogram showing comparison between the well log used for upscaling, the upscaled well log in the cell crossed by the well and the cells in the model.

Zone 5 (MI-1)

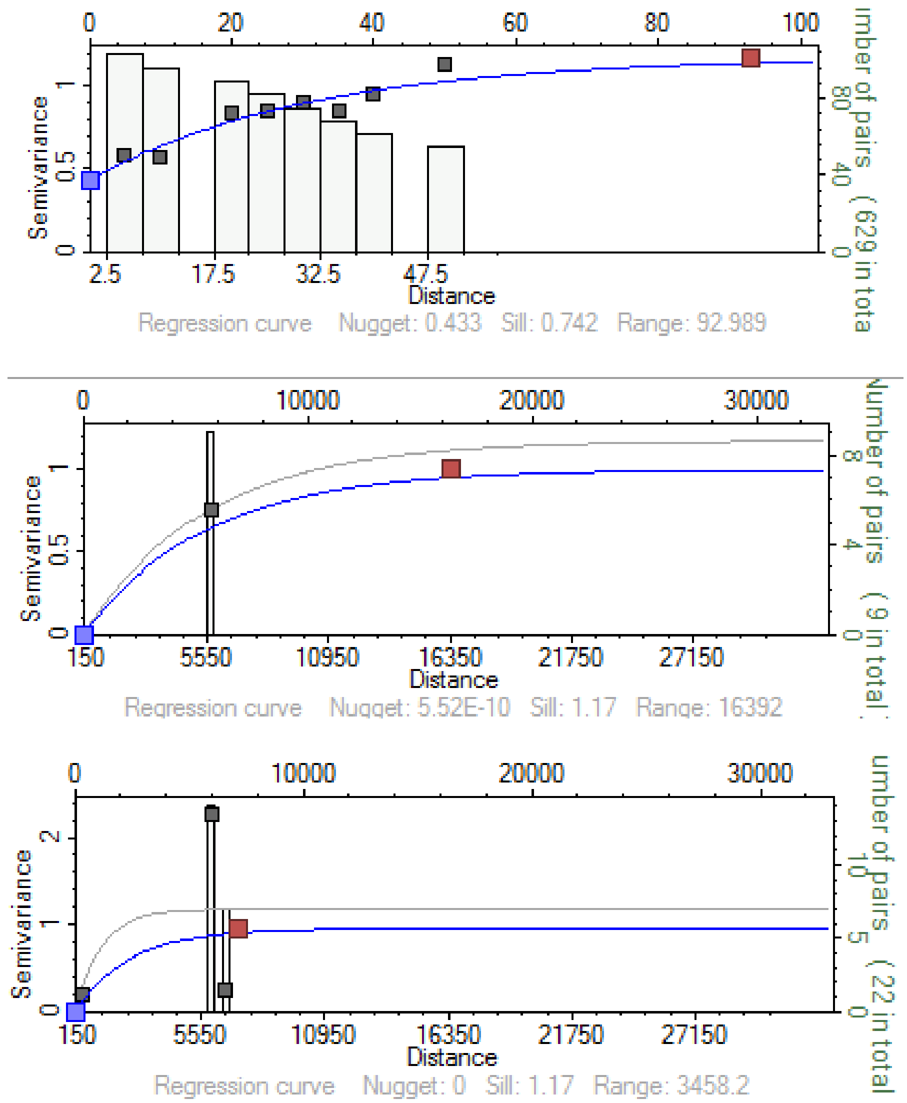

Figure A-5 Black squares represent the experimental data, the black line is the regression variogram and the blue line the variogram model. (Upper variogram in vertical direction, middle variogram in major direction and lower variogram in minor direction).

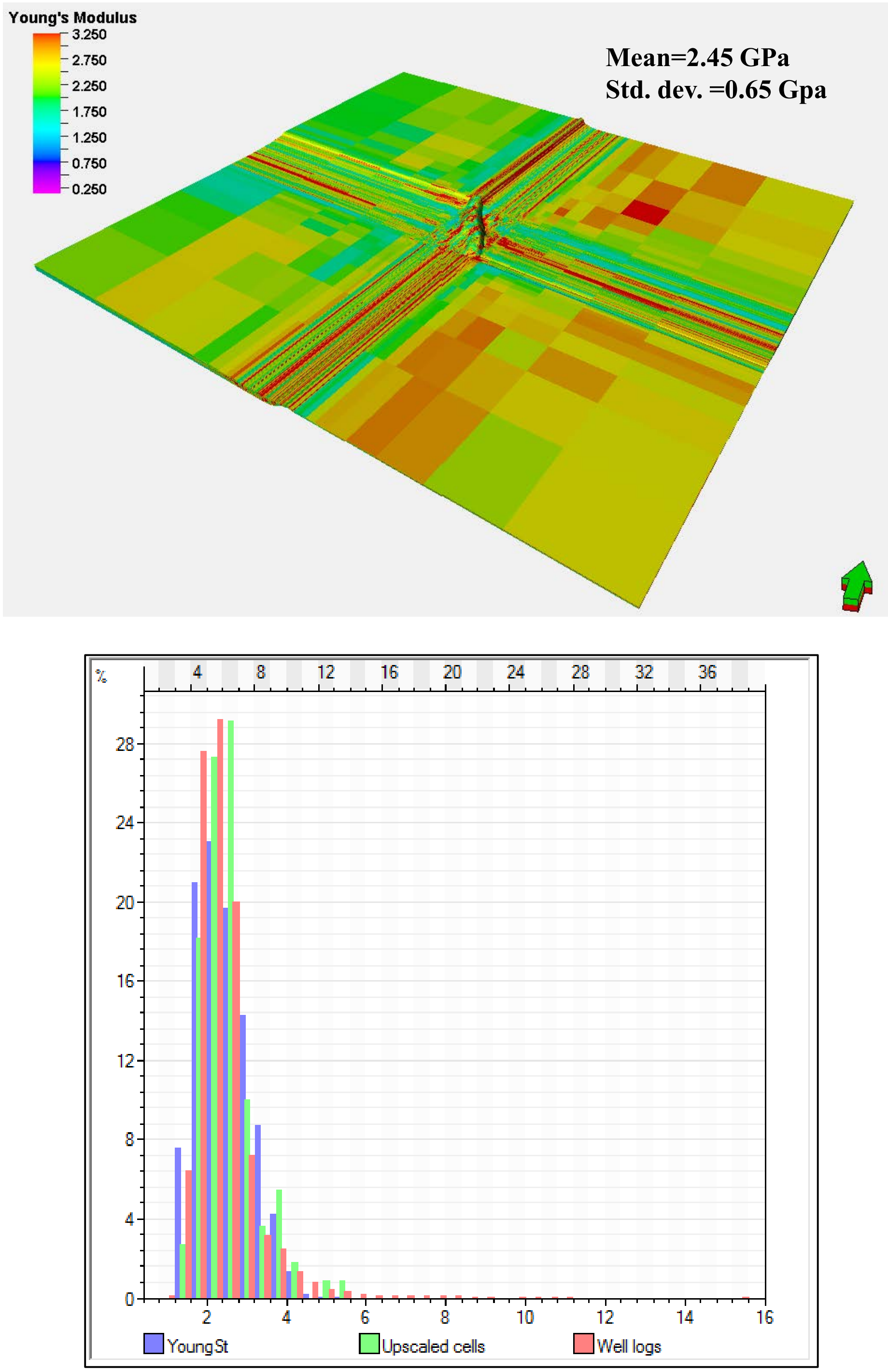

Figure A-6 MEM property distribution. (Top graph) Property distribution in the model. (Bottom) Histogram showing a comparison between the well log used for upscaling, the upscaled well log in the cell crossed by the well and the cells in the model.

A.2.2 Poisson's ratio

Zone 2 (Upper Pliocene)

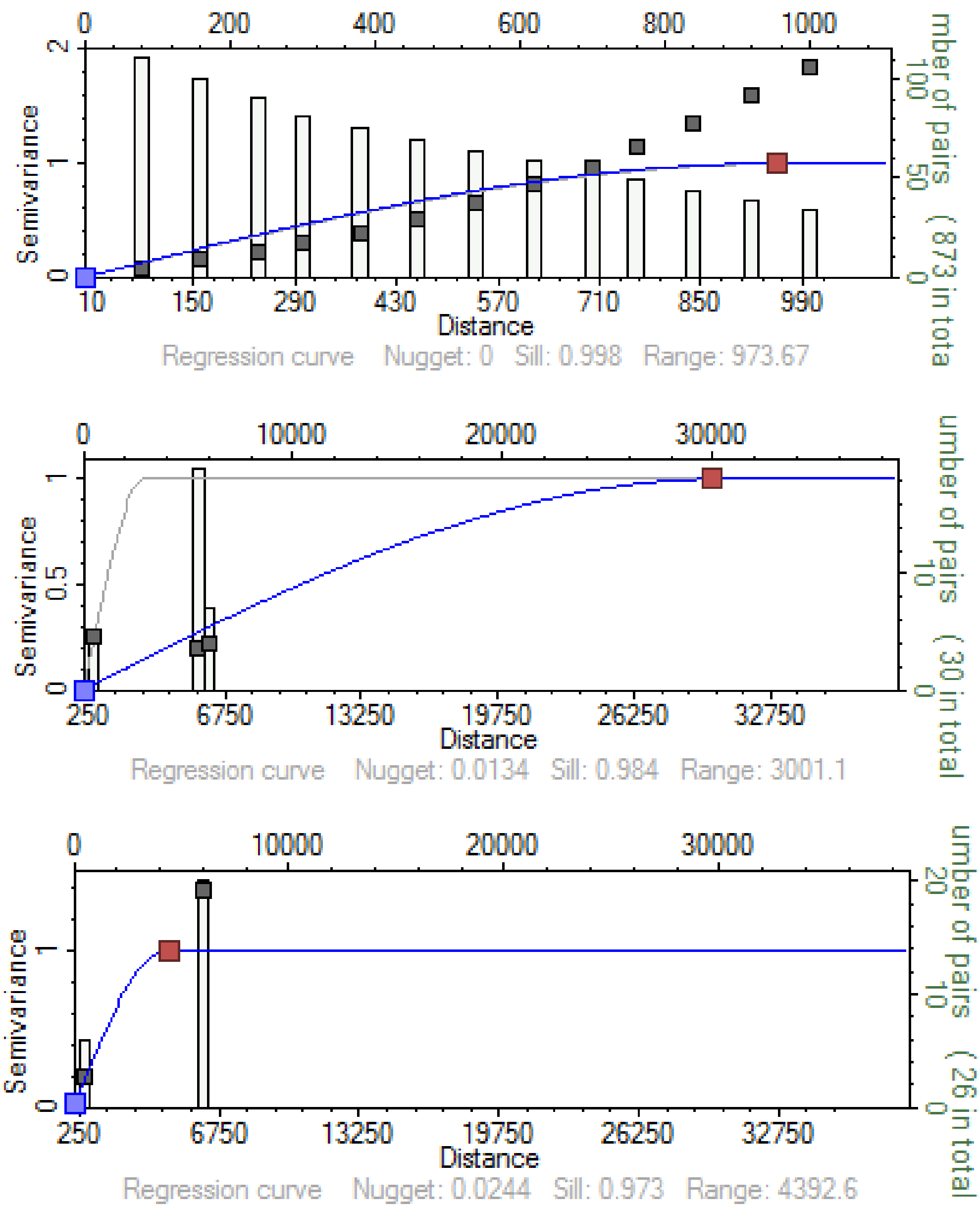

Figure A-7 Black squares represent the experimental data, the black line is the regression variogram and the blue line the variogram model. (Upper variogram in vertical direction, middle variogram in major direction and lower variogram in minor direction).

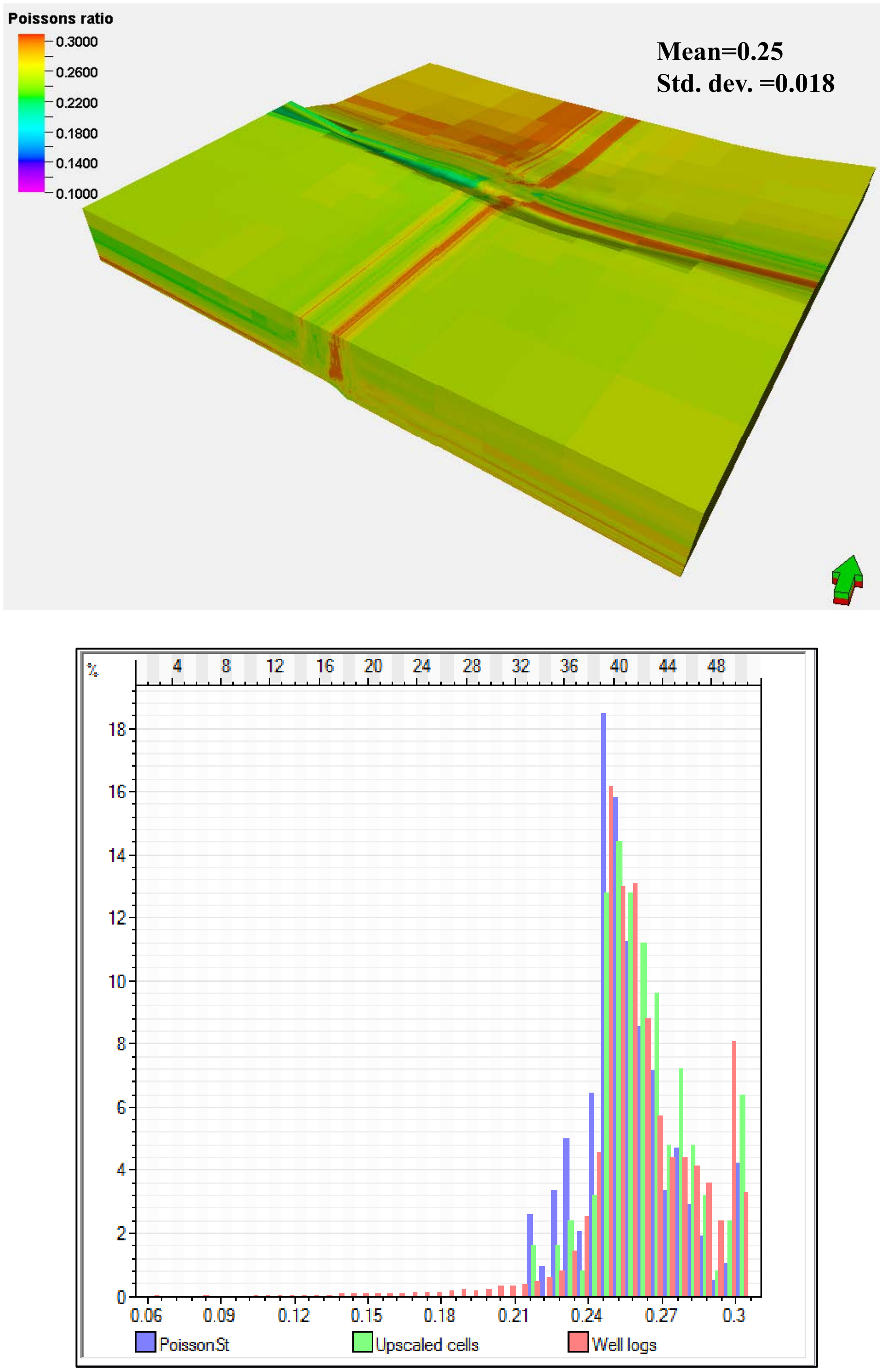

Figure A-8 MEM property distribution. (Top graph) Property distribution in the model. (Bottom) Histogram showing a comparison between the well log used for upscaling, the upscaled well log in the cell crossed by the well and the cells in the model..

Zone 3 (MI-2)

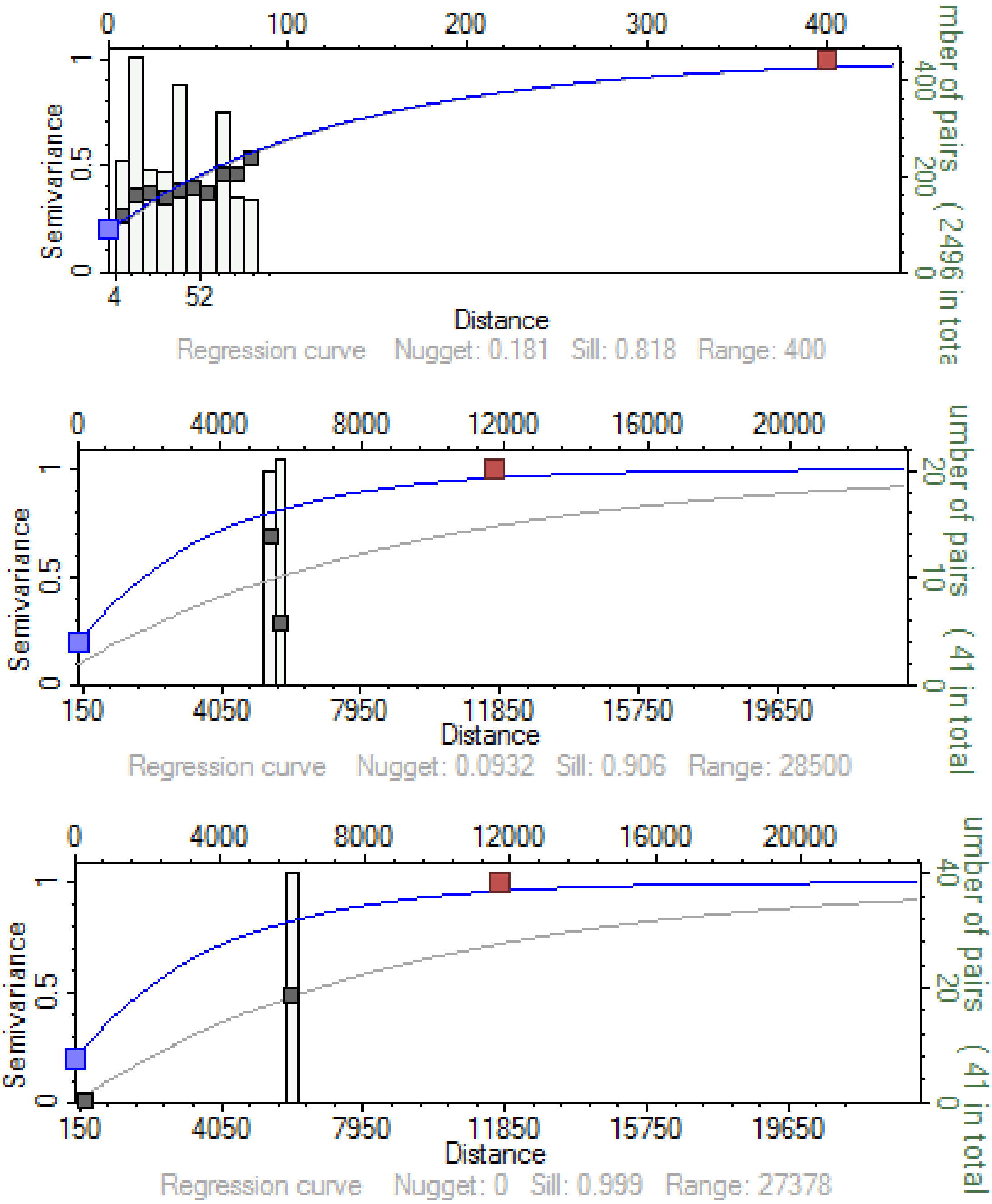

Figure A-9 Black squares represent the experimental data, the black line is the regression variogram and the blue line the variogram model. (Upper variogram in vertical direction, middle variogram in major direction and lower variogram in minor direction).

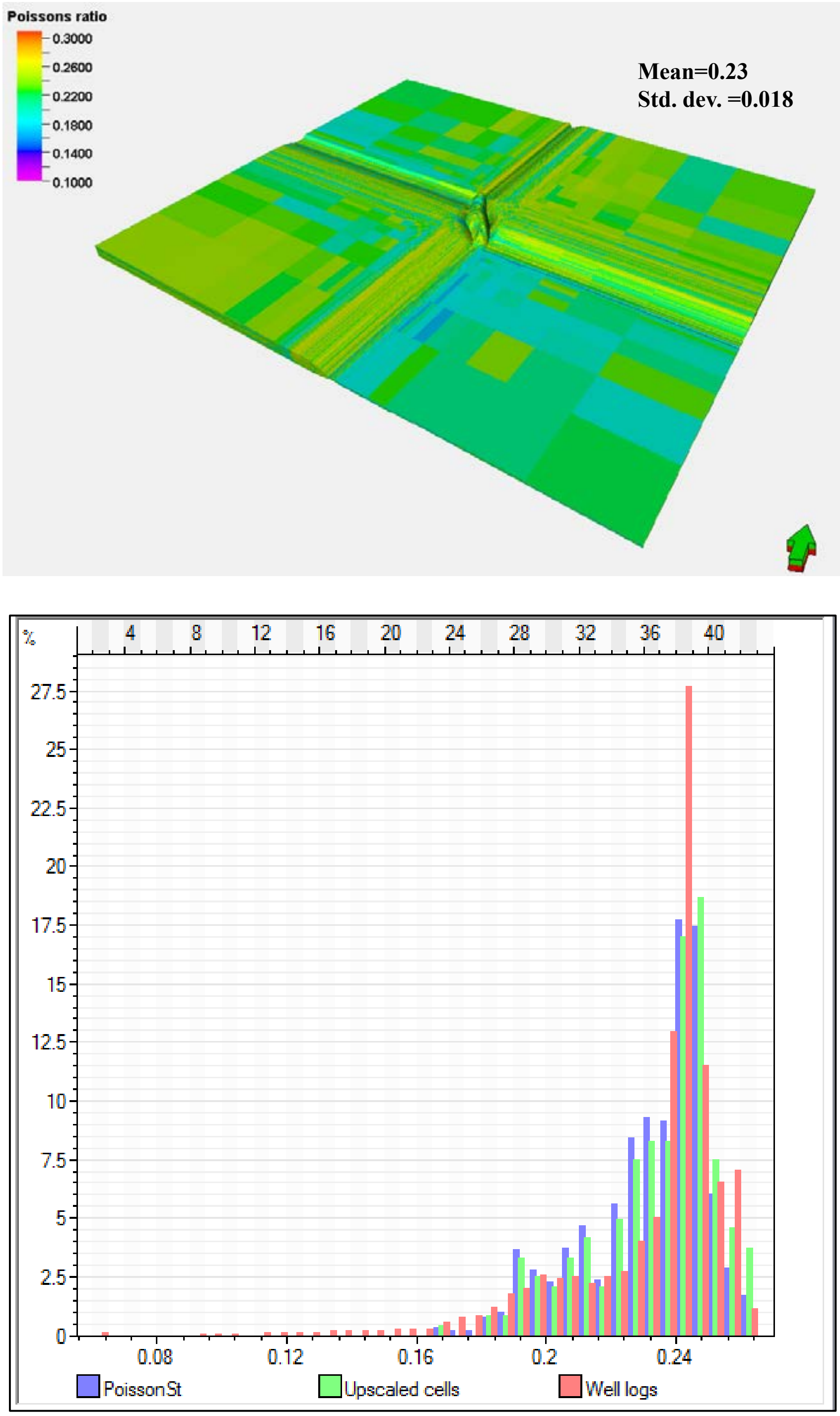

Figure A-10 MEM property distribution. (Top graph) Property distribution in the model. (Bottom) Histogram showing a comparison between the well log used for upscaling, the upscaled well log in the cell crossed by the well and the cells in the model.

Zone 5 (MI-1)

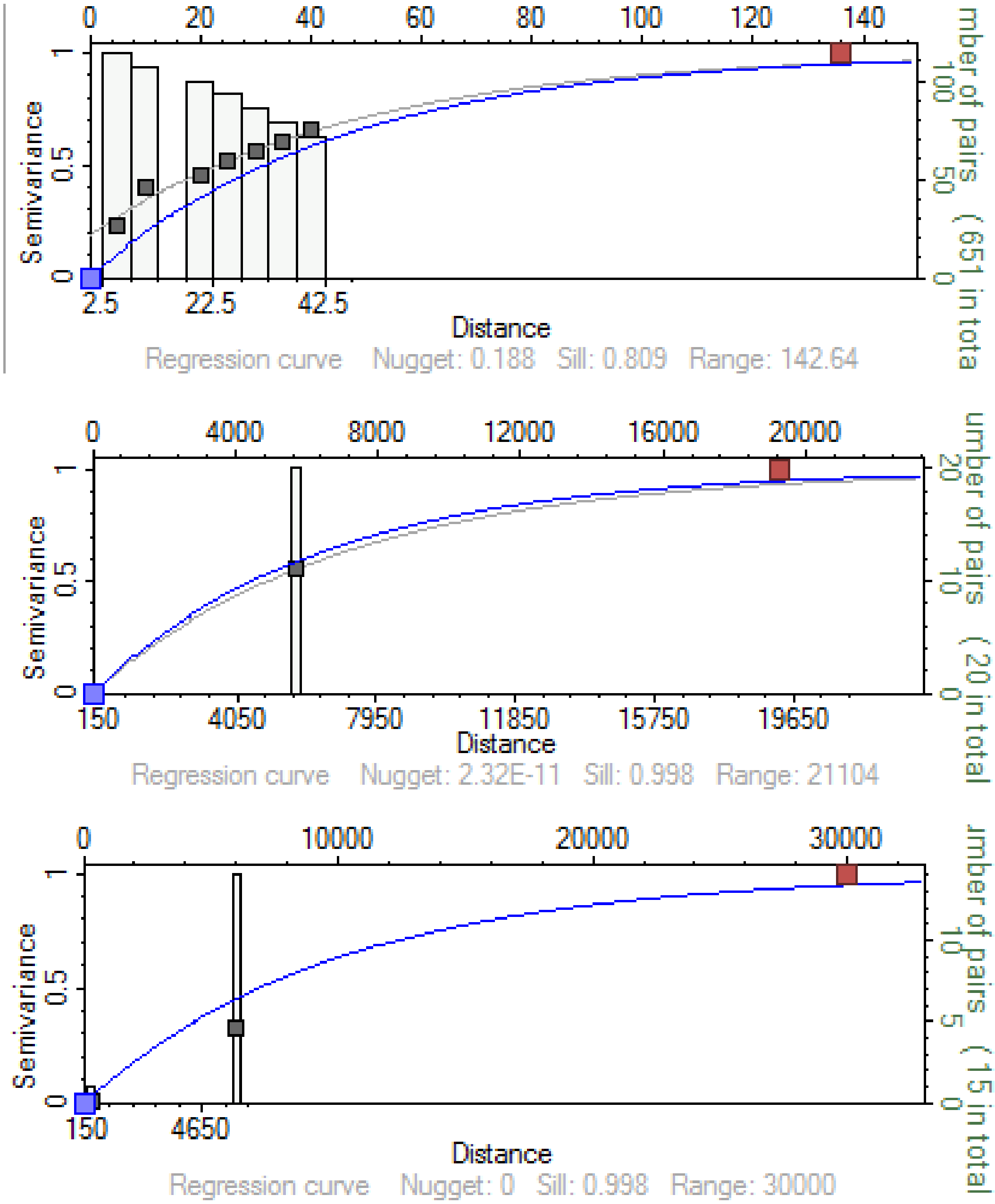

Figure A-11 Black squares represent the experimental data, the black line is the regression variogram and the blue line the variogram model. (Upper variogram in vertical direction, middle variogram in major direction and lower variogram in minor direction).

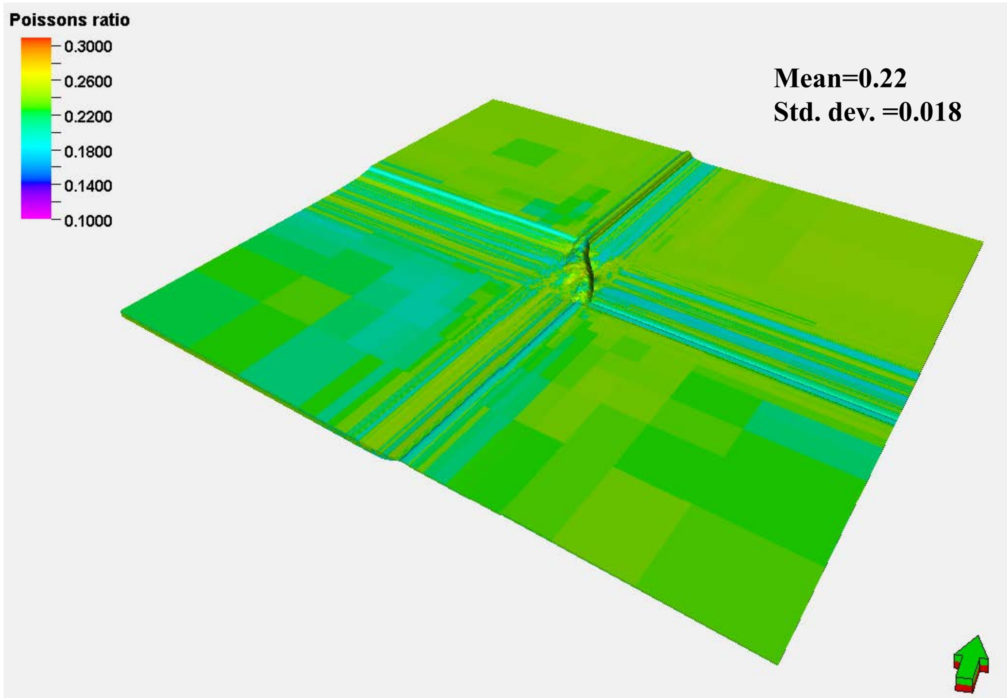

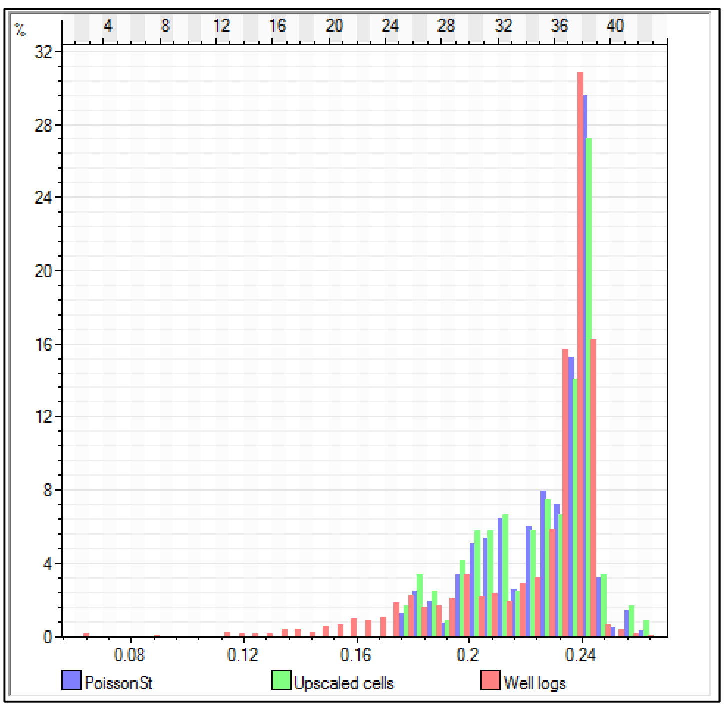

Figure A-12 MEM property distribution. (Top graph) Property distribution in the model. (Bottom) Histogram showing a comparison between the well log used for upscaling, the upscaled well log in the cell crossed by the well and the cells in the model.

A.2.3 UCS

Zone 2 (Upper Pliocene)

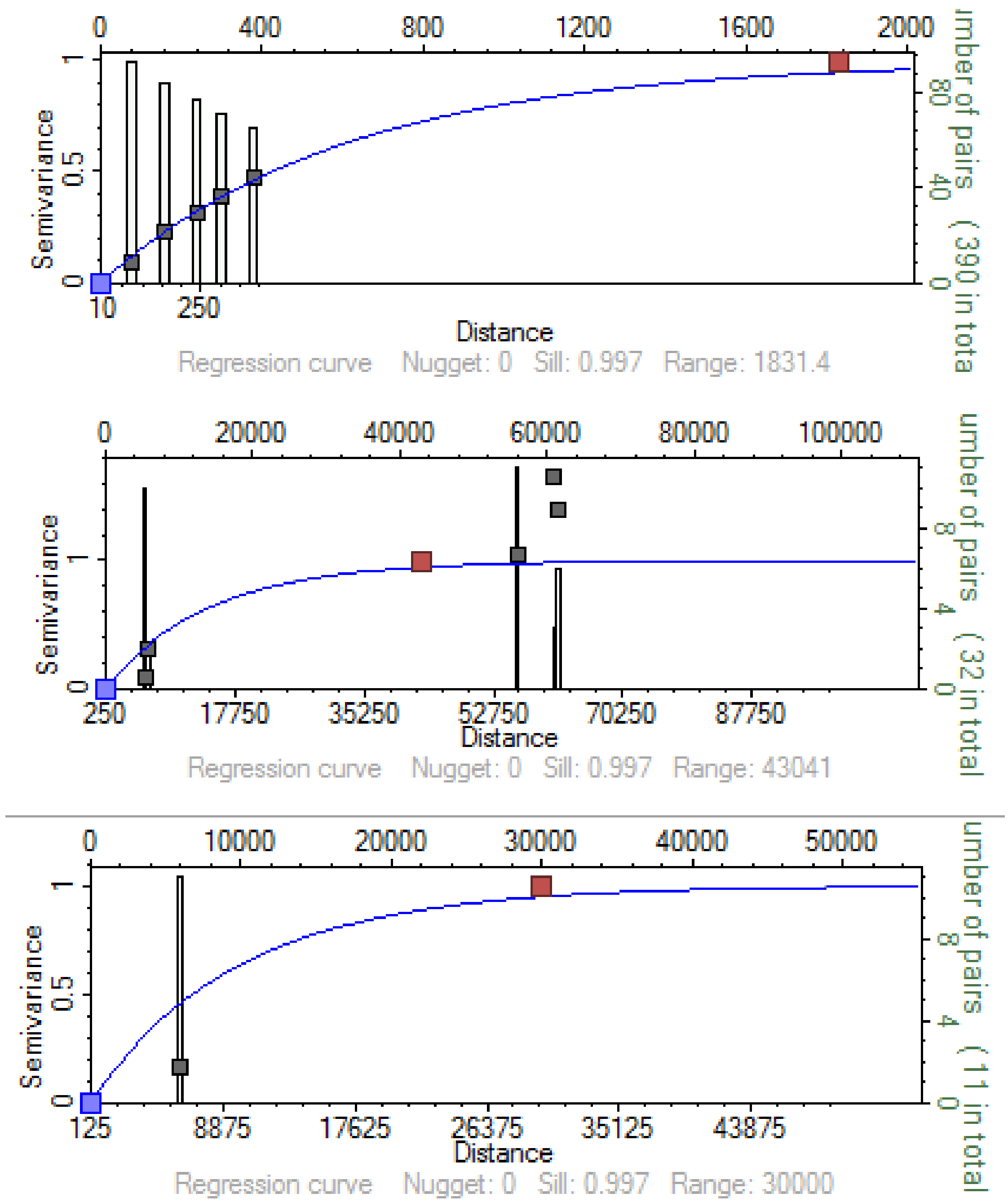

Figure A-13 Black squares represent the experimental data, the black line is the regression variogram and the blue line the variogram model. (Upper variogram in vertical direction, middle variogram in major direction and lower variogram in minor direction).

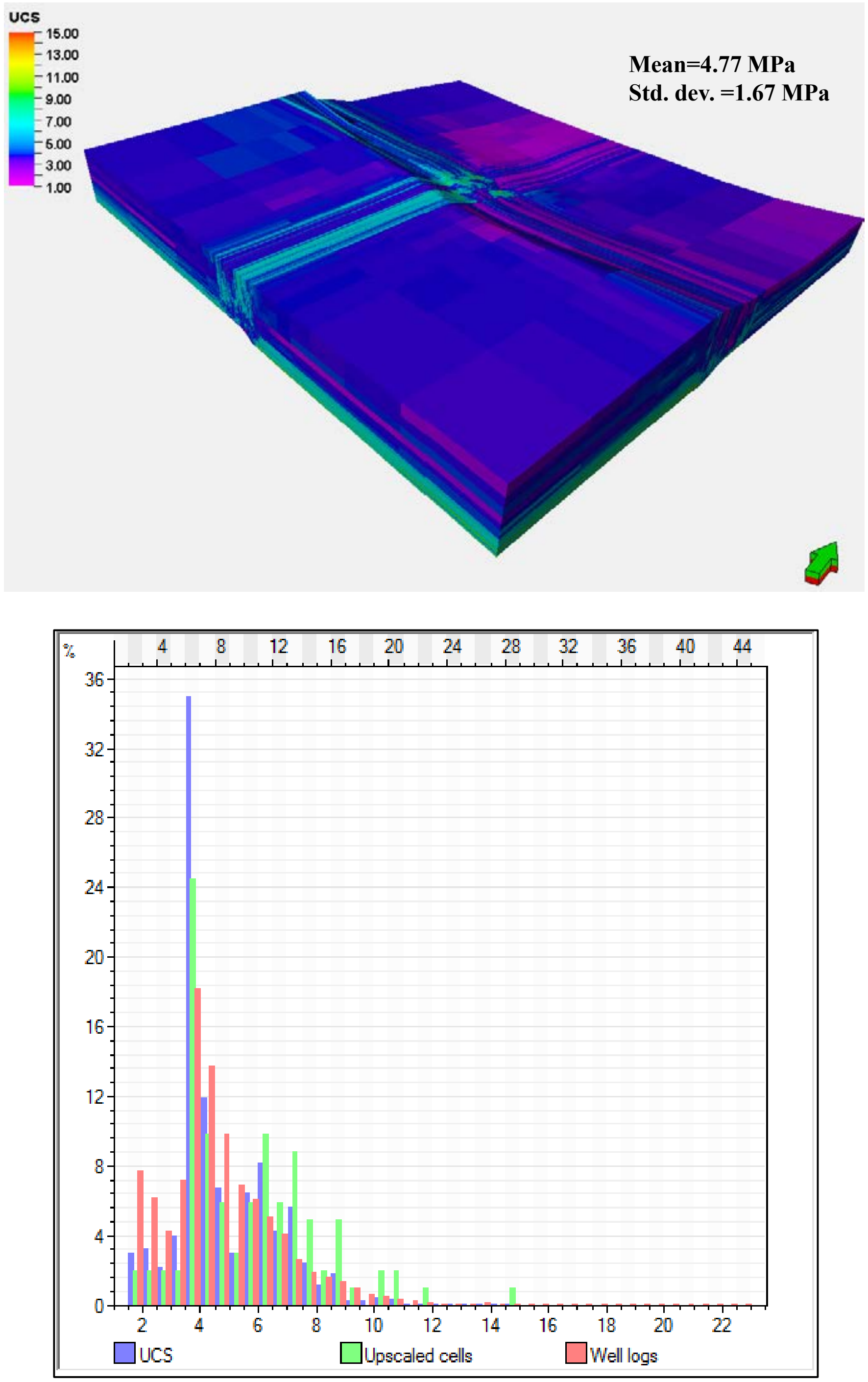

Figure A-14 MEM property distribution. (Top graph) Property distribution in the model. (Bottom) Histogram showing a comparison between the well log used for upscaling, the upscaled well log in the cell crossed by the well and the cells in the model.

Zone 3 (MI-2)

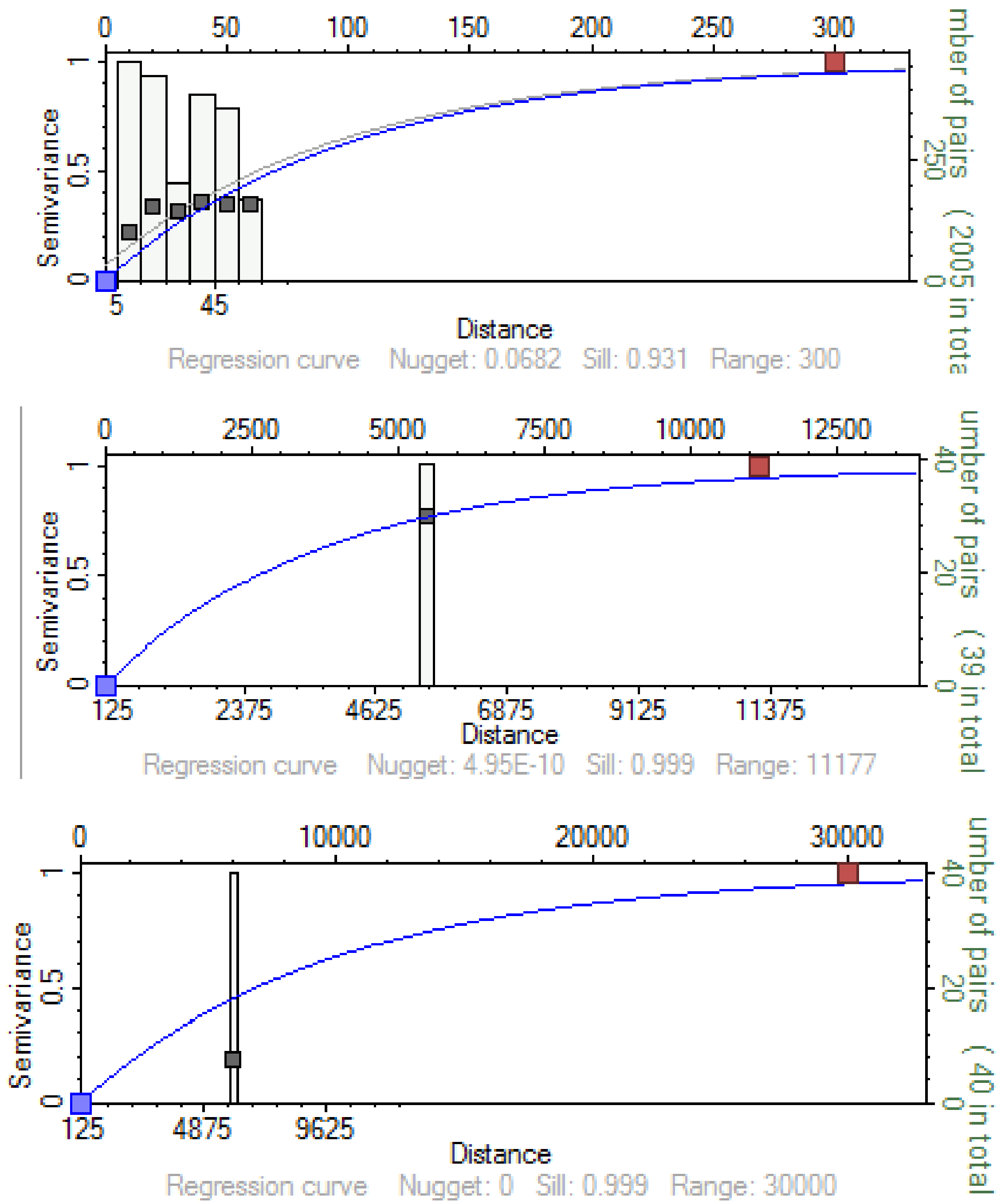

Figure A-15 Black squares represent experimental data, the black line is the regression variogram and the blue line the variogram model. (Upper variogram in vertical direction middle variogram in major direction and lower variogram in minor direction).

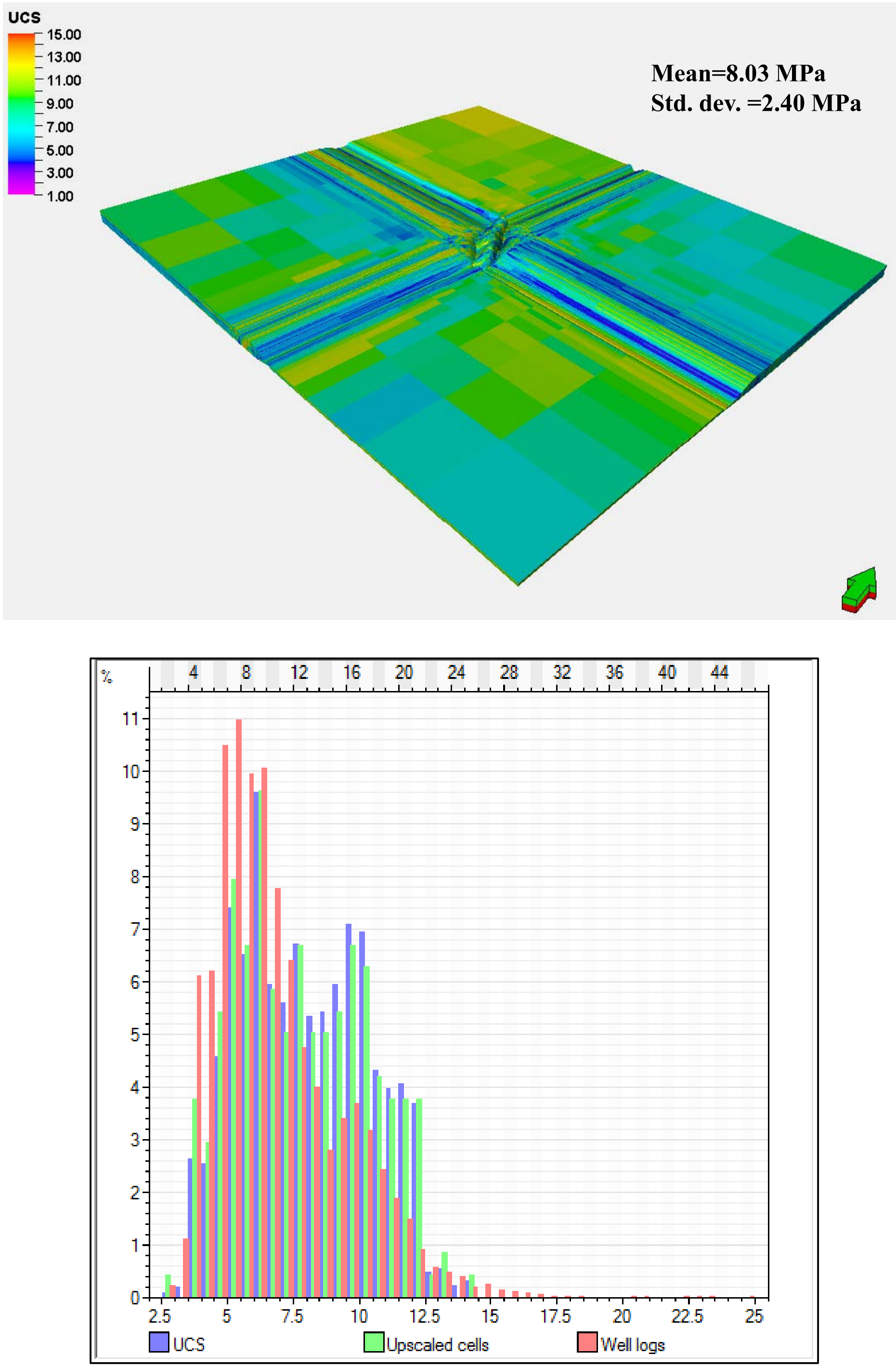

Figure A-16 MEM property distribution. (Top graph) Property distribution in the model. (Bottom) Histogram showing a comparison between the well log used for upscaling, the upscaled well log in the cell crossed by the well and the cells in the model.

Zone 5 (MI-1)

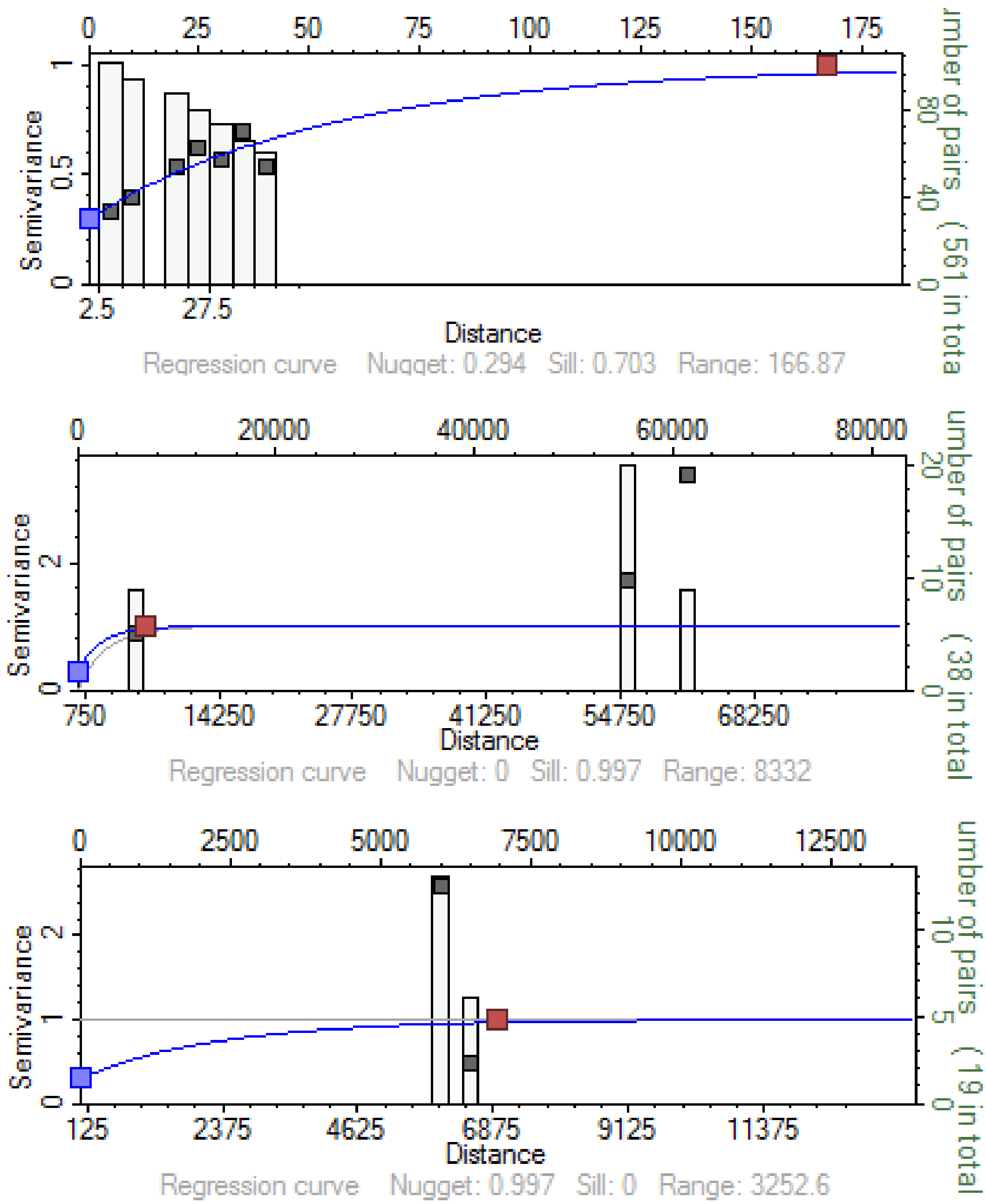

Figure A-17 Black squares represent experimental data, the black line is the regression variogram and the blue line the variogram model. (Upper variogram in vertical direction middle variogram in major direction and lower variogram in minor direction).

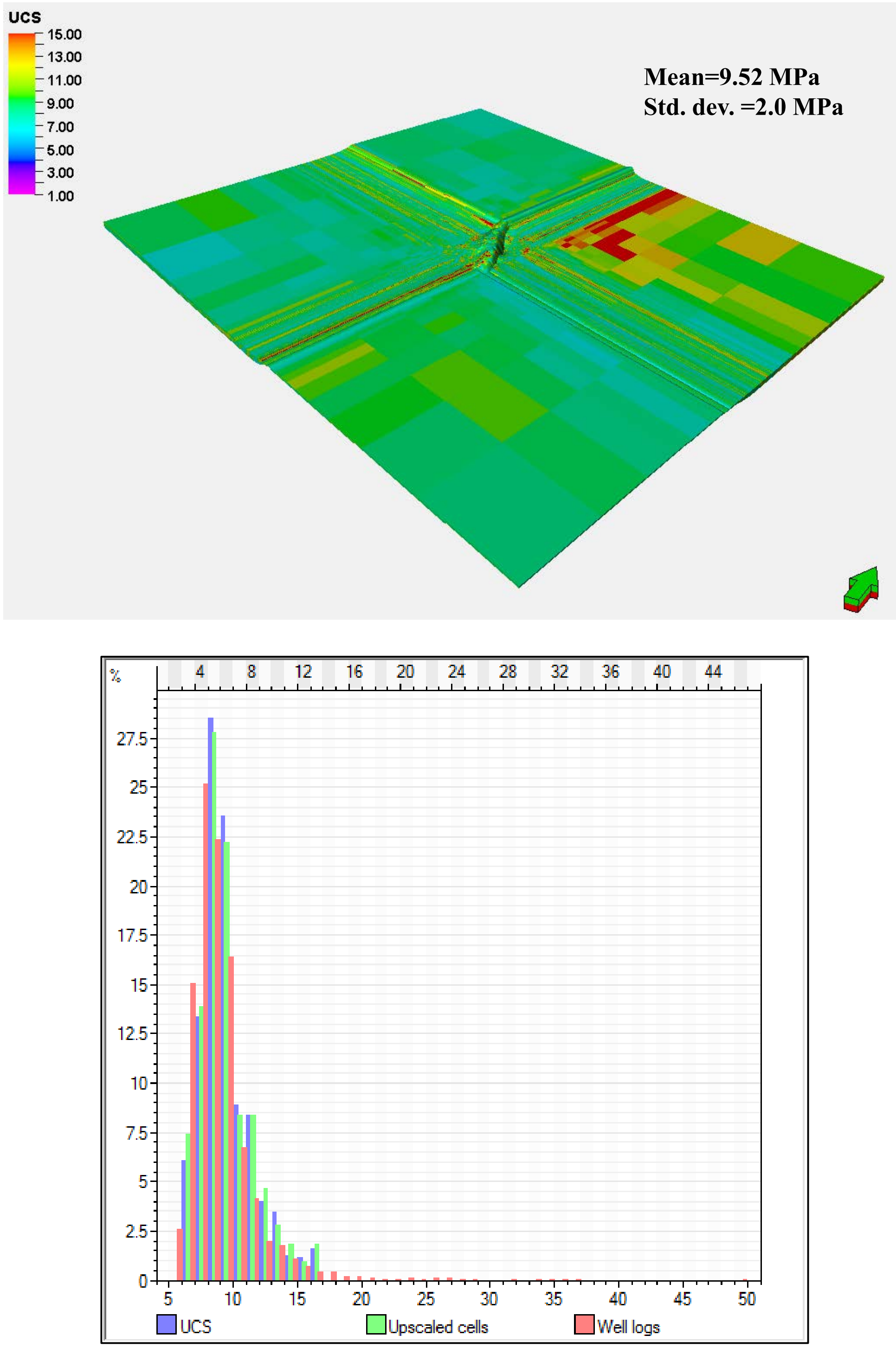

Figure A-18 MEM property distribution. (Top graph) Property distribution in the model. (Bottom) Histogram showing a comparison between the well log used for upscaling, the upscaled well log in the cell crossed by the well and the cells in the model.

A.2.4 Porosity

Zone 2 (Upper Pliocene)

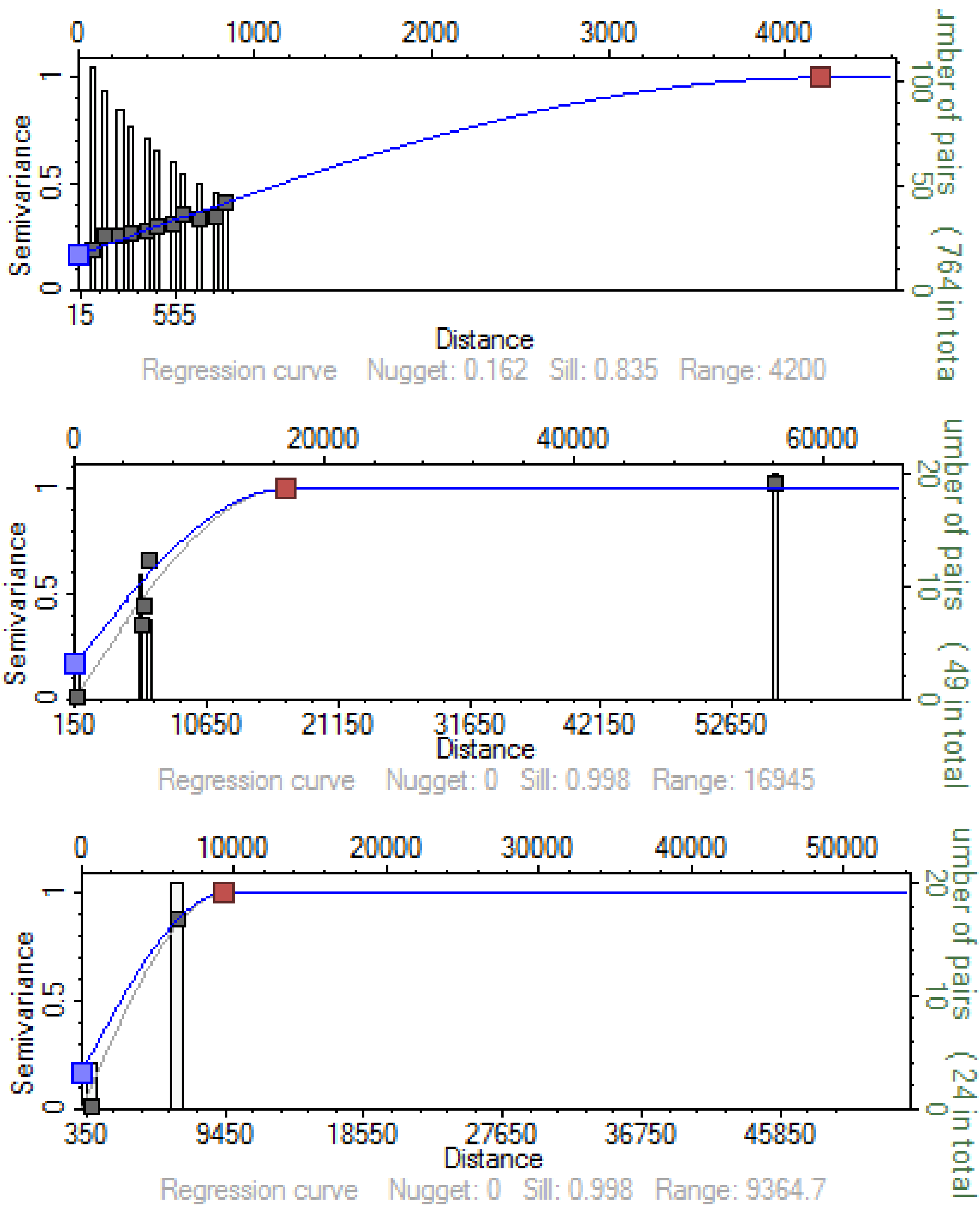

Figure A-19 Black squares represent experimental data, the black line is the regression variogram and the blue line the variogram model. (Upper variogram in vertical direction middle variogram in major direction and lower variogram in minor direction).

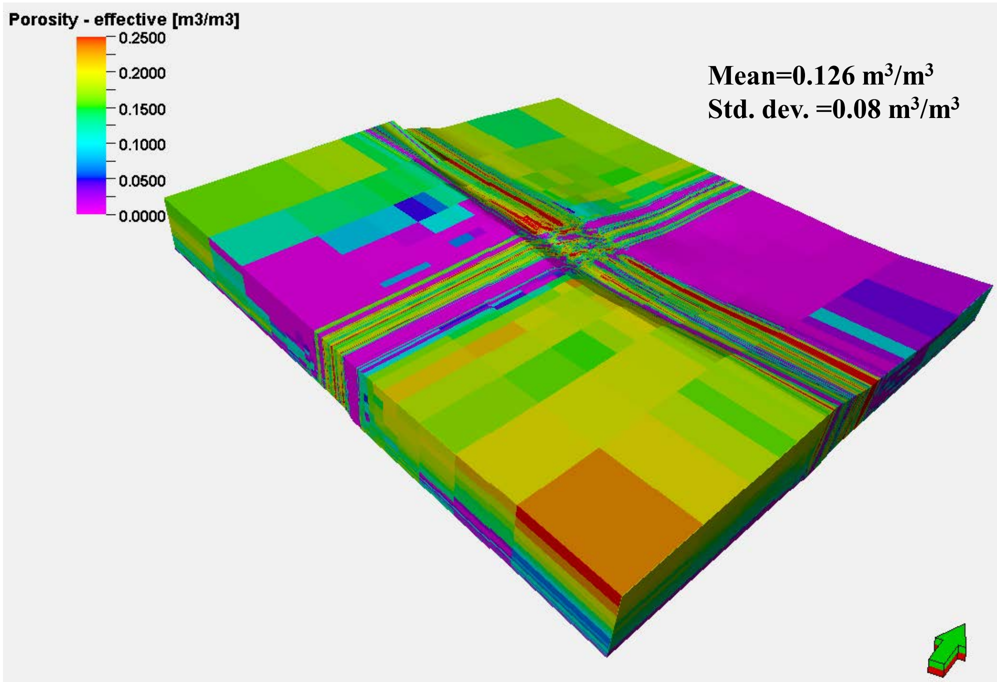

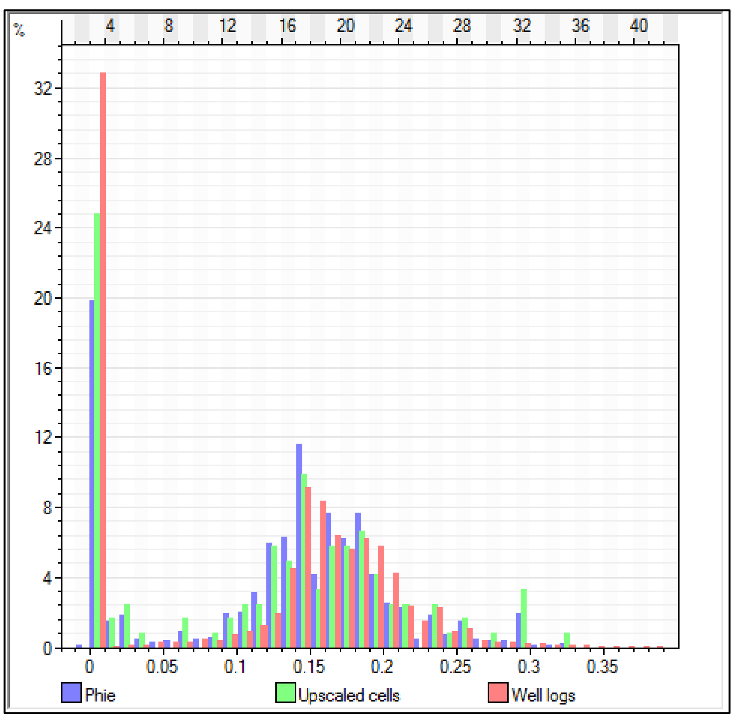

Figure A-20 MEM property distribution. (Top graph) Property distribution in the model. (Bottom) Histogram showing a comparison between the well log used for upscaling, the upscaled well log in the cell crossed by the well and the cells in the model.

Zone 3 (MI-2)

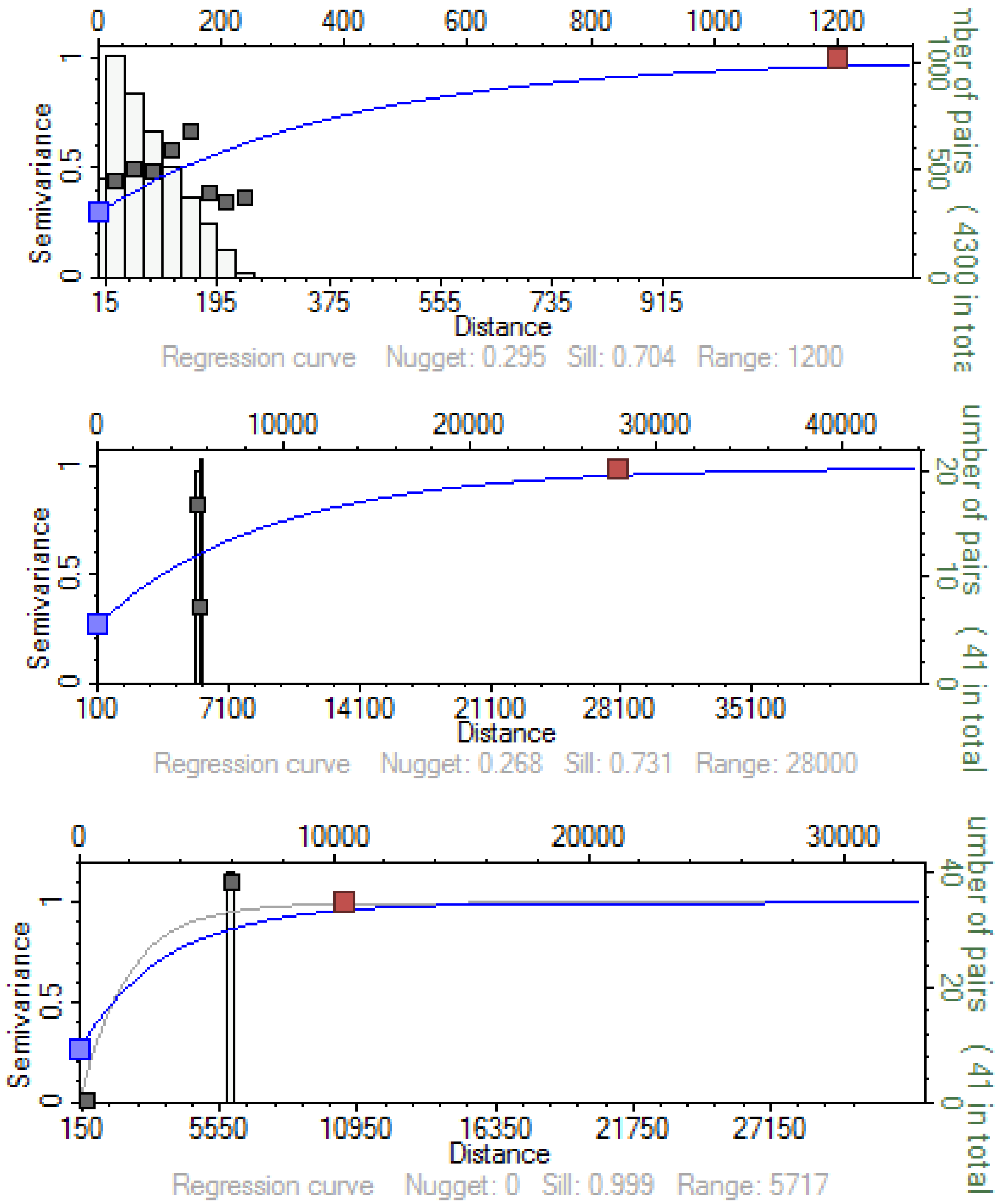

Figure A-21 Black squares represent experimental data, the black line is the regression variogram and the blue line the variogram model. (Upper variogram in vertical direction middle variogram in major direction and lower variogram in minor direction).

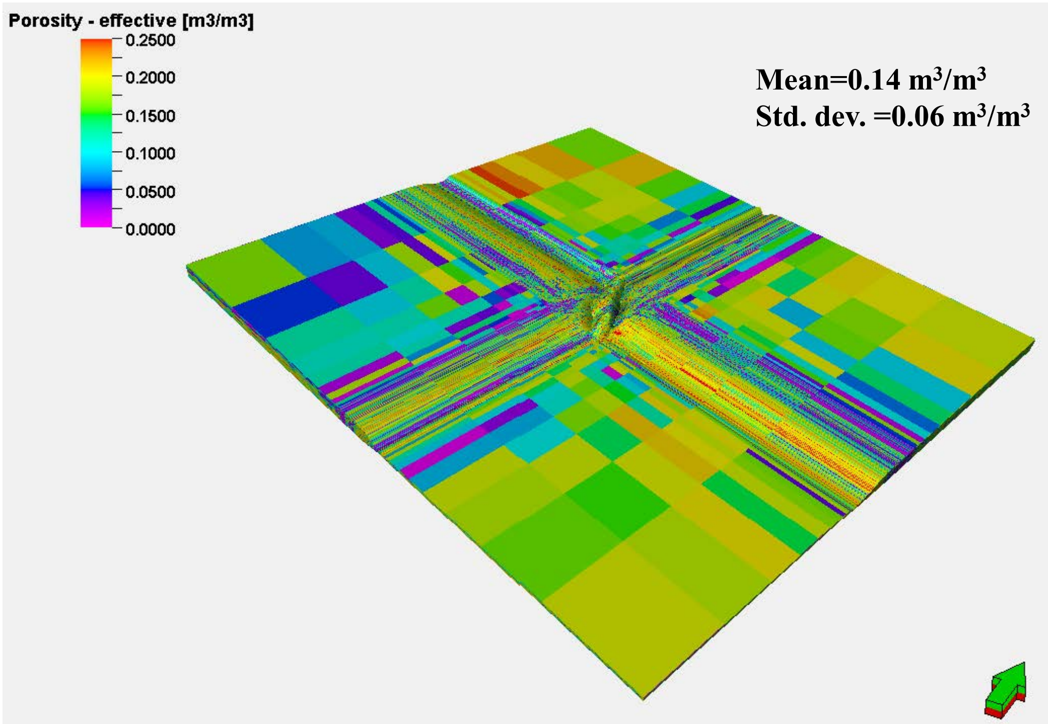

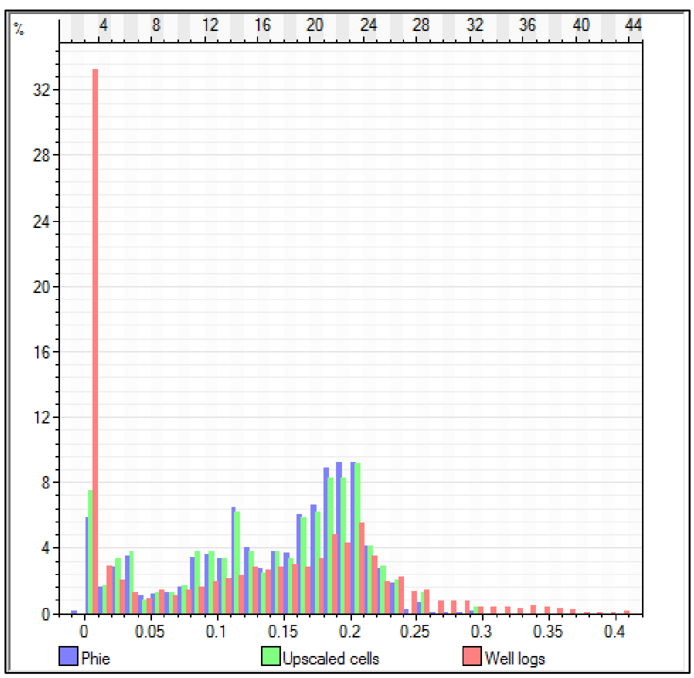

Figure A-22 MEM property distribution. (Top graph) Property distribution in the model. (Bottom) Histogram showing a comparison between the well log used for upscaling, the upscaled well log in the cell crossed by the well and the cells in the model.

Zone 5 (MI-1)

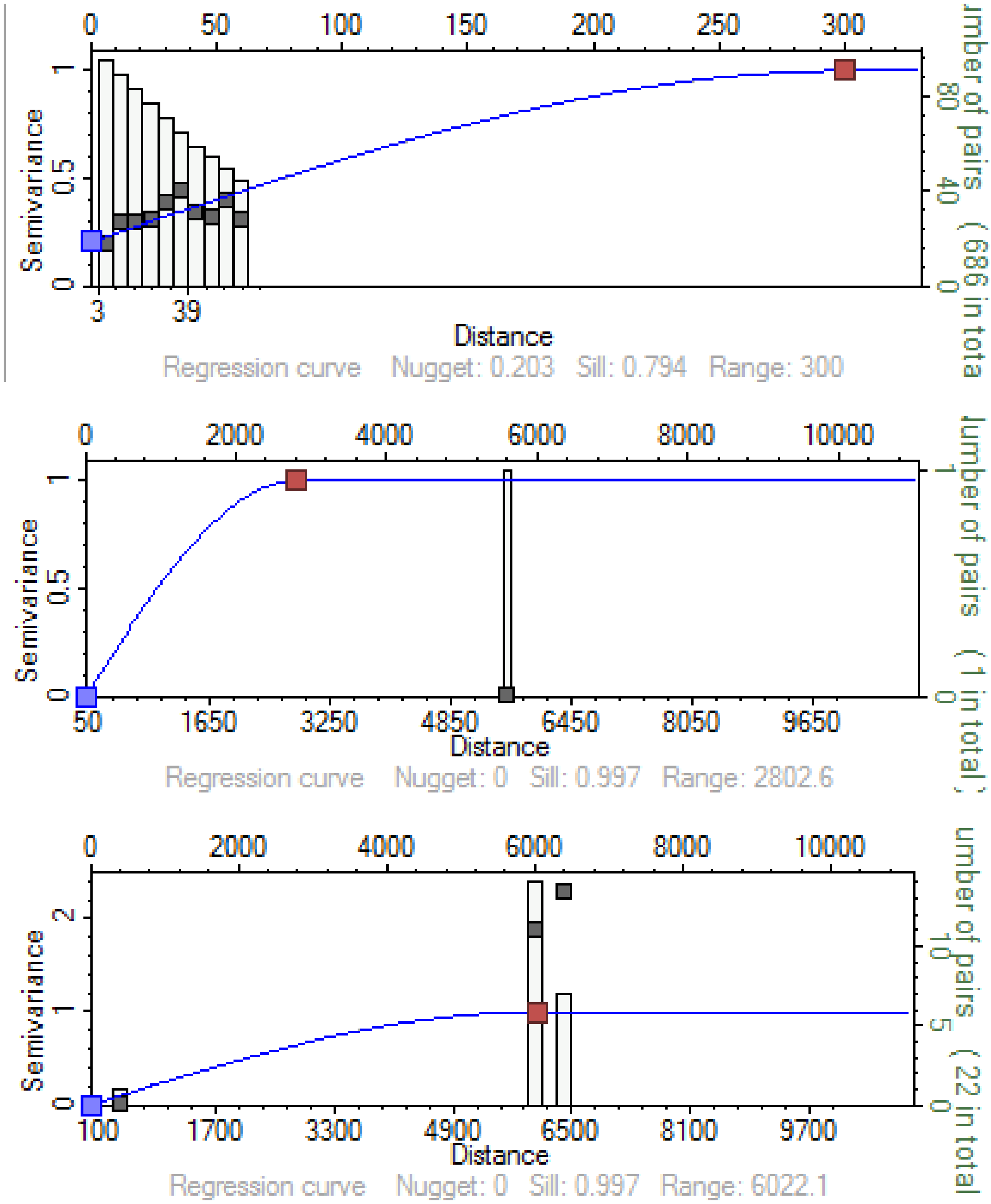

Figure A-23 Black squares represent experimental data, the black line is the regression variogram and the blue line the variogram model. (Upper variogram in vertical direction middle variogram in major direction and lower variogram in minor direction).

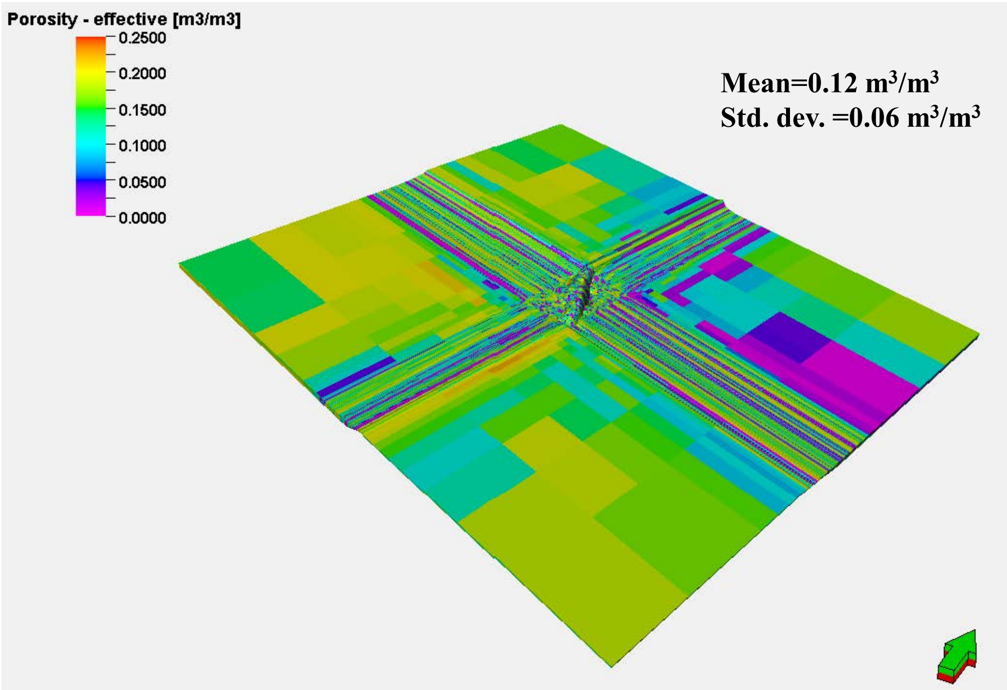

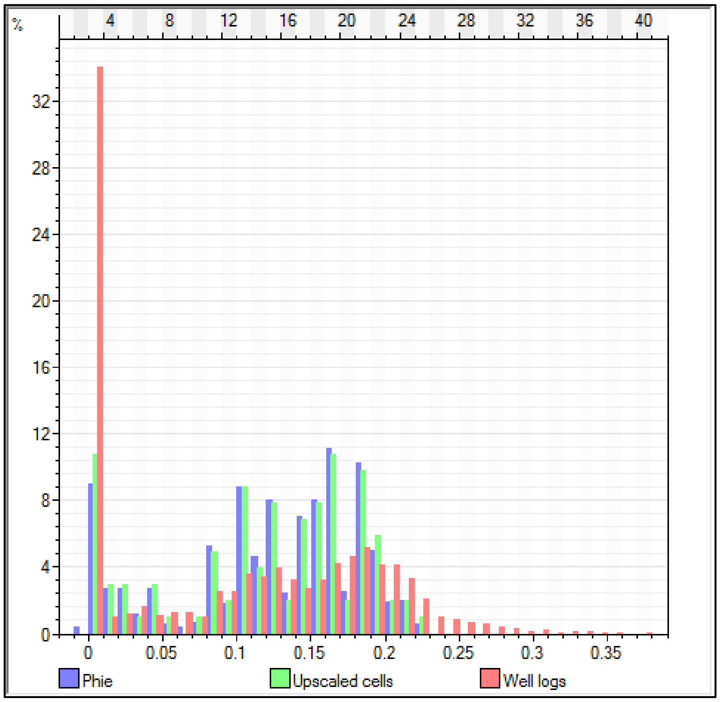

Figure A-24 MEM property distribution. (Top graph) Property distribution in the model. (Bottom) Histogram showing a comparison between the well log used for upscaling, the upscaled well log in the cell crossed by the well and the cells in the model.

A.2.5 Bulk density

Zone 2 (Upper Pliocene)

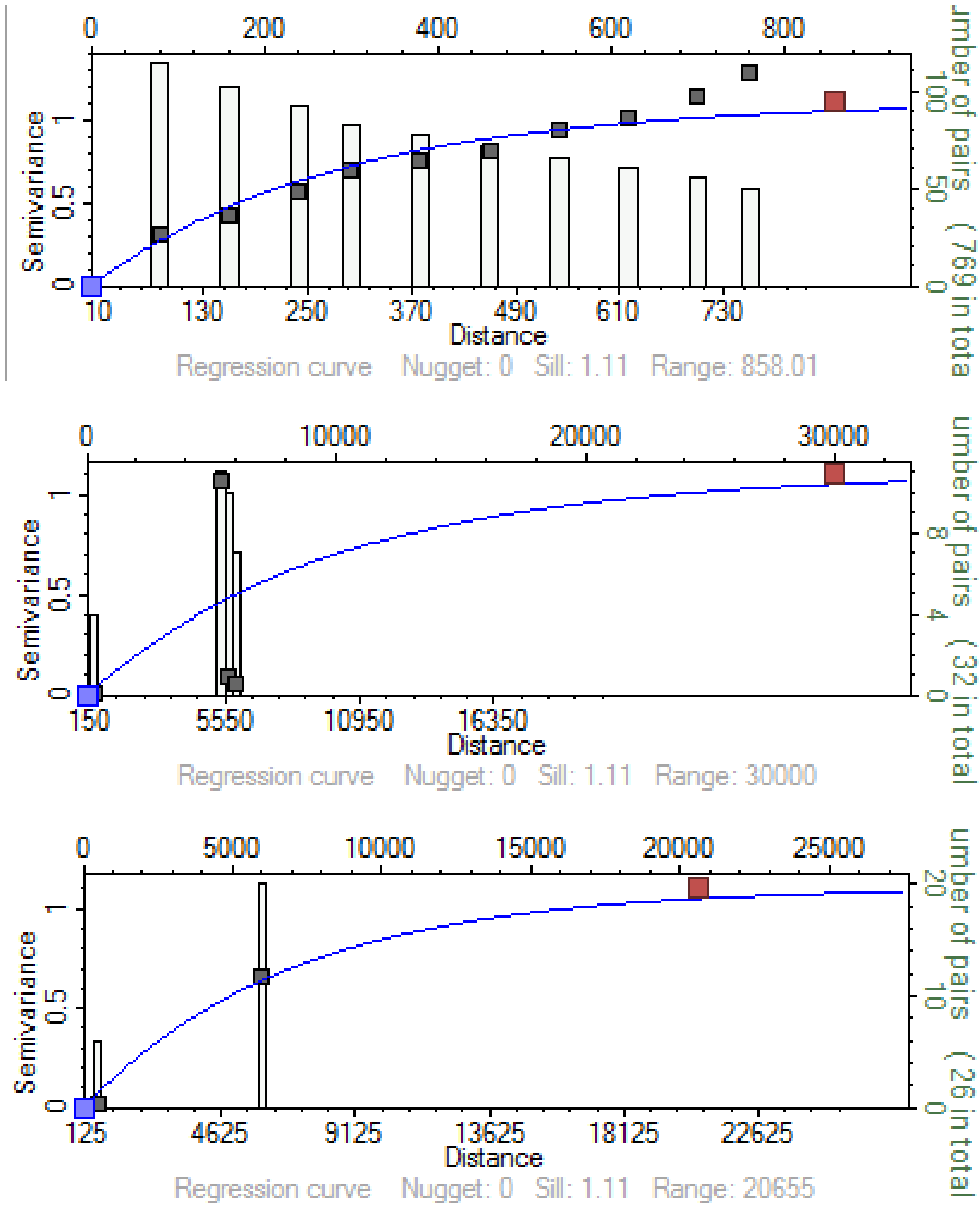

Figure A-25 Black squares represent experimental data, the black line is the regression variogram and the blue line the variogram model. (Upper variogram in vertical direction middle variogram in major direction and lower variogram in minor direction).

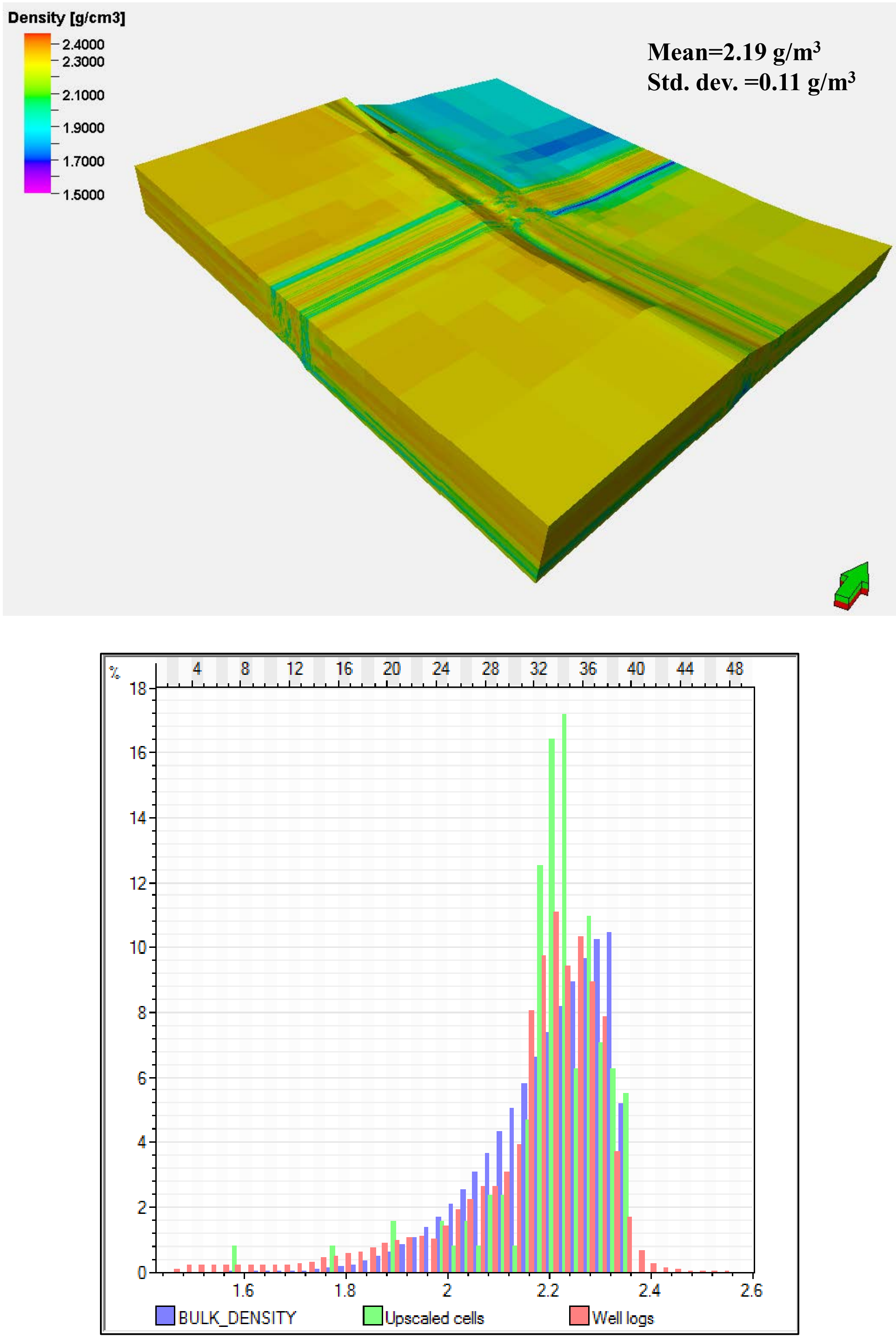

Figure A-26 MEM property distribution. (Top graph) Property distribution in the model. (Bottom) Histogram showing a comparison between the well log used for upscaling, the upscaled well log in the cell crossed by the well and the cells in the model.

Zone 3 (MI-2)

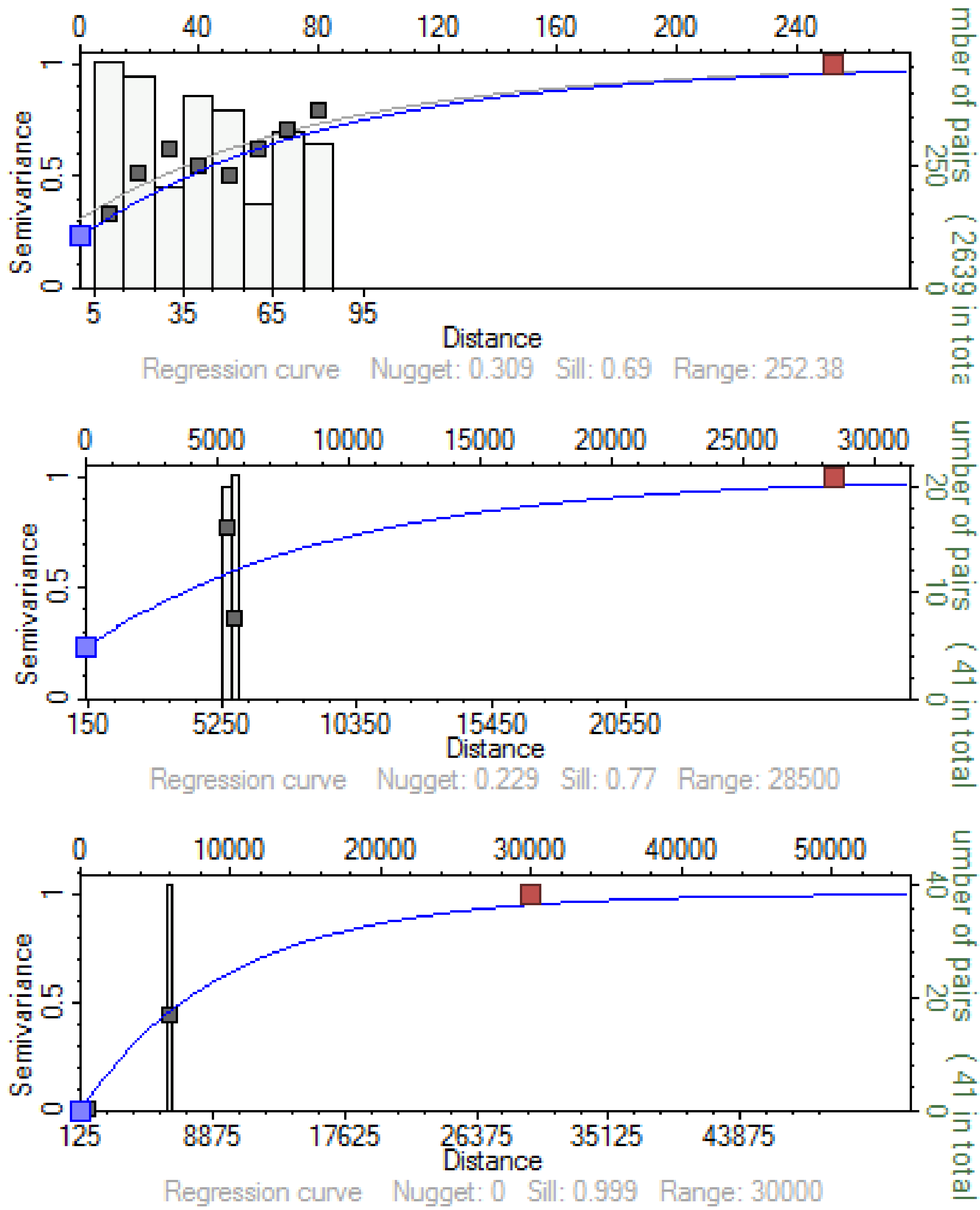

Figure A-27 Black squares represent experimental data, the black line is the regression variogram and the blue line the variogram model. (Upper variogram in vertical direction middle variogram in major direction and lower variogram in minor direction).

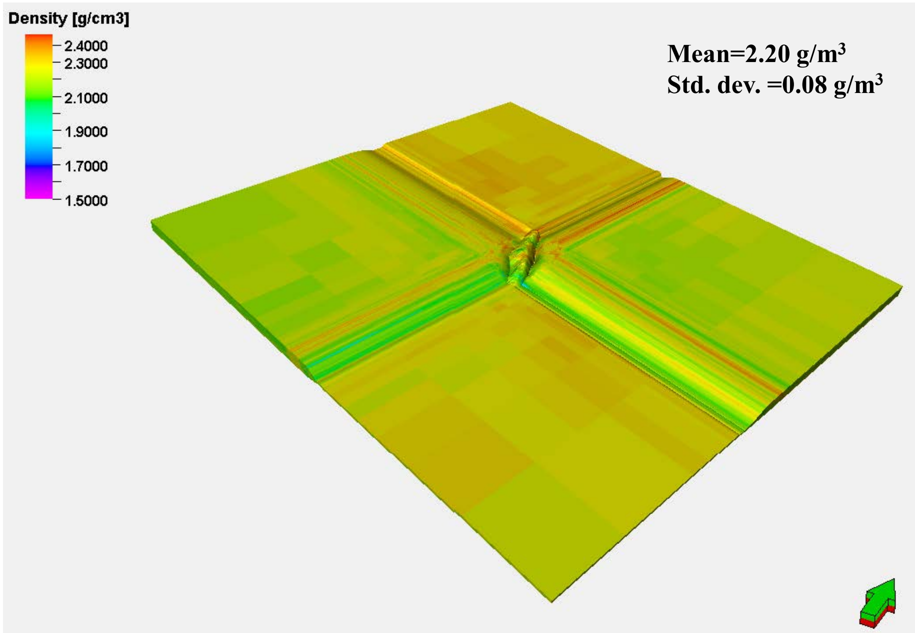

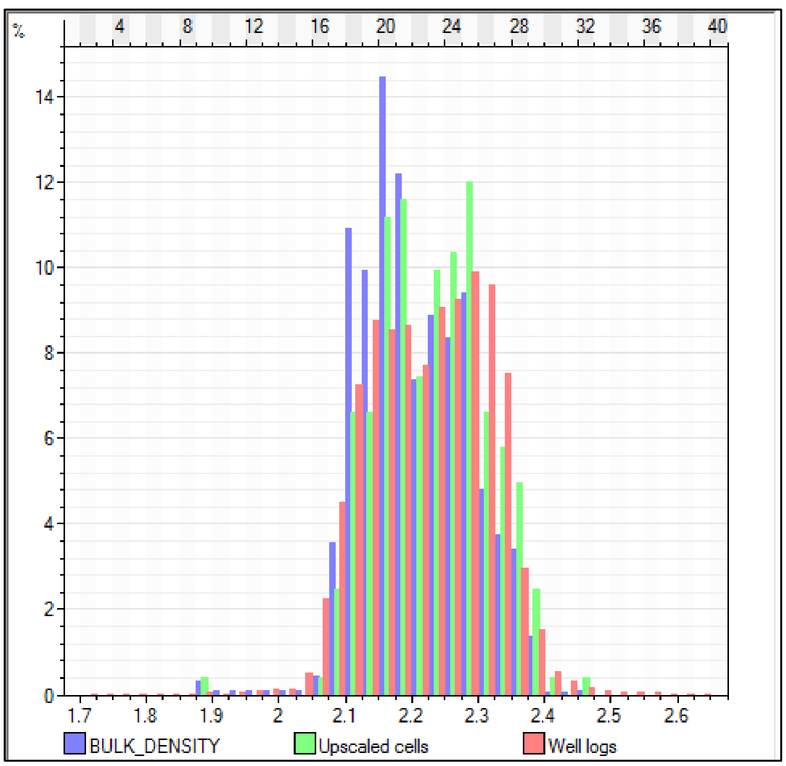

Figure A-28 MEM property distribution. (Top graph) Property distribution in the model. (Bottom) Histogram showing a comparison between the well log used for upscaling, the upscaled well log in the cell crossed by the well and the cells in the model.

Zone 5 (MI-1)

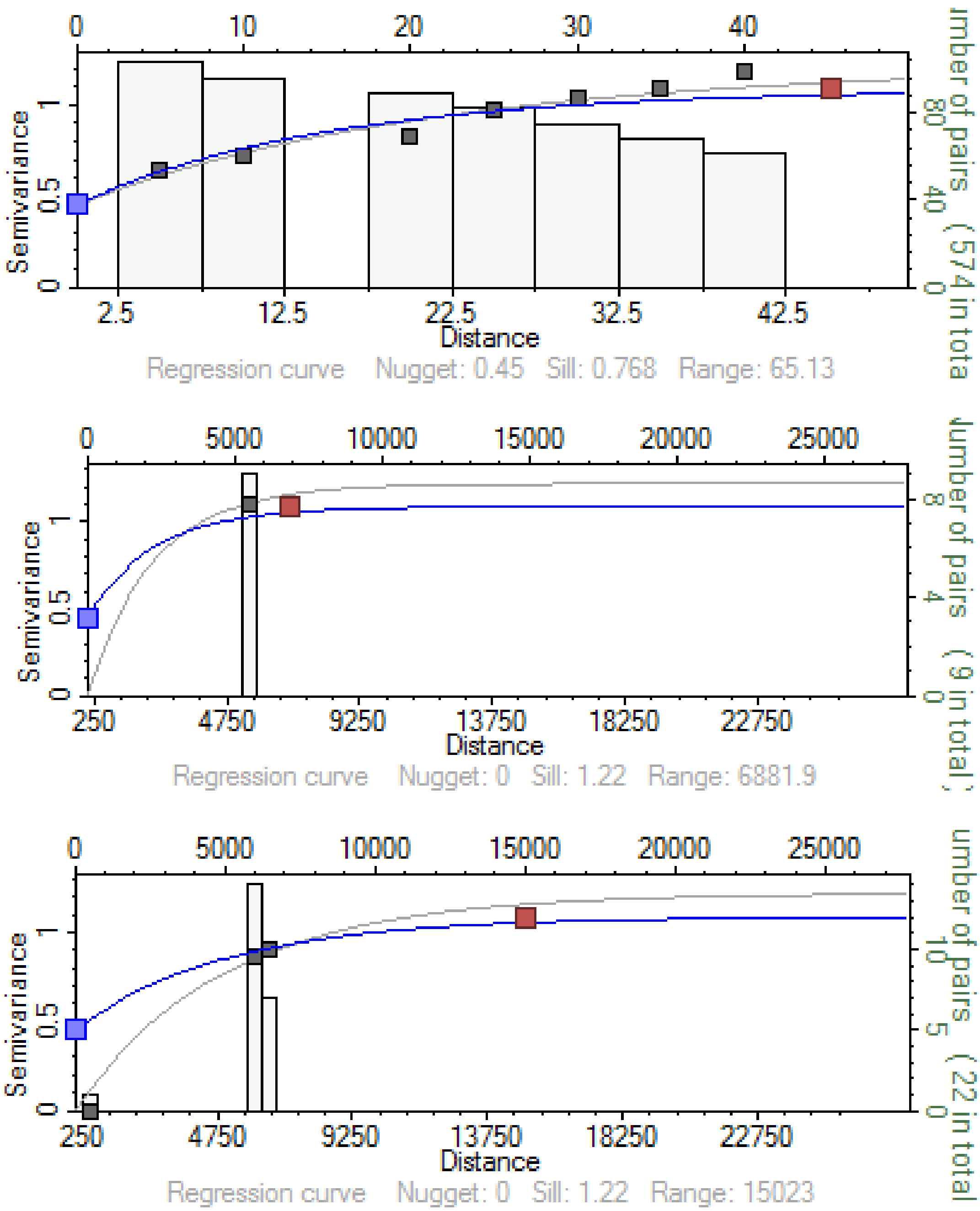

Figure A-29 Black squares represent experimental data, the black line is the regression variogram and the blue line the variogram model. (Upper variogram in vertical direction middle variogram in major direction and lower variogram in minor direction).

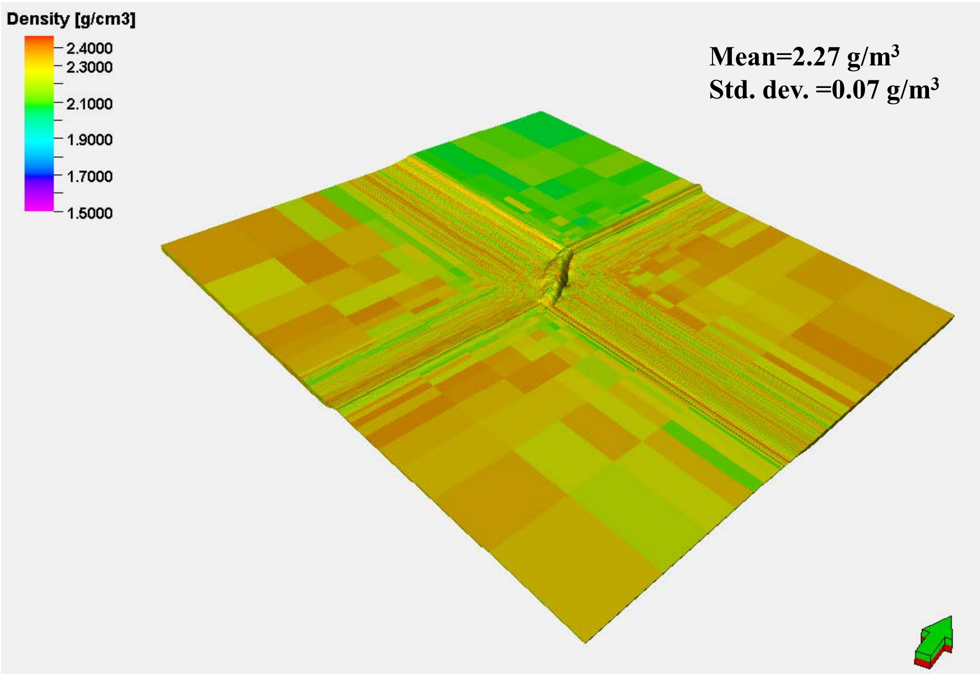

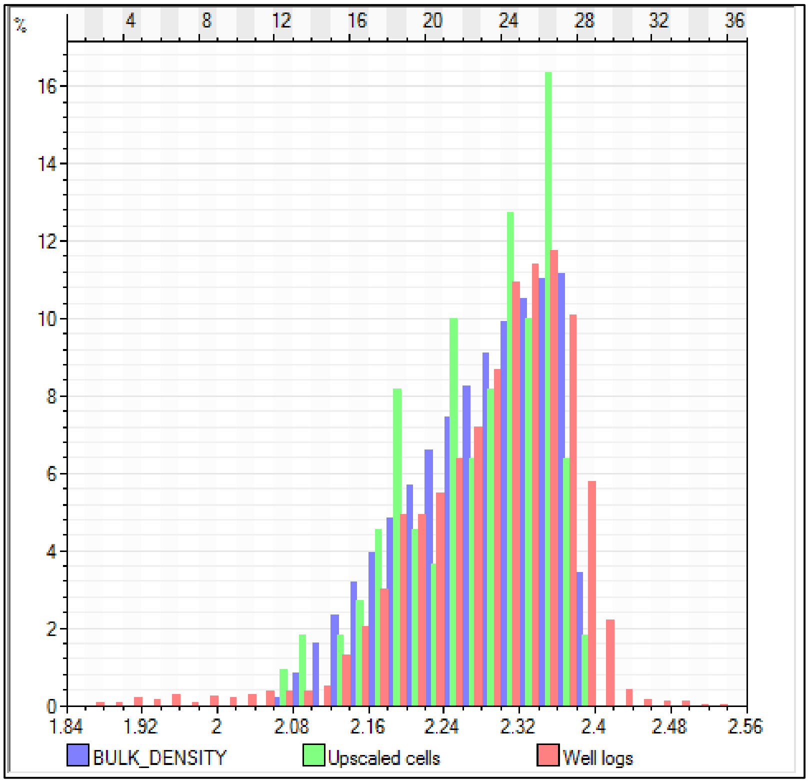

Figure A-30 MEM property distribution. (Top graph) Property distribution in the model. (Bottom) Histogram showing a comparison between the well log used for upscaling, the upscaled well log in the cell crossed by the well and the cells in the model.

A.2.6 Friction angle

Zone 2 (Upper Pliocene)

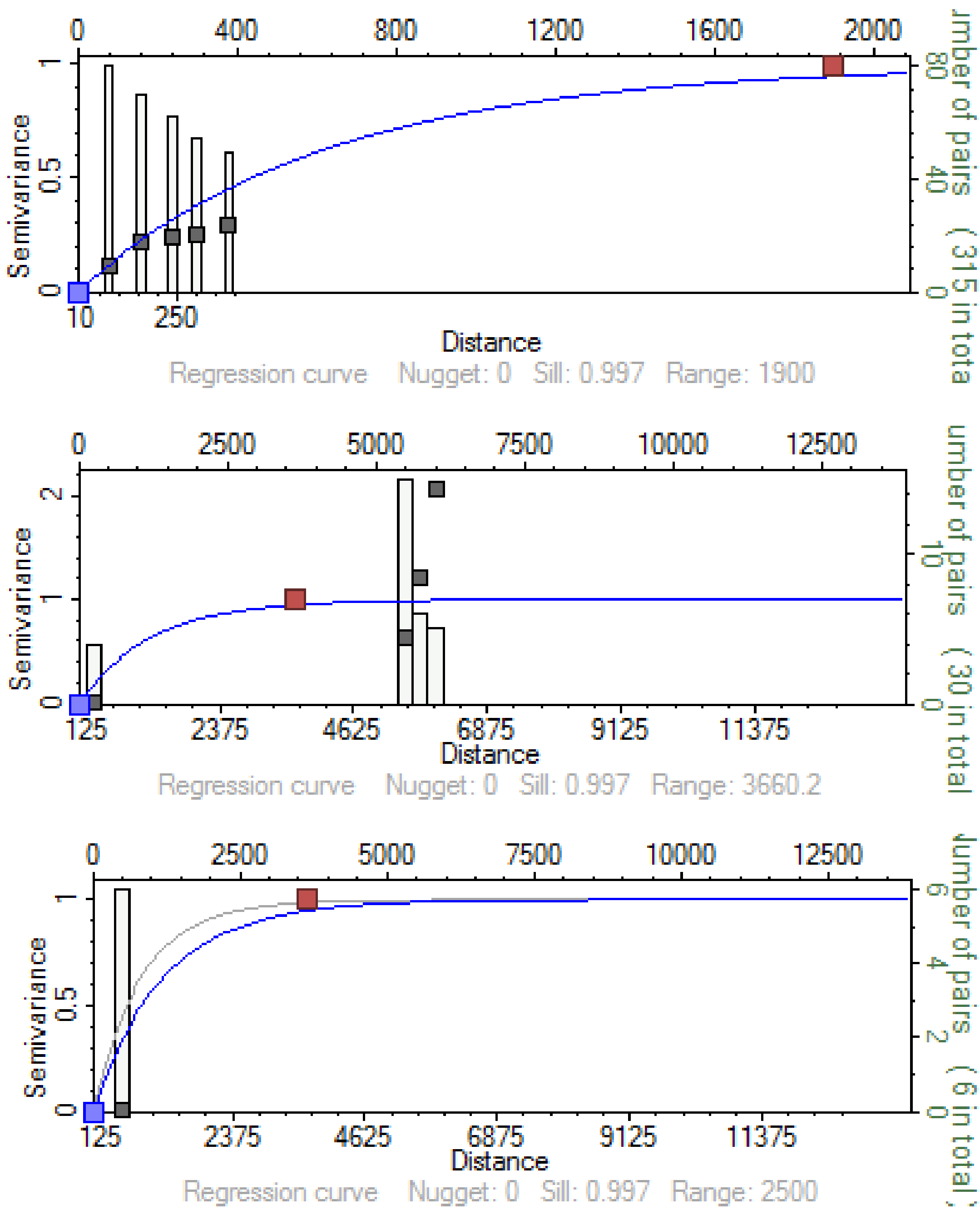

Figure A-31 Black squares represent experimental data, the black line is the regression variogram and the blue line the variogram model. (Upper variogram in vertical direction middle variogram in major direction and lower variogram in minor direction).

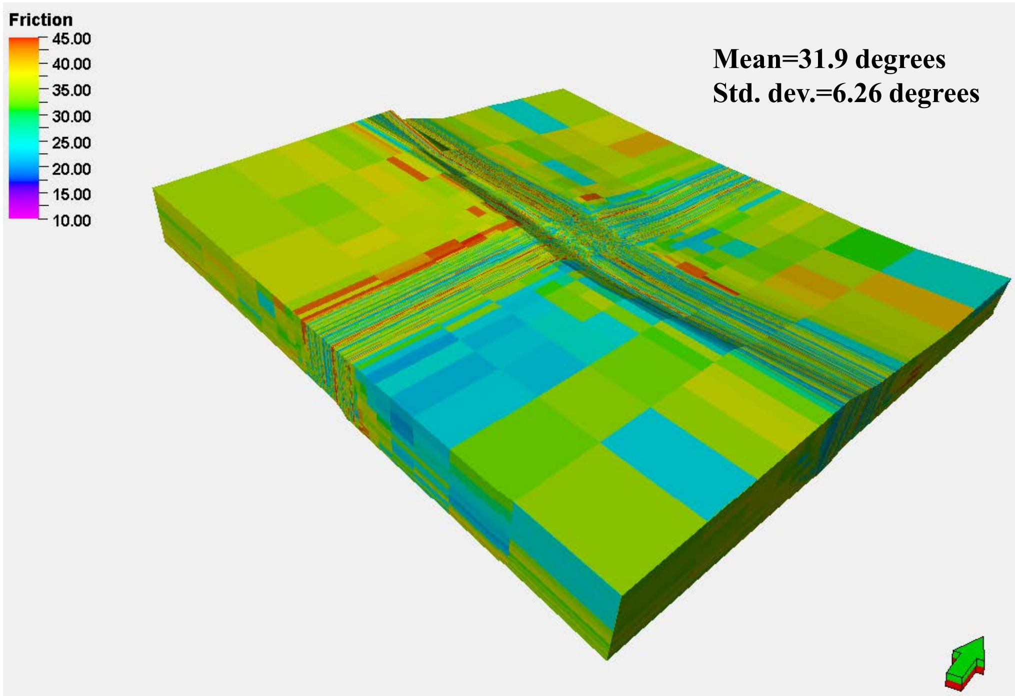

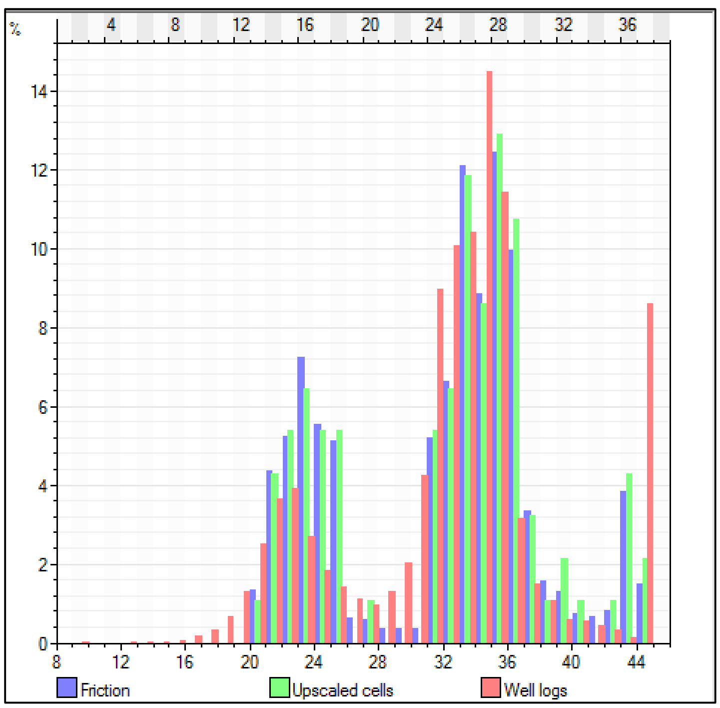

Figure A-32 MEM property distribution. (Top graph) Property distribution in the model. (Bottom) Histogram showing a comparison between the well log used for upscaling, the upscaled well log in the cell crossed by the well and the cells in the model.

Zone 3 (MI-2)

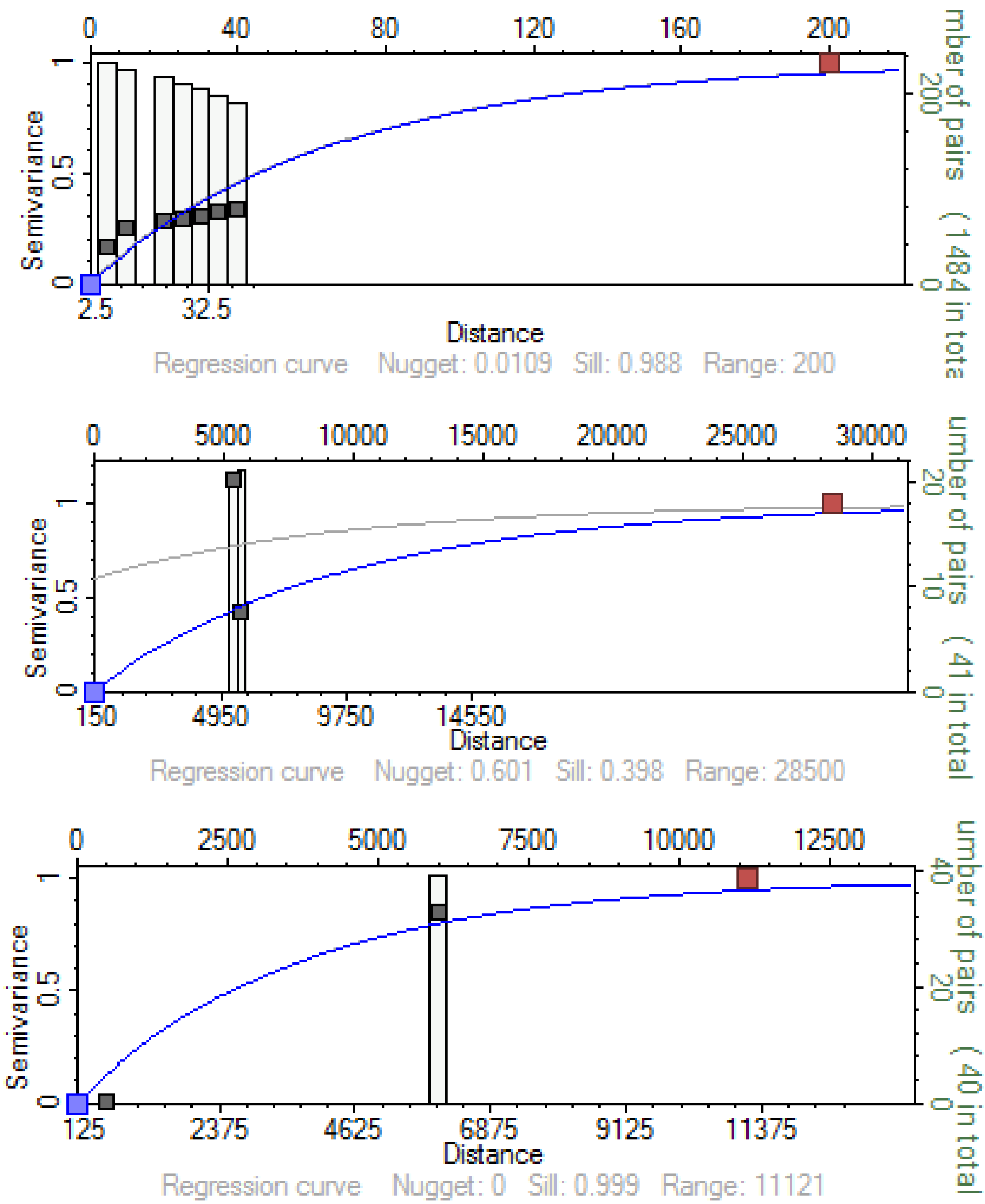

Figure A-33 Black squares represent experimental data, the black line is the regression variogram and the blue line the variogram model. (Upper variogram in vertical direction middle variogram in major direction and lower variogram in minor direction).

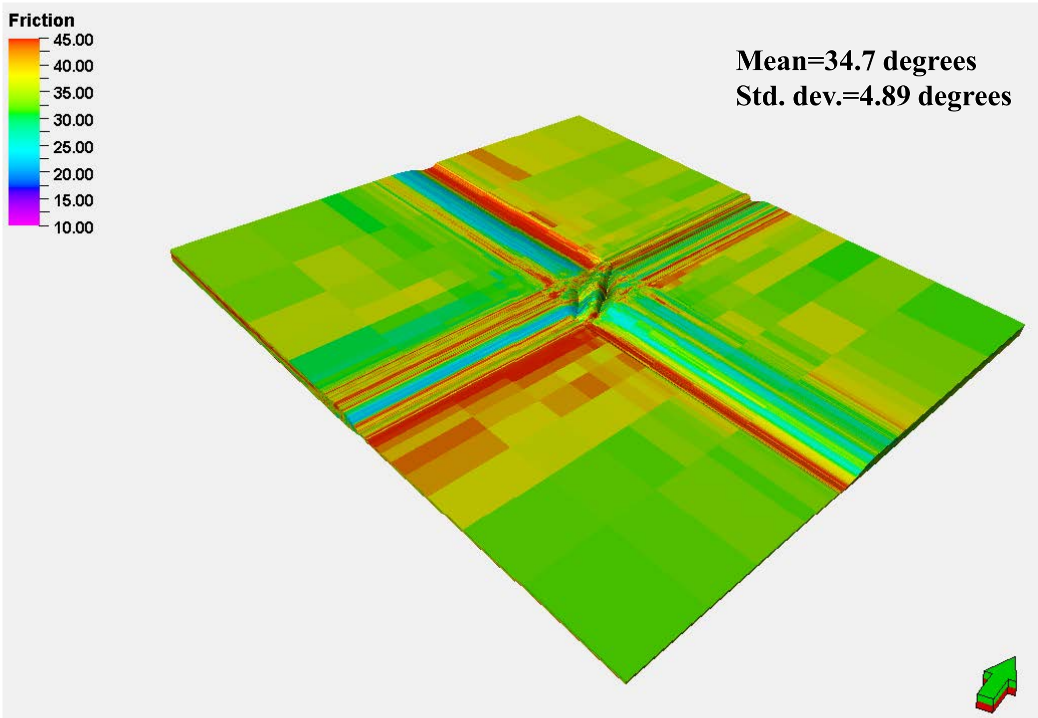

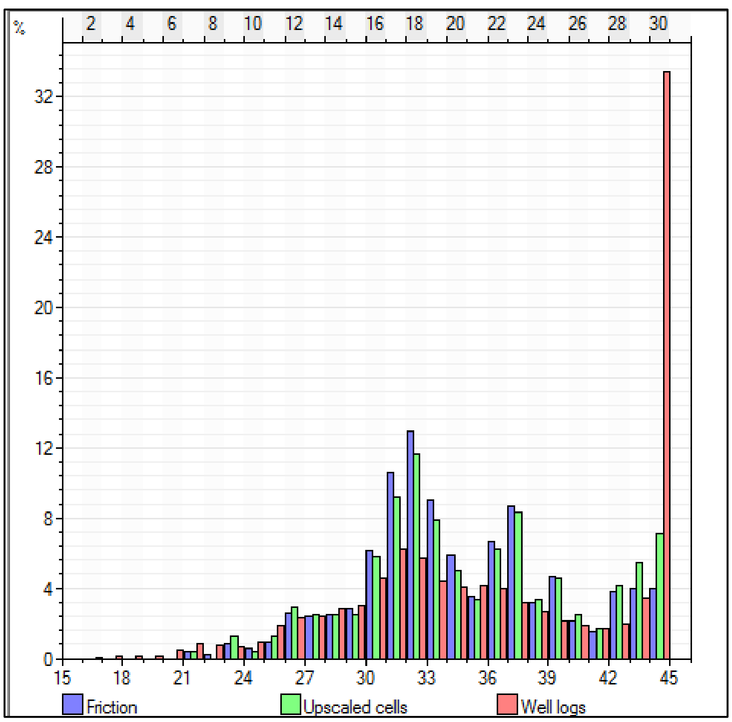

Figure A-34 MEM property distribution. (Top graph) Property distribution in the model. (Bottom) Histogram showing a comparison between the well log used for upscaling, the upscaled well log in the cell crossed by the well and the cells in the model.

Zone 5 (MI-1)

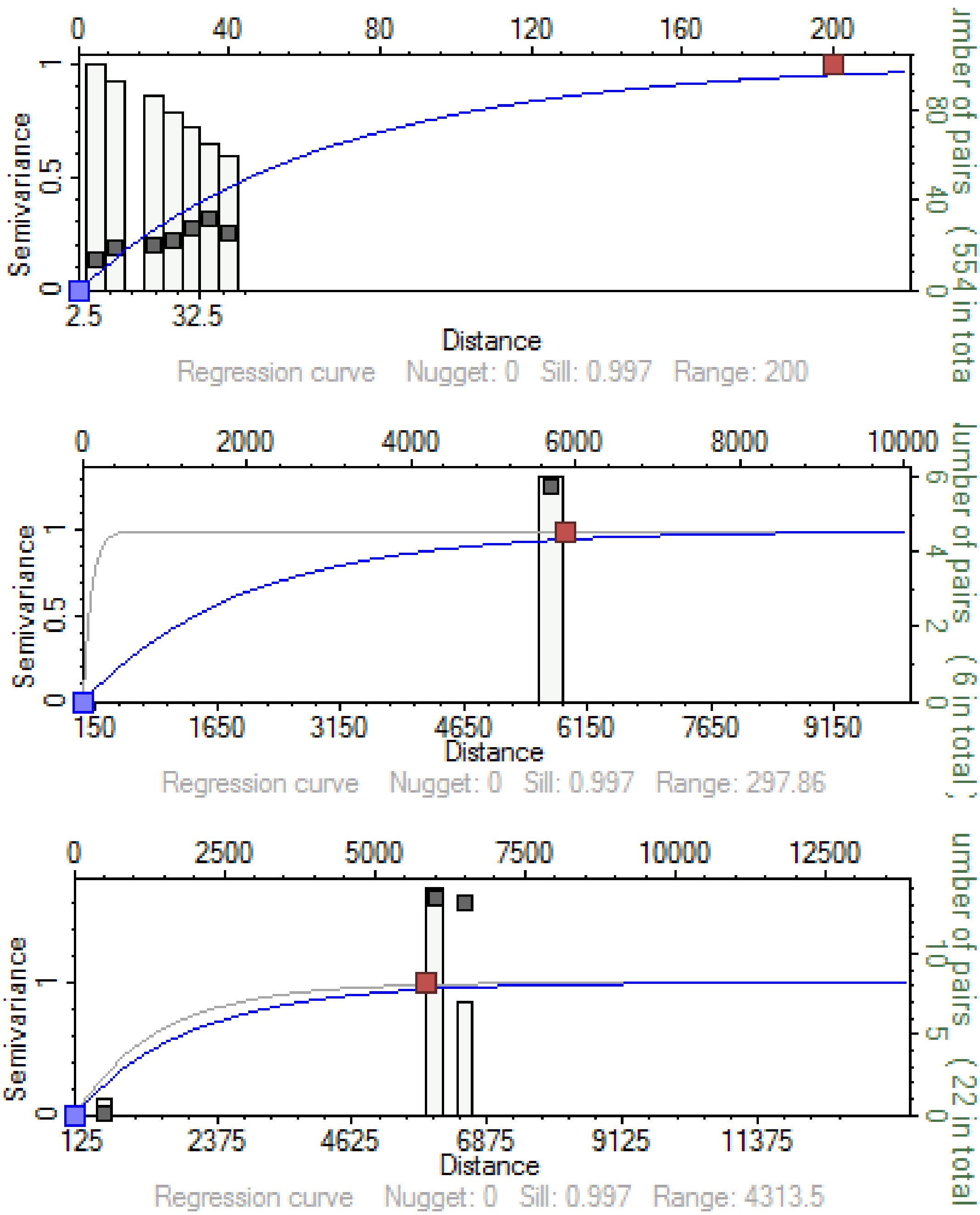

Figure A-35 Black squares represent experimental data, the black line is the regression variogram and the blue line the variogram model. (Upper variogram in vertical direction middle variogram in major direction and lower variogram in minor direction).

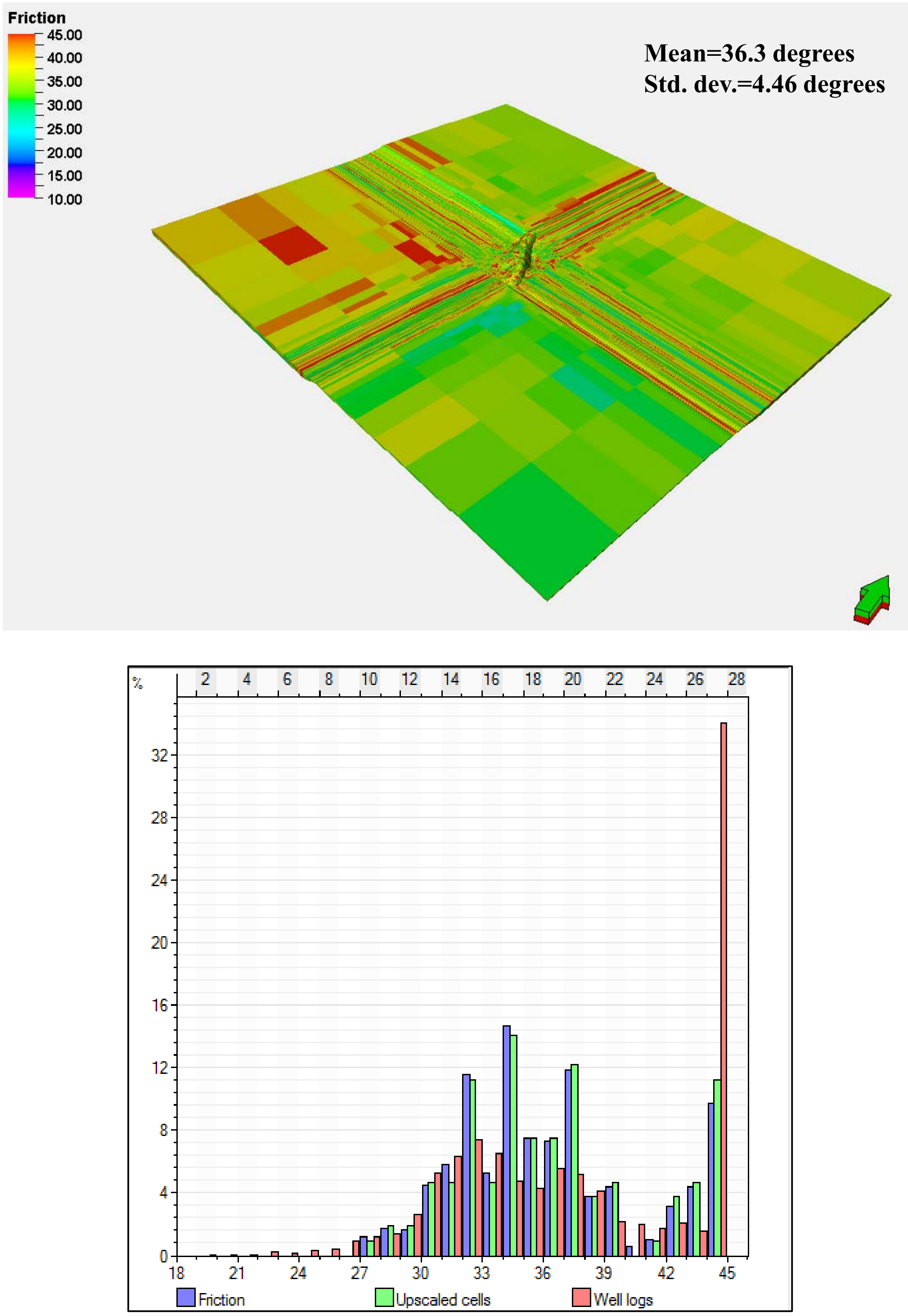

Figure A-36 MEM property distribution. (Top graph) Property distribution in the model. (Bottom) Histogram showing a comparison between the well log used for upscaling, the upscaled well log in the cell crossed by the well and the cells in the model.